Synthesis and Analysis of Model Complexes of the

Active Site of Nitrous Oxide Reductase

BY

SURESH CHANDRANATH RATHNAYAKA

B.Sc. University of Kelaniya Sri Lanka, 2013

THESIS

Submitted as partial fulfilment of the requirements
For the degree of Doctor of Philosophy in Chemistry
in the Graduate College of the
University of Illinois at Chicago, 2020

Chicago, Illinois

Defense Committee:

Neal P. Mankad, Chemistry, Chair and Advisor
Donald J. Wink, Chemistry
Stephanie M. Cologna, Chemistry
Andy I. Nguyen, Chemistry
Joshua Telser, Roosevelt University

"Don't you ever forget where you came from. Don't you ever forget your story. Your growth is found in your roots".
To all my teachers who raised me up here, to my dearest family who are waiting for their son, brother to return
home and to my beloved wife who is always there for me.

I should not forget the present either. I take this opportunity to thank the health professionals all around the world
who put their lives at risk in fighting against COVID-19 to save our lives. May you be safer, healthier and stronger.

ACKNOWLEDGEMENT

"Welcome to research" It was one of the responses that I received from my research advisor professor Neal Mankad, when I walked into his office with a frustrated mind (and some crappy results) during the early days of my PhD. From there to who I am today, I owe him so much for being patient with me, supporting, guiding and encouraging me. I have met a numerous teacher in my life and he, professor Mankad is the best mentor I have ever had. I feel like I was gifted to have him as my research advisor and I would like to thank him for spending time on me, trusting me and giving me opportunities to find my values and expand my potentials to become a successful researcher. All my hard work would not have been fruitful without his contribution and support.

The next person that I wish to express my gratitude is Dr. Brittany Johnson, a former group member who taught and trained me from the beginning. When I joined Mankad research group, I barely had any hands-on experience with the modern instruments and techniques in our lab. Brittany supported me to begin and grow myself as an individual researcher. Fun fact: I was influenced by her so much that sometimes when I faced certain research challenges, I used to ask myself, "what would Brittany do…?" Thank you for guiding me to become stronger and confident to ask myself "what would I do…?"

There are numerous other people who contributed with their talents to successfully complete the work presented and they will be individually credited here. Professor Stephanie Cologna and her Research Assistants (Chathurika Rathnayaka and Chandimal Padmasiri) helped me designing the GC-MS based N_2 quantification methods and apparatus. Without their expertise, I would not have been able to produce such precise data in completing the research objectives. Mr. Brian Schwandt from the UIC glass blowing unit helped me designing and making the special apparatus required for the precise N_2 quantifications. With the limited resources and options available, I do not know what else I would do without his expertise. Mr. Kevin and Rick from the machine shop were very much helpful providing me their machinery expertise throughout my time at UIC.

I would also like to thank John Anderson Group from University of Chicago for allowing me to use their facilities and resources for the qualitative analysis of produced water by nearIR spectroucopy. I am also grateful to Professor Joshua Telser from Roosevelt University for contributing with his EPR expertise. An immense gratitude goes to our collaborators, Dr. Shahidul Islam at UIC, Dr Sergey Lindeman at Marquette university and Professor Kyle Lancaster's group at Cornell University for their contributions in DFT, crystallographic and XAS analysis.

Graduate life is not easy without supportive group members, not just to discuss the chemistry but to share the laughter-sorrow, achievements-failures, relaxes-stresses and so on. I must acknowledge all our former and current group members (including postdocs and undergraduates) for holding to each other in needs. Their presence, contribution and ideas enlightened my work presented here. I extend my gratitude to all the staff members at the Department of Chemistry, UIC including our beloved Rhonda Staudohar and Gloria for all their support.

Finally, I would like to recognize and thank my thesis defense committee members: professors Neal P. Mankad, Donald J. Wink, Stephanie Cologna, Andy Nguyen and Joshua Telser for generously offering their time, support and guidance in reviewing the dissertation and evaluating my defense.

Suresh C. Rathnayaka

CONTRIBUTION OF AUTHORS

The research findings in each chapter and the supporting information presented at the end (Chapter 5) are contributed by multiple authors and each of them will be individually credited here. The texts, figures, tables, schemes and charts that originating from another author will be properly credited. Any reproduced data from literature including my own work has been properly referenced and the corresponding copyright permissions are given in appendices A-D.

Chapter 2

The content presented in Chapter 2 comes from published work in Rathnayaka, S. C.; Lindeman, S. V.; Mankad, N. P. Multinuclear Cu(I) Clusters Featuring a New Triply Bridging Coordination Mode of Phosphaamidinate Ligands. *Inorg. Chem.* **2018**, *57*, 9439–9445 and Rathnayaka, S. C.; Hsu, C.-W.; Johnson, B. J.; Iniguez, S. J.; Mankad, N. P. Impact of Electronic and Steric Changes of Ligands on the Assembly, Stability, and Redox Activity of $Cu_4(\mu_4$-S) Model Compounds of the Cu_Z Active Site of Nitrous Oxide Reductase (N$_2$OR). *Inorg. Chem.* **2020**, *59*, 6496–6507. While majority of the presented work in Chapter 2 is done by me, the co-authors Chia-Wei Hsu, Brittany J. Johnson and Sarah J. Iniguez helped me collecting data for the later publication. The X-ray crystallography data for complex **8**, **9** and **10** was produced by Dr. Sergey V. Lindeman at the Department of Chemistry, Marquette University (Milwaukee, WI). All the other crystallographic characterizations of new compounds presented in Chapter 2 were completed with the help of Professor Mankad at the Department of Chemistry, University of Illinois at Chicago. The X-band EPR data for complex **7h** was collected at Northwestern University by Professor Joshua Telser (Roosevelt University) and was supported by the U.S. Department of Energy (DOE), Office of Science, Basic Energy Sciences (BES) (grant DE-SC0019342 to Prof. Brian M. Hoffman).

Chapter 3

The research finding discussed in the Chapter 3 are closely following the published work in Hsu, C.-W.; Rathnayaka, S. C.; Islam, S. M.; MacMillan, S. N.; Mankad, N. P. N$_2$O Reductase Activity of a [Cu$_4$S] Cluster in the 4Cu(I) Redox State Modulated by Hydrogen Bond Donors and Proton Relays in the Secondary Coordination Sphere. *Angew. Chemie Int. Ed.* **2020**, *59*, 627–631, in which I share the co-first authorship with Chia-Wei Hsu who discovered the N$_2$O reactivity of the synthetic model complex [$Cu_4(\mu_4$-S) (dppa)$_4$]$^{2+}$ (**2**, dppa = Bis(diphenylphosphino)amine). The DTF

calculations were performed by Dr. Shahidul M. Islam at the Department of Chemistry, University of Illinois at Chicago (Chicago, IL). The single crystal data of complex **2** (in MeOH) and complex **3** were collected and processed by Dr. Samantha N. MacMillan at the Department of Chemistry and Chemical Biology, Cornell University (Ithaca, NY). Dr. Neal P. Mankad at the Department of Chemistry, University of Illinois at Chicago (Chicago, IL) authored the text and figures therein.

Chapter 4

The research outcomes presented in Chapter 4 closely follow the published content in Rathnayaka, S. C.; Islam, S. M.; DiMucci, I. M.; MacMillan, S. N.; Lancaster, K. M.; Mankad, N. P. Probing the Electronic and Mechanistic Roles of the μ_4 -Sulfur Atom in a Synthetic Cu$_Z$ Model System. *Chem. Sci.* **2020**, *11*, 3441–344. This is a collaborative work in three fields. The GC-MS quantification of produced N$_2$ was carried out by me while the supportive DFT study was conducted by Dr. Shahidul M. Islam at the Department of Chemistry, University of Illinois at Chicago (Chicago, IL). The XAS/DFT data were collected, processed and interpreted by Dr. Samantha N. MacMillan and Ida M. DiMucci at the Department of Chemistry and Chemical Biology, Cornell University (Ithaca, NY). The text and the figures on XAS/DFT analysis are authored by Professor Kyle M. Lancaster at the Department of Chemistry and Chemical Biology, Cornell University (Ithaca, NY) while the rest of the text and the figures are authored by Neal P. Mankad at the Department of Chemistry, University of Illinois at Chicago (Chicago, IL).

Chapter 5

All the supporting information found in Chapter 5 is reproduced with slight modifications from the published work in Rathnayaka, S. C.; Lindeman, S. V.; Mankad, N. P. Multinuclear Cu(I) Clusters Featuring a New Triply Bridging Coordination Mode of Phosphaamidinate Ligands. *Inorg. Chem.* **2018**, *57*, 9439–9445; Rathnayaka, S. C.; Hsu, C.-W.; Johnson, B. J.; Iniguez, S. J.; Mankad, N. P. Impact of Electronic and Steric Changes of Ligands on the Assembly, Stability, and Redox Activity of Cu$_4$(μ_4-S) Model Compounds of the Cu$_Z$ Active Site of Nitrous Oxide Reductase (N$_2$OR). *Inorg. Chem.* **2020**, *59*, 6496–6507; Hsu, C.-W.; Rathnayaka, S. C.; Islam, S. M.; MacMillan, S. N.; Mankad, N. P. N$_2$O Reductase Activity of a [Cu$_4$S] Cluster in the 4Cu(I) Redox State Modulated by Hydrogen Bond Donors and Proton Relays in the Secondary Coordination Sphere. *Angew. Chemie Int. Ed.* **2020**, *59*, 627–631 and Rathnayaka, S. C.; Islam, S. M.; DiMucci, I. M.; MacMillan, S. N.; Lancaster, K. M.; Mankad, N. P. Probing the Electronic and Mechanistic Roles of the μ_4 -Sulfur Atom in a Synthetic Cu$_Z$ Model System. *Chem. Sci.* **2020**, *11*, 3441–344. The

FIGURES S53-S56 are authored by Dr. Sergey V. Lindeman at the Department of Chemistry, Marquette university (Milwaukee, WI). The **FIGURES S57-S69** and **FIGURES S74-S77** are authored by Dr. Chia-Wei Hus at the Department of Chemistry, University of Illinois at Chicago (Chicago, IL). The **FIGURES S120-S126** are authored by Dr. Shahidul M. Islam at the Department of Chemistry, University of Illinois at Chicago (Chicago, IL). The **FIGURE S127** is authored by Professor Kyle M. Lancaster at the Department of Chemistry and Chemical Biology, Cornell University (Ithaca, NY) and the rest of the content is authored by me.

TABLE OF CONTENTS

LIST OF FIGURES

LIST OF TABLES

LIST OF SCHEMES

LIST OF CHARTS

LIST OF ABBREIVATIONS

$[CoCp_2]^+$	Cobaltocenium
BNF	Biological nitrogen fixation
CH_3	Methyl
Cl^-	Chloride
CO_2	Carbon dioxide
$CoCp_2$	Cobaltocene
CPCM	Conductor-like polarizable continuum model
CT	Charge transfer
Cu_2S	Cuprous sulfide
CuCl	Cuprous chloride
CuS	Cupric sulfide
CV	Cyclic voltammogram
DFT	Density functional theory
dpfam	*N,N′* -bis[2- (diphenylphosphino)phenyl]formamidinate
dppa	Bis(diphenylphosphino)amine
dppa'	Bis(diphenylphosphanyl)amide
dppe	Bis(diphenylphosphino)ethane
dppf	Bis(diphenylphosphino)ferrocene
dppm	Bis(diphenylphosphino)methane
dpqfam	N-(2- diphenylphosphino)phenyl-N′-8-quinolylformamidinate
EPR	Electron paramagnetic resonance
Et_2O	Diethyl ether
Fc	Ferrocene
Fp	Cyclopentadienyliron dicarbonyl
FT-IR	Fourier transform infrared
GC-MS	Gas chromatography-Mass spectrometry
GGA	Generalized gradient approximation
GWP	Global warming potential
H_2O	Water
HFCs	Hydrofluorocarbons
HOMO	Highest occupied molecular orbital
I^-	Iodide
K	Potassium
L	Ligand
LMCT	Ligand to metal charge transfer
LUMO	Lowest unoccupied molecular orbital
MeCN	Acetonitrile
MeOH	Methanol
Mes	2,4,6-trimethylphenyl
MMT	Million metric tons
MO	Molecular orbital
N_2O	Nitrous oxide
N_2OR	Nitrous oxide reductase enzyme
Na_2S	Sodium sulfide
NaHMDS	Sodium bis(trimethylsilyl)amide
NCN	Formamidinate ligand
NMR	Nuclear magnetic resonance
O^{2-}	Oxide
OAc	Acetate
o-CF_3	Ortho methoxy
OEC	Oxygen evolving complex
p-CF_3	Para trifluoromethyl
PDB	Protein data bank

PFCs	Per-and polyfluoroalkyl substances
pH	Potential hydrogen
PhC(O)Cl	Benzoyl chloride
p-OMe	Para methoxy
qfam	*N,N′*-di-8-quinolylformamidinate
RAMO	Redox-active molecular orbital
RT	Room temperature
SiMe$_3$	Trimethylsilyl
SO$_4{}^{2-}$	Sulfate
SOMO	Singly occupied molecular orbital
SSRL	Stanford Synchrotron Radiation Light
TD-DFT	Time-dependent density functional theory
THF	Tetrahydrofuran
UV-Vis	Ultra-violet visible
XANES	X-ray absorption near edge structure
XAS	X-ray absorption spectroscopy
XRD	X-ray diffractometry
ZORA	Zeroth-order regular approximation

SUMMARY

Chapter 1 summarizes the role of nitrous oxide (N_2O) in the eco system, its accumulation, impact and metabolism. Prolong accumulation of N_2O is heavily contributing to the global warming and it is a leading cause of ozone layer depletion. Anthropogenic activities like agricultural soil management, stationary combustion, manure management, mobile combustion, adipic and nitric acid production and wastewater treatments are primarily responsible for the increased levels of N_2O. Nature metabolizes the terrestrial N_2O through microbial denitrification in soils, fresh and marine waters. Nitrous oxide reductase (N_2OR) is one of the enzymes that is found in denitrification bacteria that converts N_2O to dinitrogen (N_2) and water (H_2O). The $2e^-/2H^+$ reduction of N_2O is thermodynamically favorable, yet it is metal catalyzed due to the multielectron/proton demand and the inertness of N_2O. N_2OR contains two metal domains; dicopper electron transfer site (Cu_A) and $Cu_4(\mu_4\text{-S})$ active site (Cu_Z). The introduction chapter presents the detailed descriptions of the composition and reactivity of various forms of Cu_Z, their isolation, characterization, physiological relevance, substrate (N_2O) interaction and finally the latest proposed mechanism. Most of the presented literature work that reveals the identity and function of this unusual $Cu_4(\mu_4\text{-S})$ domain is based on spectroscopic, crystallographic and computation methods. The attempted synthetic model compound studies and their important outcomes are also addressed at the end of the chapter.

Chapter 2 discusses the findings of the published work in reference Rathnayaka, S. C.; Lindeman, S. V.; Mankad, N. P. Multinuclear Cu(I) Clusters Featuring a New Triply Bridging Coordination Mode of Phosphaamidinate Ligands. *Inorg. Chem.* **2018**, *57*, 9439–9445 and Rathnayaka, S. C.; Hsu, C.-W.; Johnson, B. J.; Iniguez, S. J.; Mankad, N. P. Impact of Electronic and Steric Changes of Ligands on the Assembly, Stability, and Redox Activity of $Cu_4(\mu_4\text{-}$S) Model Compounds of the Cu_Z Active Site of Nitrous Oxide Reductase (N_2OR). *Inorg. Chem.* **2020**, *59*, 6496–6507. Our findings on the establishment of a tunable synthetic protocol for $Cu_4(\mu_4\text{-S})$ model complexes fills a vital part of the Cu_Z synthetic model chemistry. The structure, characterization and reactivity of multi copper clusters supported by phosphine, formamidinate (NCN) and phosphaamidinte ligands are presented. The assembly, structure and reactivity of the resulting clusters highly depend on the ligand environment, thus letting us discover the properties of an ideal ligand system that would closely mimic the structure and reactivity of the Cu_Z active site. Our synthetic approach uses dicopper(I) precursor complexes (Cu_2L_2) that assemble into $Cu_4(\mu_4\text{-S})L_4$ cluster with the addition of an appropriate sulfur source. Here, we summarize the features of the ligands L that stabilize precursor and $Cu_4(\mu_4\text{-S})$

clusters, along with the alternative products that form with inappropriate ligands. The precursors are more likely to rearrange to $Cu_4(\mu_4\text{-}S)$ clusters when the Cu^{1+} ions are supported by bidentate ligands with 3-atom bridges, but steric and electronic features of the ligand also play crucial roles. Neutral phosphine donors have been found to stabilize $Cu_4(\mu_4\text{-}S)$ clusters in the $4Cu^{1+}$ oxidation state, while neutral nitrogen donors could not stabilize $Cu_4(\mu_4\text{-}S)$ clusters. Anionic formamidinate ligands have been found to stabilize $Cu_4(\mu_4\text{-}S)$ clusters in the $2Cu^{2+}$ - $2Cu^{2+}$ and $1Cu^{2+}$ - $3Cu^{1+}$ states, with both the formation of the dicopper(I) precursors and subsequent assembly of clusters being governed by the steric factor at the *ortho* positions of the *N*-aryl substituents. Phosphaamidinates, which combine a neutral phosphine donor and an anionic nitrogen donor in the same ligand, form multinuclear Cu(I) clusters unless the negative charge is valence-trapped on nitrogen, in which case the resulting dicopper precursor is unable to rearrange to a multinuclear cluster. Taken together, the results presented in Chapter 2 provide design criteria for successful assembly of synthetic model clusters for the Cu_Z active site of N_2OR, which should enable future insights into the chemical behavior of Cu_Z.

The content presented in Chapter 3 closely follows the published work in reference Hsu, C.-W.; Rathnayaka, S. C.; Islam, S. M.; MacMillan, S. N.; Mankad, N. P. N_2O Reductase Activity of a $[Cu_4S]$ Cluster in the 4Cu(I) Redox State Modulated by Hydrogen Bond Donors and Proton Relays in the Secondary Coordination Sphere. *Angew. Chemie Int. Ed.* **2020**, *59*, 627–631. The impact of the secondary sphere interactions upon the structure and reactivity of a synthetic $Cu_4(\mu_4\text{-}S)$ model complex is discussed. The synthetic model complex $[Cu_4(\mu_4\text{-}S)\,(dppa)_4]^{2+}$ (**2**, dppa = Bis(diphenylphosphino)amine) has been found to have N_2O reductase activity in methanol solvent, mediating the $2H^+/2e^-$ reduction of N_2O to $N_2 + H_2O$ in the presence of an exogenous electron donor $CoCp_2$. A stoichiometric product featuring two deprotonated dppa ligands has been characterized, indicating a key role of second-sphere N–H residues as proton donors during N_2O reduction. The stoichiometry amount of produced N_2 has been quantified using GC-MS and the production of water has been qualitatively confirmed by nearIR method. The activity of **2** towards N_2O is suppressed in solvents that are unable to provide hydrogen bonding to the second-sphere N–H groups. Structural and computational data indicate that second-sphere hydrogen bonding induces structural distortion of the $[Cu_4(\mu_4\text{-}S)]$ active site, accessing a strained geometry with enhanced reactivity due to localization of electron density along a dicopper edge site. The behavior of **2** mimics several aspects of the Cu_Z catalytic site of nitrous oxide reductase: activity in the $4Cu^{1+}:1S$ redox state, use of a second-sphere proton donor, and reactivity dependence on both primary and secondary sphere effects.

Chapter 4 also closely follows the published content in Rathnayaka, S. C.; Islam, S. M.; DiMucci, I. M.; MacMillan, S. N.; Lancaster, K. M.; Mankad, N. P. Probing the Electronic and Mechanistic Roles of the μ_4-Sulfur Atom in a Synthetic Cu_Z Model System. *Chem. Sci.* **2020**, *11*, 3441–344. This chapter reports a combined experimental/computational study of a synthetic [4Cu1S] cluster supported by N-donor ligands that can be considered the closest structural and functional mimic of the Cu_Z catalytic site in N_2OR reported to date. Quantitative N_2 measurements during synthetic N_2O reduction have been used to determine reaction stoichiometry, which in turn is used as the basis for density functional theory (DFT) modeling of hypothetical reaction intermediates. The mechanism for N_2O reduction emerging from this computational modeling involves cooperative activation of N_2O across a Cu/S cluster edge. Direct interaction of the μ_4-S ligand with the N_2O substrate during coordination and N–O bond cleavage represents an unconventional mechanistic paradigm to be considered for the chemistry of Cu_Z and related metal-sulfur clusters. Consistent with hypothetical participation of the μ_4-S unit in two-electron reduction of N_2O, Cu K-edge and S K-edge X-ray absorption spectroscopy (XAS) reveal a high degree of participation by the μ_4-S in redox changes, with approximately 21% S $3p$ contribution to the redox-active molecular orbital in the highly covalent [4Cu1S] core, compared to approximately 14% Cu $3d$ contribution per copper. The XAS data included in here represent the first spectroscopic interrogation of multiple redox levels of a [4Cu1S] cluster and show high fidelity to the biological Cu_Z site.

Chapter 5 contains all the synthetic procedures, characterization data, instrument and method specifications, experimental designs and other relevant supporting information from the published work in Rathnayaka, S. C.; Lindeman, S. V.; Mankad, N. P. Multinuclear Cu(I) Clusters Featuring a New Triply Bridging Coordination Mode of Phosphaamidinate Ligands. *Inorg. Chem.* **2018**, *57*, 9439–9445; Rathnayaka, S. C.; Hsu, C.-W.; Johnson, B. J.; Iniguez, S. J.; Mankad, N. P. Impact of Electronic and Steric Changes of Ligands on the Assembly, Stability, and Redox Activity of $Cu_4(\mu_4$-S) Model Compounds of the Cu_Z Active Site of Nitrous Oxide Reductase (N_2OR). *Inorg. Chem.* **2020**, *59*, 6496–6507; Hsu, C.-W.; Rathnayaka, S. C.; Islam, S. M.; MacMillan, S. N.; Mankad, N. P. N_2O Reductase Activity of a [Cu_4S] Cluster in the 4Cu(I) Redox State Modulated by Hydrogen Bond Donors and Proton Relays in the Secondary Coordination Sphere. *Angew. Chemie Int. Ed.* **2020**, *59*, 627–631; Rathnayaka, S. C.; Islam, S. M.; DiMucci, I. M.; MacMillan, S. N.; Lancaster, K. M.; Mankad, N. P. Probing the Electronic and Mechanistic Roles of the μ_4-Sulfur Atom in a Synthetic Cu_Z Model System. *Chem. Sci.* **2020**, *11*, 3441–344.

1.   INTRODUCTION

1.1   Nitrous Oxide

Nitrous oxide (N_2O) is one of the oxidized forms of nitrogen (N_2) present in the global nitrogen cycle, in which the atmospheric N_2 is accumulated in terrestrial systems through biological nitrogen fixation (BNF) and later released back to atmosphere as N_2 by the bacterial denitrification pathways.[1] The anthropogenic production of N_2O disturbs the global nitrogen cycle, resulting in accumulation of N_2O. According to "DRAFT inventory of greenhouse gas emissions and sinks, 1990-2018" by the United States Environmental Protection Agency, the global atmospheric concentration of N_2O has increased from 270 ppb to 331 ppb (by 23%) since 1750, reaching a concentration that had not been exceeded during the last 800,000 years.[2] The increasing levels of N_2O is an emerging threat as N_2O is one of the main contributors towards global warming and ozone layer depletion.[1–4] Certainly, N_2O is not the most abundant greenhouse gas (**Figure 1.1**); nonetheless, its global warming potential (GWP) is 298-fold higher compared to CO_2 due to its atmospheric lifetime of 121 years.[2] The anthropogenic production of N_2O in the United States primarily occurs by agricultural soil management, stationary combustion, manure management, fuel combustion and adipic acid production (**Figure 1.2**).[2,3]
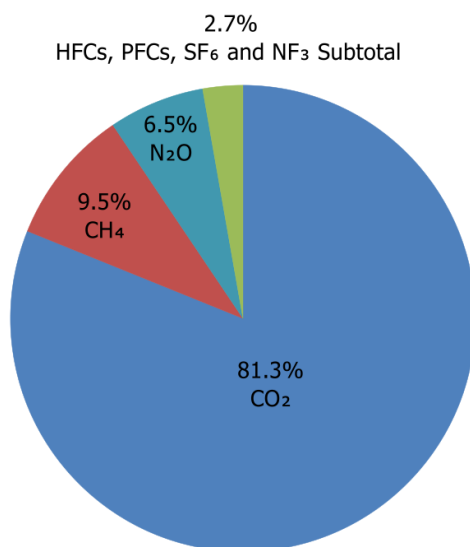
FIGURE 1. 1 2018 greenhouse gas emissions (% by MMT CO2 Eq.) by gas in the United States. Figure was taken from the "Draft Inventory of U.S. Greenhouse Gas Emissions and Sinks, 1990-2018" by EPA.[2]
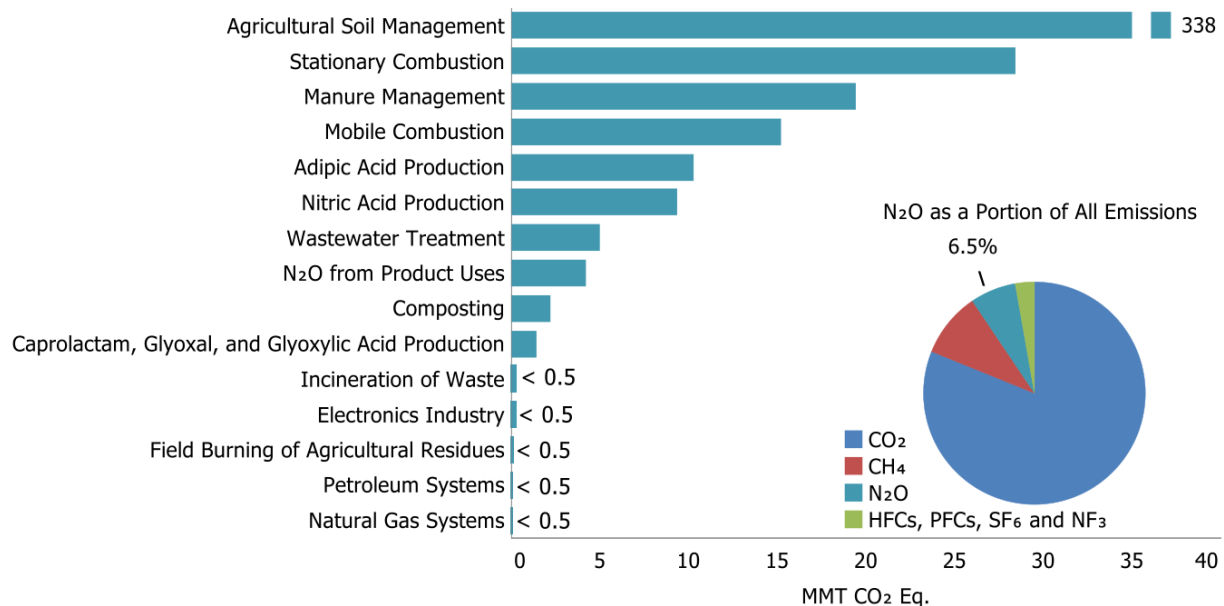
FIGURE 1. 2 2018 Sources of N_2O emissions (MMT CO_2 Eq.) in the United States. Figure was taken from the "Draft Inventory of U.S. Greenhouse Gas Emissions and Sinks, 1990-2018" by EPA.[2]

From 1990 to 2018, the total emission on CO_2 has been increased by 300.9 MMT CO_2 Eq. (5.9 %) and that of CH_4 has been decreased by 139.9 MMT CO_2 Eq. (18.1 %).[2] Despite fluctuations, the total emission of N_2O has remained constant.[2] The impact of N_2O on the ecosystem due to higher GWP, atmospheric lifetime, and ozone layer depletion raises the awareness in scientific community to explore its metabolic pathways.

1.2 N_2O metabolism

The atmospheric N_2O is primarily removed by the photolytic action of sunlight in the stratosphere,[2] while the terrestrial N_2O is metabolized through microbial denitrification in soils, fresh and marine waters.[1] Under anoxic conditions, these denitrification organisms consume the oxidized forms of N_2 in place of molecular dioxygen (O_2) for essential metabolic pathways including anerobic respiration and ATP synthesis.[5–8] Up to date only three enzymes, nitrogenase, multicopper oxidase, and nitrous oxide reductase (N_2OR), have been identified to metabolize N_2O, with the latter being the predominant. Interestingly, these metalloproteins neither share the same catalytic site nor the metal composition. Nitrogenase, a metalloenzyme found in the nitrogen fixation pathway, has a FeMo cofactor that produces NH_3 using N_2 as its substrate.[9] Studies show that N_2O acts as an competitive inhibitor; in fact, nitrogenase utilizes N_2O as a source of its substrate N_2.[10–13] The enzyme from archaeon *Pyrobaculum aerophilum* produced in *E. coli*

remains as the only example of multicopper oxidase that utilizes N_2O in place of its primary substrate O_2 to function as a metallo-oxidase for Fe^{2+} and Cu^{1+}.[14] Its catalytic site is composed of a trinuclear copper site supported by histidine groups, but the absence of sulfur and the geometric orientation may disfavor the coordination and activation of N_2O as compared to N_2OR.[14] To date, the products resulting from N_2O activation by multicopper oxidase under physiological conditions are not known, hence the N_2O utilized catalytic mechanism remains unanswered. Out of the previously mentioned enzymes, N_2OR is the most efficient and physiologically relevant enzyme in removing terrestrial N_2O. N_2OR is one of the enzymes participating in the microbial denitrification process that involves consecutive reduction of nitrate (NO_3^-) by a sequence of enzymes in which the N_2O is converted into inert N_2 and H_2O by N_2OR at the last step (**Scheme 1**).[5] The $2H^+/2e^-$ reduction of N_2O is thermodynamically favorable ($\Delta G^\circ = -339.5$ kJ/mol) but requires to be catalytically driven by N_2OR due to a high activation energy barrier (250 kJ/mol) coupled to a spin forbidden process.[6,7]

$$NO_3^- \xrightarrow{\substack{\text{Nitrate} \\ \text{Reductase}}} NO_2^- \xrightarrow{\substack{\text{Nitrite} \\ \text{Reductase}}} NO \xrightarrow{\substack{\text{Nitric Oxide} \\ \text{Reductase}}} \boxed{N_2O \xrightarrow{\substack{\textbf{Nitrous Oxide} \\ \textbf{Reductase}}} N_2}$$

$$N_2O + 2e + 2H^+ \longrightarrow N_2 + H_2O \qquad \Delta G^\circ = -339.5 \text{ kJ/mol}$$

$$\Delta G^\ddagger = 250 \text{ kJ/mol}$$
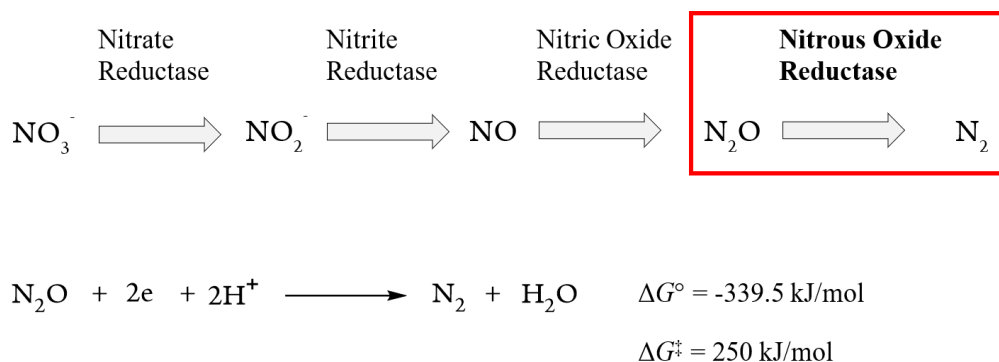
SCHEME 1. 1 The sequence of bacterial denitrification highlighting the final step of converting N_2O to N_2. The enzyme involved in each catalytic step is given on the arrow.

1.3 N_2OR overview

N_2OR is a homodimeric metalloenzyme with a molecular weight of ~120 kDa, and each monomer carries six copper atoms that are located in two distinct metal domains.[15] The electron transfer site (Cu_A) at the C-terminal holds two copper atoms while the active site (Cu_Z) at the N-terminal contains four copper atoms.[6,16] Dimers are arranged in head to tail fashion such that the Cu_A site of a monomer lies ca. 10 Å to the Cu_Z site of the other monomer while the two sites of the same monomer are approximately 40 Å apart (**Figure 1.3**).[6,17] It is more likely that the copper centers

in the same monomer are far too away for efficient electron transfer, but Cu_A and Cu_Z from two subunits are in proximity for a cooperative substrate (N_2O) reduction.[17]
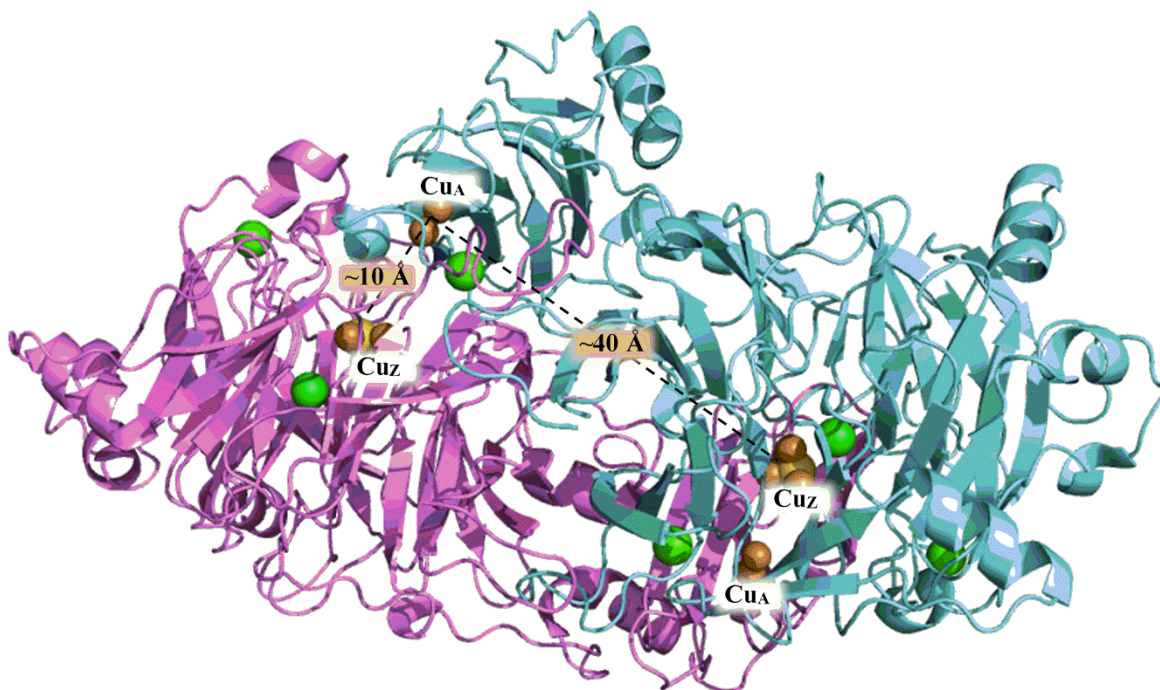
FIGURE 1. 3 Ribbon diagram of N_2OR (from *Pseudomonas nautica*, at 2.4-Å resolution, PDB ID 1QNI) dimer with the distances shown between Cu_A and Cu_Z sites of the same monomer (~40 Å) and the two different monomers (~10 Å). Two monomers are colored in violet and aquamarine, respectively, Ca^{2+} in shown in green, Cu is shown in brown, and S in yellow.[18] Image was created using PyMol educational version.

In all isolated N_2OR crystal structures, additional electron densities corresponding to Ca^{2+}/K^+ are seen close to the metal domains.[17] However, studies of nonmetalated N_2OR propose that Ca^{2+} was incorporated into the protein after the *in vivo* metalation events, implying that Ca^{2+}/K^+ ions are not required for dimer formation but presumably help the protein's structural integrity and rigidity by keeping the two monomers together.[19]

1.4 Cu_A electron transfer site

Cu_A is a binuclear copper site located at the C-terminus, and its existence was first discovered by Kroneck and his co-workers using spectroscopic techniques, primarily EPR, EXAFS and UV-Vis.[20] The multifrequency EPR studies of the oxidized form of Cu_A demonstrated a direct Cu-Cu interaction similar to cytochrome *c* oxidase and was assigned to be a mixed-valent dicopper site [$Cu^{1.5+}$-$Cu^{1.5+}$].[21–23] The X-band EPR of the oxidized form displayed a 7-

line hyperfine (intensity rations 1:2:3:4:3:2:1) pattern with $g_{\parallel} = 2.18$, $g_{\perp} = 2.13$ and $A_{\parallel} = 3.38$ mT due to the unpaired electron delocalized over the two metal centers ($I_{Cu} = 3/2$) while the reduced form [Cu^{1+}-Cu^{1+}] was EPR silent as no electron holes were present.[5,6] The EXAFS studies suggested that the Cu_A is a Cu_2S_2 cluster with 2.43 Å Cu-Cu and 2.2 Å Cu–S distances.[24] Later, the EXAFS predictions on the identity and the geometry parameters of Cu_A were confirmed with the X-ray structure of N_2OR from *Pseudomonas nautica*, at 2.4-Å resolution.[18] The visible spectrum of the oxidized form of Cu_A displays absorption maxima at 480, 525-540 nm associated with S(sys)→Cu charge transfer (LMCT) and at 800 nm for mixed valence Ψ→Ψ* IVCT.[5,6] Overall, Cu_A has been well characterized using crystallographic and spectroscopic techniques for its function as an electron shuttle for N_2O activation by Cu_Z active site.
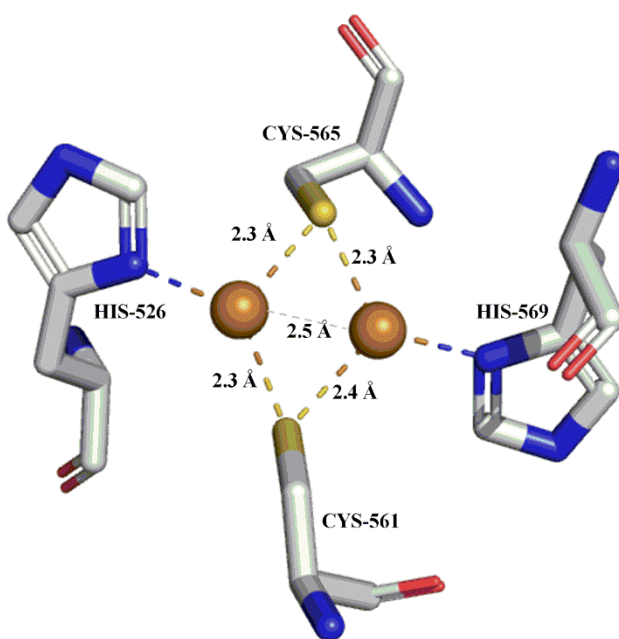
FIGURE 1. 4 The Cu_2S_2 electron transfer site (Cu_A) of N_2OR from *Pseudomonas nautica*, at 2.4-Å resolution (PDB ID 1QNI) with selected bond distances shown.18 HIS-525 and HIS 569 are coordinated to Cu ions while CYS-565 and CYS-561 residues are bridging between Cu atoms through their S atoms. Image was created using PyMol educational version.

1.5   N₂OR active site

1.5.1   Overview

The structure and the identity of the tetra nuclear copper sulfide active site of N_2OR remained obscure for several years until it was characterized using X-ray crystallography and spectroscopic techniques starting in the late 1990's.[25,26,27] To date, two forms of the active site have been biologically isolated and denoted as Cu_Z (Cu_4S_2) and Cu_Z* (Cu_4S) that differ in their composition, structure, spectroscopic and kinetic/activity features (**Figure 1.5**).[5] It is challenging to isolate N_2OR with a pure form of Cu_Z or Cu_Z*. Generally, the anerobic conditions favor the Cu_Z while aerobic isolation favors Cu_Z*, in which the sulfide along Cu_I–Cu_{IV} edge of Cu_Z has been replaced with a solvent derived molecule.[5,6] In both forms the active site resembles a distorted tetrahedral geometry supported by 7 conserved histidine residues with each copper except Cu_{IV} bound to 2 histidine groups. For both forms, the average Cu–S bond distance remains ~2.3 Å and the Cu_{II} and Cu_{IV} are closer to Cu_{II} than Cu_I with Cu_{I-IV} and Cu_I–Cu_{III} distances being ~3.3-3.6 Å while Cu_{II}–Cu_{IV} and Cu_{II}–Cu_{III} distances lie ~2.4-2.8 Å.[8,25,28]
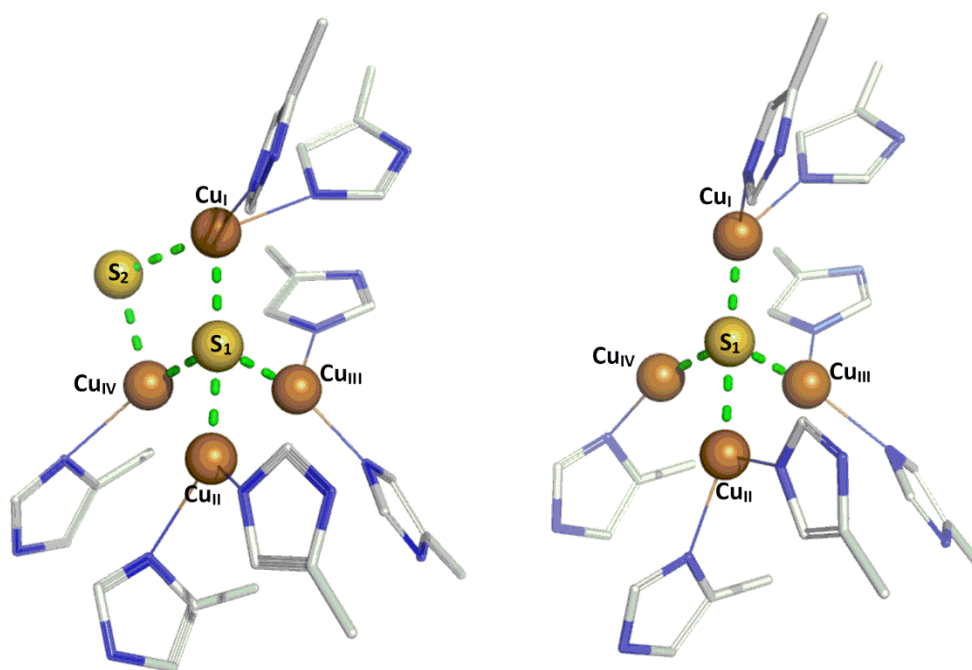
FIGURE 1. 5 The two forms of the active site of N_2OR isolated biologically. *(left)* Cu_Z isolated anaerobically from *Paracoccus denitrificans* (PDB ID 1FWX) at 2.16 Å resolution. *(right)* Cu_Z* isolated aerobically from *Pseudomonas stutzeri* (PDB ID 3SBP) at 2.1 Å resolution. Image was created using PyMol educational version.

1.5.2 Cu$_Z$, Cu$_Z$* and their redox forms

Cu$_Z$ is typically isolated as its oxidized state [2Cu^{2+} - 2Cu$^+$] with the oxidized (2Cu$^{1.5+}$) form of Cu$_A$.[5,6,17] By convention, the oxidized form of Cu$_Z$ termed as a "2-hole complex", as two Cu^{2+} (d^9) ions bring two electron holes (from now onward, oxidized form of Cu$_Z$ will be called "2-hole Cu$_Z$"). Selective reduction of Cu$_A$ by sodium ascorbate allows the isolation and spectroscopic characterization of 2-hole Cu$_Z$ with the reduced form of Cu$_A$ (2Cu^{1+}).[29] The UV-Vis spectrum of 2-hole Cu$_Z$ exhibits absorption bands ~550 and 650 nm correspond to S(3p)→Cu(3d) LMCT that has been further supported by resonance Raman spectroscopy and DFT calculations.[30,31]

Dithionite could reduce both Cu$_A$ and Cu$_Z$ sites, and the reduced form of Cu$_Z$ features a [1Cu^{2+} - 3Cu^{1+}] electronic state. Accordingly, the reduced form of Cu$_Z$ is called as "1-hole Cu$_Z$" and it becomes EPR active with the electron hole being delocalized over the four Cu atoms.[31,32] The 1-hole Cu$_Z$ has only one characteristic band at ~670 nm in the visible spectrum which is attributed to S→Cu, His→Cu CT and low energy Cu d→d transitions.[6] The reduction potential of 2-hole/1-hole pair has been estimated to be +60 mV at pH 7.5.[33] To date, no 3-hole [3Cu^{2+} - 1Cu^{1+}], 4-hole [4Cu^{2+}] or the fully reduced [4Cu^{1+}] form of Cu$_Z$ has been reported. In fact, the attempted prolonged incubation with reduced methyl viologens to reach the fully reduced [4Cu^{1+}] form of Cu$_Z$ was unsuccessful.[29]

Cu$_Z$* could also be isolated with either oxidized or reduced form of Cu$_A$. The primary differences of geometry and coordination of Cu$_Z$* and Cu$_Z$ arise from the solvent derived molecule coordinated across the Cu$_I$–Cu$_{IV}$ edge. The observed spectroscopic features[31,34,35] have been best fitted to an occupancy of a hydroxyl (OH$^-$) ligand across the Cu$_I$–Cu$_{IV}$ edge that is slightly closer to Cu$_I$ (2.00 Å) than Cu$_{IV}$ (2.09 Å).[36,37] Cu$_Z$* also possesses a [1Cu^{2+} - 3Cu^{1+}] electronic state and is accordingly called "1-hole Cu$_Z$*". The visible spectrum of Cu$_Z$* consist of a strong absorption band ~640 nm that is attributed to S→Cu, His→Cu CT and high energy Cu d→d transitions.[27,36,38] Literature reports indicate that the absorption band at ~550 nm in 2-hole Cu$_Z$ may originate from the μ_2-S$_2$ atom, as it is disappeared in the visible spectrum of 1-hole Cu$_Z$*.[17] However, it is questionable as the 1-hole Cu$_Z$ which has a μ_2-S$_2$ atom and a similar electronic state to 1-hole Cu$_Z$* does not feature the absorption band at ~550 nm. Unlike 2-hole Cu$_Z$, the 1-hole Cu$_Z$* is resistant to reduction. In fact, it can only be reduced to the spectroscopic silent fully reduced state (4Cu^{1+}) upon prolong incubation (3-5 h) with large excess of reduced viologen.[29] The reduction potential of [1Cu^{2+} - 3Cu^{1+}]/[4Cu^{1+}] has not been reported as electrochemical reduction of 1-hole Cu$_Z$* is not achievable.[39]

Apart from the above discussed redox species of N$_2$OR (**Table 1.1**), no other redox forms of the active site have been reported up to the date. However, some interesting derivatives of those forms have been characterized using spectroscopic and crystallographic techniques and will be discussed in the following sections.

TABLE 1. 1 Isolable redox forms of N$_2$OR with their purification method, active site composition, spin state and visible spectrum absorption. See ref 5,6,17 and 29 for detailed information.

Redox form of N$_2$OR		Source	Active site type/ composition	Active site Spin state	Active site visible spectrum
Cu$_A$	Active site				
[Cu$^{1.5+}$ - Cu$^{1.5+}$]	[2Cu^{2+} - 2Cu$^+$]	Anerobic purification		S = 0	N/A
[Cu^{1+} - Cu^{1+}]	[2Cu^{2+} - 2Cu$^+$]	Anerobic purification and ascorbate reduction	Cu$_Z$ (4Cu2S)	S = 0	Absorption bands ~550 and 650 nm
[Cu^{1+} - Cu^{1+}]	[1Cu^{2+} - 3Cu$^+$]	Anerobic purification and dithionate reduction		S = 1/2	Absorption band ~670 nm
[Cu$^{1.5+}$ - Cu$^{1.5+}$]	[1Cu^{2+} - 3Cu$^+$]	Aerobic purification		S = 1/2	N/A
[Cu^{1+} - Cu^{1+}]	[1Cu^{2+} - 3Cu$^+$]	Aerobic purification and ascorbate reduction	Cu$_Z$* (4CuS)	S = 1/2	Absorption band ~640 nm
[Cu^{1+} - Cu^{1+}]	[4Cu^{1+}]	Aerobic purification and prolong methyl viologen reduction		S = 0	Spectroscopic silent

1.5.3   Substrate interaction with N$_2$OR active site

Substrate binding studies of N$_2$OR are typically challenging due to N$_2$O being a weak ligand with poor σ-donor and π-acceptor ability.[6] Literature assignment of the edge site Cu$_I$–Cu$_{IV}$ as the substrate binding site of N$_2$OR is largely depent on spectroscopic measurements[40] and DFT[34] calculations. Additionally, the idea is strongly supported by the crystallograpic studies of N$_2$OR inhibition by iodide (I$^-$) and the N$_2$O-pressurised crystal structure of N$_2$OR.[28,41] It is also fundamentally supported by the fact that Cu$_{IV}$ atom is coordinated by only one histidine residue, providing a potential coordination site for the substrate (N$_2$O), while the rest of the Cu atoms are supported by two histidine

residues. Furthermore, one could imagine the labile solvent derived molecule across the Cu_I–Cu_{IV} edge being replaced by N_2O in the beginning of substrate activation.

In this context, the N_2OR inhibition study reported by Hasnain and co-worker is particularly important not only because it represented the first inhibitor bound N_2OR crystal structure but also because it strongly supported the proposed substrate binding site for N_2OR.[28] The crystallographic characterization of anaerobically isolated N_2OR from *Achromobacter cycloclastes* (*Ac*N_2OR, PDB ID 2IWF) at 1.86-Å resolution revealed ligation of two oxygen atoms (H_2O/OH^-) to Cu_I and Cu_{IV} atoms separately, which is different from conventional Cu_Z or Cu_Z* forms. However, the visible and EPR spectra confirmed the active site to be a Cu_Z* ($4Cu1S$:[$1Cu^{2+}$ - $3Cu^{1+}$) form.[28] Incubation of *Ac*N_2OR with the inhibitor NaI over a prolonged period resulted reduction of the Cu_A center as evidenced by the complete loss of spectroscopic features associated to Cu_A.[28] However, the iodide inhibited Cu_Z* active site remained unchanged ($3Cu^{1+}$ - $1Cu^{2+}$) as evidenced by characteristic 650 nm absorption band in visible spectrum, even after the attempted oxidation by $K_3Fe(CN)_6$ implying its redox-inert nature.[28]

In the native *Ac*N_2OR, the Cu_I and Cu_{IV} atoms are coordinated by Oxy_1 and Oxy_2 atoms at 2.2 and 2.5 Å respectively (**Figure 1.6A**). The distance between two oxygen atoms is 2.3 Å which could accommodate a bent N_2O molecule (where Cu_{IV} is bound to the oxygen and Cu_I is bound to the N atoms of N_2O) as proposed by DFT calculations.[28] The active site loses its redox activity upon Cu_I–Cu_{IV} edge site being occupied by iodide anion (**Figure 1.6B,** PDB ID 2IWK). Overall, the proposed reduction involves N_2O binding across the Cu_I–Cu_{IV} edge, and upon reduction and release of N_2 the remaining oxygen atom may coordinate between Cu_I and Cu_{IV} like iodide seen in the inhibitor bound complex.[28] However, such a complex will resemble the resting state of the catalytic site and will be discussed further in the following section 1.6.3.
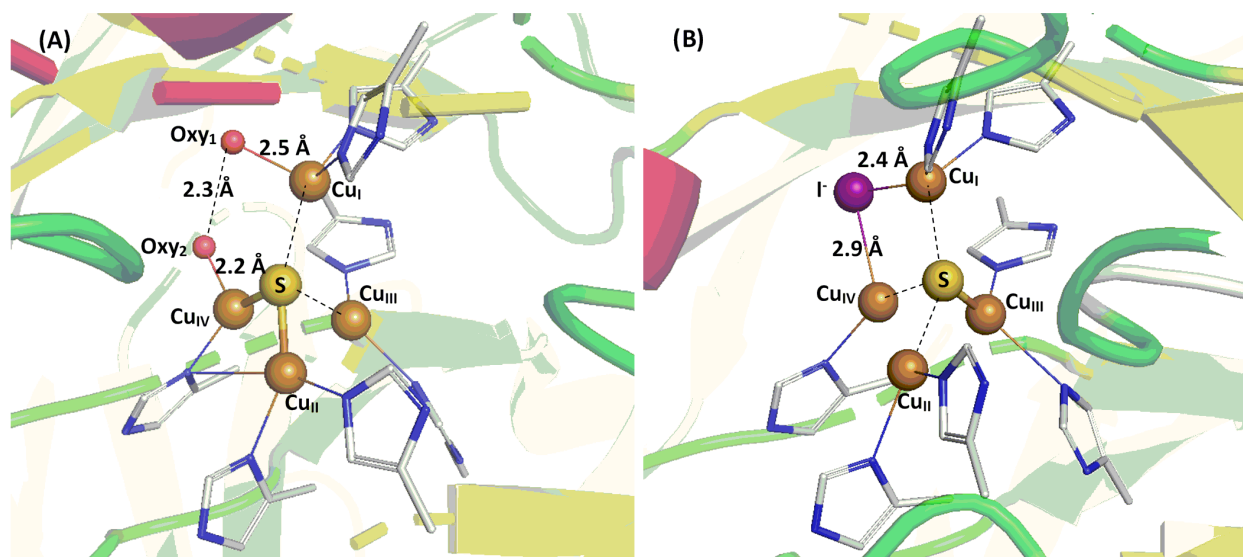
FIGURE 1. 6 (A) The active site of native N$_2$OR from *Achromobacter cycloclastes* (*Ac*N$_2$OR, PDB ID 2IWF) at 1.86 Å showing the Oxy$_1$ and Oxy$_2$ atoms coordinated to Cu$_I$ and Cu$_{IV}$ respectively. **(B)** inhibitor (I$^-$) occupies the proposed substrate binding site (PDB ID 2IWK, at 1.7 Å), causing the active site to lose its redox function. Helix-red, sheet-yellow and loop-green. Images were created using PyMol educational version.

The study reported by Einsle and co-workers remains as the only example of a N$_2$OR crystal structure, in which the substrate (N$_2$O) is occupied in proximity to the proposed substrate binding site.[41] The anoxic isolation of N$_2$OR from *P. stutzeri* contained the oxidized form of Cu$_A$ [Cu$^{1.5+}$ - Cu$^{1.5+}$] and the 2-hole form of Cu$_Z$ (4Cu2S, [2Cu^{2+} - 2Cu^{1+}]). The X-ray diffraction data collected from N$_2$O pressurized N$_2$OR crystals contained extra electron density that was adequately modeled to be a linear N$_2$O molecule (**Figure 1.7**).[41]

It is important to notice that the substrate is not located at a bonding distance to Cu$_I$ and/or Cu$_{IV}$, which is proposed to be the substrate binding site. Nonetheless, weak interactions of N$_2$O and Cu$_Z$ have been observed in EPR and UV-Vis data.[41] The authors proposed that the substrate is carried through the hydrophobic channels from the protein surface to the cluster face formed by Cu$_{ZII}$, Cu$_{ZIV}$ and S$_{Z2}$ atoms, in which the substrate is positioned in a tight binding pocket created by F621, H626 and M627 residues (**Figure 1.7**). Upon the N$_2$O activation and reduction, the produced nonpolar N$_2$ is escapes through the hydrophobic channels while the H$_2$O molecule is retained in the distal water filled cavity adjacent to the binding pocket.
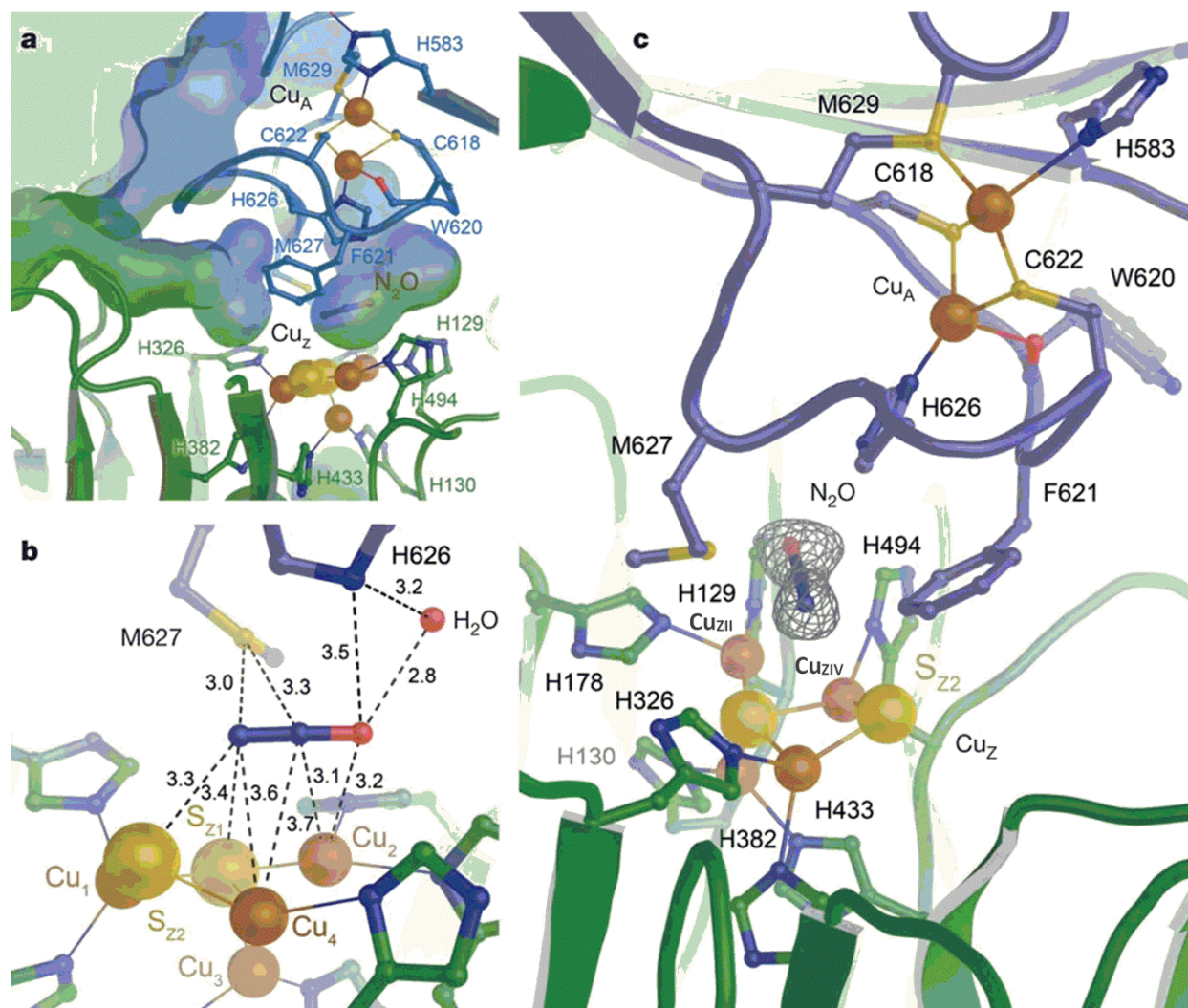
FIGURE 1. 7 N_2O pressurized crystal structure of N_2OR from *P. stutzeri* with extra electron density modeled as linear N_2O occupying proximity to CuZ center. **a-** Active site substrate binding. A hydrophobic substrate channel leads from the protein surface (left) to a proximal vestibule at Cu_Z, where the linear N_2O molecule can re-orient to displace the two residues shielding the cluster, F621 and M627. **b-** distances around the N_2O ligand in Å. **c-** A F_o - F_c difference electron density map contoured at the 3σ level showed the presence of the substrate. Reprinted by permission from RightsLink Printable License: Springer Nature, ref. 41, N_2O binding at a [4Cu:2S] copper–sulfur cluster in nitrous oxide reductase, Einsle et al., copyright 2011.

However, no subsequent reactivity or change of the redox states of either copper center has been observed with this substrate incorporated N_2OR, and the only significant structural difference to the substrate free N_2OR is that the H583 histidine residue is coordinated to the Cu_A site which otherwise is rotated ~130° away from Cu_A and participating H-bonding with backbone residues. This phenomenon suggests that the electron transfer event only occurs upon flipping and coordination of H538 to the Cu_A site, which only happens upon exposure to N_2O.[41]

1.6   The mechanism and the catalytic cycle of N_2O reduction by N_2OR

1.6.1   Dependence of catalytic activity of N_2OR

The redox activity and catalytic features of N_2OR have been proven to vary depending on the isolation procedure, the mode of activation (reducing agent), the pH, and of course the redox state of the active site.[5,6,17] Typically, the specific activity is reported as the μmol of N_2O reduced/min/mg of N_2OR and in most cases is determined by the indirect spectrometric assay by following the oxidation of reduced viologen dyes at 600 nm.[42,43] Alternatively, a direct chromatographic determination could be used by measuring the N_2O consumption or N_2 production.[42,44]

The idea that certain N_2OR requires an external activation is supported by the fact that the certain crude N_2OR extracts display specific activities ranging from 48-72 μmol of N_2O reduced/min/mg of N_2OR that drop down to 1-10 μmol of N_2O reduced/min/mg of N_2OR upon aerobic or anaerobic purification.[44,45] The latter are believed to be in an unready state of the enzyme,[46] though other possible *in vitro* mechanisms cannot be ruled out. It is a valid argument that the *in vitro* spectroscopic assays deviate from the physiological conditions as the reduction potential of the electron donors used (methyl viologen, -450 mV vs SHE, pH 7.0 and benzyl viologen, -374 mV vs SHE, pH 7.0)[47] are incomparable to the conditions found in native bacteria. However, the studies using physiologically relevant electron donors have also displayed a higher specific activity for the crude cell extracts than that of purified N_2OR.[48–50] Moreover, the purified N_2OR from *W. succinogenes* shows high specific activity (160 μmol of N_2O reduced/min/mg of N_2OR), implying that it does not require an external activation.[51] The next section will discuss the redox forms of copper sites (Cu_A and Cu_Z) found in the activated and/or non-activated N_2OR.

1.6.2 Catalytic activity of different Cu_Z forms

So far, 4 different redox forms of Cu_Z have been discussed, with either the reduced or oxidized form of Cu_A: 2-hole Cu_Z [$2Cu^{2+}$ - $2Cu^+$], 1-hole Cu_Z [$1Cu^{2+}$ - $3Cu^+$], 1-hole Cu_Z* [$1Cu^{2+}$ - $3Cu^+$] and the fully reduced state of Cu_Z* [$4Cu^{1+}$] (**Table 1.1**). Of these, 2-hole Cu_Z and 1-hole Cu_Z* do not react with N_2O even after Cu_A is reduced, as evidence by no change of the spectroscopic features in the presence of N_2O.[29] The 1-hole Cu_Z coupled to reduced Cu_A has been found to slowly react with N_2O, oxidizing back to 2-hole Cu_Z and oxidized Cu_A, completing a two-electron process.[29] However, the corresponding turnover number ($k = 0.6$ h^{-1}) is too low for this to be physiologically relevant. On the other hand, the fully reduced Cu_Z* (spectroscopic silent, $4Cu^{1+}$) resulting from prolonged incubation of 1-hole Cu_Z* with methyl viologen, reacts with N_2O as evidenced by reappearing of spectroscopic features (correspond to 1-hole Cu_Z* and oxidized Cu_A) and GC-MS detection of $^{15}N_2$ production upon using ^{15}N-labeled N_2O.[52] The turnover number for the reaction could be as high as 320 s^{-1}, but the reductive activation of 1-hole Cu_Z* requires harsh conditions followed by a low rate constant (1.2×10^{-3} s^{-1}) for this to be considered as physiologically relevant.[29,40,52]

An interesting intermediate named $Cu_Z°$ has been observed within the first two minutes of the stoichiometric reaction between fully reduced Cu_Z* and N_2O.[29,39] This intermediate is characterized by an absorption band ~680 nm ($\varepsilon = 2000$ M^{-1} cm^{-1}) and has a formation rate of 200 s^{-1} followed by decay rate of ~5×10^{-3} s^{-1} with reappearance of characteristic absorption bands for 1-hole Cu_Z*.[29,39] Both the formation and decay rates are compatible to reported enzymic N_2O reduction steady state kinetic assays, thus giving $Cu_Z°$ a potential physiological relevance.[29,39] The observed spectral features of $Cu_Z°$ are best explained by a DFT model in which the Cu_{IV} atom is coordinated to a terminal OH$^-$ ligand at 1.93 Å which is stabilized through H-bonding to a protonated lysine residue (K397) that is interacting with negatively charged glutamate residue (E435).[37]

1.6.3   Latest proposed mechanism for N$_2$O reduction by N$_2$OR

As concluded in the previous section 1.6.2, the only form of Cu$_Z$ that is catalytically competent and physiologically relevant is the fully reduced form of Cu$_Z$* [4Cu1S, 4Cu^{1+}]. The latest catalytic cycle is proposed for the *in vitro* reaction of activated N$_2$OR by reduced methyl viologen with equimolar N$_2$O.[37] The reductive activation of N$_2$OR results in a reduced Cu$_A$ [Cu^{1+} - Cu^{1+}] and a fully reduced form of Cu$_Z$* [4Cu1S, 4Cu^{1+}] (**Scheme 1.2**, intermediate **1**).
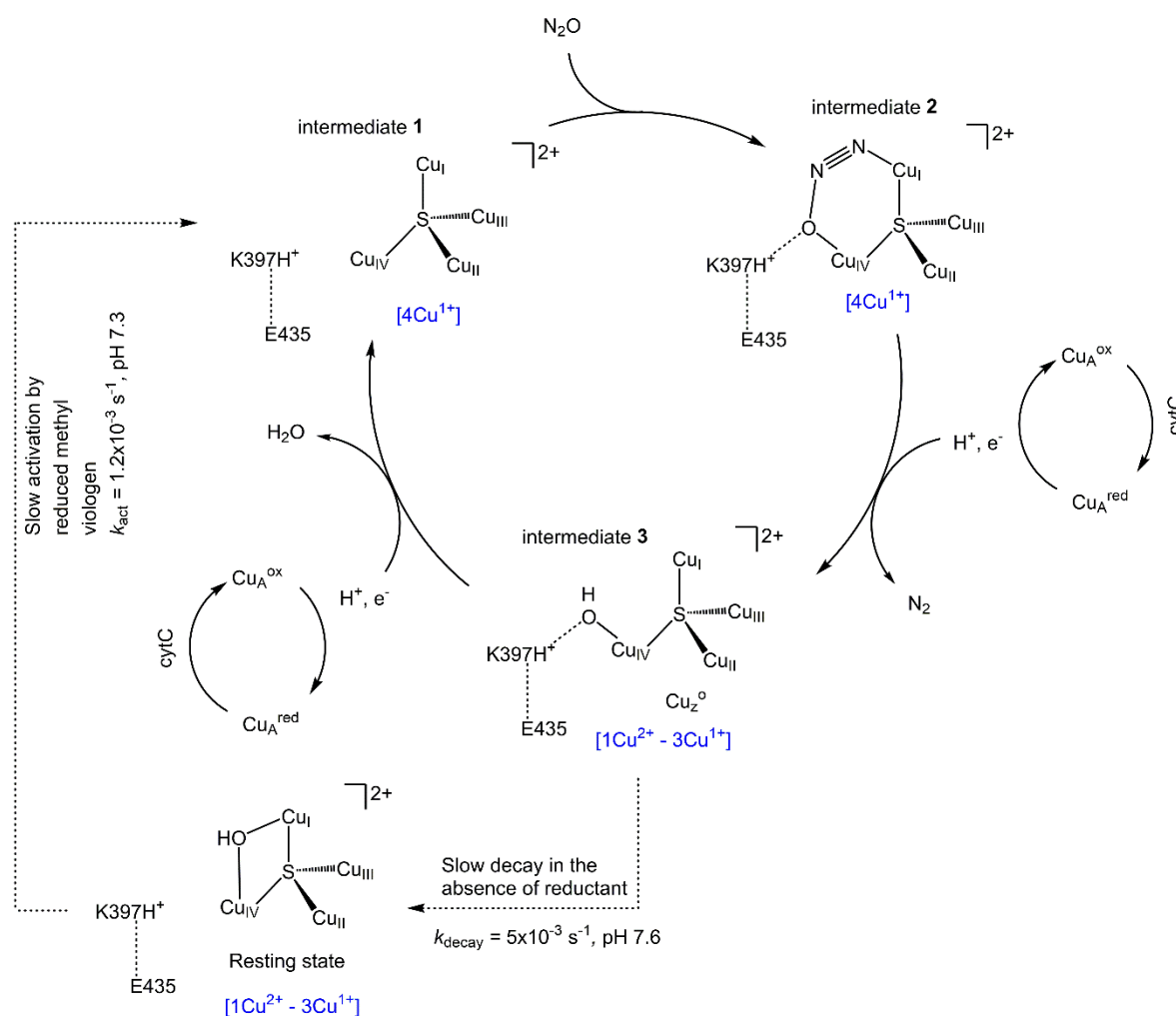
SCHEME 1. 2 The mechanism of *in vitro* reduction of equimolar molar N$_2$O by reduced N$_2$OR with Cu$_Z$* center showing the intermediates and the proton coupled electron transfer events from Cu$_A$ center. The catalytically competent cycle is shown using solid arrows while the dashes indicate the slow alternative pathway in the absence of reductants. The conserved amino acid residues are labeled according to *M. hydrocarbonoclasticus* N$_2$OR mature primary sequence.

N$_2$O coordinates across the Cu$_I$–Cu$_{IV}$ edge in bent (139°) μ-1,3 fashion with N and O termini coordinated to Cu$_I$ and Cu$_{IV}$ respectively (**Scheme 1.2**, intermediate **2**).[37,40,53] The intermediate **2** is further stabilized by H-bonding between Cu$_{IV}$ coordinated oxygen and nearby protonated lysine residue (K397).[37] The strong back bonding from Cu atoms makes the Cu$_I$–N and Cu$_{IV}$–O bonds stronger than the N–N and N–O bonds, which in turn makes the inert N$_2$O susceptible for reduction.[38,54] Next, N$_2$ is liberated upon a two electron transfer from Cu$_Z$* to N$_2$O that is required for N–O and Cu$_I$–N bond cleavage, resulting in a 2-hole [2Cu^{2+} - 2Cu^{1+}] Cu$_Z$*. This presumable, short-lived intermediate has never been observed as the N$_2$ liberation is accompanied by the subsequent protonation and single electron transfer from Cu$_A$, resulting in Cu$_Z$° (**Scheme 1.2,** intermediate **3**), evidenced by spectroscopic and DFT studies.[17] A second proton coupled intramolecular electron transfer event converts the Cu$_Z$° back to the fully reduced state, completing the catalytic cycle.[37] In the absence of reductants, the Cu$_Z$° slowly decays (5×10^{-3} s^{-1}, pH 7.6) to its resting state 1-hole CuZ* with the OH$^-$ ligand bridging along the Cu$_I$–Cu$_{IV}$ edge rather than remaining terminally attached to Cu$_{IV}$.[39] Furthermore, the intramolecular reduction rate of Cu$_Z$° by sodium ascorbate has been found to be ~10^4 times faster than that of the resting state, supporting the biological competence and physiological relevance of Cu$_Z$° over the resting state.[37] The catalytic activity of N$_2$OR has been found to be sensitive to the pH of the medium even though the precise mechanistic influence remains to be fully understood.[39] Disturbance in the H-bonding network may alter the geometric orientation around the substrate binding site and could also affect the protonation state of the interacting lysine residue that facilitates the reduction of Cu$_Z$° by increasing its reduction potential and preventing decay to its resting state.[17,36,37,39]

1.7   Structural and/or functional model complexes of Cu$_Z$

The content discussed in section 1.6 summarizes the catalytically competent Cu$_Z$ forms and the proposed intermediates of the catalytic cycle. The fully reduced Cu$_Z$* [4Cu^{1+}] and the resting state [1Cu^{2+} - 3Cu^{1+}] have been biologically isolated, but the most important intermediates **2** and **3** have been studied only using spectroscopic and DFT methods, as the biological isolation of these short-lived species are challenging. Model complexes supported by appropriate ligands could be an alternative way to isolate and study such intermediates as opposed the native enzymatic studies that are limited by physiological conditions. In this section, the reported structural and/or functional copper-sulfur model complexes of Cu$_Z$ will be briefly discussed for their relevance to the structure and activity of N$_2$OR.

Regarding structural model complexes of Cu_Z, the first $Cu_4(\mu_4\text{-S})$ complex was reported in 1993 by Yam and co-workers, way before the crystal structure of Cu_Z was revealed.[55] The phosphine supported $[Cu_4(\mu_4\text{-S})(dppm)_4][(PF_6)_2]$ (**1**) (dppm = bis(diphenylphosphino)methane) (**Chart 1.1** *(top)*) complex was studied not for its relevance to Cu_Z, but for its photochemical properties.[55] Our group adapted Yam's synthetic approach to synthesize a few other $Cu_4(\mu_4\text{-S})$ derivatives and studied their reaction with N_2O and other isoelectronic compounds.[56] Moreover, we have recently reported a sequence of formamidinate (NCN) supported $Cu_4(\mu_4\text{-S})$ complexes (**Chart 1.1** *(bottom)*) that are both structurally and functionally similar to the active site of N_2OR (discussed in detail in Chapter 2).[57,58] Apart from these, no other $Cu_4(\mu_4\text{-S})$ structural model complexes have been reported, except $Cu_4(\mu_4\text{-S})$ motifs found in multinuclear Cu–S clusters that have been studied not for the relevance in Cu_Z, but for their photochemical properties.[59–62] However, several di and tri nuclear Cu–S complexes have been reported for their relevance in N_2O activity and will be discussed in the following paragraphs.
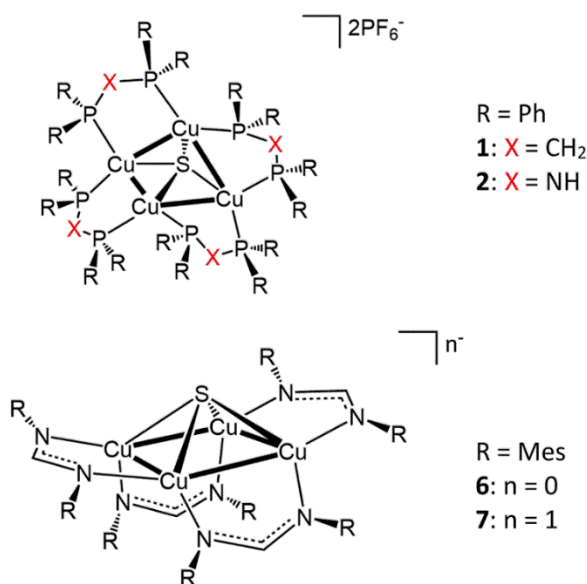
CHART 1. 1 Previously studied *(top)* phosphine supported, *(bottom)* formamidinate supported $[Cu_4(\mu_4\text{-S})]$ complexes.

Tolman and co-worker published the first Cu–S complex that could reduce N_2O to N_2.[63] The Cu_3S_2 complex supported by nitrogen rich 1,4,7-triazacyclononane ligands was not structurally similar to Cu_Z yet displayed superficially similar UV-Vis spectroscopic features and N_2O activity.[63] They proposed a mechanism in which the tricopper pre-equilibrates with a dicopper species that allows N_2O to coordinate between two copper atoms in μ-1,1 fashion through the oxygen atom, providing an alternate substrate binding mode opposed to the μ-1,3 coordination

proposed for Cu_Z.[63] In the context of N_2O reactivity, our group has studied $[Cu_4(\mu_4\text{-}S)(dppa)_4][(PF_6)_2]$ (**2**) (dppa = bis(diphenylphosphino)amine) (**chart 1.1**(*top*)) extensively.[56,64] In the presence of N_3^- (isoelectronic to N_2O) **2** decomposes to a $[Cu_3(\mu_3\text{-}S)(dppa)_3](PF_6)$ complex and with excess N_3^- the S^{2-} is replaced by two N_3^- ligands forming complex $[Cu_3(\mu_3\text{-}N_3)_2(dppa)_3](PF_6)$. Once the iodide (biological inhibitor of Cu_Z) is used, **2** decomposes to a tricopper complex $[Cu_3(\mu_3\text{-}S)(\mu_3\text{-}I)(dppa)_3]$ and in the presence of excess iodide, the S^{2-} is replaced with two iodide ligands forming $[Cu_3(\mu_3\text{-}I)_2(dppa)_3](PF_6)$ (**Figure 1.8**). Moreover **2** has been found to reduce N_2O to N_2 under very specific conditions involving secondary sphere interactions and will be discussed in Chapter 3.[64]

Recently, Torelli and co-workers have demonstrated the N_2O reduction activity of a Cu_2S complex that mimics the Cu_I–Cu_{IV} edge site of the Cu_Z.[65] The labile H_2O ligand and the metal–metal interaction in the Cu_2S unit were required for N_2O reduction since similar complexes lacking those were inactive towards N_2O.[65] The reduction is followed by an intermediate in which a OH^- ligand bridges between the two Cu atoms similar the Cu_I–Cu_{IV} edge in Cu_Z*. Our group has also studied a coordinatively unsaturated $Cu_2(\mu_2\text{-}S)$ complex supported by two bulky IPr* ligands that oxidized to $Cu_2(\mu_2\text{-}SO_4)$ upon exposing to N_2O or CO_2, implying that the Cu_{II} and Cu_{III} in the biological active site are playing an important role during the N_2O reduction by preventing $(\mu_4\text{-}S)$ from oxidation.[66] Moreover, there are few coordinatively unsaturated $Cu_2(\mu_2\text{-}S)$ and $Cu_3(\mu_3\text{-}S)$ complexes supported by nitrogen rich ligands that have been reported, and none with observed or tested reactivity towards N_2O.[67–70] Attempts have also been made to stabilize multicopper μ-S complexes yet only resulting in multicopper complexes with no sulfur incorporation.[71,72]

To date, the two complexes reported by our group that are supported by dppa and NCN ligand systems remain as the only examples of structurally and functionally faithful $Cu_4(\mu_4\text{-}S)$ model complexes. The detailed N_2O reduction mechanisms of theses complexes will be addressed in Chapters 3 and 4, respectively. One of the areas in Cu_Z modeling chemistry that has not been addressed adequately is the development of a predictable and tunable protocol to synthesize $Cu_4(\mu_4\text{-}S)$ clusters with desired features that enables the N_2O reactivity. The next Chapter will present our contribution toward developing such methodology.
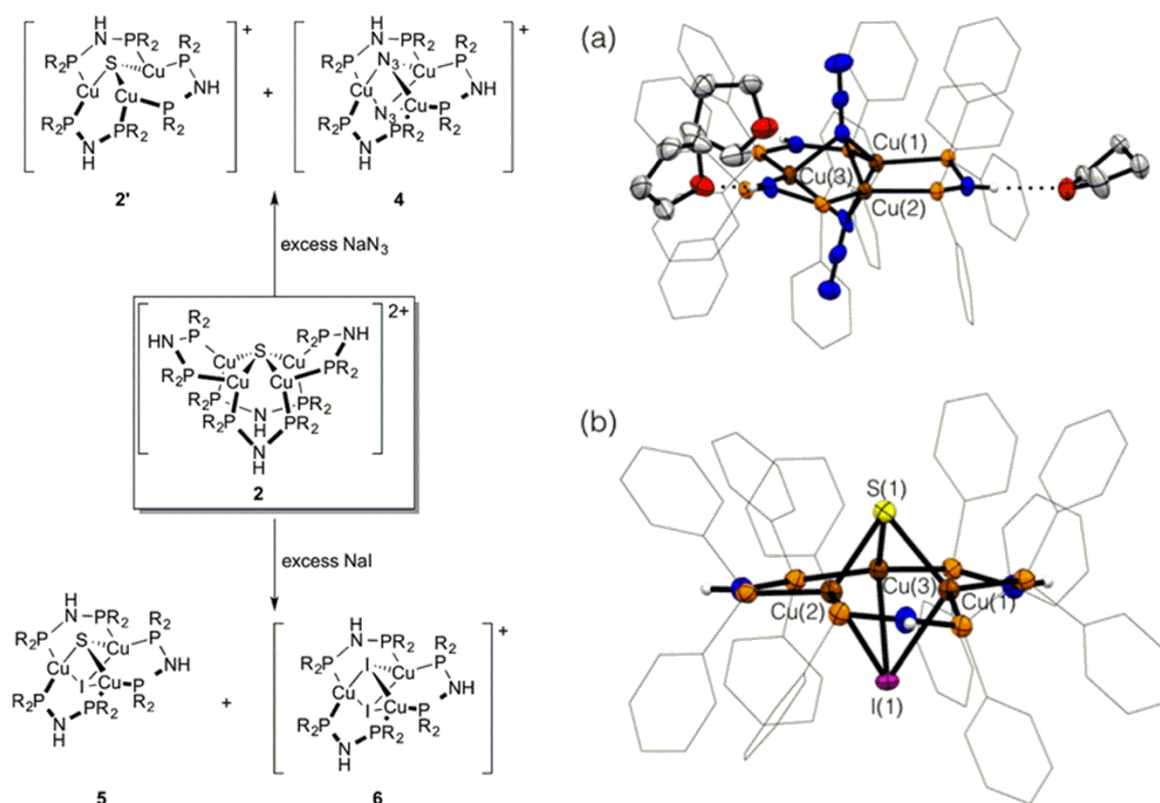
FIGURE 1. 8 *(left)* The tricopper species resulting from the reaction between [Cu$_4$(μ_4-S)(dppa)$_4$][(PF$_6$)$_2$] (**2**) and N$_3^-$/I$^-$. **2'** = [Cu$_3$(μ_3-S)(dppa)$_3$](PF$_6$), **4** = [Cu$_3$(μ_3- N$_3$)$_2$(dppa)$_3$](PF$_6$), **5** = [Cu$_3$(μ_3-S)(μ_3-I)(dppa)$_3$] and **6** = [Cu$_3$(μ_3-I)$_2$(dppa)$_3$](PF$_6$). The crystal structures of **4**·3THF *(a)* and **5** *(b)* determined by X-ray crystallography. Core atoms are shown as 50% probability ellipsoids, phosphine substituents are shown as wireframes, and C−H hydrogen atoms have been omitted for clarity. Co-crystallized anions and solvent molecules are shown only if engaged in hydrogen bonding to the cationic unit. N−H hydrogen atoms are shown in calculated positions. Atom colors: C, gray; H, white; Cu, brown; F, green; I, purple; N, blue; O, red; P, orange; S, yellow. Reprinted (adapted) with permission from ref. 56. Copyright (2014) American Chemical Society.

1.8   References

(1)   Fowler, D.; Coyle, M.; Skiba, U.; Sutton, M. A.; Cape, J. N.; Reis, S.; Sheppard, L. J.; Jenkins, A.; Grizzetti, B.; Galloway, J. N.; Vitousek, P.; Leach, A.; Bouwman, A. F.; Butterbach-Bahl, K.; Dentener, F.; Stevenson, D.; Amann, M.; Voss, M. The Global Nitrogen Cycle in the Twentyfirst Century. *Philos. Trans. R. Soc. B Biol. Sci.* **2013**, *368*.

(2)   United States Environmental Protection Agency. *Draft Inventory of U.S. Greenhouse Gas Emissions and Sinks: 1990-2018*; 2020.

(3)   Aronson, E. L.; Allison, S. D. Meta-Analysis of Environmental Impacts on Nitrous Oxide Release in Response to N Amendment. *Front. Microbiol.* **2012**, *3*, 1–6.

(4)   Saggar, S.; Jha, N.; Deslippe, J.; Bolan, N. S.; Luo, J.; Giltrap, D. L.; Kim, D. G.; Zaman, M.; Tillman, R. W. Denitrification and N2O: N2 Production in Temperate Grasslands: Processes, Measurements, Modelling and Mitigating Negative Impacts. *Sci. Total Environ.* **2013**, *465*, 173–195.

(5)   Pauleta, S. R.; Carepo, M. S. P.; Moura, I. Source and Reduction of Nitrous Oxide. *Coord. Chem. Rev.* **2019**, *387*, 436–449.

(6)   Carreira, C.; Pauleta, S. R.; Moura, I. The Catalytic Cycle of Nitrous Oxide Reductase — The Enzyme That Catalyzes the Last Step of Denitrification. *J. Inorg. Biochem.* **2017**, *177*, 423–434.

(7)   Chen, P.; Gorelsky, S. I.; Ghosh, S.; Solomon, E. I. N2O Reduction by the M4-Sulfide-Bridged Tetranuclear CuZ Cluster Active Site. *Angew. Chemie - Int. Ed.* **2004**, *43*, 4132–4140.

(8)   Wüst, A.; Schneider, L.; Pomowski, A.; Zumft, W. G.; Kroneck, P. M. H.; Einsle, O. Nature's Way of Handling a Greenhouse Gas: The Copper-Sulfur Cluster of Purple Nitrous Oxide Reductase. *Biol. Chem.* **2012**, *393*, 1067–1077.

(9)   Hoffman, B. M.; Lukoyanov, D.; Yang, Z.-Y.; Dean, D. R.; Seefeldt, L. C. Mechanism of Nitrogen Fixation by Nitrogenase: The Next Stage. *Chem. Rev.* **2014**, *114*, 4041–4062.

(10)   Rivera-Ortiz, J. M.; Burris, R. H. Interactions among Substrates and Inhibitors of Nitrogenase. *J. Bacteriol.* **1975**, *123*, 537–545.

(11)   Christiansen, J.; Seefeldt, L. C.; Dean, D. R. Competitive Substrate and Inhibitor Interactions at the Physiologically Relevant Active Site of Nitrogenase. *J. Biol. Chem.* **2000**, *275*, 36104–36107.

(12)   Liang, J.; Burris, R. H. N2O Reduction and HD Formation by Nitrogenase from a NifV Mutant of Klebsiella Pneumoniae. *J. Bacteriol.* **1989**, *171*, 3176–3180.

(13)   Liang, J.; Burris, R. H. Interactions among Nitrogen, Nitrous Oxide, and Acetylene as Substrates and Inhibitors of Nitrogenase from Azotobacter Vinelandii. *Biochemistry* **1988**, *27*, 6726–6732.

(14)   Fernandes, A. T.; Damas, J. M.; Todorovic, S.; Huber, R.; Baratto, M. C.; Pogni, R.; Soares, C. M.; Martins, L. O. The Multicopper Oxidase from the Archaeon Pyrobaculum Aerophilum Shows Nitrous Oxide Reductase Activity. *FEBS J.* **2010**, *277*, 3176–3189.

(15)   Zumft, W. G. Cell Biology and Molecular Basis of Denitrification. *Microbiol. Mol. Biol. Rev.* **1997**, *61*, 533–616.

(16)   Pauleta, S. R.; Dell'Acqua, S.; Moura, I. Nitrous Oxide Reductase. *Coord. Chem. Rev.* **2013**, *257*, 332–349.

(17)   Ferousi, C.; Majer, S. H.; DiMucci, I. M.; Lancaster, K. M. Biological and Bioinspired Inorganic N–N Bond-Forming Reactions. *Chem. Rev.* **2020**, acs.chemrev.9b00629.

(18) Brown, K.; Tegoni, M.; Prudêncio, M.; Pereira, A. S.; Besson, S.; Moura, J. J.; Moura, I.; Cambillau, C. A Novel Type of Catalytic Copper Cluster in Nitrous Oxide Reductase. *Nat. Struct. Biol.* **2000**, *7*, 191–195.

(19) Schneider, L. K.; Einsle, O. Role of Calcium in Secondary Structure Stabilization during Maturation of Nitrous Oxide Reductase. *Biochemistry* **2016**, *55*, 1433–1440.

(20) Kroneck, P. M. H.; Antholine, W. A.; Riester, J.; Zumft, W. G. The Cupric Site in Nitrous Oxide Reductase Contains a Mixed-Valence [Cu(II),Cu(I)] Binuclear Center: A Multifrequency Electron Paramagnetic Resonance Investigation. *FEBS Lett.* **1988**, *242*, 70–74.

(21) Kroneck, P. M. H.; Antholine, W. E.; Kastrau, D. H. W.; Buse, G.; Steffens, G. C. M.; Zumft, W. G. Multifrequency EPR Evidence for a Bimetallic Center at the Cu A Site in Cytochrome c Oxidase. *FEBS Lett.* **1990**, *268*, 274–276.

(22) Kroneck, P. M. H.; Antholine, W. A.; Riester, J.; Zumft, W. G. The Nature of the Cupric Site in Nitrous Oxide Reductase and of Cu A in Cytochrome c Oxidase. *FEBS Lett.* **1989**, *248*, 212–213.

(23) ANTHOLINE, W. E.; KASTRAU, D. H. W.; STEFFENS, G. C. M.; BUSE, G.; ZUMFT, W. G.; KRONECK, P. M. H. A Comparative EPR Investigation of the Multicopper Proteins Nitrous-Oxide Reductase and Cytochrome c Oxidase. *Eur. J. Biochem.* **1992**, *209*, 875–881.

(24) Charnock, J. M.; Dreusch, A.; Körner, H.; Neese, F.; Nelson, J.; Kannt, A.; Michel, H.; Garner, C. D.; Kroneck, P. M. H.; Zumft, W. G. Structural Investigations of the CuA Centre of Nitrous Oxide Reductase from Pseudomonas Stutzeri by Site-Directed Mutagenesis and X-Ray Absorption Spectroscopy. *Eur. J. Biochem.* **2000**, *267*, 1368–1381.

(25) Brown, K.; Djinovic-Carugo, K.; Haltia, T.; Cabrito, I.; Saraste, M.; Moura, J. J. G.; Moura, I.; Tegoni, M.; Cambillau, C. Revisiting the Catalytic CuZ Cluster of Nitrous Oxide (N2O) Reductase: Evidence of a Bridging Inorganic Sulfur. *J. Biol. Chem.* **2000**, *275*, 41133–41136.

(26) Kroneck, P. M. H.; Riester, J.; Zumft, W. G.; Antholine, W. E. The Copper Site in Nitrous Oxide Reductase. *Biol. Met.* **1990**, *3*, 103–109.

(27) Rasmussen, T.; Berks, B. C.; Sanders-Loehr, J.; Dooley, D. M.; Zumft, W. G.; Thomson, A. J. The Catalytic Center in Nitrous Oxide Reductase, Cu(z), Is a Copper-Sulfide Cluster. *Biochemistry*. 2000, pp 12753–12756.

(28) Paraskevopoulos, K.; Antonyuk, S. V; Sawers, R. G.; Eady, R. R.; Hasnain, S. S. Insight into Catalysis of Nitrous Oxide Reductase from High-Resolution Structures of Resting and Inhibitor-Bound Enzyme from Achromobacter Cycloclastes. *J. Mol. Biol.* **2006**, *362*, 55–65.

(29) Johnston, E. M.; Dell'Acqua, S.; Ramos, S.; Pauleta, S. R.; Moura, I.; Solomon, E. I. Determination of the Active Form of the Tetranuclear Copper Sulfur Cluster in Nitrous Oxide Reductase. *J. Am. Chem. Soc.* **2014**, *136*, 614–617.

(30) Solomon, E. I. Spectroscopic Methods in Bioinorganic Chemistry: Blue to Green to Red Copper Sites. *Inorg. Chem.* **2006**, *45*, 8012–8025.

(31) Johnston, E. M.; Dell'Acqua, S.; Pauleta, S. R.; Moura, I.; Solomon, E. I. Protonation State of the Cu4S2 CuZ Site in Nitrous Oxide Reductase: Redox Dependence and Insight into Reactivity. *Chem. Sci.* **2015**, *6*, 5670–5679.

(32) Farrar, J. A.; Thomson, A. J.; Cheesman, M. R.; Dooley, D. M.; Zumft, W. G. A Model of the Copper Centres of Nitrous Oxide Reductase (Pseudomonas Stutzeri). *FEBS Lett.* **1991**, *294*, 11–15.

(33) RASMUSSEN, T.; BERKS, B. C.; BUTT, J. N.; THOMSON, A. J. Multiple Forms of the Catalytic Centre, CuZ, in the Enzyme Nitrous Oxide Reductase from Paracoccus Pantotrophus. *Biochem. J.* **2002**, *364*, 807–815.

(34)   Chen, P.; DeBeer George, S.; Cabrito, I.; Antholine, W. E.; Moura, J. J. G.; Moura, I.; Hedman, B.; Hodgson, K. O.; Solomon, E. I. Electronic Structure Description of the μ 4 -Sulfide Bridged Tetranuclear Cu Z Center in N 2 O Reductase. *J. Am. Chem. Soc.* **2002**, *124*, 744–745.

(35)   Oganesyan, V. S.; Rasmussen, T.; Fairhurst, S.; Thomson, A. J. Characterisation of [Cu4S], the Catalytic Site in Nitrous Oxide Reductase, by EPR SpectroscopyElectronic Supplementary Information (ESI) Available: Listings of the Coordinates Used for the Calculations; Comparison of the Results from Restricted and Unrest. *Dalt. Trans.* **2004**, No. 7, 996.

(36)   Ghosh, S.; Gorelsky, S. I.; DeBeer George, S.; Chan, J. M.; Cabrito, I.; Dooley, D. M.; Moura, J. J. G.; Moura, I.; Solomon, E. I. Spectroscopic, Computational, and Kinetic Studies of the μ 4 -Sulfide-Bridged Tetranuclear Cu Z Cluster in N 2 O Reductase: PH Effect on the Edge Ligand and Its Contribution to Reactivity. *J. Am. Chem. Soc.* **2007**, *129*, 3955–3965.

(37)   Johnston, E. M.; Carreira, C.; Dell'Acqua, S.; Dey, S. G.; Pauleta, S. R.; Moura, I.; Solomon, E. I. Spectroscopic Definition of the CuZ° Intermediate in Turnover of Nitrous Oxide Reductase and Molecular Insight into the Catalytic Mechanism. *J. Am. Chem. Soc.* **2017**, *139*, 4462–4476.

(38)   Chen, P.; Cabrito, I.; Moura, J. J. G.; Moura, I.; Solomon, E. I. Spectroscopic and Electronic Structure Studies of the μ 4 -Sulfide Bridged Tetranuclear Cu Z Cluster in N 2 O Reductase: Molecular Insight into the Catalytic Mechanism. *J. Am. Chem. Soc.* **2002**, *124*, 10497–10507.

(39)   Dell'Acqua, S.; Pauleta, S. R.; Paes de Sousa, P. M.; Monzani, E.; Casella, L.; Moura, J. J. G.; Moura, I. A New CuZ Active Form in the Catalytic Reduction of N2O by Nitrous Oxide Reductase from Pseudomonas Nautica. *JBIC J. Biol. Inorg. Chem.* **2010**, *15*, 967–976.

(40)   Ghosh, S.; Gorelsky, S. I.; Chen, P.; Cabrito, I.; Moura; Moura, I.; Solomon, E. I. Activation of N 2 O Reduction by the Fully Reduced μ 4 -Sulfide Bridged Tetranuclear Cu Z Cluster in Nitrous Oxide Reductase. *J. Am. Chem. Soc.* **2003**, *125*, 15708–15709.

(41)   Pomowski, A.; Zumft, W. G.; Kroneck, P. M. H.; Einsle, O. N2O Binding at a [4Cu:2S] Copper–Sulphur Cluster in Nitrous Oxide Reductase. *Nature* **2011**, *477*, 234–237.

(42)   Frunzke, K.; Zumft, W. G. Rapid, Single Sample Analysis of H2, O2, N2, NO, CO, N2O and CO2 by Isothermal Gas Chromatography: Applications to the Study of Bacterial Denitrification. *J. Chromatogr. A* **1984**, *299*, 477–483.

(43)   Kristjansson, J. K.; Hollocher, T. C. First Practical Assay for Soluble Nitrous Oxide Reductase of Denitrifying Bacteria and a Partial Kinetic Characterization. *J. Biol. Chem.* **1980**, *255*, 704–707.

(44)   COYLE, C. L.; ZUMFT, W. G.; KRONECK, P. M. H.; KORNER, H.; JAKOB, W. Nitrous Oxide Reductase from Denitrifying. Pseudomonas Perfectomarina Purification and Properties of a Novel Multicopper Enzyme. *Eur. J. Biochem.* **1985**, *153*, 459–467.

(45)   Körner, H.; Frunzke, K.; Döhler, K.; Zumft, W. G. Immunochemical Patterns of Distribution of Nitrous Oxide Reductase and Nitrite Reductase (Cytochrome Cd1) among Denitrifying Pseudomonads. *Arch. Microbiol.* **1987**, *148*, 20–24.

(46)   Pauleta, S. R.; Carreira, C.; Moura, I. CHAPTER 7: Insights into Nitrous Oxide Reductase. In *RSC Metallobiology*; Royal Society of Chemistry, 2017; Vol. 2017-January, pp 141–169.

(47)   Wardman, P. The Reduction Potential of Benzyl Viologen: An Important Reference Compound for Oxidant/Radical Redox Couples. *Free Radic. Res.* **1991**, *14*, 57–67.

(48)   Dell'Acqua, S.; Pauleta, S. R.; Monzani, E.; Pereira, A. S.; Casella, L.; Moura, J. J. G.; Moura, I. Electron Transfer Complex between Nitrous Oxide Reductase and Cytochrome c 552 from Pseudomonas Nautica : Kinetic, Nuclear Magnetic Resonance, and Docking Studies †. *Biochemistry* **2008**, *47*, 10852–10862.

(49)   Rasmussen, T.; Brittain, T.; Berks, B. C.; Watmough, N. J.; Thomson, A. J. Formation of a Cytochrome C-Nitrous Oxide Reductase Complex Is Obligatory for N2O Reduction by Paracoccus Pantotrophus. *Dalt. Trans.* **2005**, No. 21, 3501–3506.

(50)   Fujita, K.; Hirasawa-Fujita, M.; Brown, D. E.; Obara, Y.; Ijima, F.; Kohzuma, T.; Dooley, D. M. Direct Electron Transfer from Pseudoazurin to Nitrous Oxide Reductase in Catalytic N2O Reduction. *J. Inorg. Biochem.* **2012**, *115*, 163–173.

(51)   Teraguchi, S.; Hollocher, T. C. Purification and Some Characteristics of a Cytochrome C-Containing Nitrous Oxide Reductase from Wolinella Succinogenes. *J. Biol. Chem.* **1989**, *264*, 1972–1979.

(52)   Chan, J. M.; Bollinger, J. A.; Grewell, C. L.; Dooley, D. M. Reductively Activated Nitrous Oxide Reductase Reacts Directly with Substrate. *J. Am. Chem. Soc.* **2004**, *126*, 3030–3031.

(53)   Ertem, M. Z.; Cramer, C. J.; Himo, F.; Siegbahn, P. E. M. N–O Bond Cleavage Mechanism(s) in Nitrous Oxide Reductase. *JBIC J. Biol. Inorg. Chem.* **2012**, *17*, 687–698.

(54)   Gorelsky, S. I.; Ghosh, S.; Solomon, E. I. Mechanism of N2O Reduction by the M4-S Tetranuclear CuZ Cluster of Nitrous Oxide Reductase. *J. Am. Chem. Soc.* **2006**, *128*, 278–290.

(55)   Yam, V. W.-W.; Lee, W.-K.; Lai, T.-F. Synthesis and Luminescent Properties of a Novel Tetranuclear Copper(I) Cluster Containing a M4-Sulfur Moiety. X-Ray Crystal Structure of [Cu4(μ-Dppm)4(M4-S)](PF6)2·2Me2 CO [Dppm = Bis(Diphenylphosphino)Methane]. *J. Chem. Soc., Chem. Commun.* **1993**, *4*, 1571–1573.

(56)   Johnson, B. J.; Lindeman, S. V.; Mankad, N. P. Assembly, Structure, and Reactivity of Cu4S and Cu3S Models for the Nitrous Oxide Reductase Active Site, CuZ. *Inorg. Chem.* **2014**, *53*, 10611–10619.

(57)   Johnson, B. J.; Antholine, W. E.; Lindeman, S. V.; Mankad, N. P. A Cu4S Model for the Nitrous Oxide Reductase Active Sites Supported Only by Nitrogen Ligands. *Chem. Commun.* **2015**, *51*, 11860–11863.

(58)   Johnson, B. J.; Antholine, W. E.; Lindeman, S. V.; Graham, M. J.; Mankad, N. P. A One-Hole Cu4S Cluster with N2O Reductase Activity: A Structural and Functional Model for CuZ. *J. Am. Chem. Soc.* **2016**, *138*, 13107–13110.

(59)   Khadka, C. B.; Najafabadi, B. K.; Hesari, M.; Workentin, M. S.; Corrigan, J. F. Copper Chalcogenide Clusters Stabilized with Ferrocene-Based Diphosphine Ligands. *Inorg. Chem.* **2013**, *52*, 6798–6805.

(60)   Yang, X. X.; Issac, I.; Lebedkin, S.; Kühn, M.; Weigend, F.; Fenske, D.; Fuhr, O.; Eichhöfer, A. Red-Luminescent Biphosphine Stabilized "Cu12S6" Cluster Molecules. *Chem. Commun.* **2014**, *50*, 11043–11045.

(61)   Eichhöfer, A.; Buth, G.; Lebedkin, S.; Kühn, M.; Weigend, F. Luminescence in Phosphine-Stabilized Copper Chalcogenide Cluster Molecules - A Comparative Study. *Inorg. Chem.* **2015**, *54*, 9413–9422.

(62)   Maji, R. C.; Das, P. P.; Bhandari, A.; Mishra, S.; Maji, M.; Ghiassi, K. B.; Olmstead, M. M.; Patra, A. K. Mixed Valence Copper-Sulfur Clusters of Highest Nuclearity: A Cu8 Wheel and a Cu16 Nanoball. *Chem. Commun.* **2017**, *53*, 3334–3337.

(63)   Bar-Nahum, I.; Gupta, A. K.; Huber, S. M.; Ertem, M. Z.; Cramer, C. J.; Tolman, W. B. Reduction of Nitrous Oxide to Dinitrogen by a Mixed Valenttricopper- Disulfido Cluster. *J. Am. Chem. Soc.* **2009**, *131*, 2812–2814.

(64)   Hsu, C.-W.; Rathnayaka, S. C.; Islam, S. M.; MacMillan, S. N.; Mankad, N. N2O Reductase Activity of a [Cu4S] Cluster in the 4CuI Redox State Modulated by Hydrogen Bond Donors and Proton Relays in the Secondary Coordination Sphere. *Angew. Chemie Int. Ed.* **2019**.

(65)   Esmieu, C.; Orio, M.; Ménage, S.; Torelli, S. Influence of Copper Coordination Spheres on Nitrous Oxide Reductase (N 2 Or) Activity of a Mixed-Valent Copper Complex Containing a {Cu 2 S} Core . *Inorg. Chem.* **2019**, *58*, 11649–11655.

(66) Bagherzadeh, S.; Mankad, N. P. Oxidation of a [Cu2S] Complex by N2O and CO2: Insights into a Role of Tetranuclearity in the CuZ Site of Nitrous Oxide Reductase. *Chem. Commun.* **2018**, *54*, 1097–1100.

(67) Zhai, J.; Filatov, A. S.; Hillhouse, G. L.; Hopkins, M. D. Synthesis, Structure, and Reactions of a Copper-Sulfido Cluster Comprised of the Parent Cu 2 S Unit: {(NHC)Cu} 2 (μ-S). *Chem. Sci.* **2016**, *7*, 589–595.

(68) Di Francesco, G. N.; Gaillard, A.; Ghiviriga, I.; Abboud, K. A.; Murray, L. J. Modeling Biological Copper Clusters: Synthesis of a Tricopper Complex, and Its Chloride- and Sulfide-Bridged Congeners. *Inorg. Chem.* **2014**, *53*, 4647–4654.

(69) Zhai, J.; Hopkins, M. D.; Hillhouse, G. L. Synthesis and Structure of a CuI3S Cluster Unsupported by Other Bridging Ligands. *Organometallics* **2015**, *34*, 4637–4640.

(70) Brown, E. C.; York, J. T.; Antholine, W. E.; Ruiz, E.; Alvarez, S.; Tolman, W. B. [Cu3(μ-S)2]3+ Clusters Supported by N-Donor Ligands: Progress toward a Synthetic Model of the Catalytic Site of Nitrous Oxide Reductase. *J. Am. Chem. Soc.* **2005**, *127*, 13752–13753.

(71) Rathnayaka, S. C.; Lindeman, S. V.; Mankad, N. P. Multinuclear Cu(I) Clusters Featuring a New Triply Bridging Coordination Mode of Phosphaamidinate Ligands. *Inorg. Chem.* **2018**, *57*, 9439–9445.

(72) Ghiladi, R. A.; Rheingold, A. L.; Siegler, M. A.; Karlin, K. D. Synthesis and Characterization of New Trinuclear Copper Complexes. *Inorganica Chim. Acta* **2012**, *389*, 131–137.

## 2.	SYNTHETIC PROTOCOLS FOR Cu$_Z$ MODEL COMPLEXES

The content presented in Chapter 2 comes from published work in Rathnayaka, S. C.; Lindeman, S. V.; Mankad, N. P. Multinuclear Cu(I) Clusters Featuring a New Triply Bridging Coordination Mode of Phosphaamidinate Ligands. *Inorg. Chem.* **2018**, *57*, 9439–9445 and Rathnayaka, S. C.; Hsu, C.-W.; Johnson, B. J.; Iniguez, S. J.; Mankad, N. P. Impact of Electronic and Steric Changes of Ligands on the Assembly, Stability, and Redox Activity of Cu$_4$(μ_4-S) Model Compounds of the Cu$_Z$ Active Site of Nitrous Oxide Reductase (N$_2$OR). *Inorg. Chem.* **2020**, *59*, 6496–6507.

### 2.1	Background

As discussed in Chapter 1 Section 1.2, one of the terrestrial N$_2$O metabolism pathways is anoxic bacterial denitrification that converts nitrate (NO$_3^-$) to N$_2$ and H$_2$O by a sequence of enzymes, the final step of which is the 2H$^+$/2e$^-$ reduction of nitrous oxide (N$_2$O) to N$_2$ and H$_2$O catalyzed by an enzyme called nitrous oxide reductase (N$_2$OR) (**Figure 2.1**).[1] N$_2$OR contains two metal domains, a dicopper electron transfer domain (Cu$_A$) and a catalytic Cu$_4$(μ_4-S) domain (Cu$_Z$) (**Figure 2.1**).[2] The structure and the identity of Cu$_Z$ remained obscure for several years until it was characterized using X-ray crystallography and spectroscopic techniques starting in the late 1990s.[3,4] Pioneers including those by A. J. Thomson and C. Cambillau played key roles in determining the structural identify of Cu$_Z$ as a tetranuclear copper cluster with a sulfur atom bridge, i.e. Cu$_4$(μ_4-S).[5,3] Influential spectroscopic, computational, and mechanistic studies have been performed by Solomon's group with biological isolation of different forms for Cu$_Z$, ultimately leading to the latest mechanism of N$_2$O reduction by N$_2$OR proposed recently.[6,7] However, in many cases spectroscopic, computational, and crystallographic analyses have led to mechanistic disagreement,[7–10] in part because the biological isolation of Cu$_Z$ in pure form is challenging.[11–13] Studying synthetic model compounds of Cu$_Z$ mimicking structural and/or functional features represents an alternative approach to probe its mechanistic details.

In this context, there has been great interest within the bio-inorganic community in modeling this unique Cu-S assembly, leading to new aspects of N$_2$O activation and reduction being discovered.[15–18] A diverse class of complexes[19–21] resulted from attempts in synthesizing structural and/or functional model complexes of Cu$_Z$, including notable work by the Tolman,[22,23] Murray,[24] Torelli,[25,26] and Hillhouse[27,28] groups. While these compounds partially modeled aspects of Cu$_Z$ and brought new insights into Cu-S coordination chemistry and N$_2$O activation, there are only a handful of compounds that structurally model the unique Cu$_4$(μ_4-S) core of Cu$_Z$,[15,29–33] only two of which are reactive

towards N_2O (both from our research group).[32,34] The lack of tunable and predictable synthetic protocols giving control over Cu-S complexation hinders the application of synthetic model studies for mechanistic investigation of Cu_Z. One of our group's objectives has been to develop and manipulate synthetic strategies for building $Cu_4(\mu_4\text{-S})$ model complexes while maintaining the structural integrity and redox activity of the active site that would be needed for studying N_2O reduction mechanisms.
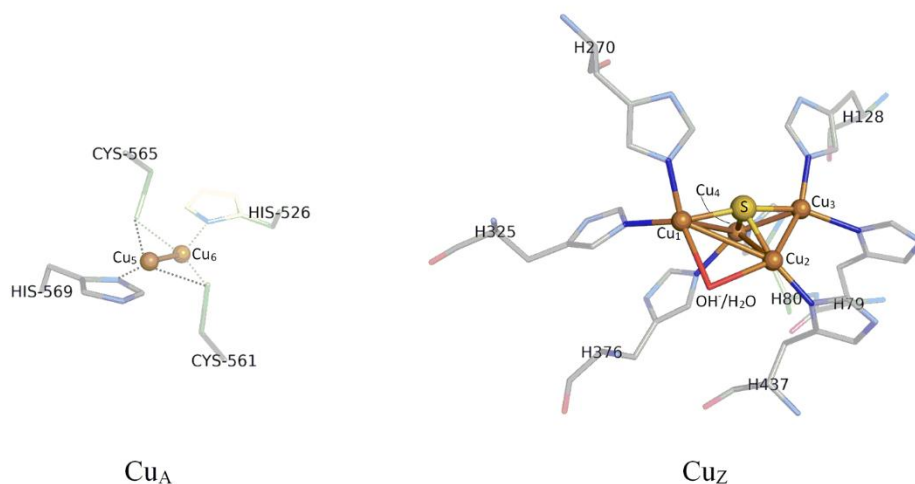
FIGURE 2. 1 The structures of Cu_A and Cu_Z of N_2OR from *Pseudomonas nautica*, at 2.4-Å resolution (PDB ID 1QNI).[14] *(left)* – Cu_A electron transfer domain. *(right)* – Cu_Z active site. The images were created using the PyMol educational version.

2.2 General synthesis of $Cu_4(\mu_4\text{-S})$ assemblies

A reported procedure[29] has been utilized as the general synthesis of $Cu_4(\mu_4\text{-S})$ assemblies, which involves two steps: (I) synthesis of a dicopper(I) precursor complex supported by two bridging ligands (Cu_2L_2), and (II) reassembly of Cu_2L_2 to $Cu_4(\mu_4\text{-S})L_4$ by reacting with a source of sulfur: neutral S_8 for neutral Cu_2L_2 or S^{2-} for cationic $[Cu_2L_2]^{n+}$. First, a $[Cu_4(\mu_4\text{-S})(dppm)_4]^{2+}$ (**1**) (dppm = bis(diphenylphosphino)methane, see **Chart 2.1**) complex originally reported by Yam[29] was tested for its activity towards N_2O. Despite being structurally similar to the active site of N_2OR, **1** did not show any reactivity with N_2O under the tested conditions. In fact, **1** does not possess any well-defined redox chemistry according to cyclic voltammetry, and it is even air stable. The next attempt to test our general synthesis protocol was to apply a slightly different ligand, dppa (dppa = bis(diphenylphosphino)amine), in place of dppm. Additionally, we were keen to see any alteration of the activity that may arise due to the potential hydrogen

bonding interactions by the -NH- groups. To our delight, the corresponding $[Cu_4(\mu_4\text{-}S)(dppa)_4]^{2+}$ (**2**, see **Chart 2.1**) complex was isolated in good yields,[30] and we recently reported that its reactivity with N_2O can be modulated by manipulating second-sphere hydrogen bonding interactions (see Chapter 3).[34]
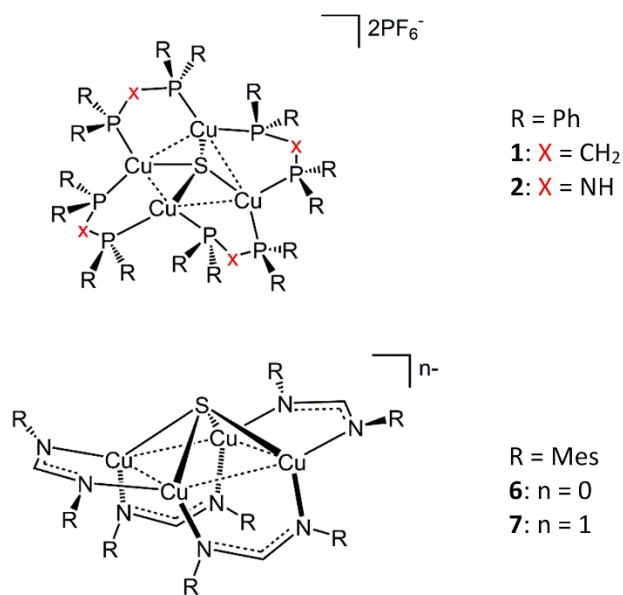
CHART 2. 1 Previously studied *(top)* phosphine supported, *(bottom)* formamidinate supported $[Cu_4(\mu_4\text{-}S)]$ complexes.

Both **1** and **2** have a lack of well-defined redox chemistry, which is an essential aspect enabling Cu_Z to mediate multielectron reduction of N_2O. Hence, a series of different ligands was applied in place of dppm and dppa to understand the steric and electronic requirements for stabilizing a redox active $Cu_4(\mu_4\text{-}S)$ assembly, with the goal of identifying ligands that could support reversible redox behavior and N_2O reactivity.

2.3   Bidentate phosphines ligands with longer bridges

It is important to notice that both dppm and dppa span adjacent Cu ions through 3-atom bridges (PCP or PNP). Ligands having larger bridges between the phosphine donors prefer to chelate a single Cu(I) ion rather than bridging in the absence of ancillary halides ligands.[35] However, bis(diphenylphosphino)ferrocene (dppf) has been found to stabilize dicopper complexes (similar to our precursors) in the presence of halides.[36] So, we performed the reaction between dppf and $Cu(MeCN)_4PF_6$ (1 eq), and it resulted a mononuclear complex with Cu(I) being chelated

by one dppf and supported by two MeCN molecules, Cu(dppf)(MeCN)$_2$(PF$_6$).[36] We were interested to characterize the reaction between this complex and a sulfur source, even if it does not resemble the dicopper precursors used previously. An overnight reaction of Cu(dppf)(MeCN)$_2$(PF$_6$) with Na$_2$S (0.25 eq) yielded complex **3** (major product) and **4** (minor product) (**Figure 2.2**).
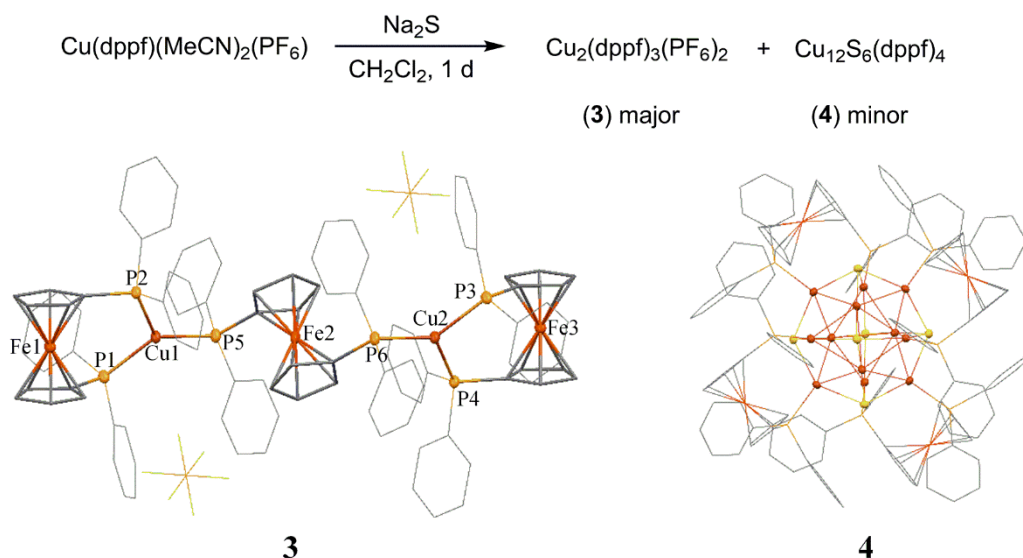
FIGURE 2. 2 *(top)* Synthesis of dicopper complex **3** and dodecacopper complex **4**. *(bottom)* The crystal structures of complexes **3** and **4**. Hydrogens have been omitted and only the core atoms are shown as 50 % probability thermal ellipsoids for clarity. Crystal structure images were processed using Mercury 3.7 (Build RC1).

Complex **3** has been synthesized before by refluxing a mixture of Cu(MeCN)$_4$PF$_6$ and dppf (2 eq) for 48 hours.[37] Complex **4** has also been synthesized before by reacting an equimolar mixture of CuOAc and dppf with S(SiMe$_3$)$_2$ at -75 °C.[33] In our case, both **3** and **4** have been simply prepared by reacting Cu(dppf)(MeCN)$_2$PF$_6$ with Na$_2$S (0.25 eq) at room temperature. In complex **3**, two Cu(I) ions are far apart (Cu-Cu distance = 9.568(2) Å) and are supported by both bridging and chelating dppf ligands. All the added S^{2-} ended up in complex **4**.

2.3.1   Molecular geometry of dodecacopper complex (**4**)

It is noteworthy that the dodecacopper cluster is composed of six $Cu_4(\mu_4\text{-S})$ units. Precisely, there are two types of $Cu_4(\mu_4\text{-S})$ motifs (**Figure 2.3**). Four out of twelve Cu(I) ions are not attached to any dppf ligand and the dissociated ligands end up presumably in complex **3** and as free ligands.

| | Type **A** | Type **A**-side view | Type **B** | Type **B**-side view |
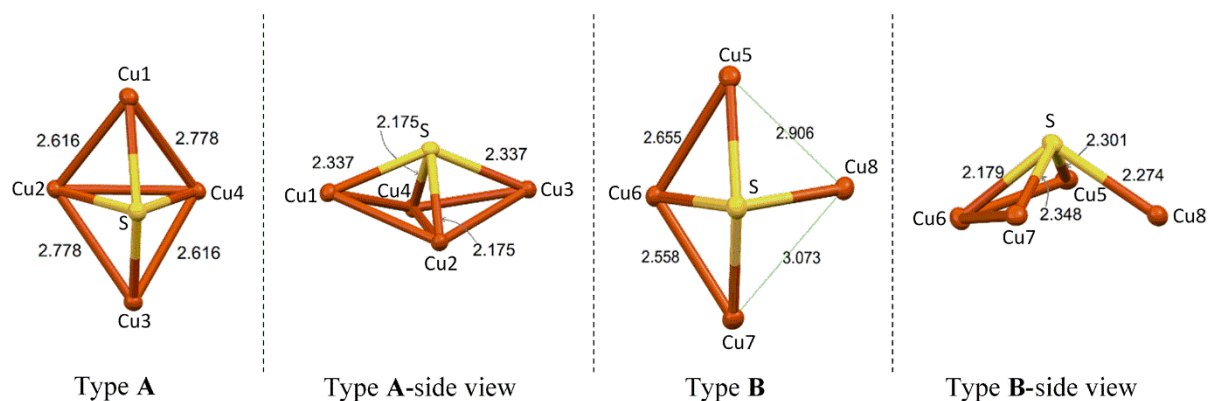
FIGURE 2. 3 Two types of $Cu_4(\mu_4\text{-S})$ arrangements found in complex **4** and their geometry parameters. Core atoms are shown as 50 % probability thermal ellipsoids. Images of the core atom structures were processed using Mercury 3.7 (Build RC1).

The Type **A** motif resembles a distorted square-based pyramid with each opposite side of the base being equal. The average adjacent Cu-Cu distance is 2.697(9) Å, and the Cu2-Cu4 diagonal (2.885(9) Å) is shorter than the Cu1-Cu3 diagonal (4.318(9) Å). Cu-S bonds that fall along a diagonal have equal lengths and the average Cu-S distance is 2.256(26) Å. In the Type **B** motif, Cu8 resides significantly away from the rest of the Cu ions. All Cu-Cu and Cu-S bonds have distinct bond lengths. The average adjacent Cu-Cu distance is 2.798(13) Å, and the average Cu-S distance is 2.276(4) Å. Overall, the average Cu-Cu and Cu-S distances of Type **B** are longer than those of type **A**.

2.4   Use of hemi-labile ligands

Complexation behavior of dppf, dppe,[35] dppm and dppa implies that 3-atom bridged ligands are more likely to stabilize a single $Cu_4(\mu_4\text{-S})$ unit via spanning each dicopper edge of the cluster, whereas longer bridges may result in complexes with higher nuclearity and/or S:Cu ratios.[33,38,39] This was a vital observation in understanding the requirements for assembling $Cu_4(\mu_4\text{-S})$ clusters. On the other hand, both structural models (**1**, **2**) were inactive towards N_2O (except

under very specialized conditions for **2**), and our primary reasoning was that they possess coordinatively saturated Cu(I) ions, leaving no open coordination sites for N_2O to bind. So, $Ph_2P(CH)NMes$[40] (**a**) was applied in place of bis(diphosphino) ligands. Having an imine nitrogen that is less σ-donating than a phosphine, (**a**) is expected to behave as a hemi-labile ligand. The reaction of (**a**) with $Cu(MeCN)_4PF_6$ yielded a dicopper precursor complex (**a'**) as expected. However, the reaction of (**a'**) with Na_2S yielded a complex mixture of products according to NMR spectroscopy with no obvious Cu_2S precipitate (**Figure 2.4**).
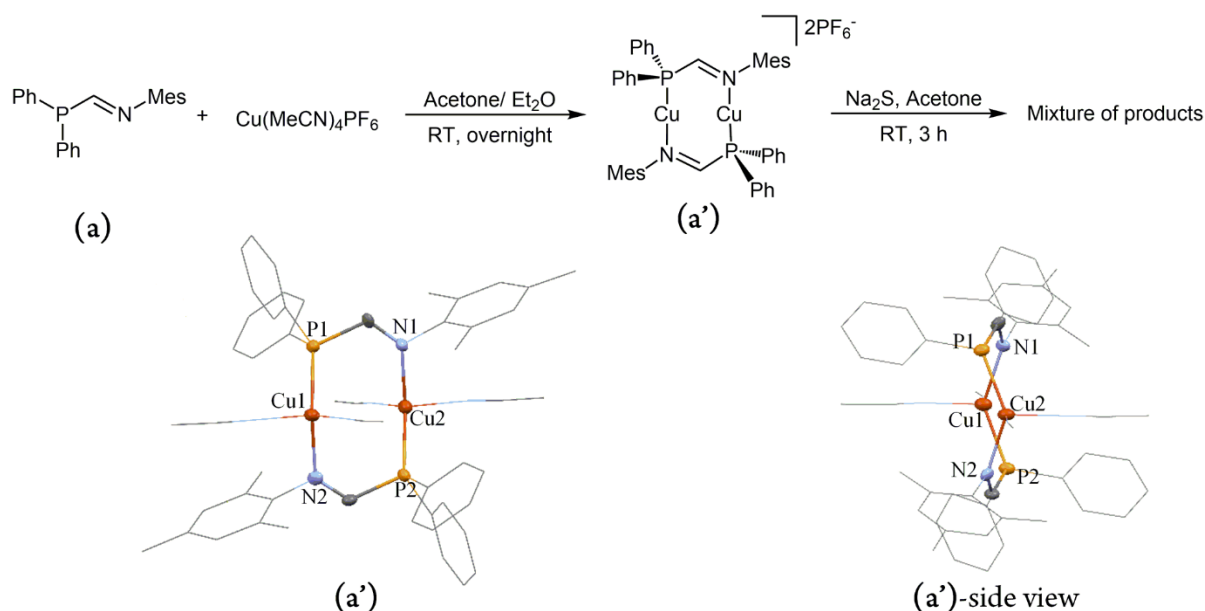
FIGURE 2. 4 *(top)* Synthesis of dicopper complex (**a'**) and its reaction with S^{2-}. *(bottom)* The crystal structures of complex (**a'**). Anion (PF_6^-) and the hydrogens have been omitted and only the core atoms are shown as 50 % probability thermal ellipsoids for clarity. Crystal structure images were processed using Mercury 3.7 (Build RC1).

Ligand (**b**) was then prepared[41] by changing the imine to a diethylamine group , but its reaction with $Cu(MeCN)_4PF_6$ (1 eq) gave inconclusive results. However, the reaction of (**b**) with CuCl (1 eq) delivered a tetracopper complex (**5**) supported by two ligands and four bridging Cl^- ions (**Figure 2.5**).

The four Cu(I) ions of **5** resemble a parallelogram with the longer sides (2.730(2) Å) supported by two bridging (**b**) ligands and the shorter sides (2.659(2) Å) held by two μ_2-Cl ligands. Additionally, each face of the parallelogram is capped by a μ_3-Cl ligand. All the chloride ions reside in a plane that bisects the shorter side of the parallelogram at 95.5(1) °. Unfortunately, **5** was not stable in the presence of S^{2-}, also decomposing to Cu_2S as evident by formation of a brown precipitate.
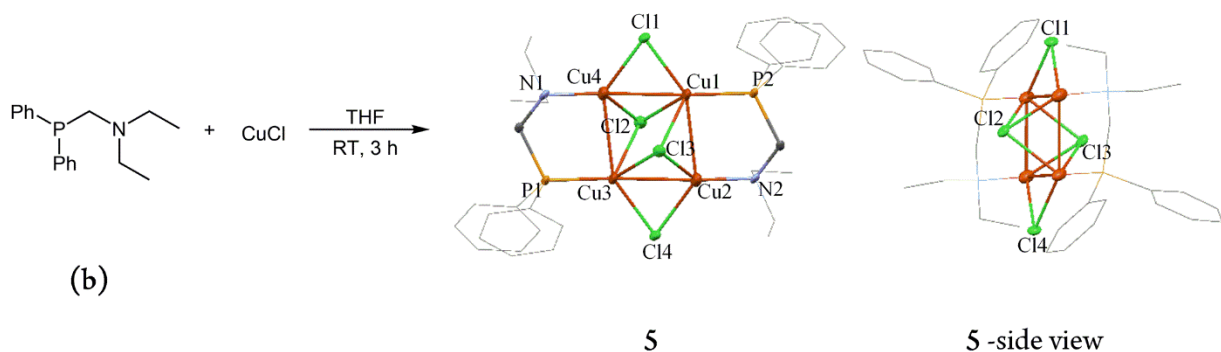
FIGURE 2. 5 Synthesis and the crystal structure of tetra copper complex **5**. Hydrogens have been omitted and only the core atoms are shown as 50 % probability thermal ellipsoids for clarity. Crystal structure images were processed using Mercury 3.7 (Build RC1).

2.5 $Cu_4(\mu_4$-S) clusters supported by formamidinate ligands (NCN)

The preceding ligands provided new insights into the formation of dicopper precursors and $Cu_4(\mu_4$-S) complexes, yet the available model compounds described above are redox inactive, and features of these phosphorous ligands that may enable redox activity is yet to be discovered. In this context, we previously reported the use of amidinate based ligand bis(2,4,6-trimethylphenyl)formamidinate (NCN) [deprotonated (**c**)] in place of phosphine-based ligands.[31,32] Being negatively charged, (**c**) was found to form a neutral dicopper(I) precursor complex (**c'**). The reaction of (**c'**) with S_8 resulted a $Cu_4(\mu_4$-S) complex (**6c**) in the 2-hole redox state (formally $2Cu^{2+}$ - $2Cu^{1+}$).[31] The 2-hole species was chemically reduced to a 1-hole (**7c**) complex (formally $1Cu^{2+}$ - $3Cu^{1+}$) using K(18-crown-6)Fp as an external electron donor (Fp = FeCp(CO)$_2$) (see **Chart 2.1**; an analogous reaction sequence in shown in **Figure 2.7**).[32] To our delight, the 1-hole complex was found to mediate the 2e$^-$ reduction of N_2O to N_2 and O^{2-}, at that time representing the first reported structural and functional model complex for the Cu_Z active site of N_2OR.[32] However, cyclic voltammetry experiments indicated that the fully-reduced 4Cu(I) state was not stabilized by this ligand.[31]

2.5.1   NCN ligand with electron withdrawing groups

The above discussed NCN ligand system could not stabilize the fully reduced redox state (formally 4Cu(I)) either electrochemically or by chemical reduction, presumably due to the anionic nature of the four NCN ligands destabilizing the doubly anionic target. So, *p*-CF$_3$ groups were introduced to prepare an electron deficient

formamidinate ligand (**d**) that might better stabilize a dianionic complex.[42] The reaction between (**d**) and

Cu(MeCN)$_4$PF$_6$ (1 eq) was carried out in attempt to synthesize a dicopper(I) precursor complex. Surprisingly, it instead

resulted in a tetracopper complex supported by four ligands (**8**) as confirmed by X-ray crystallography (**Figure 2.6**).
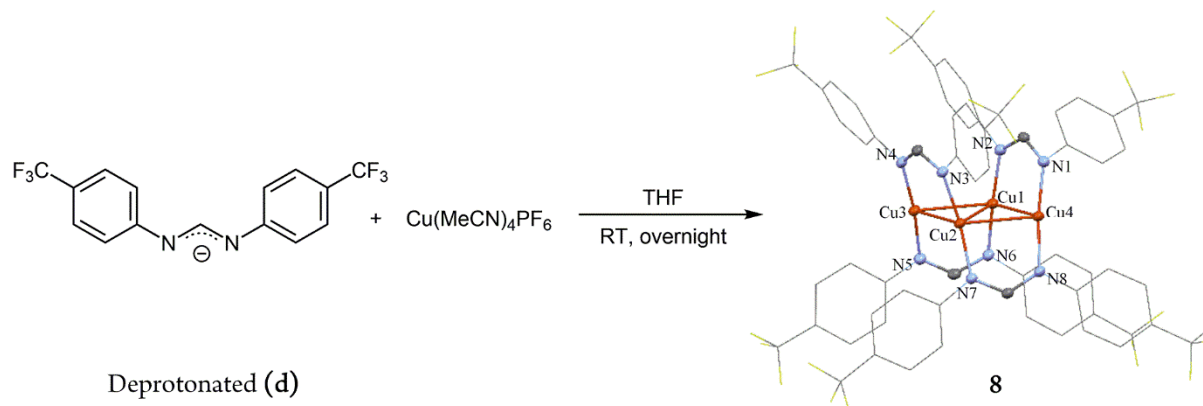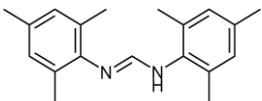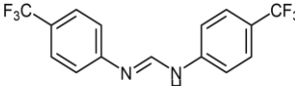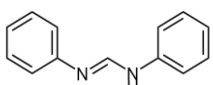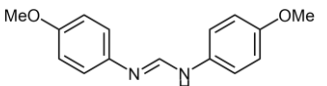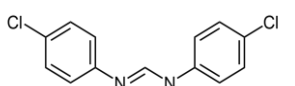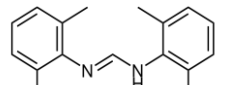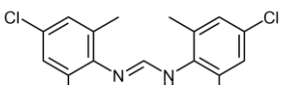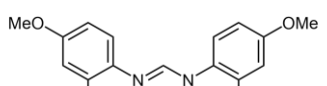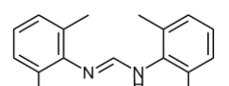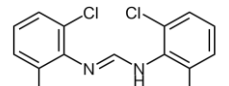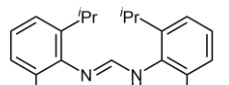
FIGURE 2. 6 Synthesis and the crystal structure of tetra copper complex **8**. Hydrogens have been omitted and only the core atoms are shown as 50 % probability thermal ellipsoids for clarity. Crystal structure images were processed using Mercury 3.7 (Build RC1).

The four Cu(I) ions in **8** resemble a slightly distorted rhombus with an average Cu-Cu distance of 2.692(8)

Å. The shorter dicopper diagonal is 2.843(6) Å, and the longer one is 4.571(4) Å. Each side of the rhombus is bridged

by an NCN ligand from top and bottom alternatively, leading to π-stacking between the phenyl substituents on the

same face of the rhombus. Essentially, complex **8** resembles the Cu$_Z$ site lacking its sulfur atom. We were unable to

identify any conditions for introducing a sulfur atom into the tetracopper core of **8**.

2.5.2   Effect of NCN ligand residual substituent on complex formation

The complexation behavior of (**d**) suggested that our general synthetic protocol for assembling Cu$_4$(μ_4-S)

complexes might be sensitive to the residual substituents on NCN ligand. To confirm this, ligands (**e**)-(**m**) were

prepared and tested for their complexation behavior (**Table 2.1**). Formation of the dicopper(I) precursor complexes

were primarily confirmed by ^{1}H NMR spectroscopy and solubility behavior. To test for formation of 2-hole Cu$_4$(μ_4-

S) clusters, the characteristic intense purple color (or lack thereof) was monitored by UV-Vis spectrometry (see

Chapter 5, Section 5.1.4 Experimental spectra and relevant data tables).

TABLE 2. 1 The effects of NCN ligand residual substituents on the formation of dicopper precursor, tetra copper-sulfur 2-hole and/or 1-hole clusters.

Ligand (L)		Precursor Cu_2L_2	2-hole $Cu_4(\mu_4\text{-}S)L_4$	1-hole $Cu_4(\mu_4\text{-}S)L_4$
	(c)	(c')	6c	7c
	(d)	No, forms **8**	-	-
	(e)	No	-	-
	(f)	No	-	-
	(g)	No	-	-
	(h)	(h')	6h	7h
	(i)	(i')	6i	-
	(j)	(j')	6j	-
	(k)	(k')	No	-
	(l)	(l')	6l	-
	(m)	(m')	No	-

Ligand (**c**) featuring methyl substituents at both *ortho* and *para* positions was chosen as the reference point. The reaction of Cu(MeCN)₄PF₆ (1 eq) with ligands (**e**)-(**g**) forms yellowish solids with poor solubilities in common organic solvents. Typical dicopper formamidinate complexes are colorless and have significant solubilities in common organic solvents. This leads us to believe that ligands (**e**)-(**g**) form multicopper complexes like **8**; however, we could not confirm that by solution NMR or X-ray crystallography because of the poor solubilities. Changing the *para* substituent to -H and maintaining *ortho*-methyl groups (**h**) reestablished the general synthesis. We were able to isolate **6h** in good yields, followed by chemical reduction to get **7h** using K(18-crown-6)Fp (**Figure 2.7**). Assignment of **7h** was further confirmed by observing similar features in X-band EPR (g = 2.05, 2.01) and UV-Vis (λ_{max} = 571 nm) to those of **7c**. Changing the *para* substituent to -Cl while having -CH₃ groups at *ortho* positions (**i**), had minimal effects to the synthesis. However, the isolation of **6i** was challenging and the chemical reduction to a 1-hole species was not attempted. At this point it was clear that a steric factor similar to -CH₃ is required at the *ortho* positions of the formamidinate ligands to stabilize a Cu₄(μ_4-S) assembly. Change in the steric factor at the *para* position has a minimum effect to the stability but affects the solubility and isolation of Cu₄(μ_4-S) complexes.
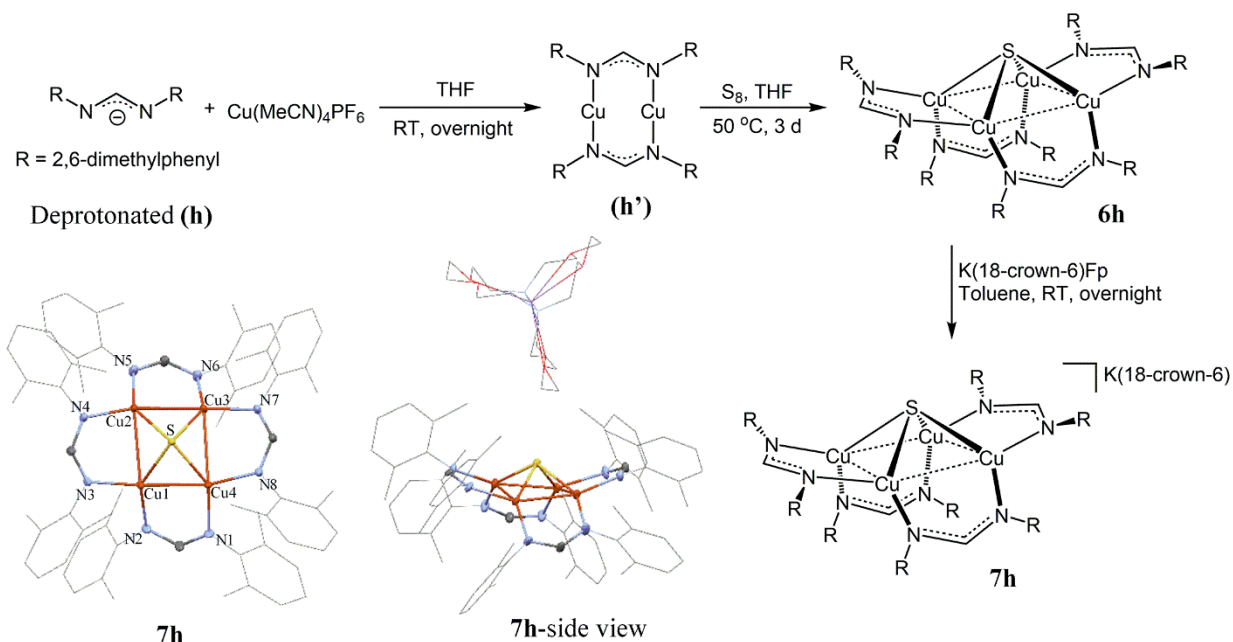
FIGURE 2. 7 Synthesis of dicopper precursor complex (**h'**), 2-hole tetra copper-sulfur complex **6h** and its subsequent chemical reduction to 1-hole complex **7h**. The 18-crown-6 of **7h** was exchanged with 2,2,2-cryptand before crystallization. crystal structures of complexes (**h'**), **6h** and **7h**. Hydrogens have been omitted and only the core atoms are shown as 50 % probability thermal ellipsoids for clarity. Crystal structure images were processed using Mercury 3.7 (Build RC1).

Ligands (**j**)-(**m**) show that the dicopper(I) precursor could be stabilized as long as neither *ortho* position is unsubstituted. Under the tested conditions, -CH$_3$, -Cl, -OMe and isopropyl substituents at *ortho* positions are amenable to stabilizing the dicopper(I) precursor structure. Moreover, *ortho* substituents bigger than -CH$_3$ [(**k**), (**m**)] destabilize the formation of the Cu$_4$(μ_4-S) assembly due to their steric repulsions, while both -CH$_3$ and -Cl with similar steric factors[43,44] have been able to stabilize **6h** and **6l** even with different electronics (**Table 2.1**). Collectively, the formation of the dicopper precursor and the 2-hole Cu$_4$(μ_4-S) cluster is controlled mainly by the steric factor at the *ortho* positions of the formamidinate ligands and is relatively insensitive to the *para* position.

2.5.3 Redox features of 2-hole complexes supported by NCN ligands

The redox behavior of **6h** and **6i** was compared to that of **6c** using cyclic voltammetry (**Figure 2.8**). The cyclic voltammogram, reported previously[32], of **6c** features a reversible one electron redox event at -1.28 V vs Fc$^+$/Fc. Change of the *para* substituent from -CH$_3$ to -H (**6h**) shifts the reduction potential to -1.15 V (vs Fc$^+$/Fc) (E_{pa} = -1.09 V, E_{pc} = -1.21 V). Changing the *para* substituent to -Cl (**6i**) shifts the reduction potential to -1.24 V (vs Fc$^+$/ Fc) (E_{pa} = -1.18 V, E_{pc} = -1.30 V). Both **6c**[32] and **6h** could be chemically reduced to the corresponding 1-hole clusters **7c** and **7h**, but the chemical reduction of **6i** was not attempted.
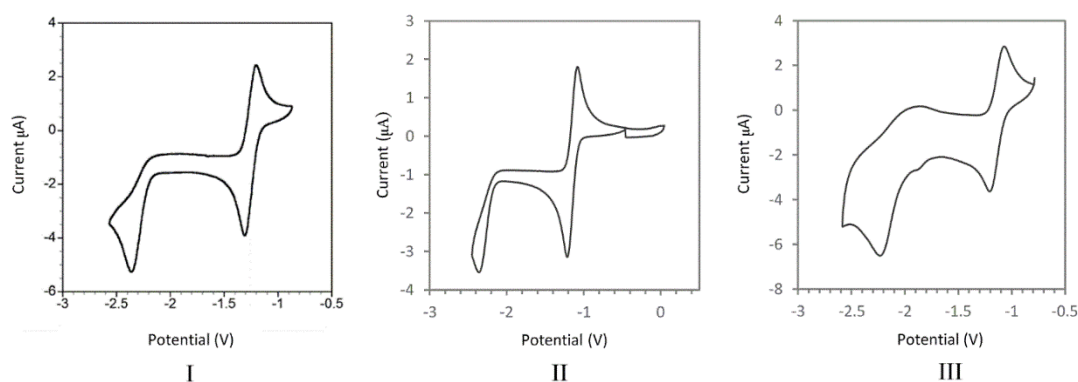
FIGURE 2. 8 Cyclic voltammograms of **6c** (I), **6h** (II) and **6i** (III) with 0.1 M [NBu$_4$][PF$_6$] in THF, referenced to Fc$^+$/ Fc = 0 V (0.46 V vs. the Ag$^+$/Ag^0 reference electrode) . Initial potential for (II) = -0.46 V, initial potential for (III) = -0.80 V, scan direction = falling, sweep rate = 0.1 V/S. The CV of **6c** (I) is reproduced with permission from reference 31. Copyright 2015 chemical communication, The Royal Society of Chemistry.

2.6   Multi copper complexes supported by phosphaamidine ligands

The results thus far indicate that neutral phosphine donors (soft) are suitable for stabilizing $Cu_4(\mu_4\text{-S})$ assemblies in the fully reduced 4Cu(I) state, while the anionic formamidinate donors (hard) are suitable for 2-hole and 1-hole states. However, neither neutral nor anionic ligand could individually support a $Cu_4(\mu_4\text{-S})$ complex that shows a completely reversible two-electron redox chemistry as is observed for the biological Cu_Z site. We next hypothesized that a $Cu_4(\mu_4\text{-S})$ cluster supported by a ligand composed of both neutral phosphine and anionic nitrogen donors would enable two-electron redox chemistry.

2.6.1   Background of phosphaamidinate ligands

The coordination chemistry of phosphaamidinate analogues, $[RNC(R')PR]^-$, is less well known since the initial discovery of phosphorous–carbon multiple bond chemistry by Issleib et al. in 1978,[45] and only a few examples of transition metal phosphaamidinate complexes are reported including a binuclear Pt(II) complex chelated by N and P,[45] a Tl(I) complex supported by P and an aryl substituent on N,[46] a trinuclear-Au(I) complex only coordinated through P,[47] a Rh(I) complex chelated with both N and P (**Chart 2.2**).[47]

(i)	(ii)	(iii)	(iv)
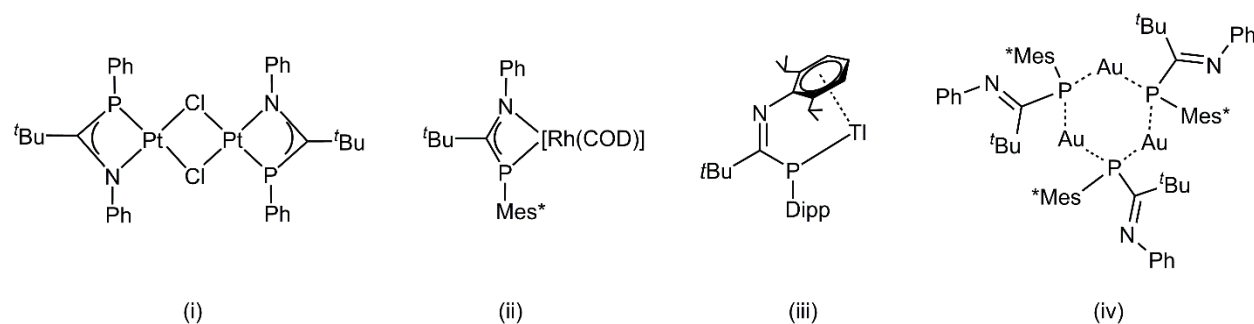
CHART 2. 2 Different modes of coordination reported for phosphaamidinate/phosphaamidine ligands. (i) and (ii) represent chelating phosphaamidinates and (iii) and (iv) shows coordination/ bridging of phosphaamidine through phosphorous donor.

The coordination chemistry of phosphaamidinates thus far consists of chelation to single metal sites or $\mu_2\text{-P}$ bridging between two metal sites. Phosphaamidinates possess different electronic properties to that of amidinates, due to the softer P-donor atom and different π-donor behavior of P=C vs. N=C multiple bonds. Hence, additional coordination modes may be available to phosphaamidinates that are unavailable to amidinates. Specially,

phosphaamidinates must be able to bridge between two copper atoms for them to be applicable in our precursor and tetracopper-sulfur complex synthesis. The different electronic features and coordination modes of phosphamidinates have the potential to complement the established behavior of the prolific amidinate ligands, allowing them to be versatile for designing organometallic architectures.

2.6.2   Use of phosphabenzamidinate ligand

In attempt to test our hypothesis first, phosphabenzamidine $(\textbf{n}_1)/(\textbf{n}_2)$ was synthesized by adopting the synthetic routes reported in literature,[47,48] utilizing N-benzylidyne-2,4,6-trimethylbenzenaminium triflate **C** and mesitylphosphane **D** (**Scheme 2.1**). The reaction conditions drive 1,3 hydrogen shift to afford $(\textbf{n}_1)$ ~80 % and $(\textbf{n}_2)$ ~20 %. Without purification, both $(\textbf{n}_1)$ and $(\textbf{n}_2)$ can be transformed into corresponding lithium phosphabenzamidinate **(o)** by deprotonation with *n*-butyllithium.[49]
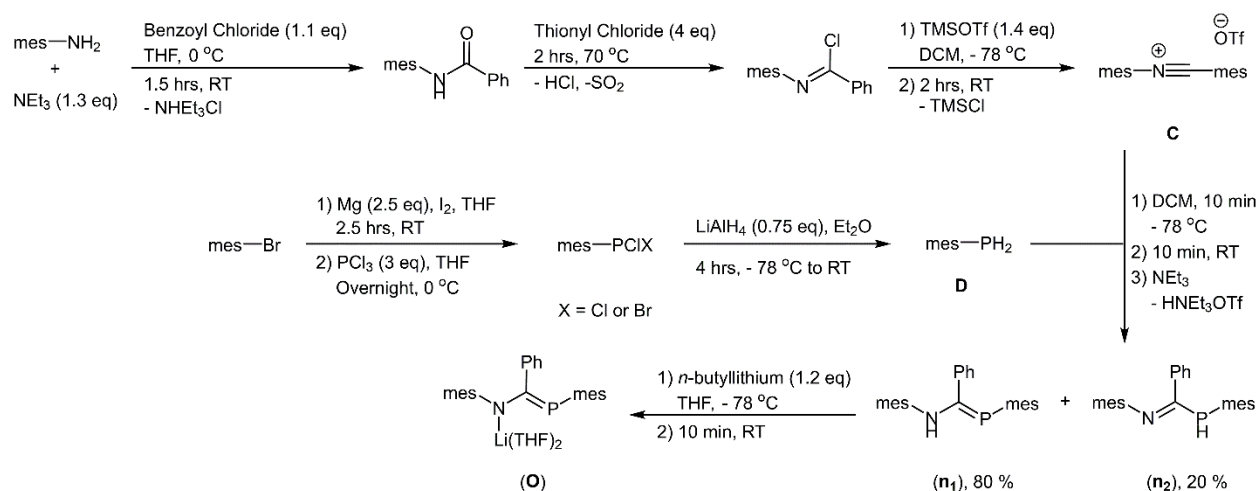
SCHEME 2. 1 Synthetic procedure of phosphabenzamidine (**n**) and phosphabenzamidinate (**o**)

With **(o)** in hand, we were interested in studying its coordination with Cu(I) ions. Cu(I)Cl was chosen as the source of copper, with the expectation that precipitation of LiCl salt would facilitate coordination. The reaction of **(o)** with 3 eq of Cu(I)Cl in THF delivered an orange solid that showed distinct peaks for inequivalent mesityl CH_3 groups in the ^{1}H NMR spectrum, possibly due to π-π stacking interactions restricting rotation of the mesityl groups. The crystal structure revealed this orange solid to be $Cu_6[mes-N=C(Ph)-P-mes]_3Cl_4Li(THF)_2$ **(9)** (**Figure 2.9**). To our surprise, four Cl$^-$ anions and a Li$^+$ cation were retained in the structure. We have been unable to induce LiCl

precipitation from **3** through a variety of methods, and addition of Na$_2$S simply results in partial Li$^+$/Na$^+$ exchange as judged by NMR spectroscopy and crude X-ray crystallography.
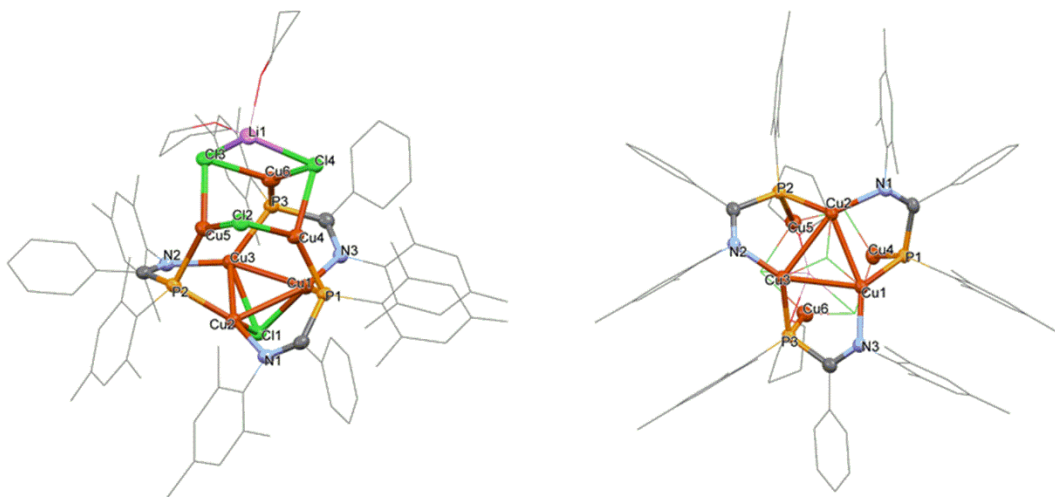
FIGURE 2. 9 Side *(left)* and the bottom *(right)* views of the crystal structure of the hexacopper complex **9**. Hydrogens have been omitted and only the core atoms are shown as 50 % probability thermal ellipsoids for clarity. Crystal structure images were processed using Mercury 3.7 (Build RC1).

The solid-state structure of complex **9** consists of two triangular Cu(I) clusters arranged on top of each other as a hexacopper antiprism. The "bottom" Cu1$\cdots$Cu2$\cdots$Cu3 base is capped by a Cl$^-$ ligand, and the "top" Cu4$\cdots$Cu5$\cdots$Cu6 base is supported by three μ_2-Cl$^-$ ligands that, in turn, are capped by a Li$^+$ ion. The Li$^+$ ion has also two coordinated THF ligands. The phosphabenzamidinate ligands are arranged in a regular propeller-like chiral fashion, with their N-atoms coordinating the "bottom" 3Cu(I) base and their P-atoms acting as μ_2-ligands bridging the "bottom" and "top" bases of the antiprism. The Cu$\cdots$Cu separations within the "bottom" base are shorter (2.69-2.75 Å) than in the "top" (2.95-3.14 Å), and both are shorter than Cu$\cdots$Cu separations between the bases (~3.3 Å for P-bridged Cu(I) ions and 3.6-3.8 Å between non-bridged ones).

We are interested in more reactive complexes with coordinatively unsaturated Cu(I) ions, as precursors to construct tetranuclear copper sulfide clusters. To attempt to address this, (**o**) was reacted with 1 and 2 eq of Cu(I)Cl, to target a di- or trinuclear cluster with a 1:1 ratio of bidentate phosphabenzamidinate to Cu(I). Interestingly, the ^{31}P NMR spectra showed formation of **9** and unreacted (**o**) in both reactions, suggesting that the formation of **9** is highly favorable regardless of metal:ligand stoichiometry in the reaction mixture. As confirmed by the crystal structure, the presence of μ_2-Cl ligands stabilizes **9** by balancing the charge and saturating the Cu centers. Such coordination of halides is

common, and a similar coordination has been reported by Jessop and co-workers in a phosphaamidine-Cu(I)Br cluster.[50] So, we next wondered whether a more reactive complex could be attained by applying a halide-free copper source. Mesitylcopper was an ideal candidate for this purpose, as it allows the simultaneous deprotonation and coordination. To begin with, (**o**) was reacted with 1 eq of mesitylcopper at room temperature, and after 3 hours (**o**) was partially consumed and a new product was observed by ^{31}P NMR spectroscopy. The formation of mesitylene was confirmed by ^{1}H NMR spectroscopy. After purification, the ^{1}H NMR spectrum of the new species indicated restricted rotation of the mesityl groups, like **9.** However, the solubility of the new species was poor in most of the available solvents, hence making it is difficult to grow X-ray quality crystals or analyze the structure by solution methods.

2.6.2 Use of phosphaformamidinate ligand

Next, phosphaformamidine (**p**) was synthesized and applied in place of (**o**). The previous synthetic route (**Scheme 2.1**) could not be applied as multiple attempts to make the imidoyl chloride (precursor of **C**) were unsuccessful. Hence, ethyl-*N*-mesitylformimidate (**E**) was synthesized[40] and reacted with lithium mesitylhydrophosphanide to afford (**p**) as a yellow green solid (**Scheme 2.2**). Production of mesityl phosphane was also observed as the lithium mesitylhydrophosphanide is basic enough to deprotonate (**p**). However, an overnight long reaction time followed by the addition of NH$_4$Cl, shifted the equilibrium towards the formation of (**p**).[49]
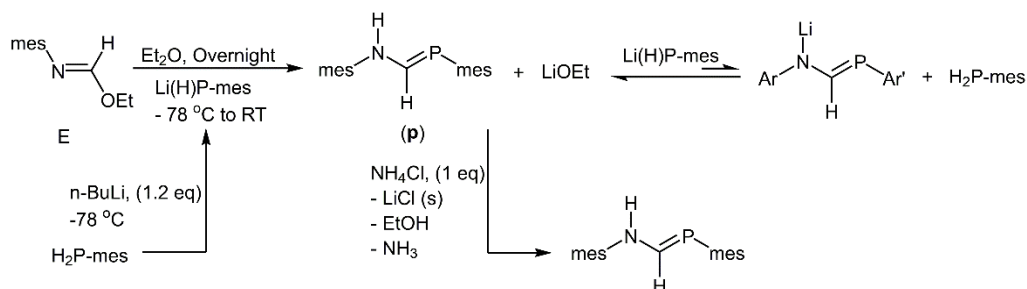
SCHEME 2. 2 Synthesis of scheme of phosphaformamidine (**p**).

A small-scale reaction of (**p**) (0.0673 mmol) with mesitylcopper in Et$_2$O afforded **10** as an orange solid after 2 days. However, scaling up the reaction by 10-fold required 8 days to complete the reaction as evidenced by ^{31}P NMR. So, an alternative approach was applied by first deprotonating (**p**) with sodium bis(trimethylsilyl)amide

(NaHMDS) and the adding $Cu(MeCN)_4PF_6$ in Et_2O, resulting in rapid formation of **10**. The ^1H NMR spectrum of **10** exhibited restricted mesityl bond rotation like **9**, and the single crystal XRD confirmed the identity of **10** as $Cu_4(mes-N=CH-P-mes]_4$ (**Figure 2.10**).
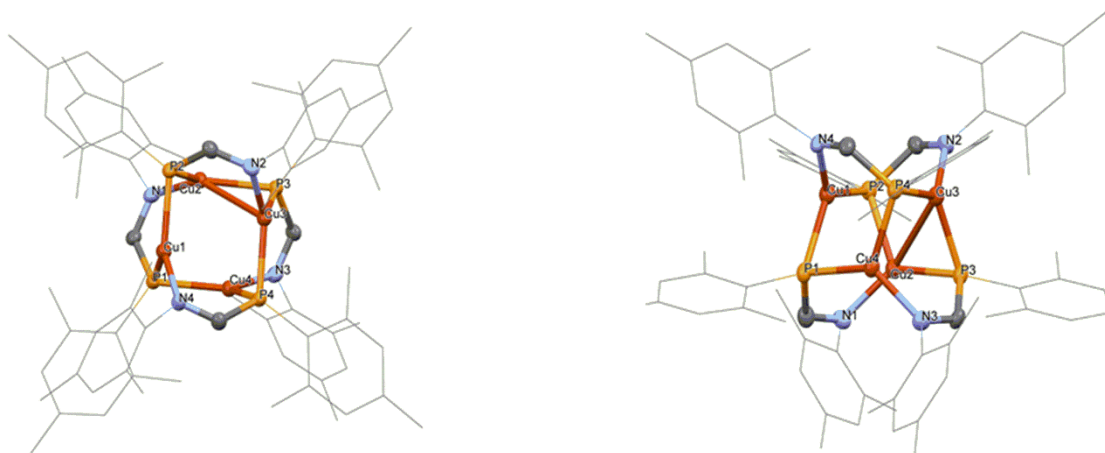
FIGURE 2. 10 Top *(left)* and the side *(right)* views of the crystal structure of the tetracopper complex **10**. Hydrogens have been omitted and only the core atoms are shown as 50 % probability thermal ellipsoids for clarity. Crystal structure images were processed using Mercury 3.7 (Build RC1).

The structure of **10** contains a tetrahedron of Cu(I) ions, with the overall cluster having non-crystallographic S_4 symmetry. Each ligand caps one of the faces of the tetrahedron with N-atoms reaching Cu atom opposite to the bridged edge at a 2.01 Å distance. All P-Cu bond lengths are in a narrow range 2.26-2.28 Å and have an average Cu⋯Cu separation 2.94 Å. The two opposite non-bridged Cu atoms are elongated to a distance of 3.13 Å.

Even in the absences of halides, **10** still has μ_2-bridging phosphorous atoms, implying that the triply bridging coordination behavior of phosphaamidinates is intrinsic. To our knowledge, this coordination mode has not been observed previously in the phosphaamidinate literature. Analogous behavior is not seen in formamidinates, as the nitrogen lone pairs are resonance delocalized and thus unavailable to bridge two metals at a single N-atom. In conjugate base of (**n**) and (**p**), there is apparently less delocalization due to poor overlap of the phosphorous 3p orbitals with the carbon 2p orbitals, making the phosphorous lone pairs available for an extra coordination to a third metal center.

2.6.3 Electrochemistry of phosphaamidinate supported multi copper clusters

The redox behavior of both **9** and **10** was studied using cyclic voltammetry. Complex **9** displayed few redox events that are not well defined and, surprisingly, complex **10** was redox innocent (see Chapter 5, Section 5.1.4 Experimental spectra and relevant data tables) despite being supported by electron rich phosphorous σ-donors. In addition, due to our interest in constructing tetranuclear copper-sulfide clusters, we added several sulfur-atom donor reagents to **10**. Unfortunately, no reaction was observed under the conditions we examined, indicating the inert nature of **10** (which is even air-stable).

2.6.4 μ_2-coordinated P, N mixed donor ligand

Coordination pattern of the complexes **9** and **10** confirms that the synthesized[40,51] phosphaamidinates (**o**) and (**p**) do not behave as their formamidinate counterparts; instead the negatively charged phosphide units bridge between three Cu(I) ions, assembling them into a hexa- and tetracopper(I) clusters, respectively (**Table 2.2**).[49] Apparently, the negative charge should be valence-trapped on nitrogen to facilitate μ_2-coordination of the 3-atom bridge; delocalization of negative charge on phosphorous instead favors binding to three copper centers. However, literature reports of such ligands having a negative charge on nitrogen indicate that they may be unstable towards P-C bond cleavage.[52] Nonetheless, there are a few ways to stabilize such an arrangement, including pre-coordination of Cu to phosphorous before N deprotonation or having cyclohexyl substituents on phosphorous.[52] Alternatively, we could deconjugate nitrogen and phosphorous. To test our hypothesis, the ligand (**q**) containing a pyrrole anion was synthesized adopting a literature procedure.[53] The reaction of (**q**) with Cu(MeCN)$_4$PF$_6$ (1 eq) resulted a dicopper precursor complex (**q'**) as expected (**Table 2.2**). However, our target was to synthesize a precursor in which each copper is supported by both neutral and anionic donors. Instead, in (**q'**) each Cu(I) was supported by either two neutral or two anionic donors as confirmed by the X-ray crystallography (**Figure 2.11**).
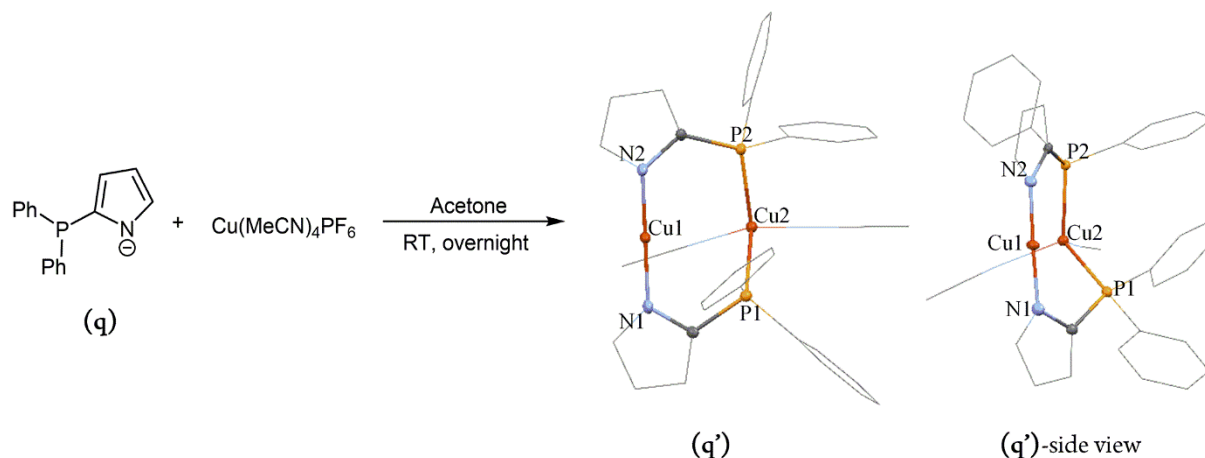
FIGURE 2. 11 Synthesis and the crystal structure of the dicopper precursor complex (**q'**). Hydrogens have been omitted and only the core atoms are shown as 50 % probability thermal ellipsoids for clarity. Crystal structure images were processed using Mercury 3.7 (Build RC1).

TABLE 2. 2 Multi copper(I) complexes stabilized by phosphaamidine (**a**) and phosphaamidinates (**o-q**) ligands.

Ligand		Complexation with Cu(MeCN)₄PF₆
	(**a**)	Forms a dicopper precursor complex (**a'**)
	(**o**)	Forms a hexacopper complex **9**
	(**p**)	Forms a tetra copper complex **10**
	(**q**)	Forms a dicopper precursor complex (**q'**)

In (**q'**), the average Cu-N and Cu-P bond lengths are 1.863(4) Å and 2.258(1) Å, respectively. The N-Cu-N unit is linear, while the P-Cu-P unit is bent to accommodate a coordinated solvent molecule. Unfortunately, the reaction of (**q'**) with S_8 gave inconclusive results, forming a brown precipitate that we assume is Cu_2S. Ideally, neither neutral phosphorous nor anionic nitrogen donors should allow the decomposition of the dicopper precursor (**q**) to solid Cu_2S. Perhaps, the precursor with two electronically different Cu(I) ions disrupts the assembly of a $Cu_4(\mu_4\text{-S})$ cluster.

Attempts to synthesize a precursor with electronically similar Cu(I) ions yet supported by both neutral and anionic donors are currently underway.

2.7 Conclusion

A series of ligands consisting of neutral and/or anionic donors have been tested for their ability to stabilize corresponding dicopper precursor complexes that are in turn able to assemble into $Cu_4(\mu_4\text{-}S)$ clusters. Ligands having a 3-atom bridge between the Cu(I) ions in the precursor are more likely to assemble a $Cu_4(\mu_4\text{-}S)$ cluster in the presence of a sulfur source. The $Cu_4(\mu_4\text{-}S)$ complexes (**1, 2**) that are supported by dppm and dppa are structurally close to the active site of N_2OR.[30] Attempts to make analogues of **1** with hemi-labile ligands failed as the Cu(I) ions was stripped out of the complex by S^{2-}. Ligand (**c**) stabilized a redox-active $Cu_4(\mu_4\text{-}S)$ system, representing the first reported structural and functional model complex of the Cu_Z active site of N_2OR.[32] Complexation behavior of ligands (**d**)-(**m**) indicates that formation of the dicopper(I) precursor and then the 2-hole $Cu_4(\mu_4\text{-}S)$ cluster is governed by the steric factor at the *ortho* positions of the formamidinate ligands. Collectively, the neutral phosphine donors are suitable to stabilize the formally 4Cu(I) state of a $Cu_4(\mu_4\text{-}S)$ cluster, and the anionic nitrogen donors are required to stabilize the $2Cu^{2+}$ - $2Cu^{1+}$ and $1Cu^{2+}$ - $3Cu^{1+}$ redox states. Phosphaamidinates (**o**)-(**q**) were rationally designed to incorporate both neutral and anionic donors. The anionic charge delocalization onto phosphorous results in μ_3-bridging coordination[49], but valence-trapping the charge on nitrogen allows the isolation of a dicopper complex.

2.8 Future directions

An ideal ligand system that would stabilize all three redox states of a $Cu_4(\mu_4\text{-}S)$ complex is yet to be discovered. Our approach of using anionic P, N mixed donor (hard and soft) ligands was not successful in stabilizing $Cu_4(\mu_4\text{-}S)$ assembly. Our next strategy to have a mixed donor ligand is to extend the formamidinate system to accommodate neutral N or P donor groups. Such ligands (**Chart 2.3**) have already been published.[54–56]

qfam   dpfam   dpqfam
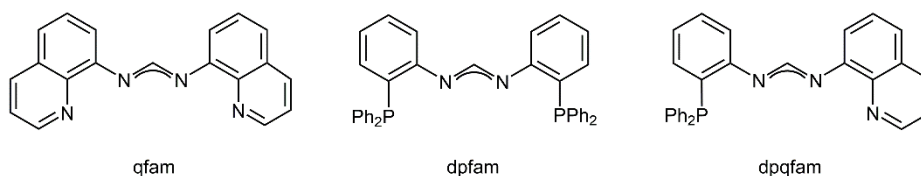
CHART 2. 3 Literature reported formamidinate ligands with neutral P/N donor groups. qfam = N,N′-di-8-quinolylformamidinate, dpfam = N,N′ -bis[2- (diphenylphosphino)phenyl]formamidinate and dpqfam = N-(2-diphenylphosphino)phenyl-N′-8-quinolylformamidinate.

A 1:1 reaction of qfam with $Cu(MeCN)_4PF_6$ yielded a dark red color solid which has a poor solubility in common organic solvents. Presumably, it is a dicopper precursor complex as evidenced by no remaining reactants at the end of the reaction. However, leaving a THF solution of this red colored product under open air resulted in the formation of dark blue-purple crystals and the crude single crystal analysis revealed its identity as $Cu_4(\mu_4\text{-O})(qfam)_4$ (**Figure 2.12**). Characteristic blue purple color of the crystals implies this to be a 2-hole complex, but the product has not been fully characterized yet. However, this observation makes us believe that qfam could stabilize a $Cu_4(\mu_4\text{-S})$ assembly. Currently, experiments are underway to characterize the presumable precursor complex $[Cu_2(qfam)_2]$ and to explore its reactivity with neutral sulfur reagents. If it stabilizes a $Cu_4(\mu_4\text{-S})(qfam)_4$ cluster, it will be interesting to study its redox behavior because such complex may have the two electron redox stability (2-hole to fully reduced and vice versa) that is required for N_2O reduction activity.
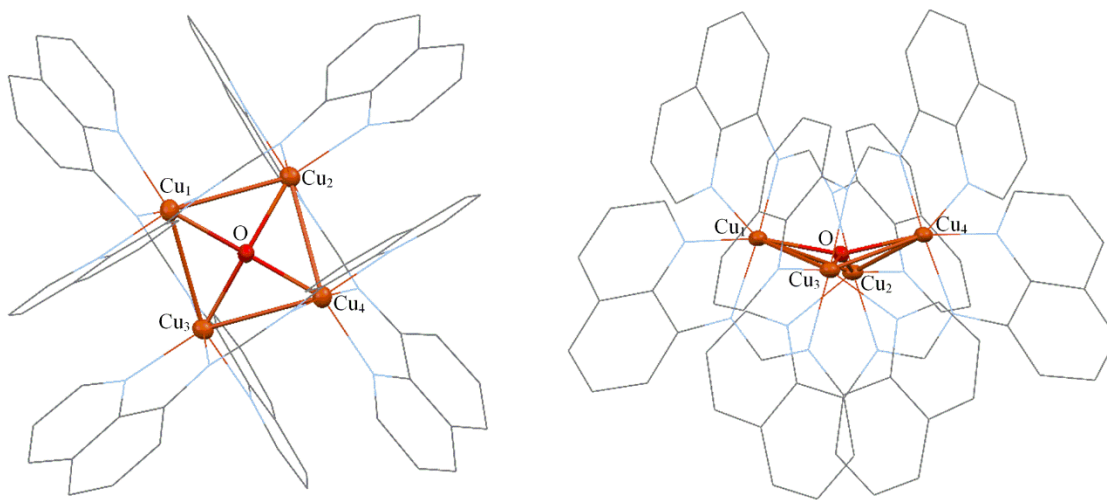
FIGURE 2. 12 Top *(left)* and side *(right)* view of the crude crystal structure of $Cu_4(\mu_4\text{-O})(qfam)_4$. Hydrogens have been omitted and only the core atoms are shown as 50 % probability thermal ellipsoids for clarity. Crystal structure images were processed using Mercury 3.7 (Build RC1).

2.9   References

(1)   Pauleta, S. R.; Carepo, M. S. P.; Moura, I. Source and Reduction of Nitrous Oxide. *Coord. Chem. Rev.* **2019**, *387*, 436–449.

(2)   Carreira, C.; Pauleta, S. R.; Moura, I. The Catalytic Cycle of Nitrous Oxide Reductase — The Enzyme That Catalyzes the Last Step of Denitrification. *J. Inorg. Biochem.* **2017**, *177*, 423–434.

(3)   Brown, K.; Djinovic-Carugo, K.; Haltia, T.; Cabrito, I.; Saraste, M.; Moura, J. J. G.; Moura, I.; Tegoni, M.; Cambillau, C. Revisiting the Catalytic CuZ Cluster of Nitrous Oxide (N2O) Reductase: Evidence of a Bridging Inorganic Sulfur. *J. Biol. Chem.* **2000**, *275*, 41133–41136.

(4)   Kroneck, P. M. H.; Riester, J.; Zumft, W. G.; Antholine, W. E. The Copper Site in Nitrous Oxide Reductase. *Biol. Met.* **1990**, *3*, 103–109.

(5)   Rasmussen, T.; Berks, B. C.; Sanders-Loehr, J.; Dooley, D. M.; Zumft, W. G.; Thomson, A. J. The Catalytic Center in Nitrous Oxide Reductase, Cu(z), Is a Copper-Sulfide Cluster. *Biochemistry* **2000**, *39*, 12753–12756.

(6)   Chen, P.; Gorelsky, S. I.; Ghosh, S.; Solomon, E. I. N2O Reduction by the M4-Sulfide-Bridged Tetranuclear CuZ Cluster Active Site. *Angew. Chemie - Int. Ed.* **2004**, *43*, 4132–4140.

(7)   Johnston, E. M.; Carreira, C.; Dell'Acqua, S.; Dey, S. G.; Pauleta, S. R.; Moura, I.; Solomon, E. I. Spectroscopic Definition of the CuZ° Intermediate in Turnover of Nitrous Oxide Reductase and Molecular Insight into the Catalytic Mechanism. *J. Am. Chem. Soc.* **2017**, *139*, 4462–4476.

(8)   Tolman, W. B. Binding and Activation of N2O at Transition-Metal Centers: Recent Mechanistic Insights. *Angew. Chemie - Int. Ed.* **2010**, *49*, 1018–1024.

(9)   Fujita, K.; Dooley, D. M. Insights into the Mechanism of N2O Reduction by Reductively Activated N2O Reductase from Kinetics and Spectroscopic Studies of PH Effects. *Inorg. Chem.* **2007**, *46*, 613–615.

(10)   Pomowski, A.; Zumft, W. G.; Kroneck, P. M. H.; Einsle, O. N2O Binding at a [4Cu:2S] Copper-Sulphur Cluster in Nitrous Oxide Reductase. *Nature* **2011**, *477*, 234–237.

(11)   Johnston, E. M.; Dell'Acqua, S.; Ramos, S.; Pauleta, S. R.; Moura, I.; Solomon, E. I. Determination of the Active Form of the Tetranuclear Copper Sulfur Cluster in Nitrous Oxide Reductase. *J. Am. Chem. Soc.* **2014**, *136*, 614–617.

(12)   Wüst, A.; Schneider, L.; Pomowski, A.; Zumft, W. G.; Kroneck, P. M. H.; Einsle, O. Nature's Way of Handling a Greenhouse Gas: The Copper-Sulfur Cluster of Purple Nitrous Oxide Reductase. *Biol. Chem.* **2012**, *393*, 1067–1077.

(13)   Johnston, E. M.; Dell'Acqua, S.; Pauleta, S. R.; Moura, I.; Solomon, E. I. Protonation State of the Cu 4 S 2 Cu Z Site in Nitrous Oxide Reductase: Redox Dependence and Insight into Reactivity. *Chem. Sci.* **2015**, *6*, 5670–5679.

(14)   Brown, K.; Tegoni, M.; Prudêncio, M.; Pereira, A. S.; Besson, S.; Moura, J. J.; Moura, I.; Cambillau, C. A Novel Type of Catalytic Copper Cluster in Nitrous Oxide Reductase. *Nat. Struct. Biol.* **2000**, *7*, 191–195.

(15)   Maji, R. C.; Das, P. P.; Bhandari, A.; Mishra, S.; Maji, M.; Ghiassi, K. B.; Olmstead, M. M.; Patra, A. K. Mixed Valence Copper-Sulfur Clusters of Highest Nuclearity: A Cu8 Wheel and a Cu16 Nanoball. *Chem. Commun.* **2017**, *53*, 3334–3337.

(16)   Helton, M. E.; Chen, P.; Paul, P. P.; Tyeklár, Z.; Sommer, R. D.; Zakharov, L. N.; Rheingold, A. L.; Solomon, E. I.; Karlin, K. D. Reaction of Elemental Sulfur with a Copper(I) Complex Forming a Trans-μ-1,2 End-on Disulfide Complex: New Directions in Copper-Sulfur Chemistry. *J. Am. Chem. Soc.* **2003**, *125*, 1160–1161.

(17)   Ghiladi, R. A.; Rheingold, A. L.; Siegler, M. A.; Karlin, K. D. Synthesis and Characterization of New Trinuclear Copper Complexes. *Inorganica Chim. Acta* **2012**, *389*, 131–137.

(18)   Bagherzadeh, S.; Mankad, N. P. Oxidation of a [Cu2S] Complex by N2O and CO2: Insights into a Role of Tetranuclearity in the CuZ Site of Nitrous Oxide Reductase. *Chem. Commun.* **2018**, *54*, 1097–1100.

(19)   Sarangi, R.; York, J. T.; Helton, M. E.; Fujisawa, K.; Karlin, K. D.; Tolman, W. B.; Hodgson, K. O.; Hedman, B.; Solomon, E. I. X-Ray Absorption Spectroscopic and Theoretical Studies on (L) 2[Cu2(S2)n]2+ Complexes: Disulfide versus Disulfide(•1-) Bonding. *J. Am. Chem. Soc.* **2008**, *130*, 676–686.

(20)   Brown, E. C.; York, J. T.; Antholine, W. E.; Ruiz, E.; Alvarez, S.; Tolman, W. B. [Cu3(μ-S)2]3+ Clusters Supported by N-Donor Ligands: Progress toward a Synthetic Model of the Catalytic Site of Nitrous Oxide Reductase. *J. Am. Chem. Soc.* **2005**, *127*, 13752–13753.

(21)   Bar-Nahum, I.; Gupta, A. K.; Huber, S. M.; Ertem, M. Z.; Cramer, C. J.; Tolman, W. B. Reduction of Nitrous Oxide to Dinitrogen by a Mixed Valenttricopper- Disulfido Cluster. *J. Am. Chem. Soc.* **2009**, *131*, 2812–2814.

(22)   York, J. T.; Bar-Nahum, I.; Tolman, W. B. Structural Diversity in Copper-Sulfur Chemistry: Synthesis of Novel Cu/S Clusters through Metathesis Reactions. *Inorg. Chem.* **2007**, *46*, 8105–8107.

(23)   York, J. T.; Bar-Nahum, I.; Tolman, W. B. Copper-Sulfur Complexes Supported by N-Donor Ligands: Towards Models of the CuZ Site in Nitrous Oxide Reductase. *Inorganica Chim. Acta* **2008**, *361*, 885–893.

(24)   Di Francesco, G. N.; Gaillard, A.; Ghiviriga, I.; Abboud, K. A.; Murray, L. J. Modeling Biological Copper Clusters: Synthesis of a Tricopper Complex, and Its Chloride- and Sulfide-Bridged Congeners. *Inorg. Chem.* **2014**, *53*, 4647–4654.

(25)   Esmieu, C.; Orio, M.; Torelli, S.; Le Pape, L.; Pécaut, J.; Lebrun, C.; Ménage, S. N2O Reduction at a Dissymmetric {Cu2S}-Containing Mixed-Valent Center. *Chem. Sci.* **2014**, *5*, 4774–4784.

(26)   Esmieu, C.; Orio, M.; Ménage, S.; Torelli, S. Influence of Copper Coordination Spheres on Nitrous Oxide Reductase (N 2 Or) Activity of a Mixed-Valent Copper Complex Containing a {Cu 2 S} Core . *Inorg. Chem.* **2019**, *58*, 11649–11655.

(27)   Zhai, J.; Filatov, A. S.; Hillhouse, G. L.; Hopkins, M. D. Synthesis, Structure, and Reactions of a Copper-Sulfido Cluster Comprised of the Parent Cu 2 S Unit: {(NHC)Cu} 2 (μ-S). *Chem. Sci.* **2016**, *7*, 589–595.

(28)   Zhai, J.; Hopkins, M. D.; Hillhouse, G. L. Synthesis and Structure of a CuI3S Cluster Unsupported by Other Bridging Ligands. *Organometallics* **2015**, *34*, 4637–4640.

(29)   Yam, V. W.-W.; Lee, W.-K.; Lai, T.-F. Synthesis and Luminescent Properties of a Novel Tetranuclear Copper(I) Cluster Containing a M4-Sulfur Moiety. X-Ray Crystal Structure of [Cu4(μ-Dppm)4(M4-S)](PF6)2·2Me2 CO [Dppm = Bis(Diphenylphosphino)Methane]. *J. Chem. Soc., Chem. Commun.* **1993**, *4*, 1571–1573.

(30)   Johnson, B. J.; Lindeman, S. V.; Mankad, N. P. Assembly, Structure, and Reactivity of Cu 4 S and Cu 3 S Models for the Nitrous Oxide Reductase Active Site, Cu Z *. *Inorg. Chem.* **2014**, *53*, 10611–10619.

(31)   Johnson, B. J.; Antholine, W. E.; Lindeman, S. V.; Mankad, N. P. A Cu4S Model for the Nitrous Oxide Reductase Active Sites Supported Only by Nitrogen Ligands. *Chem. Commun.* **2015**, *51*, 11860–11863.

(32)   Johnson, B. J.; Antholine, W. E.; Lindeman, S. V.; Graham, M. J.; Mankad, N. P. A One-Hole Cu4S Cluster with N2O Reductase Activity: A Structural and Functional Model for CuZ. *J. Am. Chem. Soc.* **2016**, *138*, 13107–13110.

(33)   Khadka, C. B.; Najafabadi, B. K.; Hesari, M.; Workentin, M. S.; Corrigan, J. F. Copper Chalcogenide Clusters Stabilized with Ferrocene-Based Diphosphine Ligands. *Inorg. Chem.* **2013**, *52*, 6798–6805.

(34) Hsu, C.-W.; Rathnayaka, S. C.; Islam, S. M.; MacMillan, S. N.; Mankad, N. P. N 2 O Reductase Activity of a [Cu 4 S] Cluster in the 4Cu I Redox State Modulated by Hydrogen Bond Donors and Proton Relays in the Secondary Coordination Sphere. *Angew. Chemie Int. Ed.* **2020**, *59*, 627–631.

(35) Comba, P.; Katsichtis, C.; Nuber, B.; Pritzkow, H. Solid-State and Solution Structural Properties of Copper(I) Compounds with Bidentate Phosphane Ligands. *Eur. J. Inorg. Chem.* **1999**, *1999*, 777–783.

(36) Díez, J.; Gamasa, M. P.; Gimeno, J.; Aguirre, A.; García-Granda, S.; Holubova, J.; Falvello, L. R. Novel Copper(I) Complexes Containing 1,1′-Bis(Diphenylphosphino)Ferrocene (Dppf) as a Chelate and Bridging Ligand: Synthesis of Tetrabridged Dicopper(I) Complexes [Cu2(μ-H1-C≡R)2(μ-Dppf) 2] and X-Ray Crystal Structure. *Organometallics* **1999**, *18*, 662–669.

(37) Pinto, P.; Calhorda, M. J.; Félix, V.; Avilés, T.; Drew, M. G. B. Syntheses and Crystal Structures of Polynuclear Cu(I) Complexes Containing the 1,1′-Bis-(Diphenylphosphino)-Ferrocene Ligand. *Monatshefte fur Chemie* **2000**, *131*, 1253–1265.

(38) Yang, X.-X.; Issac, I.; Lebedkin, S.; Kü, M.; Weigend, F.; Fenske, D.; Fuhr, O.; Eichhö, A. Red-Luminescent Biphosphine Stabilized 'Cu 12 S 6 ' Cluster Molecules † ChemComm. *Chem. Commun* **2014**, *50*, 11043–11045.

(39) Eichhö, A.; Buth, G.; Lebedkin, S.; Kü, M.; Weigend, F. Luminescence in Phosphine-Stabilized Copper Chalcogenide Cluster Molecules□A Comparative Study. *Inorg. Chem* **2015**, *16*, 9.

(40) Song, M.; Donnadieu, B.; Soleilhavoup, M.; Bertrand, G. Synthesis of Phosphaformamidines and Phosphaformamidinates. *Chem. - An Asian J.* **2007**, *2*, 904–908.

(41) Peulecke, N.; Kindermann, M. K.; Köckerling, M.; Heinicke, J. Phosphonium Bis(Glycolates) and Phosphinoglycolates: Synthesis, Solvolysis, Oxidation to (Thio)Phosphinoylglycolates and Use as Ligands in Ni-Catalyzed Ethylene Oligomerization. *Polyhedron* **2012**, *41*, 61–69.

(42) Krackl, S.; Inoue, S.; Driess, M.; Enthaler, S. Intermolecular Hydrogen-Fluorine Interaction in Dimolybdenum Triply Bonded Complexes Modified by Fluorinated Formamidine Ligands for the Construction of 2D- and 3D-Networks. *Eur. J. Inorg. Chem.* **2011**, No. 13, 2103–2111.

(43) White, D. P.; Anthony, J. C.; Oyefeso, A. O. Computational Measurement of Steric Effects: The Size of Organic Substituents Computed by Ligand Repulsive Energies. *J. Org. Chem.* **1999**, *64*, 7707–7716.

(44) Belot, V.; Farran, D.; Jean, M.; Albalat, M.; Vanthuyne, N.; Roussel, C. Steric Scale of Common Substituents from Rotational Barriers of N-(o-Substituted Aryl)Thiazoline-2-Thione Atropisomers. *J. Org. Chem.* **2017**, *82*, 10188–10200.

(45) Issleib, K.; Schmidt, H.; Meyer, H. Phospha-Amidine. *J. Organomet. Chem.* **1978**, *160*, 47–57.

(46) Li, X.; Song, H.; Cui, C. Azaphosphaallyl Anion Lithium [ArNC(But)PAr]−Li+(THF)4 and Its Monomeric Potassium and Thallium Complexes (Ar = 2, 6-IPr2C6H3). *Dalt. Trans.* **2009**, No. 44, 9728.

(47) van Dijk, T.; Burck, S.; Rong, M. K.; Rosenthal, A. J.; Nieger, M.; Slootweg, J. C.; Lammertsma, K. Facile Synthesis of Phosphaamidines and Phosphaamidinates Using Nitrilium Ions as an Imine Synthon. *Angew. Chemie* **2014**, *126*, 9214–9217.

(48) Takeda, Y.; Nishida, T.; Minakata, S. 2,6-Diphospha- s -Indacene-1,3,5,7(2 H ,6 H)-Tetraone: A Phosphorus Analogue of Aromatic Diimides with the Minimal Core Exhibiting High Electron-Accepting Ability. *Chem. - A Eur. J.* **2014**, *20*, 10266–10270.

(49) Rathnayaka, S. C.; Lindeman, S. V.; Mankad, N. P. Multinuclear Cu(I) Clusters Featuring a New Triply Bridging Coordination Mode of Phosphaamidinate Ligands. *Inorg. Chem.* **2018**, *57*, 9439–9445.

(50) Kandel, R.; Huynh, K.; Dalgliesh, L.; Wang, R.; Jessop, P. G. Contrasting Connectivity of Amidine and

Phosphaamidine (1,3-P,N) Cu(I) Complexes. *Inorganica Chim. Acta* **2016**, *445*, 117–123.

(51)   Van Dijk, T.; Burck, S.; Rong, M. K.; Rosenthal, A. J.; Nieger, M.; Slootweg, J. C.; Lammertsma, K. Facile Synthesis of Phosphaamidines and Phosphaamidinates Using Nitrilium Ions as an Imine Synthon. *Angew. Chemie - Int. Ed.* **2014**, *53*, 9068–9071.

(52)   Payet, E.; Auffrant, A.; Le Goff, X. F.; Floch, P. Le. Phosphine- and Thiophosphorane-Amine Ligands: Lithiation and Coordination to Rh(I). *J. Organomet. Chem.* **2010**, *695*, 1499–1506.

(53)   Semmelhack, M. F.; Chlenov, A.; Ho, D. M. Accelerated Arene Ligand Exchange in the (Arene)Cr(CO)2L Series. *J. Am. Chem. Soc.* **2005**, *127*, 7759–7773.

(54)   Tsukada, N.; Tamura, O.; Inoue, Y. Synthesis and Structures of Palladium and Platinum A-Frame Complexes Bridged by a Novel Binucleating Ligand, N , N '-Bis[(2-Diphenylphosphino)Phenyl]- Formamidine. *Organometallics* **2002**, *21*, 2521–2528.

(55)   Yamaguchi, Y.; Yamanishi, K.; Kondo, M.; Tsukada, N. Synthesis of Dinuclear (μ-η 3 -Allyl)Palladium(I) and -Platinum(I) Complexes Supported by Chelate-Bridging Ligands. *Organometallics* **2013**, *32*, 4837–4842.

(56)   Nakane, T.; Tanioka, Y.; Tsukada, N. Synthesis of Multinuclear Copper Complexes Bridged by Diquinolylamidinates and Their Application to Copper-Catalyzed Coupling of Terminal Alkynes and Aryl, Allyl, and Benzyl Halides. *Organometallics* **2015**, *34*, 1191–1196.

3. INFLUENCE OF SECONDARY COORDINATION SPHERE INTERACTIONS ON THE N₂O REDUCTION BY A SYNTHETIC Cu$_Z$ MODEL COMPLEX

The content presented in Chapter 3 closely follows the published work in reference Hsu, C.-W.; Rathnayaka, S. C.; Islam, S. M.; MacMillan, S. N.; Mankad, N. P. N₂O Reductase Activity of a [Cu₄S] Cluster in the 4Cu(I) Redox State Modulated by Hydrogen Bond Donors and Proton Relays in the Secondary Coordination Sphere. *Angew. Chemie Int. Ed.* **2020**, *59*, 627–631.

3.1   Background

As part of bacterial denitrification, the $2H^+/2e^-$ reduction of N₂O is catalysed by the metalloenzyme, *nitrous oxide reductase* (N₂OR).[1] Structural characterization of N₂OR reveals that its catalytic site, Cu$_Z$, has an unusual [Cu₄(μ_4-S)] core structure.[2,3] Given the difficulties of designing synthetic catalysts for N₂O activation, it is intriguing to consider how this unusual 4Cu:1S cluster binds and activates N₂O under physiological conditions. The hydrogen bonding network found in native Cu$_Z$ could play a crucial role in the catalytic cycle by manipulating substrate binding and activation.[4,5] In this content, the interaction of N₂O with synthetic model complexes of Cu$_Z$ could provide useful insights, but it is challenge as N₂O bound transition metal complexes are rare. In fact, such complexes featuring N₂O ligands have only been crystallographically characterized recently,[6–9] in part because weakly donating ligands such as N₂ have long been known to bind competitively with N₂O in classic complexes such as [Ru(NH₃)₅L]²⁺ (L = N₂O or N₂).[10] Thus, fundamental knowledge about how transition metal active sites can be designed to bind and activate N₂O is very valuable.

A large body of enzymological, spectroscopic, and computational work from Solomon, Moura, and co-workers[11] has led to a recently updated mechanistic proposal for N₂O reduction at Cu$_Z$.[4] In this proposal (**Scheme 3.1**), the fully-reduced 4Cu^I state of Cu$_Z$ binds N₂O along the Cu$_I$–Cu$_{IV}$ edge of the cluster with assistance from a second-sphere LysH$^+$ residue (K397). Bending of the N₂O molecule upon coordination, along with electron donation from Cu$_Z$ into the N₂O π^* levels, induces N–O bond cleavage and loss of N₂. The hydroxy ligand thus produced from N₂O is subsequently converted to H₂O with assistance from K397 acting as a proton shuttle during coupled proton/electron transfer. The structural asymmetry of the 4Cu:1S core is thought to be crucial for this mechanism, as the asymmetric distribution of electron density among the four Cu sites is thought to provide a low-energy pathway for electron transfer from Cu$_Z$ to N₂O via Cu$_{IV}$. It should be noted, however, that this proposal is under some doubt as Einsle and

co-workers showed that anoxic preparations of N_2OR feature a $[Cu_4(\mu_4\text{-S})(\mu_2\text{-S})]$ form of Cu_Z where the additional μ_2-S ligand blocks access to the dicopper edge proposed by Solomon et al. to be the N_2O binding site.[3,12]
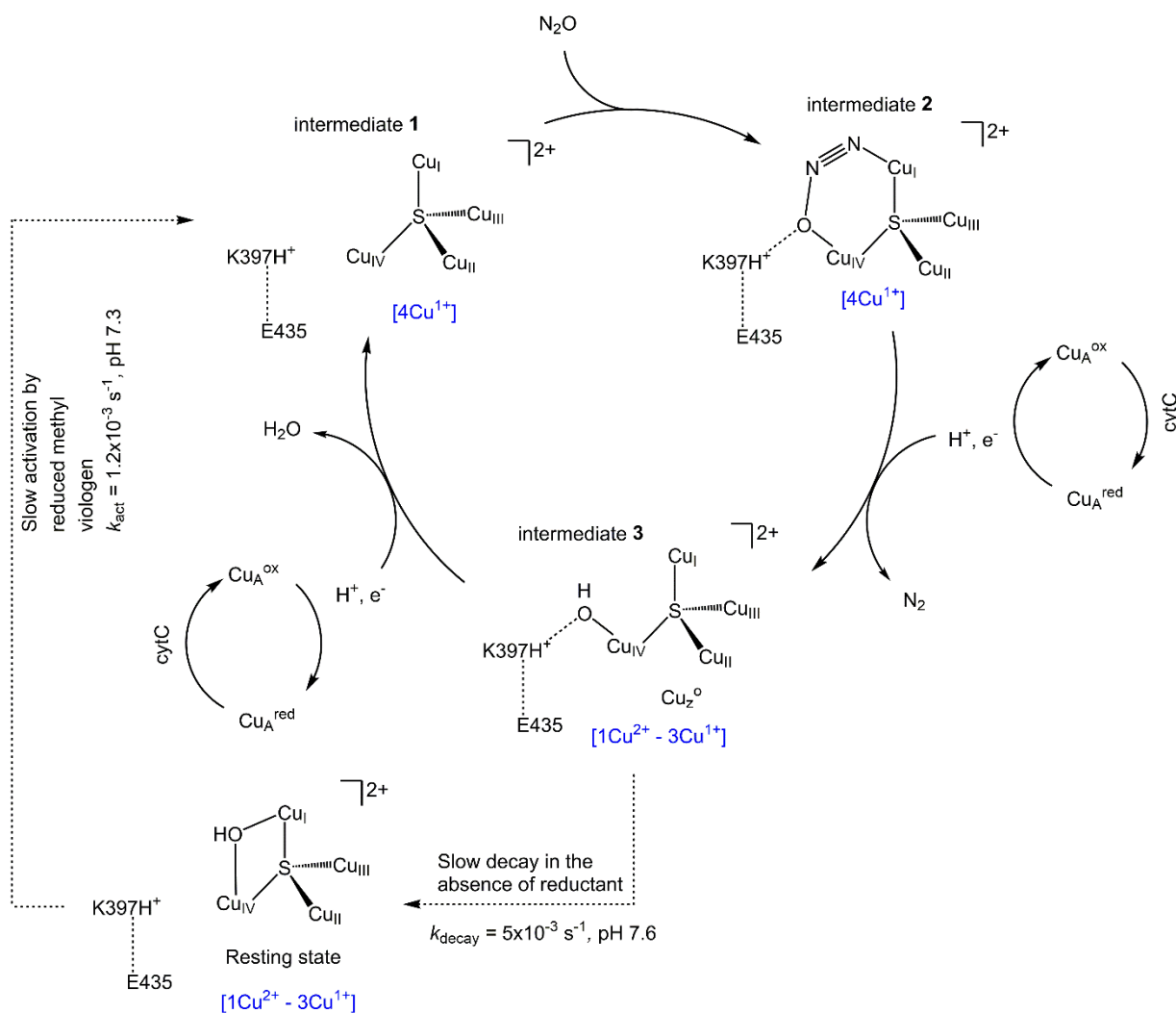
SCHEME 3. 1 The mechanism of *in vitro* reduction of equimolar molar N_2O by reduced N_2OR with Cu_Z* center showing the intermediates and the proton coupled electron transfer events from Cu_A center. The catalytically competent cycle is shown using solid arrows while the dashes indicate the slow alternative pathway in the absence of reductants. The conserved amino acid residues are labeled according to *M. hydrocarbonoclasticus* N_2OR mature primary sequence.

3.2 The N_2O reduction by Cu_Z model complex $[Cu_4(\mu_4\text{-S})(dppa)_4]^{2+}$ (**2**)

Synthetic model compounds can be used to probe various aspects of the Cu_Z mechanism.[13] Tolman, Torelli, and our group have each reported N_2O reductase activity with copper-sulfur clusters that do not mimic the structural

features of Cu_Z in terms of aggregation state or Cu:S stoichiometry.[14–16] The first [$Cu_4(\mu_4$-S)] cluster (**1**) was reported in 1993 by Yam and co-workers using bridging dppm ligands (dppm = bis(diphenylphosphino)methane).[17] This 4Cu[I] complex lacks any well-defined redox chemistry or N_2O reactivity but, separately, has shown intriguing photochemical properties.[18] Our group recently accessed the 2Cu[2+] - 2Cu[1+] and 1Cu[2+] - 3Cu[2+] redox states of a [$Cu_4(\mu_4$-S)] cluster using the bridging formamidinate ligands [(2,4,6-$Me_3C_6H_2N)_2$CH][-],[19,20] but the 4Cu[1+] state that would model the active form of Cu_Z was unstable and could not be accessed synthetically.

Our group has also reported new derivatives of the original Yam-type 4Cu[1+] complex, including [$Cu_4(\mu_4$-S)(dppa)$_4$][2+] (**2**, dppa = bis(diphenylphosphino)amine).[21] A unique feature of **2** is the ability of its second-sphere N–H groups to act as hydrogen bond donors towards anions and solvent molecules. In our previous study, we showed that complex **2** exhibits reactivity that complex **1** lacks, including activation of triatomic substrates isoelectronic to N_2O (e.g. N_3^-) and strong binding of I[-], which is a known inhibitor of N_2OR.[22] Then we disclosed conditions under which **2** mediates 2H[+]/2e[-] reduction of N_2O, with two second-sphere N–H groups acting as the terminal proton donors to produce H_2O.[23] The activity of **2** is modulated by second-sphere hydrogen bonding interactions and can be suppressed in the absence of effective hydrogen bond acceptors. Significant aspects of these findings include: 1) the first report of a synthetic cluster in the physiologically relevant 4Cu[1+]:S[2-] redox state activating N_2O, 2) second-sphere amine residues that model the K397 residue of N_2OR, and 3) biomimetic interplay of primary and secondary structure on active site function.
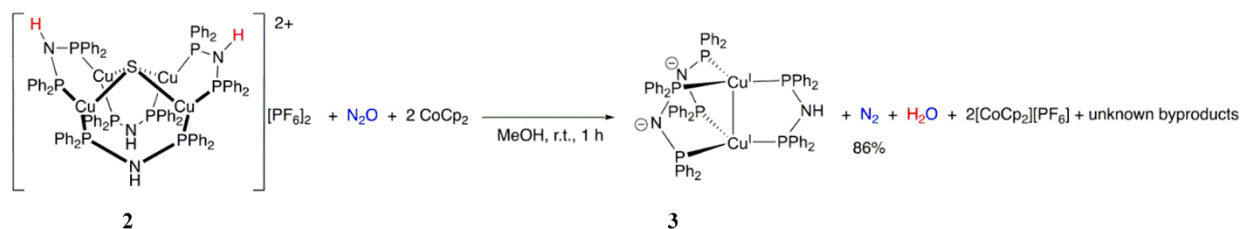
SCHEME 3. 2 2H[+]/2e[-] conversion of N_2O mediated by **2** in methanol using two equivalents of $CoCp_2$ as an external electron donor. Production of stoichiometric amounts of **3** and [$CoCp_2$][+] were confirmed by ^{1}H/^{31}P NMR while production of N_2 was quantified by GC-MS analysis. Formation of H_2O was detected by near-IR analysis (see Chapter 5 - Section 5.2.2, 5.2.3, 5.2.4 and 5.2.5).

In our initial study,[21] we reported that complex **2** did not react with N_2O under any conditions we examined. Later, we have found that bubbling excess N_2O into a MeOH solution of **2**, followed by slow addition of $CoCp_2$ (2 equiv) as an electron donor, results in a rapid color change, with complete conversion within one hour as determined

by ^{31}P NMR spectroscopy. The main Cu-containing product was identified as neutral $Cu_2(dppa)(dppa')_2$ (**3**, dppa' = $(Ph_2P)_2N^-$), which was produced in 90% yield according to ^{31}P NMR and was isolated in 67% recrystallized yield. Adding less than two equivalents of $CoCp_2$ resulted in incomplete conversion of **2** according to ^{31}P NMR spectroscopy, consistent with a two-electron reduction reaction. No reaction was observed between $CoCp_2$ and N_2O in the absence of **2**. Upon scale-up, the resulting $[CoCp_2][PF_6]$ was isolated in pure form after workup (see Chapter 5 – Section 5.2.3). Based on these observations, we hypothesize a balanced reaction as shown in **Scheme 3.2**. The formation of N_2 was verified by GC-MS headspace analysis, and its yield was determined to be 86 ($\pm$5) %. Thus, the yield of **3** is representative of the production of N_2 from N_2O. Due to the incompatibility of various reaction components with reagents employed in Karl-Fischer and other chemical H_2O assays, the formation of H_2O was verified qualitatively using an established near-IR assay,[24] although H_2O quantification proved to be challenging by this method (see Chapter 5 – Section 5.2.4).

2   **3**
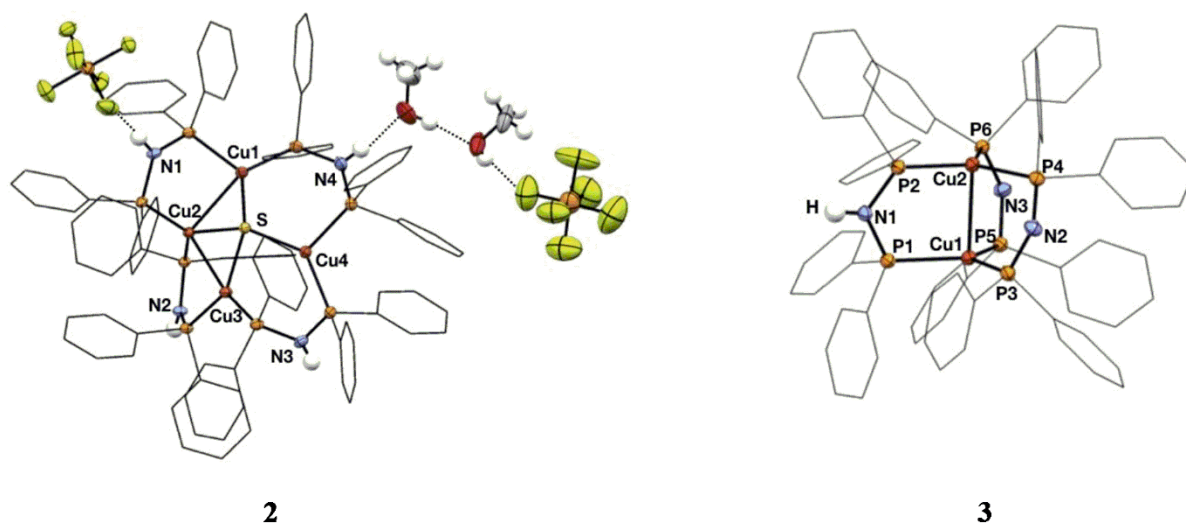
FIGURE 3. 1 Solid-state structure of *(left)* **2** (from MeOH solution) and *(right)* **3** as 50%-probability ellipsoids (non-C,H atoms) or wireframe (C atoms). C-H hydrogens have been omitted, and the N-H hydrogens shown were located in the Fourier difference map and allowed to refine freely. Selected distances (Å) and angles (°) for **3**: Cu1-Cu2, 2.6718(6); P1–N1, 1.6824(15); P2–N1, 1.680(2); P3–N2, 1.6312(15); P4–N2, 1.635(2); P5–N3, 1.6340(15); P6–N3, 1.634(2); P1–N1–P2, 123.3(1); P3–N2–P4, 117.3(1); P5–N3–P6, 120.0(1). For **2**: Cu1–Cu2, 2.6969(6) Å; Cu2–Cu3, 2.6690(6) Å; Cu3–Cu4, 3.0175(7) Å; Cu1–Cu4, 3.542(1).

Single-crystal X-ray diffraction studies of **3** (**Figure 3.1**) revealed a pseudo-threefold symmetric dicopper(I) lantern structure with a Cu···Cu distance of 2.6718(6) Å. The N–H proton for the single dppa ligand was located in

the Fourier difference map, but no evidence for N–H protons was found for the two dppa' ligands. The dppa ligand also has elongated P–N distances (P1–N1, 1.6824(15) Å; P2–N1, 1.680(2) Å) compared to the dppa' ligands (P3–N2, 1.6312(15) Å; P4–N2, 1.635(2) Å; P5–N3, 1.6340(15) Å; P6–N3, 1.634(2) Å), presumably due to enhanced N/P hyperconjugation in the anionic dppa' ligands involving the π-symmetry N lone pair. The ^{1}H NMR spectrum of **3** is consistent with this structural assignment: the integral of the N–H resonance indicates the presence of only one remaining N-H proton (see Chapter 5 – **Figure S57**). The ^{31}P{^{1}H} NMR spectrum of **3** features two distinct resonances for the two chemically inequivalent phosphorous ligands, with each displaying complex second order J_{PP} coupling patterns.

3.3   Optimizations and control experiments of the reaction between **2** and N$_2$O

Varying the reactions conditions gave further insight into the factors controlling the ability of **2** to mediate N$_2$O reduction (**Table 3.1**). The conversion to **3** was determined to be 90% by NMR spectroscopy when conducted as described above (Entry 1). Performing the reaction under N$_2$ atmosphere rather than N$_2$O resulted in decomposition of **2** to tricopper(I) species **2'** (Entry 2), as we have noted before,[21] with no evidence for formation of **3**. Exposing **2** to N$_2$O in the absence of CoCp$_2$ also resulted in **2'** (Entry 3), indicating that any meta-stable N$_2$O adduct of **2** must immediately be trapped by (proton-coupled) reduction for the reaction to proceed. Use of just one equivalent of CoCp$_2$ resulted in only partial conversion to **3** along with decay to **2'** (Entry 4), consistent with our proposal of a two-electron reaction. Performing the reaction in the poor hydrogen bond acceptor solvents THF or toluene gave only unreacted **2** and decomposition product **2'** (Entries 5-6), indicating that N$_2$O activation by **2** requires the second-sphere N–H groups to be engaged in hydrogen-bonding interactions with the solvent medium. Indeed, performing the reaction in the stronger H-bond acceptor solvent, acetone, reestablished the reaction (Entry 7).[25] Interestingly, replacing MeOH with MeOH-d_4 also suppressed N$_2$O activation and resulted in unreacted **2** (Entry 8). The ^{1}H NMR spectrum of **2** in MeOH-d_4 does not have an observable N–H resonance, indicating deuterium exchange with the solvent. The complete suppression of reactivity due to this deuteration is puzzling. One possibility is the presence of a particularly large kinetic isotope effect during one or both O-H(D) bond forming steps. Exposing Yam's [Cu$_4$(μ_4-S)(dppm)$_4$]$^{2+}$ complex (**1**)[17] to the reaction conditions did not result in any conversion (Entry 9). Collectively, considering the observations that replacing MeOH solvent with acetone solvent does not turn off the reaction but replacing NH groups in the ligand

backbone with CH_2 groups does, it is likely that the backbone NH groups are acting as the hydrogen atom source to generate H_2O, akin to the K397 residue in N_2OR.

TABLE 3. 1 Variations of N_2O reduction reaction by **2** upon deviating from the standard conditions. [a]
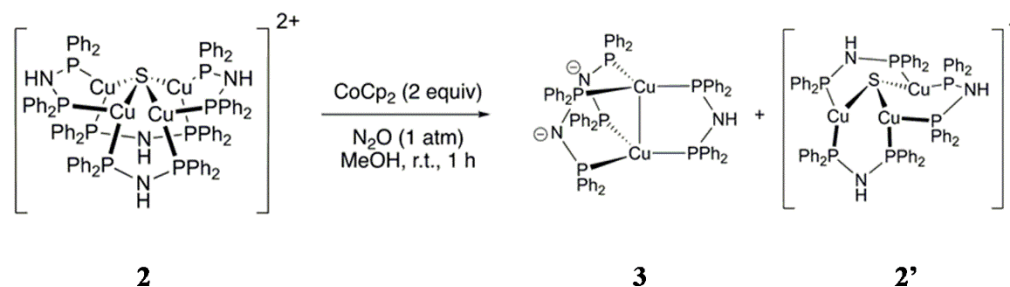
Entry	Variation from standard conditions	Unreacted **2** (%)	Product **3** (%)	Decomposition product **2'** (%)
1	None	0	90(67[b])	0
2	N_2 atmosphere	54	0	25
3	No CoCp2	60	0	15
4	1 equiv CoCp2	6	38	44
5	THF solvent	38	0	48
6	Toluene solvent	67	0	6
7	Acetone solvent	0	42	0
8	MeOH-d_4 solvent	77	0	0
9	dppm in place of dppa	>95	0	0

[a] Yields were determined by ^{31}P NMR using tri-*o*-tolylphosphine as the internal standard.
[b] Isolated yield.

3.4 Crystallographic evaluation of secondary sphere H-boning interactions of complex **2**

To better understand the sensitivity of N_2O reductase activity of **2** to solvent environment, we decided to examine its solvent-dependent structure. Repeated attempts at solving the solid-state structure of **2** using single crystals grown from MeOH-d_4 indicated the presence hydrogen-bonded solvent molecules in the second sphere. However, Yam's $[Cu_4(\mu_4\text{-}S)(dppm)_4]^{2+}$ complex (**1**)[17] can be viewed as a model for the structure of **2** in the absence of any

hydrogen-bonding interactions. The [Cu$_4$S] core of **1** has local C_{2v} symmetry, with a rectangle-based pyramidal core featuring Cu···Cu distances of 2.869(2) and 3.128(1) Å, and a μ$_4$-S-atom with a τ_4' parameter[26] of 0.56. Crystals of **2** obtained MeOH solution provided a structure with some key differences (**Figure 3.1**). Two of the N–H groups are acting as hydrogen bond donors in the solid-state: the N1–H group to a PF$_6^-$ counterion, and the N4–H group initiating a NH···MeOH···MeOH···PF$_6^-$ network. The [Cu$_4$S] core of **2** is highly unsymmetrical, with the three Cu sites distal to the N4–H hydrogen-bonding network clustered close together (Cu1···Cu2, 2.6969(6) Å; Cu2···Cu3, 2.6690(6) Å) while the Cu4 site is pulled further away (Cu4···Cu3, 3.0175(7) Å; Cu4···Cu1, 3.542(1) Å) (**Figure 3.2**). The S-atom geometry is also perturbed (τ_4' = 0.72) compared to **1**. These metrical parameters are almost identical to what we previously reported for **2** interacting with acetone molecules.[21] Furthermore, these parameters are quite similar to the Cu$_Z$ structure,[2] which is also highly unsymmetrical with one Cu site distal (3.00-3.33 Å) from the other three and which has a similar S-atom geometry (τ_4' = 0.77). Structural comparisons of the two synthetic [Cu$_4$S] cores are shown in **Figure 3.2**.

3.5   Electronic impact of the structural changes of complex **2**

To evaluate the electronic impact of these structural changes, we studied **1** and **2** computationally. When examining calculated NBO atomic charges, a notable difference between the two complexes is the buildup of additional negative charge on the Cu2 site, i.e. the middle site among the more closely clustered Cu centers, in unsymmetrical **2** (**Figure 3.2**-*top right*). When examining the frontier MOs produced by DFT calculations, another notable difference involves the HOMO-3 level, which is highly delocalized across the entire [Cu$_4$S] core for **1** but is localized mostly at the Cu1 and Cu2 sites in **2** (**Figure 3.2**-*middle*) and is also 573 cm^{-1} closer to the HOMO level. A similar phenomenon is observed for the LUMO level, which is localized at the sulfur atom for **1** but mostly localized at the Cu2 site for **2** (**Figure 3.2**-*bottom)* Collectively, these observations indicate that for **2**, hydrogen bond-induced structural distortion creates localization of frontier MO density at the Cu1-Cu2 edge site, both making Cu2 more electrophilic towards N$_2$O binding and making the Cu1-Cu2 edge better able to π-backdonate into the π* manifold of bound N$_2$O. In a related discovery, recently Agapie showed that structural distortion of tetrametallic models of the oxygen evolving complex (OEC) of photosystem-II through steric pressure modulates the clusters' reduction potentials.[27] The additional contribution of our system is the correlation between structure and chemical reactivity with the relevant substrate, N$_2$O. A similar correlation between substrate activation and localization of frontier MO

density has recently emerged to describe the octanuclear FeMo-cofactor of nitrogenase.[28] In our system, no visual

changes are observed unless all three reaction components (**2**, CoCp$_2$, and N$_2$O) are present. Because complex **2** is in

the 4Cu^{1+}:1S^{2-} redox state, it is unlikely that reactivity initiates with reduction of **2** by CoCp$_2$. Instead, we favor a

sequence where the π-accepting molecule N$_2$O binds to **2**, likely along the Cu1-Cu2 edge, thus raising the reduction

potential such that CoCp$_2$ can donate to the newly introduced electron holes of **2**·N$_2$O.

HOMO-3 of **1**   HOMO-3 of **2**

LUMO of **1**   LUMO of **2**
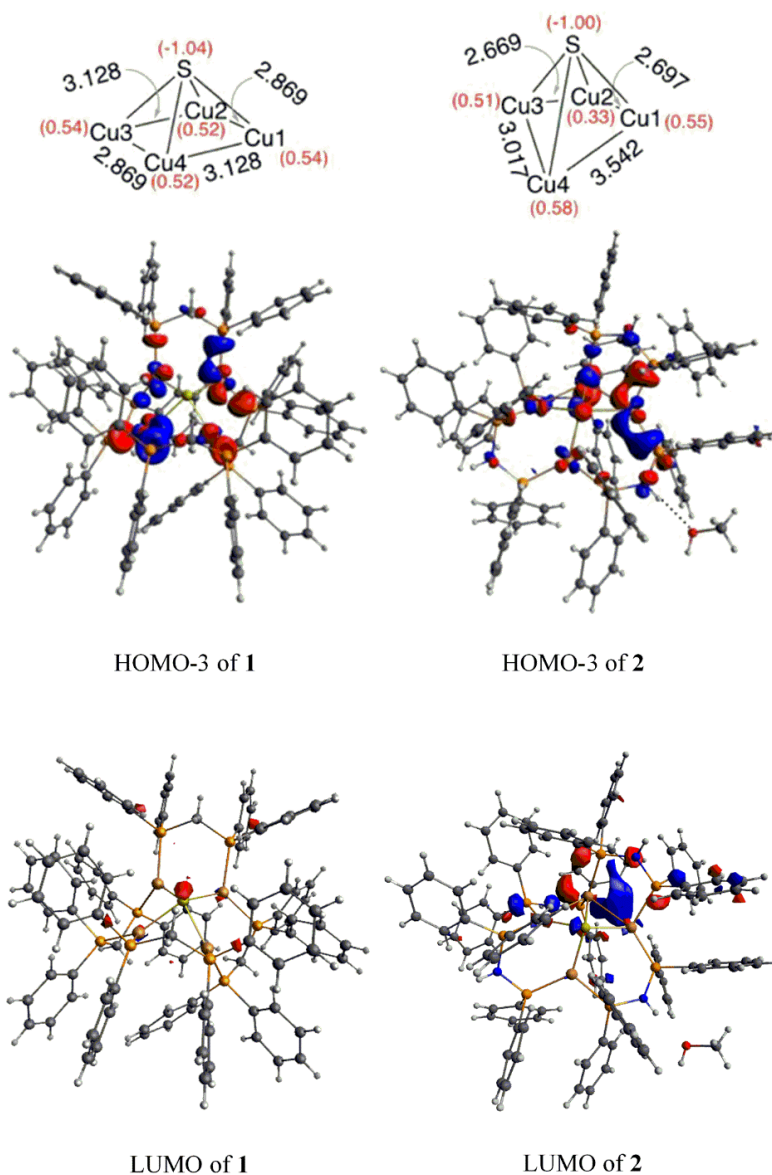
FIGURE 3. 2 *(top)* Comparisons of the [Cu$_4$(μ_4-S)] cores of **1** and **2**, with bond distances shown in black and NBO charges shown in red. Comparisons of the HOMO-3 *(middle)* and LUMO *(bottom)* for **1** and **2** (B3LYP/6-31++G**).

3.6   Concluding remarks

The synthetic model complex $[Cu_4(\mu_4\text{-}S)(dppa)_4]^{2+}$ (**2**, dppa = bis(diphenylphosphino)amine) was found to have N_2O reductase activity in methanol solvent, mediating the $2H^+/2e^-$ reduction of N_2O to $N_2 + H_2O$ in the presence of an exogenous electron donor ($CoCp_2$). A stoichiometric product featuring two deprotonated dppa ligands was characterized, indicating a key role of second-sphere N–H residues as proton donors during N_2O reduction. The activity of **2** towards N_2O was suppressed in solvents that are unable to provide hydrogen bonding to the second-sphere N–H groups. Structural and computational data indicated that second-sphere hydrogen bonding induces structural distortion of the $[Cu_4(\mu_4\text{-}S)]$ active site, accessing a strained geometry with enhanced reactivity due to localization of electron density along a dicopper edge site. Upon activation, the N_2O substrate is converted to N_2 and H_2O with H^+ donation directly from the second coordination sphere. The behavior of **2** mimics several aspects of the Cu_Z catalytic site of nitrous oxide reductase: activity in the $4Cu^{1+}$:1S redox state, use of a second-sphere proton donor, and reactivity dependence on both primary and secondary sphere effects thus providing an entryway to future Cu_Z modeling studies.

3.7   References

(1)   Pauleta, S. R.; Dell'Acqua, S.; Moura, I. Nitrous Oxide Reductase. *Coord. Chem. Rev.* **2013**, *257*, 332–349.

(2)   HALTIA, T.; BROWN, K.; TEGONI, M.; CAMBILLAU, C.; SARASTE, M.; MATTILA, K.; DJINOVIC-CARUGO, K. Crystal Structure of Nitrous Oxide Reductase from Paracoccus Denitrificans at 1.6 A Resolution. *Biochem. J.* **2003**, *369*, 77–88.

(3)   Pomowski, A.; Zumft, W. G.; Kroneck, P. M. H.; Einsle, O. N2O Binding at a [4Cu:2S] Copper–Sulphur Cluster in Nitrous Oxide Reductase. *Nature* **2011**, *477*, 234–237.

(4)   Johnston, E. M.; Carreira, C.; Dell'Acqua, S.; Dey, S. G.; Pauleta, S. R.; Moura, I.; Solomon, E. I. Spectroscopic Definition of the CuZ° Intermediate in Turnover of Nitrous Oxide Reductase and Molecular Insight into the Catalytic Mechanism. *J. Am. Chem. Soc.* **2017**, *139*, 4462–4476.

(5)   Pomowski, A.; Zumft, W. G.; Kroneck, P. M. H.; Einsle, O. N2O Binding at a [4Cu:2S] Copper–Sulphur Cluster in Nitrous Oxide Reductase. *Nature* **2011**, *477*, 234–237.

(6)   Piro, N. A.; Lichterman, M. F.; Harman, W. H.; Chang, C. J. A Structurally Characterized Nitrous Oxide Complex of Vanadium. *J. Am. Chem. Soc.* **2011**, *133*, 2108–2111.

(7)   Zhuravlev, V.; Malinowski, P. J. A Stable Crystalline Copper(I)–N 2 O Complex Stabilized as the Salt of a Weakly Coordinating Anion. *Angew. Chemie Int. Ed.* **2018**, *57*, 11697–11700.

(8)   Mokhtarzadeh, C. C.; Chan, C.; Moore, C. E.; Rheingold, A. L.; Figueroa, J. S. Side-On Coordination of Nitrous Oxide to a Mononuclear Cobalt Center. *J. Am. Chem. Soc.* **2019**, *141*, 15003–15007.

(9)   Gyton, M. R.; Leforestier, B.; Chaplin, A. B. Rhodium(I) Pincer Complexes of Nitrous Oxide. *Angew. Chemie Int. Ed.* **2019**, *58*, 15295–15298.

(10)   Armor, J. N.; Taube, H. Formation and Reactions of [(NH3)5RuN2O2+]. *J. Am. Chem. Soc.* **1969**, *91*, 6874–6876.

(11)   Solomon, E. I.; Heppner, D. E.; Johnston, E. M.; Ginsbach, J. W.; Cirera, J.; Qayyum, M.; Kieber-Emmons, M. T.; Kjaergaard, C. H.; Hadt, R. G.; Tian, L. Copper Active Sites in Biology. *Chem. Rev.* **2014**, *114*, 3659–3853.

(12)   Wüst, A.; Schneider, L.; Pomowski, A.; Zumft, W. G.; Kroneck, P. M. H.; Einsle, O. Nature's Way of Handling a Greenhouse Gas: The Copper-Sulfur Cluster of Purple Nitrous Oxide Reductase. *Biol. Chem.* **2012**, *393*, 1067–1077.

(13)   Johnson, B. J.; Mankad, N. P. CHAPTER 10. Model Compounds of Copper-Containing Enzymes Involved in Bacterial Denitrification. In *RSC Metallobiology*; Moura, I., Moura, J. J. G., Pauleta, S. R., Maia, L. B., Eds.; Institutionen för biokemi och biofysik: Cambridge, 2017; Vol. 2017-Janua, pp 225–251.

(14)   Bar-Nahum, I.; Gupta, A. K.; Huber, S. M.; Ertem, M. Z.; Cramer, C. J.; Tolman, W. B. Reduction of Nitrous Oxide to Dinitrogen by a Mixed Valent Tricopper-Disulfido Cluster. *J. Am. Chem. Soc.* **2009**, *131*, 2812–2814.

(15)   Esmieu, C.; Orio, M.; Torelli, S.; Le Pape, L.; Pécaut, J.; Lebrun, C.; Ménage, S. N2O Reduction at a Dissymmetric {Cu2S}-Containing Mixed-Valent Center. *Chem. Sci.* **2014**, *5*, 4774–4784.

(16)   Bagherzadeh, S.; Mankad, N. P. Oxidation of a [Cu 2 S] Complex by N 2 O and CO 2 : Insights into a Role of Tetranuclearity in the Cu Z Site of Nitrous Oxide Reductase. *Chem. Commun.* **2018**, *54*, 1097–1100.

(17)   Yam, V. W.-W.; Lee, W.-K.; Lai, T.-F. Synthesis and Luminescent Properties of a Novel Tetranuclear Copper(I) Cluster Containing a M4-Sulfur Moiety. X-Ray Crystal Structure of [Cu4(μ-Dppm)4(M4-S)](PF6)2·. *J. Chem. Soc., Chem. Commun.* **1993**, No. 20, 1571–1573.

(18)   Wing-Wah Yam, V.; Kam-Wing Lo, K.; Kit-Mai Fung, W.; Wang, C.-R. Design of Luminescent Polynuclear Copper(I) and Silver(I) Complexes with Chalcogenides and Acetylides as the Bridging Ligands. *Coord. Chem. Rev.* **1998**, *171*, 17–41.

(19)   Johnson, B. J.; Antholine, W. E.; Lindeman, S. V; Mankad, N. P. A Cu 4 S Model for the Nitrous Oxide Reductase Active Sites Supported Only by Nitrogen Ligands. *Chem. Commun.* **2015**, *51*, 11860–11863.

(20)   Johnson, B. J.; Antholine, W. E.; Lindeman, S. V; Graham, M. J.; Mankad, N. P. A One-Hole Cu 4 S Cluster with N 2 O Reductase Activity: A Structural and Functional Model for Cu Z *. *J. Am. Chem. Soc.* **2016**, *138*, 13107–13110.

(21)   Johnson, B. J.; Lindeman, S. V.; Mankad, N. P. Assembly, Structure, and Reactivity of Cu 4 S and Cu 3 S Models for the Nitrous Oxide Reductase Active Site, Cu Z *. *Inorg. Chem.* **2014**, *53*, 10611–10619.

(22)   Pauleta, S. R.; Dell'Acqua, S.; Moura, I. Nitrous Oxide Reductase. *Coord. Chem. Rev.* **2013**, *257*, 332–349.

(23)   Hsu, C.-W.; Rathnayaka, S. C.; Islam, S. M.; MacMillan, S. N.; Mankad, N. P. N 2 O Reductase Activity of a [Cu 4 S] Cluster in the 4Cu I Redox State Modulated by Hydrogen Bond Donors and Proton Relays in the Secondary Coordination Sphere. *Angew. Chemie Int. Ed.* **2020**, *59*, 627–631.

(24)   Meeker, R. L.; Critchfield, F. E.; Bishop, E. T. Water Determination by Near Infrared Spectrophotometry. *Anal. Chem.* **1962**, *34*, 1510–1511.

(25)   Sugawara, E.; Nikaido, H. Properties of AdeABC and AdeIJK Efflux Systems of Acinetobacter Baumannii Compared with Those of the AcrAB-TolC System of Escherichia Coli. *Antimicrob. Agents Chemother.* **2014**, *58*, 7250–7257.

(26)   Okuniewski, A.; Rosiak, D.; Chojnacki, J.; Becker, B. Coordination Polymers and Molecular Structures among Complexes of Mercury(II) Halides with Selected 1-Benzoylthioureas. *Polyhedron* **2015**, *90*, 47–57.

(27)   Lee, H. B.; Agapie, T. Redox Tuning via Ligand-Induced Geometric Distortions at a YMn 3 O 4 Cubane Model of the Biological Oxygen Evolving Complex. *Inorg. Chem.* **2019**, *58*, 14998–15003.

(28)   Henthorn, J. T.; Arias, R. J.; Koroidov, S.; Kroll, T.; Sokaras, D.; Bergmann, U.; Rees, D. C.; DeBeer, S. Localized Electronic Structure of Nitrogenase FeMoco Revealed by Selenium K-Edge High Resolution X-Ray Absorption Spectroscopy. *J. Am. Chem. Soc.* **2019**, *141*, 13676–13688.

4. PROBING THE ELECTRONIC AND MECHANISTIC ROLES OF THE μ_4-SULFUR ATOM IN A SYNTHETIC Cu$_Z$ MODEL SYSTEM

This closely follows the published content in Rathnayaka, S. C.; Islam, S. M.; DiMucci, I. M.; MacMillan, S. N.; Lancaster, K. M.; Mankad, N. P. Probing the Electronic and Mechanistic Roles of the μ_4-Sulfur Atom in a Synthetic Cu$_Z$ Model System. *Chem. Sci.* **2020**, *11*, 3441–344.

4.1   Background

During bacterial denitrification, nitrous oxide (N$_2$O) is converted to N$_2$ + H$_2$O in a 2e$^-$/2H$^+$ reaction catalyzed by the metalloenzyme, nitrous oxide reductase (N$_2$OR).[1] The catalytic site of N$_2$OR is a tetranuclear copper-sulfur cluster, Cu$_Z$, which has been structurally characterized in both Cu$_Z$ [4Cu2S] and Cu$_Z$* [4Cu1S] forms (Chapter 1, section 1.5.1).[2,3] Both forms show N$_2$O reductase activity to some extent, and both require physiological reduction to their most reduced redox states to activate N$_2$O: the 4Cu^{1+} (fully reduced Cu$_Z$*) state for the [4Cu1S] cluster and the 1Cu^{2+} - 3Cu^{1+} (1-hole Cu$_Z$) state for the [4Cu2S] cluster (Chapter 1, section 1.6.2).[4] For the [4Cu1S] cluster, Solomon has proposed N$_2$O binding across a dicopper(I) cluster edge, with the N$_2$O molecule occupying a μ-1,3 binding mode, based on computational modeling (**Figure 4.1** *(left)*).[5] For the [4Cu2S] form, Einsle has reported crystallographic data on N$_2$O-pressurized crystals of N$_2$OR showing a N$_2$O molecule within van der Waals contact of Cu$_Z$, but the N$_2$O molecule was not found within coordination distance of Cu$_Z$ and had not undergone significant activation (**Figure 4.1** *(middle)*).[3] In neither case has experimental data emerged to probe the nature of N$_2$O activation by the copper-sulfur clusters. The iodide bound N$_2$OR from *Achromobacter cycloclastes* (*Ac*N$_2$OR, PDB ID 2IWF at 1.86 Å) provides the only isolable example with the known inhibitor I$^-$ bound across the Cu$_{II}$–Cu$_{IV}$ edge of Cu$_Z$ [4Cu1S].[6] However, iodide could act as an allosteric inhibitor, raising doubts on Cu$_{II}$–Cu$_{IV}$ edge being the substrate binding site (**Figure 4.1** *(right)*) (see Chapter 1, section 1.5.3 for more information). Studying synthetic model systems can aid understanding of how these unusual inorganic copper-sulfur functional groups behave,[7] which is particularly crucial knowledge in the context of N$_2$O's significant impact as a greenhouse and an ozone layer depleting agent.[8,9]
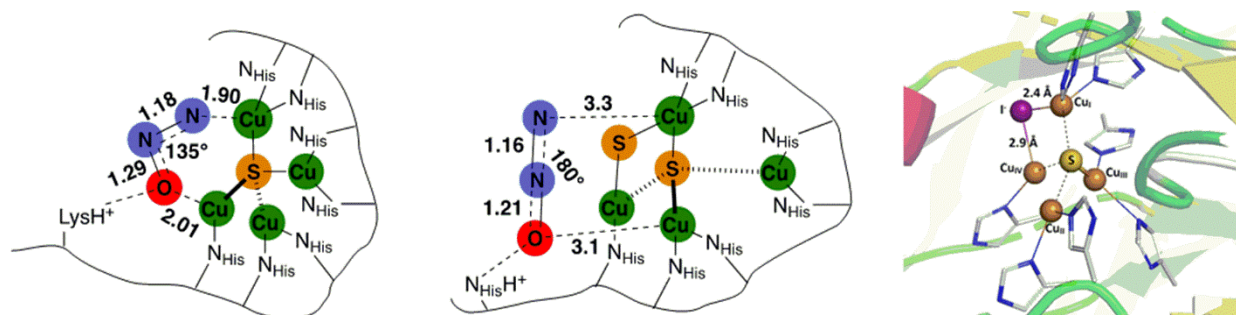
FIGURE 4. 1 *(left)* Interactions of N_2O with a computation model of Cu_Z* form as predicted by Solomon group.[5] *(middle)* Interactions of N_2O with a Cu_Z form (from N_2O pressurized N_2OR from *P. stutzeri*) reported by Einsel group.[3] *(right)* Iodide bound N_2OR crystal structure of *Achromobacter cycloclastes* (PDB ID 2IWK, at 1.7 Å) reported by Hasnain group.[6]

4.2   Synthetic model systems with N_2O activity

Among the synthetic copper compounds and materials known to activate N_2O,[10–13] our group has reported the only examples of N_2O activation by synthetic copper cluster complexes with unsupported sulfur-atom bridges (see Chapter 1, section 1.7 for more information on synthetic model systems of N_2OR). In one case, a dicuprous [Cu_2S] cluster with an unsupported μ_2-sulfide bridge[14] was found to reduce multiple N_2O equivalents to N_2, resulting in exhaustive oxidation of the sulfur center to a μ_2-sulfate ligand (**Scheme 4.1** *(top)*).[15] Here, the copper centers remained redox inactive while the μ_2-sulfide ligand was not only the redox-active center but also acted as an oxygen atom acceptor. In another case, a phosphine-supported tetranuclear [$Cu_4(\mu_4\text{-}S)$] cluster in its $4Cu^{1+}$ state showed reactivity towards N_2O reduction,[16] but the cluster lost structural integrity during the reaction, losing the sulfur atom to unknown products in the reaction medium and thus limiting insight that can be gained about its role (see Chapter 3 for more information). Finally, a formamidinate-supported [$Cu_4(\mu_4\text{-}S)$] cluster in its formally $1Cu^{2+}$ - $3Cu^{1+}$ ([4Cu1S]$^{1-}$) state was found to reduce $^{15}N_2O$ to $^{15}N_2$ (**Scheme 4.1** *(bottom left)*).[17,18] Here the μ_4-sulfide bridge remained intact during a formal oxidation to the $2Cu^{2+}$ - $2Cu^{1+}$ ([4Cu1S]^0) redox state of the cluster, allowing us to establish a closed cycle for N_2O reduction. Based on these results, the potential role (or lack thereof) of the bridging sulfide ligand in copper-sulfur clusters merits further investigation.

This chapter discloses a combined experimental/computational study of the latter system that collectively implicates the μ_4-sulfide ligand as participating in redox changes and directly interacting with N_2O during its activation

(Scheme 4.1 *(bottom right)*). Our data includes the first spectroscopic interrogation of multiple [4Cu1S] redox levels, which has proven challenging in the metalloenzyme system,[1,19] and highlights the fidelity of our synthetic model to the biological Cu_Z site. Even though the organic sulfur ligands in metalloenzymes are often found to assist the reactivity,[34-36] the direct interaction of N_2O with the bridging sulfur atom(s) in Cu_Z has not been proposed before and such reaction pathways should be considered for the chemistry of Cu_Z and related model studies of synthetic metal-sulfide clusters.
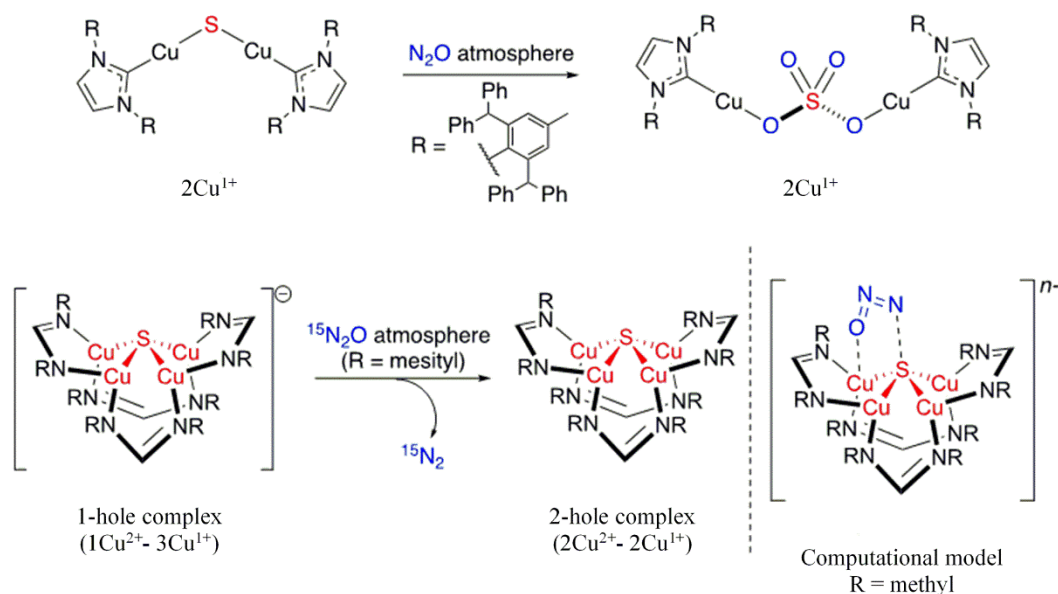
SCHEME 4. 1 Active participation of bridging sulfide ligands in N_2O activation by synthetic copper sulfide model complexes of the active site of N_2OR.

4.3 Determining reaction stoichiometry for the reduction of N_2O by the synthetic model complex $[Cu_4(\mu_4\text{-}S)(NCN)_4]$ $[K(18\text{-crown-6})]$

In one of our previous study of N_2O reduction by the anionic complex $[Cu_4(\mu_4\text{-}S)(NCN)_4]^{1-}$ (the 1-hole cluster, referred to here as $[4Cu1S]^{1-}$) as its $[K(18\text{-crown-6})]^+$ salt (NCN = $[MesNC(H)NMes]^{1-}$),[17] we were able to use NMR spectroscopy, isotopic labeling experiments, and *post-situ* electrophilic trapping to establish the presence of three products: neutral $[Cu_4(\mu_4\text{-}S)(NCN)_4]$ (the 2-hole cluster, referred to here as $[4Cu1S]^0$), N_2, and O^{2-} (**Scheme 4.2**). However, a definitive reaction stoichiometry was not able to establish the at that time. Such information is vital in

developing a reaction mechanism; hence a quantitative GC-MS analysis of the reaction headspace was utilized to determine the yield of N_2.

Our goal was to quantify a minimum of two species out of the reactants and products to establish the stoichiometry of the reaction, but all presented experimental challenges. Quantification of N_2 produced is particularly challenging mainly due to the background contamination. Furthermore, our model complexes are typically handled inside N_2 filled glove box as they are sensitive to air and moisture. Poor solubility of $[4Cu1S]^{1-}$, the low temperature reaction conditions and the detection limits of the GC-MS instrument made the N_2 quantification even more challenging. Quantification of $[4Cu1S]^{1-}$ consumed was troublesome as it is susceptible to thermal decomposition. Quantification of consumed N_2O was difficult as large excess of N_2O was used, thereby making any difference of N_2O too insignificant to detect. The presence of an oxide (O^{2-}) species was indeed detected by *post situ* trapping agent [Me_3SiCl or PhC(O)Cl], but attempted quantification by NMR methods failed due to incompatibility issues upon scaling up the reaction. The only remaining species was the $[4Cu1S]^0$ (2-hole complex) product, and its attempted quantification by spectroscopic methods was unsuccessful due to the poor solubility of $[4Cu1S]^0$. However, because $[4Cu1S]^0$ is insoluble in acetone, we hypothesized that it could be quantitatively recovered by filtration upon scaling up the reaction. Hence, the strategy was to scale up the reaction such that a measurable amount of N_2 is produced in the headspace and a recoverable and measurable (by weight) quantity of $[4Cu1S]^0$ is produced in the solution phase.
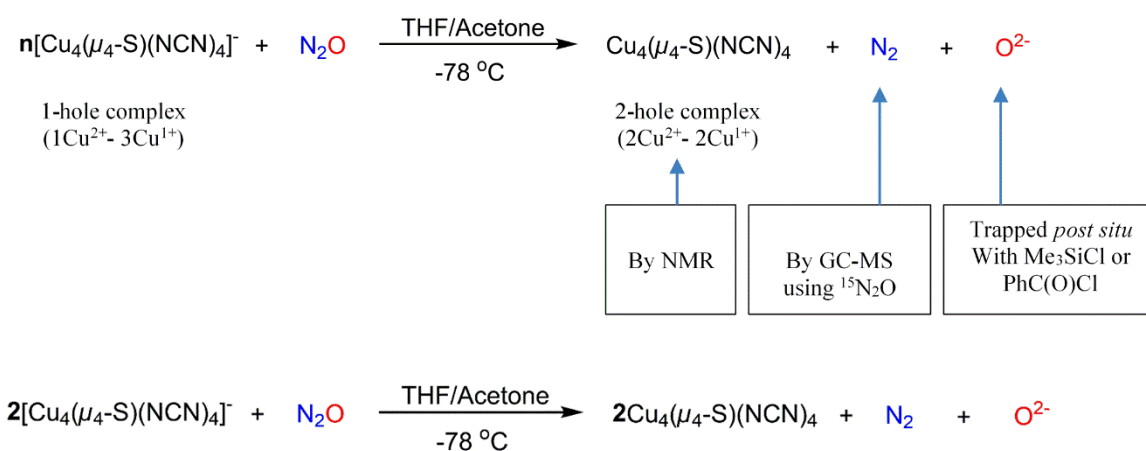
SCHEME 4. 2 The unbalanced *(top)* and the balanced *(bottom)* equations for the reduction of N_2O by the synthetic model complex $[Cu_4(\mu_4\text{-}S)(NCN)_4]$ [K(18-crown-6)]

An apparatus and a GC-MS method were developed (see Chapter 5, Section 5.3.2) to minimize the background N_2 contamination from solvent, reaction headspace, sample handling and injection. Any unavoidable contaminations were subtracted by having proper control experiments. Finally, the reaction was carried out and a portion of the headspace was analyzed using GC-MS while also recovering the solid $[4Cu1S]^0$ produced from the same reaction mixture. Experiments were repeated 3 times and the results were averaged. According to the analysis (see Chapter 5, Section 5.3.2), 0.53 ± 0.06 mol of N_2 are produced per mole of the $[4Cu1S]^{1-}$ complex. Combined results of N_2 and $[4Cu1S]^0$ yield allowed us to construct the balanced reaction for the N_2O reduction by $[4Cu1S]^{1-}$ complex (**Scheme 4.2** *(bottom)*). Based on this reaction stoichiometry, the working hypothesis was developed as one equivalent of $[4Cu1S]^{1-}$ is responsible for N_2O activation while a second equivalent is acting as a sacrificial reductant, thus accounting for the overall two-electron redox reaction.

4.4   Computational investigation of N_2O reduction mechanism

Since we have been unable to observe any intermediates experimentally, we sought to examine the binding mode of N_2O using DFT modeling at the B3LYP/6-31G(d) level in the gas phase. To save computational time, the mesityl groups on the supporting NCN ligands were replaced with methyl groups. After attempting to simulate several types of adducts between the $[4Cu1S]^{1-}$ model complex and N_2O, we were able to locate minima associated with N_2O coordination to both the $[4Cu1S]^{1-}$ model (intermediate $[\mathbf{A}]^{1-}$) and to its closed-shell, fully reduced $[4Cu1S]^{2-}$ analogue (intermediate $[\mathbf{A}]^{2-}$). In both cases N_2O occupied a μ-1,3 binding mode, but to our surprise the N_2O molecule was found to bridge one of the Cu centers and the S atom (**Figure 4.2**(a)). In each case, one of the other Cu centers has moved away from the S atom to facilitate its direct interaction with N_2O. An alternative, μ_3-1,2 binding mode in which the N_2O molecule bridges two Cu centers as well as the S atom of $[\mathbf{A}]^-$ also was located but was determined to be significantly higher in energy by $+53.2$ kcal/mol on the Gibbs free energy surface (**Figure 4.2**(c) and Chapter 5, Section 5.3.3). The preferred binding mode for this model system is distinct from the μ-1,3 bridging between two Cu centers that is proposed for Cu_Z (**Figure 4.1**), where the μ_4-S^{2-} ligand is not proposed to interact directly with N_2O. It should be noted that a mononuclear intermediate in which N_2O bridges across a terminal nickel-sulfide bond has been isolated and crystallographically characterized by Hayton and coworkers.[20,21] The accord between the metrical parameters of the activated N_2O in our computational model with Hayton's experimental data (**Figure 4.2**(b)) lends

further support to the intermediacy of $[\mathbf{A}]^{1-}$. Binding of N_2O to the 1-hole $[4Cu1S]^{1-}$ model to form $[\mathbf{A}]^{1-}$ was calculated to be endothermic by +18.5 kcal/mol, consistent with our inability to observe an N_2O-bound intermediate experimentally.
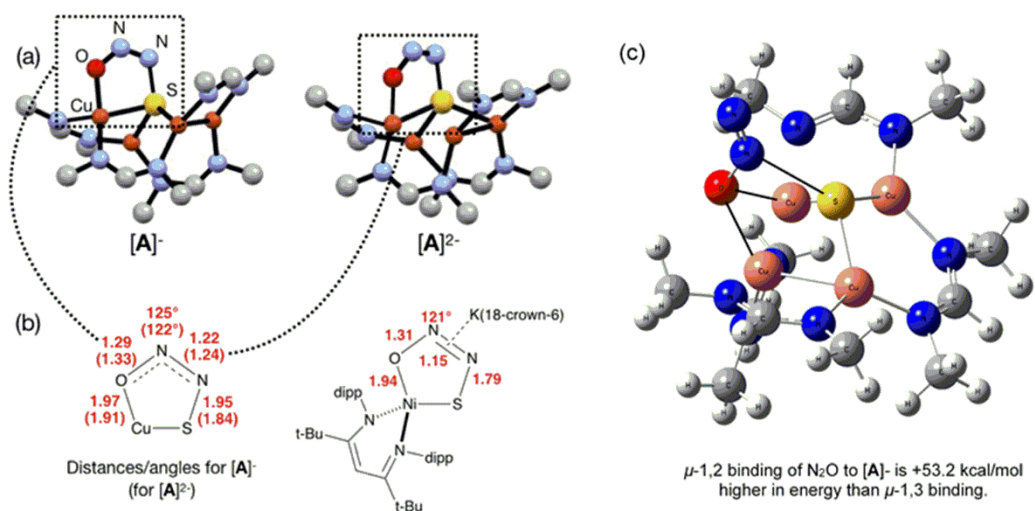
FIGURE 4. 2 (a) Optimized structures of μ-1,3 N_2O-activated intermediates $[\mathbf{A}]^{1-}$ and $[\mathbf{A}]^{2-}$. (b) Comparison of the cyclic core structures of $[\mathbf{A}]^{n-}$ and a related mononuclear Ni complex characterized by Hayton;[20] distances are given in Å. (c) Optimized structures of less favored μ-1,2 N_2O-activated intermediates $[\mathbf{A}]^{1-}$. (color code: Cu, orange; S, yellow; O, red; N, blue; C, gray).

Assuming that small equilibrium concentrations of an N_2O-bound intermediate akin to $[\mathbf{A}]^{1-}$ form under N_2O atmosphere, we next considered the potential reaction pathway to $N_2 + O^{2-}$ (**Scheme 4.3**). We expect that N_2O binding to the $[4Cu1S]^{1-}$ complex would raise its reduction potential, due to the π-accepting nature of N_2O.[22] Thus, there would be a driving force for $[\mathbf{A}]^{1-}$ to undergo reduction by a sacrificial 1-hole complex to provide $[\mathbf{A}]^{2-}$. As in the $[4Cu1S]$ form of Cu_Z,[5] $[\mathbf{A}]^{2-}$ is in the fully-reduced $4Cu^I$ state and thus is expected to π-back donate sufficient electron density into the N_2O π^* manifold to induce N-O bond cleavage. Conversion to the resulting intermediate $[\mathbf{B}]^{2-}$ from N_2 loss was calculated to be exothermic relative to $[\mathbf{A}]^{2-}$. Further energy lowering was found by shifting the terminal O^{2-} ligand in $[\mathbf{B}]^{2-}$ to a μ_2-bridging position in $[\mathbf{C}]^{2-}$. In the case of Cu_Z, Solomon group has reported that the on-cycle intermediate $Cu_Z°$ formed after N_2 loss features a terminal oxygen ligand stabilized by hydrogen bonding with a nearby lysine residue, and has found that disruption of hydrogen bonding produces the off-cycle intermediate Cu_Z^* in which

the oxygen ligand occupies its thermodynamically preferred bridging position.[5] Because we propose O^{2-} to be a stoichiometric product of our aprotic model reaction, we assume that O^{2-} dissociates from either $[\mathbf{B}]^{2-}$ or $[\mathbf{C}]^{2-}$.

An alternative pathway (**Scheme 4.3**, dotted arrows) would involve N_2 loss directly from 1-hole $[\mathbf{A}]^{1-}$ prior to reduction, producing intermediate $[\mathbf{B}]^{1-}$. Reduction of $[\mathbf{B}]^{1-}$ by a sacrificial $[4Cu:1S]^{1-}$ complex would then produce intermediate $[\mathbf{B}]^{2-}$ that is common to both pathways. However, because O^{2-} is expected to lower the reduction potential of the tetracopper cluster due to its π-donor character, it should be unfavorable for $[\mathbf{B}]^{1-}$ to undergo reduction by the sacrificial 1-hole species. Indeed, $[\mathbf{A}]^{1-}$ was calculated to be more oxidizing than $[\mathbf{B}]^{1-}$ by 0.21 V. Thus, we consider this alternative pathway to be unlikely, but we cannot rule it out definitively.
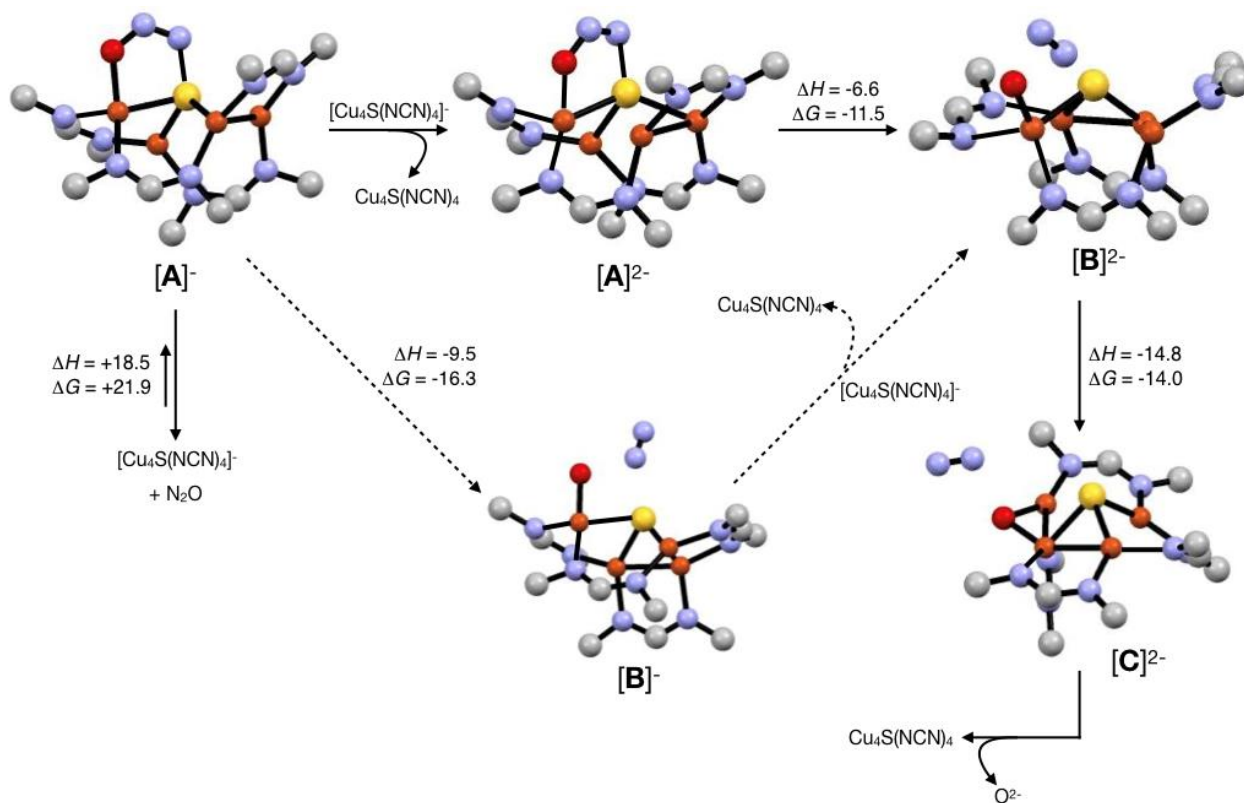
SCHEME 4. 3 Reaction pathways for N_2O reduction modeled by DFT (B3LYP/6-31G(d)). Energies at 298 K are shown in kcal/mol. The favored pathway is shown with solid arrows, and the disfavored pathway with dotted arrows.

4.5 Frontier molecular orbital description of $[4Cu1S]^{0/1-}$ redox couple

Because the μ_4-sulfide ligand seems to play a crucial and direct role in N_2O activation according to our DFT modeling, we wondered whether the frontier orbitals of these synthetic [4Cu1S] complexes have notable sulfur

character. In order to validate our mechanistic model, we thus undertook multi-edge X-ray absorption spectroscopy (XAS) combined with higher-level computational modeling to interrogate the electronic structural changes underpinning the $[4Cu1S]^{0/1-}$ redox process.

4.5.1 Cu K-edge XAS data for $[4Cu1S]^{0/1-}$

Cu K-edge XAS data obtained for $[4Cu1S]^{1-}$ and $[4Cu1S]^{0}$ are shown in **Figure 4.3**(a). Spectral subtraction was carried out to remove a minor contribution of $[4Cu1S]^{0}$ in the spectrum of the monoanion (*vide infra*). Neither spectrum presents a resolved pre-edge (1s → 3d) feature, although both spectra feature a shoulder that gives a peak in the second derivative spectrum at 8979.8 eV, consistent with the presence of Cu $3d$ vacancies (**Figure 4.3**(b)). The rising edges of the two spectra have qualitatively similar fine structure including maxima at ca. 8983 eV suggesting the presence of Cu^{1+} centers,[23] although the spectrum of the $[4Cu1S]^{1-}$ cluster is shifted, with inflection points occurring at 0.8 to 1.1 eV lower energy relative to $[4Cu1S]^{0}$. Given the effectively identical coordination environments between the two species, the shift in rising edge position largely reflects some Cu participation in the redox process. Moreover, the lack of dramatic intensity changes for the rising edge features suggests a delocalized redox process, i.e. that a localized $[2Cu^{2+} - 2Cu^{1+}]/[1Cu^{2+} - 3Cu^{2+}]$ description is not appropriate.
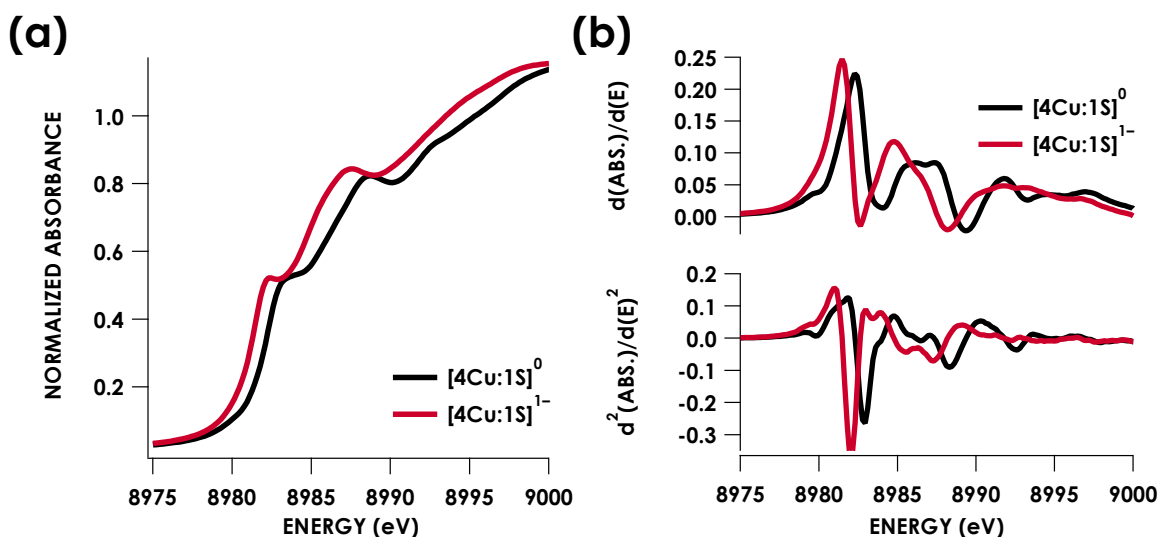
FIGURE 4. 3 (a) Cu K-edge XAS spectra obtained for the $[4Cu1S]^{0/1-}$ redox couple. (b) First *(top)* and second *(bottom)* derivative Cu K-edge XAS spectra. Isoenergetic pre-edge (1s → 3d) excitations are evident in the second-derivative spectra at 8979.8 eV. Rising edge inflection points occur at 8982.3 and 8985.9 eV for $[4Cu1S]^{0}$ and 8981.5 and 8984.8 eV for $[4Cu1S]^{1-}$.

4.5.2   S K-edge XAS data for [4Cu1S]$^{0/1-}$

Quantitative estimates of S participation in the redox-active molecular orbital (RAMO) can be gleaned through analysis of S K-edge XAS data[24] obtained for the two clusters, which are presented in Figure 4. Well-resolved pre-edge peaks are apparent in both spectra, occurring at 2470.2 eV for [4Cu1S]^0 and 2469.5 eV in the spectrum of [4Cu1S]$^{1-}$. A ca. 18% [4Cu1S]^0 impurity was evident in the spectrum of [4Cu1S]$^{1-}$ which was removed by subtraction and re-normalization as carried out by Solomon and co-workers to remove S K-edge XAS contributions from Cu$_A$ in N$_2$OR[25,26] (Figure S15). Notably, the 2469.9 eV [4Cu1S]$^{1-}$ pre-edge peak energy value closely matches pre-edge peak energies reported by Solomon and co-workers for the Cu$_Z$ sites of resting *Achromobacter cycloclastes*[26] and *Paracoccus denitrificans*[25] N$_2$OR at 2469.2 and 2469.0 eV, respectively. On the basis of Cu K-edge XAS analysis, Solomon and co-workers assigned resting Cu$_Z$ as a 1Cu^{2+}:3Cu^{1+} cluster,[25] consistent with the formal oxidation state distribution expected for the [4Cu1S]$^{1-}$ cluster.
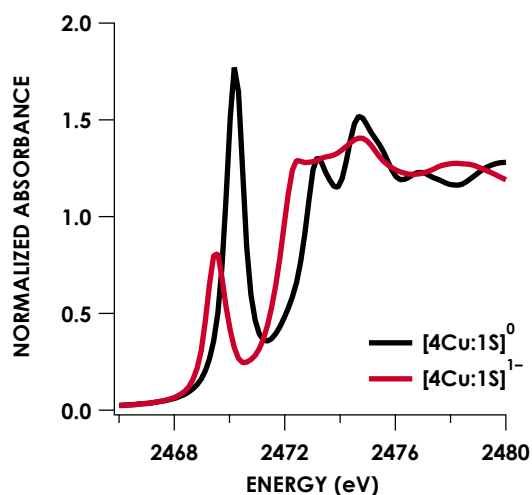
FIGURE 4. 4 S K-edge XAS data obtained for the [4Cu1S]$^{0/1-}$ redox couple. Pre-edge peaks corresponding to S 1s → ψ* excitations are located at 2470.2 eV for [4Cu1S]^0 and 2469.5 eV for [4Cu1S]$^{1-}$.

Pre-edge peaks in the S K-edge XAS spectra of metal complexes and clusters bearing S-donor ligands reflect excitations from S 1s → ψ*, where ψ*, the acceptor MO, is an anti-bonding ligand field MO born of metal-sulfur mixing:

$$\psi^* \approx \alpha^2\ \text{S 3p} - (1-\alpha)^2\ \text{M 3d} \qquad \textbf{Equation 4.1}$$

where α^2 reflects the % 3p contribution in the acceptor MO.[24]

Pre-edge peak intensities (D_0) are then given by the relationship:

$$D_0 = \frac{\alpha^2 I_S h}{3n}$$ **Equation 4.2**

Where,

    h = The number of holes in the acceptor MO
    n = The number of photoabsorbing nuclei from which electrons can be excited into the acceptor MO
    I_s = The radial dipole integral <3p|r|1s> governing the intensity of a "pure" S 1s $\rightarrow$ 3p excitation.

Solomon and co-workers[27] have estimated the value of I_s as a function of the S 1s $\rightarrow$ 4p excitation energy, which can itself be gleaned from S K-edge XAS data and will vary according to the nature of the S photoabsorber and its chemical environment. Using TDDFT calculations to facilitate the assignments (*vide infra*), the S 1s $\rightarrow$ 4p transition for $[4Cu1S]^0$ occurs at 2477.0 eV and at 2475.9 eV for $[4Cu1S]^{1-}$. Using the relationship from Solomon and co-workers,[27] the value of I_s for $[4Cu1S]^0$ is 14.9 and is 12.9 for $[4Cu1S]^{1-}$.

Fitting pseudo-Voigt peaks to the pre-edge peaks in the S K-edge data give integrated peak areas D_0 for the two clusters of 2.03 $\pm$ 0.01 for $[4Cu1S]^0$ and 0.91 $\pm$ 0.02 for $[4Cu1S]^{1-}$. The ca. twofold decrease in D_0 upon reduction confirms S 3p contribution to the RAMO shared by the redox couple. Application of **Equation 4.2** then gives 20.5 $\pm$ 0.1 % S 3p in the RAMO of $[4Cu1S]^0$ and 21.1 $\pm$ 0.5 % S 3p in the RAMO of $[4Cu1S]^{1-}$. The latter values are comparable to the estimate given by Solomon and co-workers for the RAMO of the Cu_Z site in resting *Paracoccus denitrificans* N_2OR at 15–22%.[25]

4.5.3 DFT interpretation of frontier orbitals

DFT calculations were carried out to further interrogate the nature of the RAMO in the $[4Cu1S]^{0/1-}$ redox couple. Calculations were carried out on truncated models as described above and employed the B3LYP hybrid density functional with the CP(PPP) basis set[29,30] on Cu and the scalar relativistically recontracted ZORA-def2-TZVP(-f)[31] basis on all other atoms. The LUMO of $[4Cu1S]^0$ and SOMO of $[4Cu1S]^{1-}$ are depicted in **Figure 4.5**.

(a)   **(b)**

LUMO
12.7% Average Cu 3d
13.1% Cu$_1$ 3d
12.4% Cu$_2$ 3d
13.0% Cu$_3$ 3d
12.4% Cu$_4$ 3d
20.6% S 3p

SOMO
14.5% Average Cu 3d
14.9% Cu$_1$ 3d
14.4% Cu$_2$ 3d
14.6% Cu$_3$ 3d
14.2% Cu$_4$ 3d
20.5% S 3p
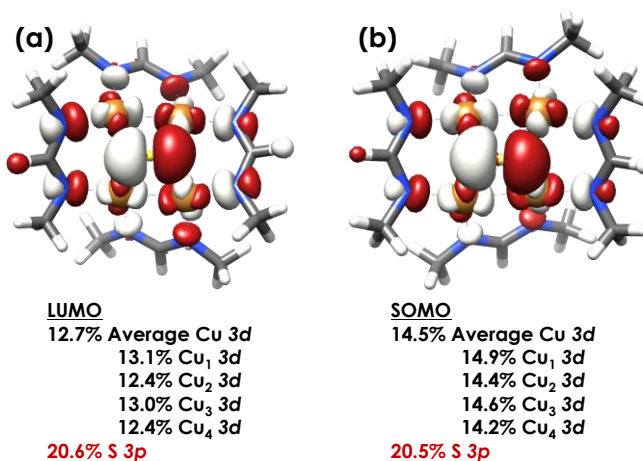
FIGURE 4. 5 (a) Restricted Kohn-Sham LUMO for $[4Cu1S]^0$ and (b) quasi-restricted (QRO)[28] SOMO for $[4Cu1S]^{1-}$. Both MOs were calculated for truncated models using the B3LYP hybrid density functional with the CP(PPP) basis set on Cu and the scalar-relativstically recontracted ZORA-def2-TZVP(-f) basis set on all other atoms. Orbitals are plotted at an isovalue of 0.03 au.

These are qualitatively similar, indicating that the RAMO is a highly delocalized orbital featuring effectively equal participation of Cu 3d from all 4 metal centers along with a significant contribution from S 3p. Equal participation of all four Cu centers in the SOMO was previously indicated by simulation of experimental EPR parameters.[22] The equal contributions from Cu also accord with observation that the Cu K-edge XANES shift in energy but do not exhibit differences in fine structure. Calculated S 3p contributions are 20.6% for $[4Cu1S]^0$ and 21.1% for $[4Cu1S]^{1-}$, in splendid agreement with experiment as well as with previous EPR analysis of the $[4Cu1S]^{1-}$ species that indicated anomalously small Cu hyperfine coupling.[17] Moreover, TDDFT calculations[32] of the S K-edge XAS for both species initiated from the aforementioned single-point DFT calculations give spectra that nicely reproduce the energy and intensity differences encountered in the experimental data (**Figure 4.6**).
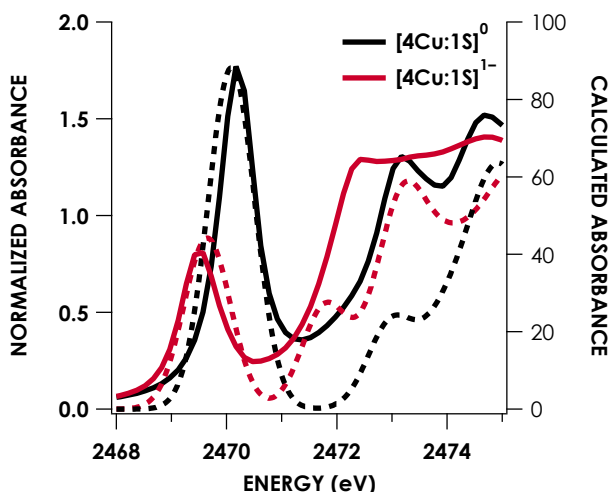
FIGURE 4. 6 Overlay of TDDFT-calculated S K-edge XAS with experimental spectra obtained for the $[4Cu1S]^{0/1-}$ redox series. TDDFT calculations were initiated from B3LYP single-point calculations with the CP(PPP)[29] basis set on Cu and the ZORA-def2-TZVP(-f)[33] basis set on all other atoms. Calculated spectra are shifted by +40.4 eV to correct for inaccurate core potential modeling endemic to standard hybrid DFT calculations.

4.6 Concluding remarks

The 1-hole $[4Cu1S]^{1-}$ model cluster of Cu_Z is oxidized to its 2-hole $[4Cu1S]^0$ state by N_2O with N_2 evolution.[17] Here, we have established reaction stoichiometry by quantification of N_2 and $[4Cu1S]^0$, allowing us to conclude that the overall 2-electron reduction of N_2O requires two equivalents of the $[4Cu1S]^{1-}$ cluster molecule, with each equivalent mediating a 1-electron redox process individually. Under the assumption that one equivalent activates N_2O while the other acts as a sacrificial reductant, a computational model of the reaction intermediates indicated cooperative Cu/S coordination of N_2O.

This cooperative binding mode implies direct participation of the bridging S-atom in N_2O activation and N-O cleavage, in contrast to the passive role of bridging S-atoms in typical metal-sulfur active sites. Consistent with this proposal, XAS analysis of the 1-hole $[4Cu1S]^{1-}$ and 2-hole $[4Cu1S]^0$ clusters indicated that the μ_4-S center contributes appreciably to the redox-active molecular orbital. Crucially, the S K-edge energies and estimated S-atom participation in redox chemistry closely match previous characterization of the biological Cu_Z site, making this synthetic system a faithful model in terms of electronic structure as well as atomic connectivity and chemical reactivity. Moreover, to

our knowledge this data represents the first spectroscopic interrogation of multiple redox levels of a conserved [4Cu1S] cluster.

Key to the model cluster's reactivity, and in particular to the μ_4-S center's active participation in N$_2$O activation and reduction, is the high degree of covalency within the [4Cu1S] core. This Cu/S covalency allows the S-atom to exhibit characteristics typically associated with transition metals, such as the ability to simultaneously accept and donate electron density to the substrate and to vary its oxidation level during a chemical process, that are necessary for a catalytic active site mediating a multielectron redox process. Thus, it is important to consider both metal/metal and metal/ligand cooperation when interrogating highly covalent multinuclear catalysts such as Cu$_Z$ and related systems.

4.7   References

(1)   Pauleta, S. R.; Dell'Acqua, S.; Moura, I. Nitrous Oxide Reductase. *Coord. Chem. Rev.* **2013**, *257*, 332–349.

(2)   Brown, K.; Tegoni, M.; Prudêncio, M.; Pereira, A. S.; Besson, S.; Moura, J. J.; Moura, I.; Cambillau, C. A Novel Type of Catalytic Copper Cluster in Nitrous Oxide Reductase. *Nat. Struct. Biol.* **2000**, *7*, 191–195.

(3)   Pomowski, A.; Zumft, W. G.; Kroneck, P. M. H.; Einsle, O. N2O Binding at a [4Cu:2S] Copper–Sulphur Cluster in Nitrous Oxide Reductase. *Nature* **2011**, *477*, 234–237.

(4)   Johnston, E. M.; Dell'Acqua, S.; Ramos, S.; Pauleta, S. R.; Moura, I.; Solomon, E. I. Determination of the Active Form of the Tetranuclear Copper Sulfur Cluster in Nitrous Oxide Reductase. *J. Am. Chem. Soc.* **2014**, *136*, 614–617.

(5)   Johnston, E. M.; Carreira, C.; Dell'Acqua, S.; Dey, S. G.; Pauleta, S. R.; Moura, I.; Solomon, E. I. Spectroscopic Definition of the CuZ° Intermediate in Turnover of Nitrous Oxide Reductase and Molecular Insight into the Catalytic Mechanism. *J. Am. Chem. Soc.* **2017**, *139*, 4462–4476.

(6)   Paraskevopoulos, K.; Antonyuk, S. V.; Sawers, R. G.; Eady, R. R.; Hasnain, S. S. Insight into Catalysis of Nitrous Oxide Reductase from High-Resolution Structures of Resting and Inhibitor-Bound Enzyme from Achromobacter Cycloclastes. *J. Mol. Biol.* **2006**, *362*, 55–65.

(7)   Holm, R. H.; Solomon, E. I. Preface: Biomimetic Inorganic Chemistry. *Chem. Rev.* **2004**, *104*, 347–348.

(8)   Ravishankara, A. R.; Daniel, J. S.; Portmann, R. W. Nitrous Oxide (N2O): The Dominant Ozone-Depleting Substance Emitted in the 21st Century. *Science (80-.).* **2009**, *326*, 123–125.

(9)   Thomson, A. J.; Giannopoulos, G.; Pretty, J.; Baggs, E. M.; Richardson, D. J. Biological Sources and Sinks of Nitrous Oxide and Strategies to Mitigate Emissions. *Philos. Trans. R. Soc. B Biol. Sci.* **2012**, *367*, 1157–1168.

(10)   Bar-Nahum, I.; Gupta, A. K.; Huber, S. M.; Ertem, M. Z.; Cramer, C. J.; Tolman, W. B. Reduction of Nitrous Oxide to Dinitrogen by a Mixed Valent Tricopper-Disulfido Cluster. *J. Am. Chem. Soc.* **2009**, *131*, 2812–

2814.

(11) Esmieu, C.; Orio, M.; Torelli, S.; Le Pape, L.; Pécaut, J.; Lebrun, C.; Ménage, S. N2O Reduction at a Dissymmetric {Cu2S}-Containing Mixed-Valent Center. *Chem. Sci.* **2014**, *5*, 4774–4784.

(12) Tsai, M.-L.; Hadt, R. G.; Vanelderen, P.; Sels, B. F.; Schoonheydt, R. A.; Solomon, E. I. [Cu 2 O] 2+ Active Site Formation in Cu–ZSM-5: Geometric and Electronic Structure Requirements for N 2 O Activation. *J. Am. Chem. Soc.* **2014**, *136*, 3522–3529.

(13) Zhuravlev, V.; Malinowski, P. J. A Stable Crystalline Copper(I)–N 2 O Complex Stabilized as the Salt of a Weakly Coordinating Anion. *Angew. Chemie Int. Ed.* **2018**, *57*, 11697–11700.

(14) Zhai, J.; Filatov, A. S.; Hillhouse, G. L.; Hopkins, M. D. Synthesis, Structure, and Reactions of a Copper–Sulfido Cluster Comprised of the Parent Cu 2 S Unit: {(NHC)Cu} 2 (μ-S). *Chem. Sci.* **2016**, *7*, 589–595.

(15) Bagherzadeh, S.; Mankad, N. P. Oxidation of a [Cu 2 S] Complex by N 2 O and CO 2 : Insights into a Role of Tetranuclearity in the Cu Z Site of Nitrous Oxide Reductase. *Chem. Commun.* **2018**, *54*, 1097–1100.

(16) Hsu, C.; Rathnayaka, S. C.; Islam, S. M.; MacMillan, S. N.; Mankad, N. P. N 2 O Reductase Activity of a [Cu 4 S] Cluster in the 4Cu I Redox State Modulated by Hydrogen Bond Donors and Proton Relays in the Secondary Coordination Sphere. *Angew. Chemie Int. Ed.* **2020**, *59*, 627–631.

(17) Johnson, B. J.; Antholine, W. E.; Lindeman, S. V; Graham, M. J.; Mankad, N. P. A One-Hole Cu 4 S Cluster with N 2 O Reductase Activity: A Structural and Functional Model for Cu Z *. *J. Am. Chem. Soc.* **2016**, *138*, 13107–13110.

(18) Johnson, B. J.; Antholine, W. E.; Lindeman, S. V; Mankad, N. P. A Cu 4 S Model for the Nitrous Oxide Reductase Active Sites Supported Only by Nitrogen Ligands. *Chem. Commun.* **2015**, *51*, 11860–11863.

(19) Solomon, E. I.; Heppner, D. E.; Johnston, E. M.; Ginsbach, J. W.; Cirera, J.; Qayyum, M.; Kieber-Emmons, M. T.; Kjaergaard, C. H.; Hadt, R. G.; Tian, L. Copper Active Sites in Biology. *Chem. Rev.* **2014**, *114*, 3659–3853.

(20) Hartmann, N. J.; Wu, G.; Hayton, T. W. Synthesis of a "Masked" Terminal Nickel(II) Sulfide by Reductive Deprotection and Its Reaction with Nitrous Oxide. *Angew. Chemie* **2015**, *127*, 15169–15172.

(21) Hartmann, N. J.; Wu, G.; Hayton, T. W. Synthesis and Reactivity of a Nickel(<scp>ii</Scp>) Thioperoxide Complex: Demonstration of Sulfide-Mediated N 2 O Reduction. *Chem. Sci.* **2018**, *9*, 6580–6588.

(22) Trogler, W. C. Physical Properties and Mechanisms of Formation of Nitrous Oxide. *Coord. Chem. Rev.* **1999**, *187*, 303–327.

(23) Kau, L. S.; Spira-Solomon, D. J.; Penner-Hahn, J. E.; Hodgson, K. O.; Solomon, E. I. X-Ray Absorption Edge Determination of the Oxidation State and Coordination Number of Copper. Application to the Type 3 Site in Rhus Vernicifera Laccase and Its Reaction with Oxygen. *J. Am. Chem. Soc.* **1987**, *109*, 6433–6442.

(24) Glaser, T.; Hedman, B.; Hodgson, K. O.; Solomon, E. I. Ligand K-Edge X-Ray Absorption Spectroscopy: A Direct Probe of Ligand−Metal Covalency. *Acc. Chem. Res.* **2000**, *33*, 859–868.

(25) Chen, P.; Gorelsky, S. I.; Ghosh, S.; Solomon, E. I. N2O Reduction by Theμ4-Sulfide-Bridged Tetranuclear CuZ Cluster Active Site. *Angew. Chemie Int. Ed.* **2004**, *43*, 4132–4140.

(26) Ghosh, S.; Gorelsky, S. I.; DeBeer George, S.; Chan, J. M.; Cabrito, I.; Dooley, D. M.; Moura, J. J. G.; Moura, I.; Solomon, E. I. Spectroscopic, Computational, and Kinetic Studies of the μ 4 -Sulfide-Bridged Tetranuclear Cu Z Cluster in N 2 O Reductase: PH Effect on the Edge Ligand and Its Contribution to Reactivity. *J. Am. Chem. Soc.* **2007**, *129*, 3955–3965.

(27) Sarangi, R.; DeBeer George, S.; Rudd, D. J.; Szilagyi, R. K.; Ribas, X.; Rovira, C.; Almeida, M.; Hodgson,

K. O.; Hedman, B.; Solomon, E. I. Sulfur K-Edge X-Ray Absorption Spectroscopy as a Probe of Ligand−Metal Bond Covalency: Metal vs Ligand Oxidation in Copper and Nickel Dithiolene Complexes. *J. Am. Chem. Soc.* **2007**, *129*, 2316–2326.

(28)   Neese, F. Importance of Direct Spin−Spin Coupling and Spin-Flip Excitations for the Zero-Field Splittings of Transition Metal Complexes: A Case Study. *J. Am. Chem. Soc.* **2006**, *128*, 10213–10222.

(29)   Neese, F. Prediction and Interpretation of the 57Fe Isomer Shift in Mössbauer Spectra by Density Functional Theory. *Inorganica Chim. Acta* **2002**, *337*, 181–192.

(30)   Sinnecker, S.; Slep, L. D.; Bill, E.; Neese, F. Performance of Nonrelativistic and Quasi-Relativistic Hybrid DFT for the Prediction of Electric and Magnetic Hyperfine Parameters in 57 Fe Mössbauer Spectra. *Inorg. Chem.* **2005**, *44*, 2245–2254.

(31)   Pantazis, D. A.; Chen, X.-Y.; Landis, C. R.; Neese, F. All-Electron Scalar Relativistic Basis Sets for Third-Row Transition Metal Atoms. *J. Chem. Theory Comput.* **2008**, *4*, 908–919.

(32)   DeBeer George, S.; Neese, F. Calibration of Scalar Relativistic Density Functional Theory for the Calculation of Sulfur K-Edge X-Ray Absorption Spectra. *Inorg. Chem.* **2010**, *49*, 1849–1853.

(33)   Weigend, F.; Ahlrichs, R. Balanced Basis Sets of Split Valence, Triple Zeta Valence and Quadruple Zeta Valence Quality for H to Rn: Design and Assessment of Accuracy. *Phys. Chem. Chem. Phys.* **2005**, *7*, 3297.

(34)   Slater, J. W.; Marguet, S. C.; Monaco, H. A.; Shafaat, H. S. Going beyond Structure: Nickel-Substituted Rubredoxin as a Mechanistic Model for the [NiFe] Hydrogenases. *J. Am. Chem. Soc.* **2018**, *140*, 10250–10262.

(35)   Walters, E. M.; Garcia-Serres, R.; Jameson, G. N. L.; Glauser, D. A.; Bourquin, F.; Manieri, W.; Schürmann, P.; Johnson, M. K.; Huynh, B. H. Spectroscopic Characterization of Site-Specific [Fe$_4$S$_4$] Cluster Chemistry in Ferredoxin:Thioredoxin Reductase: Implications for the Catalytic Mechanism. *J. Am. Chem. Soc.* **2005**, *127*, 9612–9624.

(36)   Tao, L.; Stich, T. A.; Fugate, C. J.; Jarrett, J. T.; Britt, R. D. EPR-Derived Structure of a Paramagnetic Intermediate Generated by Biotin Synthase BioB. *J. Am. Chem. Soc.* **2018**, *140*, 12947–12963.

5. EXPERIMENTAL SECTION

5.1 Supporting information for Chapter 2

Reproduced with permission from Rathnayaka, S. C.; Lindeman, S. V.; Mankad, N. P. Multinuclear Cu(I) Clusters Featuring a New Triply Bridging Coordination Mode of Phosphaamidinate Ligands. *Inorg. Chem.* **2018**, *57*, 9439–9445. Copyright (2014) American Chemical Society, and Rathnayaka, S. C.; Hsu, C.-W.; Johnson, B. J.; Iniguez, S. J.; Mankad, N. P. Impact of Electronic and Steric Changes of Ligands on the Assembly, Stability, and Redox Activity of $Cu_4(\mu_4$-S) Model Compounds of the Cu_Z Active Site of Nitrous Oxide Reductase (N_2OR). *Inorg. Chem.* **2020**, *59*, 6496–6507.

5.1.1 General remarks

Unless otherwise mentioned, all experiments were performed under N_2 atmosphere in a glovebox or using standard Schlenk line techniques. All the chemicals purchased from commercial sources were used without further purification. Solvents were dried using a Glass Contour solvent purification system built by Pure Process Technology, LLC. Deuterated solvents that were packed under Ar, were stored in 3-Å molecular sieves without further degassing. Ligands dppf and (**e**) were purchased from commercial vendors and used without further purification. Compounds (**a**),[40] (**b**),[41] (**d**)[42],(**q**),[53] **C**,[47] **D**[57] and **E**[40] were synthesized by adopting synthetic routes reported in literature. *(**Caution:** Synthesis of (**a**) and (**q**) involves n-butyllithium and necessary precautions should be taken to avoid accidents. Any waste or glassware containing residual phosphines should be properly cleaned as phosphines are highly smelly. Synthesis of **D** involves quenching $LiAlH_4$ with H_2O. Extreme care should be taken when adding the first few drops of H_2O, as the quenching is highly exothermic and H_2 is evolved. Any waste or glassware containing Phosphane (**D**) should be properly cleaned as phosphanes are highly smelly. Proper PPE must be worn to avoid any frostbite as some synthesis involve -78 °C cold bath).*

5.1.2 Instrumentation

$^{31}P\{^1H\}$, ^1H and $^{19}F\{^1H\}$ NMR spectra were recorded at ambient temperature using a Bruker Avance DPX-400 MHz instrument, and chemical shifts are reported in ppm units relative to the residual signal of the deuterated solvent for (^1H) or relative to external standards for ^{31}P and ^{19}F. Mass analysis were performed with an Advion

Expression[L] CMS mass spectrometer in APCI(+) mode. Cyclic voltammetry experiments were performed in a classic three-electrode system (Pt working electrode, Pt counter electrode and Ag/AgNO$_3$ (0.01 M in MeCN) reference electrode using a WaveNow USB Potentiostat from Pine Research Instrumentation. X-ray crystallography data for complex **8, 9** and **10** were collected at the X-ray Structural Laboratory at Marquette University (Milwaukee, WI) using a SuperNova, Dual, Cu at home/near, Atlas diffractometer [CuKα (λ = 1.54184)] at 100.15 K. The structure was solved with the Olex2 structure solution program using Charge Flipping and refined with the ShelXL refinement package using Least Squares minimization. X-ray crystallography data for complexes (**a'**), **3**, **4**, **5**, **7h and** (**q'**) were collected on Bruker D8 Quest ECO A30 diffractometer [MoKα (λ = 0.71073 Å)] at 100.15 K using a Bruker Photon II detector. The structures were solved using APEX3 package and refined with SHELXS-2014/7.[58] UV-Vis analysis was performed using Varian CARY 300 Bio spectrophotometer and Cary WinUV scan application. The X-band EPR spectrum of **7h** was collected using a modified Varian E-4 EPR spectrometer with a liquid nitrogen finger dewar at -195 ºC (Microwave frequency, 9.255 GHz; microwave power, 6 mW; scan time, 240 s; time constant, 0.03 s; field modulation amplitude, 1 mT. g=2.05 and 2.01).

5.1.3   Synthesis procedures

General synthesis of Formamidine ligands (**c**), (**f**)-(**m**)

Mesityl aniline (1.0 g, 7.40 mmol), triethyl orthoformate (0.55g, 3.7 mmol) and acetic acid (3-5 drops) were mixed in a 25-mL round bottom flask. The flask was fitted with a condenser and a receiving flask and heated at 140 ºC for 1 hour, condensing MeOH. After that the temperature was raised to 170 ºC and heated for another 2 hours. The reaction mixture was then allowed to reach room temperature. The resulting off-white hard solid was mixed with Et$_2$O and ground with a glass rod until a fine powder was produced. The white powder was collected by filtration and washed with several portions of Et$_2$O and vacuum dried. Yield: 0.85 g, 82 %. Other derivatives were prepared using the same procedure with the appropriate aniline in place of mesityl aniline.

Compound (**f**): 4-methoxyaniline (1.0 g, 8.12 mmol), triethyl orthoformate (0.60 g, 4.06 mmol), Yield: 0.78 g, 75 %. ^{1}H NMR (400 MHz, CDCl$_3$) δ 8.37 (s, 1H), 8.04 (s, 1H), 7.05 – 6.78 (m, 8H), 3.79 (s, 6H). Compound (**g**): 4-chloroaniline (1.0 g, 7.84 mmol), triethyl orthoformate (0.58 g, 3.92 mmol), Yield: 0.84 g, 81 %. ^{1}H NMR (400 MHz, CDCl$_3$) δ 8.17 (s, 1H), 7.31 (s, 8H), 2.84 (brs, residual H$_2$O). Compound (**h**): 2,6-dimethylaniline (1.0 g, 8.25

mmol), triethyl orthoformate (0.61 g, 4.15 mmol), Yield: 0.82 g, 79 %. ^{1}H NMR (400 MHz, CDCl$_3$) δ 7.30 (brs, 1H), 7.28 – 6.72 (m, 6H), 2.28 (s, 12H). m/z theoretical: 252.16, 253.17, 254.17. Found: 253.1, 254.2, 255.1. Dimeric form shows up: 505.3, 506.3, 507.2. Compound (**i**): 4-chloro-2,6-dimethylaniline (1.0 g, 6.43 mmol), triethyl orthoformate (0.48 g, 3.21 mmol), Yield: 0.79 g, 77 %. ^{1}H NMR (400 MHz, CDCl$_3$) δ 7.31 (brs, 1H), 7.20 – 6.98 (m, 4H), 2.22 (d, J = 4.5 Hz, 12H). m/z theoretical: 320.08, 321.09, 322.08. Found: 321.3, 322.3, 323.3. Compound (**j**): 4-methoxy-2-methylaniline (1.0 g, 7.23 mmol), triethyl orthoformate (0.54 g, 3.66 mmol), Yield: 0.87 g, 84 %. ^{1}H NMR (400 MHz, CDCl$_3$) δ 7.82 (brs, 1H), 6.91 – 7.02 (m, 2H), 6.80 – 6.68 (m, 4H), 3.78 (s, 6H), 2.31 (s, 6H). m/z theoretical: 284.15, 285.16, 286.16. Found: 285.3, 286.3, 287.3. Compound (**k**): 6-methoxy-2-methylaniline (1.0 g, 7.23 mmol), triethyl orthoformate (0.54 g, 3.66 mmol), Yield: 0.87 g, 84 %. ^{1}H NMR (400 MHz, CDCl$_3$) δ 7.88 (s, 1H), 7.56 (s, 1H), 7.04 – 6.70 (m, 6H), 3.90 – 3.70 (m, 6H), 2.37 – 2.22 (m, 6H). m/z theoretical: 284.15, 285.16, 286.16. Found: 285.3, 286.3, 287.4. Compound (**l**): 2-chloro-6-methylaniline (1.0 g, 7.06 mmol), triethyl orthoformate (0.52 g, 3.53 mmol), Yield: 0.89 g, 86 %. ^{1}H NMR (400 MHz, CDCl$_3$) δ 7.69 – 6.89 (m, 6H), 6.67 (brs, 1H), 5.86 (brs, 1H), 2.60 – 2.15 (m, 6H). m/z theoretical: 292.05, 293.06, 294.05. Found: 293.2, 294.2, 295.2. Compound (**m**): 2,6-diisopropylaniline (1.0 g, 5.64 mmol), triethyl orthoformate (0.42 g, 2.82 mmol), Yield: 0.81 g, 79 %. ^{1}H NMR (400 MHz, CDCl$_3$) δ 7.29 – 7.01 (m, 6H), 5.55 (d, J = 11.9 Hz, 1H), 3.42 – 3.13 (m, 4H), 1.36 – 1.06 (m, 24H). m/z theoretical: 364.29, 365.29, 366.29. Found: 365.5, 366.4

General synthesis for dicopper formamidinate precursor complexes (c'),[31] (h')-(m')

NaHMDS (0.36 g, 1.96 mmol) in THF (~2 mL) was added dropwise to a solution of N,N-dimesitylformamidine (0.50 g, 1.78 mmol) in THF (~ 5 mL). It was stirred for 1 hour at room temperature and Cu(MeCN)$_4$PF$_6$ (0.67 g, 1.78 mmol) was added as a solid. Reaction mixture was stirred at room temperature for 3 hours and the solvent was removed under vacuum, providing (**c'**) as a white precipitate. It was collected by filtration, washed with Et$_2$O (2×3 mL) and vacuum dried. Yield: 0.45 g, 74 %. Other derivatives were prepared using the same procedure with the appropriate formamidine in place of the dimesityl derivative.

Compound (**h'**): Bis(2,6-dimethylphenyl)formamidine (0.5 g, 1.98 mmol), NaHMDS (0.40 g, 2.18 mmol), Cu(MeCN)$_4$PF$_6$ (0.74 g, 1.98 mmol), Yield: 0.80 g, 64 %. ^{1}H NMR (400 MHz, CDCl$_3$) δ 7.09 – 7.01 (m, 10H), 6.96 (s, 1.4H), 6.94 (d, J = 1.2 Hz, 2H), 6.92 (s, 0.6H), 2.41 (s, 24H). Compound (**i'**): Bis(4-chloro-2,6-dimethylphenyl)formamidine (0.5 g, 1.42 mmol), NaHMDS (0.29 g, 1.57 mmol), Cu(MeCN)$_4$PF$_6$ (0.53 g, 1.42 mmol),

Yield: 0.77 g, 70 %. ^{1}H NMR (400 MHz, CDCl$_3$) δ 6.99 (s, 8H), 6.94 (s, 1H), 2.29 (s, 24H). Compound (**j'**): Bis(4-methoxy-2-methylphenyl)formamidine (0.5 g, 1.76 mmol), NaHMDS (0.35 g, 1.93 mmol), Cu(MeCN)$_4$PF$_6$ (0.66 g, 1.76 mmol), Yield: 0.84 g, 69 %. ^{1}H NMR (400 MHz, CDCl$_3$) δ 7.53 (s, 2H), 6.85 (d, *J* = 8.4 Hz, 4H), 6.69 (d, *J* = 3.0 Hz, 4H), 6.66 – 6.61 (m, 4H), 3.75 (s, 12H), 2.39 (s, 12H), 0.28(s, residual HMDS). Compound (**k'**): Bis(6-methoxy-2-methylphenyl)formamidine (0.5 g, 1.76 mmol), NaHMDS (0.35 g, 1.93 mmol), Cu(MeCN)$_4$PF$_6$ (0.66 g, 1.76 mmol), Yield: 0.79 g, 65 %. ^{1}H NMR (400 MHz, CDCl$_3$) δ 7.43 (s, 2H), 6.88 (t, J = 8.0 Hz, 4H), 6.75 (d, J = 7.5 Hz, 4H), 6.69 (d, J = 8.0 Hz, 4H), 3.66 (s, 12H), 2.41 (s, 12H). Compound (**l'**): Bis(6-chloro-2-methylphenyl)formamidine (0.5 g, 1.71 mmol), NaHMDS (0.34 g, 1.88 mmol), Cu(MeCN)$_4$PF$_6$ (0.64 g, 1.71 mmol), Yield: 0.86 g, 71 %. ^{1}H NMR (400 MHz, CDCl$_3$) δ 7.20 (d, J = 7.9 Hz, 4H), 7.18 (s, 2H), 7.06 (d, J = 7.5 Hz, 4H), 6.91 (t, J = 7.8 Hz, 4H), 2.42 (s, 12H). Compound (**m'**): Bis(2,6-diisopropylphenyl)formamidine (0.5 g, 1.37 mmol), NaHMDS (0.28 g, 1.51 mmol), Cu(MeCN)$_4$PF$_6$ (0.51 g, 1.37 mmol), Yield: 0.86 g, 73 %. ^{1}H NMR (400 MHz, CDCl$_3$) δ 7.09 – 7.02 (m, 14H), 3.61 (hept, J = 6.9 Hz, 8H), 1.26 (d, J = 6.9 Hz, 24H), 1.18 (d, J = 6.9 Hz, 24H).

Synthesis of [Cu$_2$((diphenylphosphanyl)-*N*-mesitylmethanimine)$_2$](PF$_6$)$_2$ (a')

Cu(MeCN)$_4$(PF$_6$) (0.5140 g, 1.38 mmol) was dissolved in acetone (~3 mL) and was added dropwise to a solution of (**a**) (0.4570 g, 1.38 mmol) in Et$_2$O (~12 mL). Formation of a yellow suspension was seen. (If yellow clumps are formed, adding few drops of acetone would break them up and make a nice solid.) Reaction mixture was stirred overnight at room temperature and filtered to obtain the title compound as a yellow powder. It was washed with Et$_2$O (2×5 mL) and vacuum dried. Yield: 0.6451 g, 81%. ^{1}H NMR (400 MHz, CDCl$_3$) δ 8.56 (d, *J* = 23.6 Hz, 2H), 7.68 – 7.43 (m, 20H), 6.82 (s, 4H), 2.22 (s, 6H), 2.03 (s, 12H), 1.79 (s, 12H-metal coordinated MeCN). ^{31}P{^{1}H} NMR (400 MHz, CDCl$_3$) δ -3.22 (s), -145.89 (sept, PF$_6$). Anal. Cacld. for C$_{48}$H$_{50}$Cu$_2$F$_{12}$N$_4$P$_4$: C, 49.62; H, 4.34; N, 4.82. Found: C, 50.09; H, 4.57; N, 4.72.

Synthesis of Cu$_2$(2-(diphenylphosphanyl)pyrrolide)$_2$ (q')

A solution of lithium 2-(diphenylphosphanyl)pyrrolide (**q**) (0.1000 g, 0.39 mmol) in THF (~3 mL) was added dropwise to a suspension of Cu(MeCN)$_4$PF$_6$ (0.1449 g, 0.39 mmol) in THF (~6 mL). Resulting pale orange color solution became cloudy over time. Reaction mixture was stirred at room temperature overnight and filtered to collect the title compound as a white solid. It was washed with THF (2×2 mL) and Et$_2$O (2×3 mL) and vacuum dried. Title

compound has poor solubility in common organic solvents but significantly dissolves in MeCN. Yield: 0.1712 g, 62 %. X-ray quality crystals were grown using a saturated solution of (**q'**) in MeCN at RT. ^{1}H NMR (400 MHz, CD$_3$CN) δ 7.39 – 7.25 (m, 20H), 7.06 (s, 2H), 6.23 (dd, J = 3.4, 2.0 Hz, 2H), 6.15 (d, J = 2.2 Hz, 2H), 2.12 (s, coordinated CH$_3$CN). ^{31}P{^{1}H} NMR (400 MHz, CD$_3$CN) δ -14.24. Anal. Calcd. for (C$_{36}$H$_{32}$Cu$_2$N$_4$P$_2$**.** (1.4 MeCN): C, 61.01; H, 4.44; N, 6.95. Found: C, 58.78; H, 4.44; N, 6.77. Repeated attempts gave consistent low %C values, possibly due to variability in solvent coordination.

Synthesis of Cu$_2$(dppf)$_3$(PF$_6$)$_2$ (3) and Cu$_{12}$(μ_4-S$_6$)(dppf)$_4$ (4)

[Cu(dppf)(MeCN)$_2$]PF$_6$ (0.5418 g, 0.640 mmol) was dissolved in DCM (8 mL) and a solution of Na$_2$S (0.0125 g, 0.160 mmol) in MeOH (5 mL) was added dropwise. Resulting reddish orange mixture was stirred overnight and filtered through a fine frit to collect **4** as a reddish solid. It was washed with Et$_2$O (2×5 mL) and vacuum dried. Yield: 0.0642 g. ^{1}H and ^{31}P{^{1}H} NMR in CDCl$_3$ was similar to the reported values[33]. X-ray quality crystals were grown overnight at room temperature using a saturated solution of **4** in CDCl$_3$. The filtrate was added with Et$_2$O (10 mL) to get a shiny yellow-orange precipitate. It was collected by vacuum filtration and the filtrate was reduced to half followed by addition of Et$_2$O (10 ML) to get a second crop. Two crops were combined and washed with Et$_2$O (2×5 mL) and vacuum dried to afford **3** as a yellow-orange powder. Yield: 0.1983 g. ^{1}H NMR (400 MHz, CDCl$_3$) δ 7.47 – 7.15 (m, 60H), 4.25 (s, 12H), 4.04 (s, 12H), 3.74 (t, THF), 1.85 (q, THF). ^{31}P{^{1}H} NMR (400 MHz, CDCl$_3$) δ -10.35 (brs), -145.79 (sept, PF$_6$). X-ray quality crystals were grown by diffusion of Et$_2$O into a solution of **3** in DCM at room temperature.

Synthesis of Cu$_4$(*N*-((diphenylphosphanyl)methyl)-*N*-ethylethanamine)$_2$Cl$_4$ (5)

N-((diphenylphosphanyl)methyl)-*N*-ethylethanamine[41] (**b**) (0.3369 g, 1.24 mmol) in THF (~2 mL) was added to a suspension of CuCl (0.2458 g, 2.48 mmol) in THF (~12 mL) and the mixture was stirred at room temperature for 24 hours. Next day, an off-white suspension was observed and it was filtered through a fine frit to collect the solid. The solid was washed with 2×5 mL of Et$_2$O and dried under vacuum to afford the title compound as an off-white solid. Yield: 0.35 g, 60 %. ^{1}H NMR (400 MHz, DMSO-*d$_6$*) δ 7.75 – 7.42 (m, 20H), 3.55 (d, J = 1.7 Hz, 4H), 2.69 (q, 8H), 3.32 (s, residual H$_2$O in DMSO-*d$_6$*), 0.91 (t, 12H). ^{31}P{^{1}H} NMR (400 MHz, DMSO-*d$_6$*) δ -19.27. Anal. Calcd. for C$_{34}$H$_{44}$Cl$_4$Cu$_4$N$_2$P$_2$·1.4CuCl: C, 37.91; H, 4.12; N, 2.60. Found: C, 37.76; H, 4.22; N, 2.48. Despite attempted

purifications indicated above, unreacted CuCl (reproducibly 1.4 equiv.) was seen consistently in elemental analysis results.

Synthesis of Cu$_4$(μ$_4$-S)(2,6-dimethylformamidinate)$_4$ (6h)

Inside a N$_2$ filled glove box a solution of S$_8$ (0.0204 g, 0.64 mmol) in toluene (~2 mL) was added dropwise to a solution of Cu$_2$(2,6-dimethylformamidinate)$_2$ (**h'**) (0.8000 g, 1.27 mmol) in THF (~10 mL) in a Schlenk flask (50 mL). Resulting purple reaction mixture was taken out and connected to a N$_2$ Schlenk line. After purging the connecting tube, the flask was open to N$_2$ and the mixture was heated at 50 °C for 3 days under N$_2$. At the end, the reaction mixture appeared to be dark color with a purple tint. Flask was pumped back to the glove box and the solvent was completely evaporated leaving a dark solid. DCM (~2 mL) was added to the residue and mixed well to get a uniform suspension. It was filtered through a medium frit and the dark residue on the frit was washed with DCM (2×1 mL), MeCN (2×2 mL), Et$_2$O (3×2 mL) and dried under vacuum to afford the title compound as a dark solid (intense purple in solution). Yield: 0.4340 g, 53 %. ^{1}H NMR (400 MHz, C$_6$D$_6$) δ 6.92 (d, J = 7.1 Hz, 8H), 6.82 (t, J = 7.5 Hz, 8H), 6.59 (dd, J = 17.3, 7.5 Hz, 8H), 6.34 (s, 2H), 5.75 (s, 2H), 2.94 (s, 12H), 2.79 (s, 12H), 1.51 (s, 12H), 1.41 (s, 12H). Anal. Calcd. for C$_{68}$H$_{76}$Cu$_4$N$_8$S$_1$: C, 63.32; H, 5.93; N, 8.68. Found: C, 62.37; H, 5.96; N, 8.26.

Synthesis of [Cu$_4$(μ$_4$-S)(2,6-dimethylformamidinate)$_4$] [K(18-crown-6)] (7h)

K(18-crown-6)Fp (0.6096 g, 0.82 mmol) was added as solid portions to a solution of **6h** (0.9600 g, 0.74 mmol) in toluene (50 mL). Resulting mixture was stirred at room temperature overnight and filtered off to get a deep blue residue. It was washed with toluene (2×5 mL), Et$_2$O (4×5 mL) and vacuum dried to afford the title compound as a deep blue solid. Yield: 0.5671 g, 48 %. (^{1}H NMR (400 MHz, Acetone-d$_6$) δ 3.63 (s, 18-crown-6 -CH2-). Repeated attempts at combustion analysis consistently yielded low %C, %H and %N percentage values indicating incomplete combustion, similar to our previously reported 1-hole **7c**.[32] For X-ray quality crystals, the 18-crown-6 was exchanged with excess 2,2,2-cryptand and a solution of (**7h**) in THF was layered with pentane at -25°C.

Synthesis of Cu$_4$(*N,N′*-bis(4-(trifluoromethyl)phenyl)formamidinate)$_4$ (8)

Separate solutions of *N,N′*-bis(4-(trifluoromethyl)phenyl)formamidinate[42] (**d**) (0.8916 g, 2.68 mmol) in THF (~10 mL) and NaHMDS (0.5413 g, 2.95 mmol) in THF (~6 mL) were kept in freezer for 15 min. Cold solution of NaHMDS was added to cold solution of (**d**) and the resulting bright yellow solution was allowed to reach room

temperature for 1 hour. Cu(MeCN)$_4$PF$_6$ (1.0002 g, 2.68 mmol) was added as a solid (solution became cloudy lime green) and the reaction mixture was stirred at room temperature overnight. Then the solvent was completely evaporated the greenish residue was reconstituted in DCM and filtered through a pad of Celite (any remaining greenish residue on Celite was wash into the filtrate with more DCM). Filtrate was concentrated under vacuum and kept in freezer for 30 min. Resulting greenish solid was collected by filtration (while cold), washed with pentane (2×5 mL) and vacuum dried to afford the title compound as a greenish solid. Yield: 0.4222 g, 40 %. ^{1}H NMR (400 MHz, CD$_2$Cl$_2$) δ 8.21 (s, 4H), 7.35 (s, 8H), 7.33 (s, 8H), 7.02 (s, 8H), 7.00 (s, 8H). ^{19}F{^{1}H} NMR (400 MHz, CD$_2$Cl$_2$) δ -62.87 (s, -CF$_3$). Anal. Calcd. for C$_{60}$H$_{36}$Cu$_4$N$_8$F$_{24}$: C, 45.64; H, 2.30; N, 7.10. Found: C, 43.95; H, 2.43; N, 6.25.

Synthesis of N-((mesitylphosphanylidene)(phenyl)methyl)-2,4,6-trimethylaniline (n)
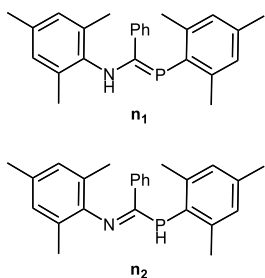
A solution of 2,4,6-trimethylphenylphosphane (0.2500 g, 1.64 mmol) in DCM (2 mL) was drop wisely added to a suspension of *N*-benzylidyne-2,4,6-trimethylbenzenaminium trifluoromethanesulfonate (0.6101 g, 1.64 mmol) in DCM (2.5 mL) at -78 ºC. The reaction mixture was stirred for 10 min at -78 ºC and the cooling bath was removed. The mixture was further stirred for 30 min, while allowing it to warm up to the room temperature. Triethylamine (252 µL, 1.80 mmol) was added and the color of the solution changed from red-orange to yellow. The mixture was stirred for 15 min and volatiles were removed under vacuum leaving yellow-orange oily residue. It was purified (under normal atmosphere) by filtering over a pad of neutral, activated alumina eluting with pentane. Volatiles were removed under vacuum leaving (**n**) as a yellow solid. The gram scale synthesis gave (**1**) as a yellow sticky product which solidified in weeks. Reaction conditions yield (**n**) as a mixture of (**n$_1$**) ~ 80% and (**n$_2$**) ~ 20%. Total yield: 0.3506 g, 72 %. ^{1}H NMR of (**n$_1$**) (500 MHz, CDCl$_3$) δ 7.34 (d, *J* = 8.2 Hz, 2H), 7.21 (t, *J* = 7.3 Hz, 1H), 7.14 (t, *J* = 7.5 Hz, 2H), 6.99 (s, 2H), 6.67 (s, 2H), 6.17 (s, 1H), 2.59 (s, 6H), 2.29 (s, 3H), 2.15 (s, 3H), 2.04 (s, 6H). ^{31}P NMR of (**n$_1$**) (162 MHz, CDCl$_3$) δ 61.74 (s), (**n$_2$**) (162 MHz, CDCl$_3$) -74.51 (d, *J* = 241.1 Hz). m/z theoretical: 373.20, 374.20, 375.20. Found 374.3, 375.3, 376.3

Synthesis of bis(tetrahydrofuran)lithium mesityl((mesitylphosphanylidene)(phenyl)methyl)amide (o)
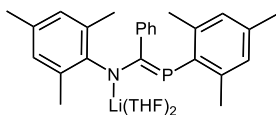
n-butyllithium (12.5 mL of 1.6 M in hexanes, 19.9 mmol) was drop wisely added to a solution of **(n)** (4.9544 g, 16.6 mmol) in THF (25 mL) at -78 °C. The color of the mixture was changed from yellow to orange to dark brown. Resulted mixture was allowed to warm up to room temperature and stirred for further 10 min. The volatiles were removed under vacuum leaving a brown residue, which was dissolved in a minimum amount of THF and kept at -20 °C to afford **(o)** as an orange solid. It was filtered and washed with cold pentane. The filtrate was completely evaporated and re-dissolved in minimum amount of THF and kept at -20 °C to afford a second crop. A third crop was obtained in a similar way. Total yield: 5.3342 g, 61 %. ^{1}H NMR (400 MHz, THF-d8) δ 7.21 – 7.12 (m, 2H), 6.86 – 6.79 (m, 3H), 6.75 (s, 2H), 6.41 (s, 2H), 3.64 – 3.59 (m, 4H; THF), 2.40 (s, 6H), 2.28 (s, 6H), 2.21 (s, 3H), 1.99 (s, 3H), 1.79 – 1.74 (m, 4H; THF). ^{31}P NMR (162 MHz, THF-d8) δ 25.55 (s).

Synthesis of Cu$_6$[mes-NC(Ph)=P-mes]$_3$Cl$_4$Li$_1$(THF)$_2$ (9)

A solution of **(o)** (0.1014 g, 0.19 mmol) in THF (3 mL) was drop wisely added to a suspension of CuCl (0.0575 g, 0.58 mmol) in THF (5 mL) over 10 min. The reaction mixture immediately changed to yellow and to cloudy orange at the end of the slow addition. It was stirred at room temperature for 1 hr and filtered through a pad of celite. The filtrate was completely evaporated leaving a yellow solid. It was added with DCM (6 mL) and filtered through a pad of celite to remove insoluble LiCl. The celite pad was washed with DCM (1 mL × 2). The filtrate was completely evaporated leaving **9** as a yellow-orange solid. Yield: 0.0890g, 77 %. X-ray quality crystals were grown by cooling a saturated solution of **9** in THF at -20 °C. ^{1}H NMR (400 MHz, CDCl$_3$) δ 6.97 (s, 2H), 6.82 (t, *J* = 7.2 Hz, 1H), 6.75 (t, *J* = 7.5 Hz, 2H), 6.65 (s, 1H), 6.62 (s, 1H), 5.86 (s, 1H), 5.62 (s, 1H), 3.77 (s, 4H; THF), 3.03 (s, 3H), 2.60 (s, 3H), 1.99 (s, 3H), 1.98 (s, 3H), 1.97 (s, 3H), 1.86 (s, 8H; THF), 1.19 (s, 3H). ^{31}P NMR (162 MHz, CDCl$_3$) δ -61.95 (s). Anal. calcd. For C$_{83}$H$_{97}$Cu$_6$Cl$_4$LiO$_2$P$_3$: C, 55.64; H, 5.46; N, 2.35. Found: C, 54.92; H, 5.12; N, 2.04. (The error of %C was greater than the limit of satisfactory due to the solvent coordination).

Synthesis of *N*-((mesitylphosphanylidene)methyl)-2,4,6-trimethylaniline (p)
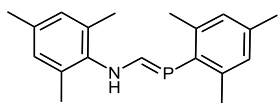
n-Butyllithium (1.6 M solution in hexane, 4.9 mL, 7.86 mmol) was drop wisely added over 15 min to a solution of 2,4,6-trimethylphenylphosphane (1.0000 g, 6.57 mmol) in Et$_2$O (45 mL) at -78 ºC. Resulted mixture was stirred for 30 min at the same temperature, followed by another 30 min outside the cold well allowing it to warm up to room temperature to afford lithium 2,4,6-trimethylphenylhydrophosphanide as a yellow cloudy solution. It was drop wisely added over 30 min to a solution of ethyl *N*-mesitylformimidate (1.2569 g, 6.57 mmol) in Et$_2$O (10 mL) at -78 ºC. Resulted mixture was stirred for 30 min at the same temperature and allowed to warm up to room temperature overnight. Resulted yellow solution was added with solid NH$_4$Cl (0.3515 g, 6.57 mmol) and stirred for 30 min and then filtered through a pad of celite to remove the insoluble LiCl. The filtrate was completely evaporated leaving a yellow solid which was added with pentane (20 – 25 mL) and filtered off using a coarse frit and washed with pentane (2 mL × 6) to afford **(p)** as a yellow-green solid. (If any unreacted ethyl N-mesitylformimidate or 2,4,6-trimethylphenylphosphane present, the yellow solid which is resulted by completely evaporating the filtrate, will appear as wet and sticky. In that case, washing with pentane will remove the any unreacted materials and the byproducts, leaving **(p)** as a dry solid). Yield: 1.0161 g, 52 %. ^{1}H NMR (400 MHz, C$_6$D$_6$) δ 7.63 (dd, *J* = 44.1, 13.9 Hz, 1H), 6.88 (s, 2H), 6.54 (s, 2H), 2.61 (s, 6H), 2.15 (s, 3H), 2.05 (s, 3H), 1.89 (s, 6H). ^{31}P NMR (162 MHz, C$_6$D$_6$) δ 54.43 (d, *J* = 44.2 Hz). m/ z theoretical: 297.16, 298.17, 299.17. Found: 298.4,299.4, 300.4.

Synthesis of Cu$_4$[mes-NCH=P-mes]$_4$ using Misitylcopper (10)

A solution of mesitylcopper (0.1342 g, 0.73 mmol) in Et$_2$O (11 mL) was drop wisely added over 20 min to a solution of **(p)** (0.2184 g, 0.73 mmol) in Et$_2$O (12 mL). The reaction mixture was well capped and stirred at 40 ºC for 3 hrs. The ^{31}P nmr of an aliquot showed the complete consumption of **(p)** giving rise to multiplets around -55 to -80 ppm. The reaction mixture was further stirred for 8 days at 40 ºC resulting a yellow precipitate. The precipitate was collected by filtration and re-dissolved in benzene and filtered off through a pad of celite to remove a brown color by product (possibly decomposed Cu from Cu-mes). Resulted yellow-orange filtrate was completely evaporated leaving **10** as a yellow-orange solid. Yield: 0.1728 g, 65 %. ^{1}H NMR (400 MHz, C$_6$D$_6$) δ 8.38 (s, 1H), 6.87 (s, 1H), 6.84 (s, 1H), 6.78 (s, 1H), 6.55 (s, 1H), 2.92 (s, 3H), 2.53 (s, 3H), 2.50 (s, 3H), 2.17 (s, 3H), 2.08 (s, 3H), 1.53 (s, 3H). ^{31}P

NMR (162 MHz, C_6D_6) δ -74.39 (s). Anal. calcd. For $C_{76}H_{92}Cu_4N_4P_4$: C, 63.41; H, 6.44; N, 3.89. Found: C, 61.53; H, 6.32; N, 3.60. (Repeated attempts gave consistent results implying incomplete combustion)

Synthesis of complex 10 using Cu(MeCN)$_4$PF$_6$ (p)

(0.1771 g, 5.96 mmol) and NaHMDS (0.1201 g, 6.55 mmol) were mixed in Et_2O (8 mL) and stirred for 1 hr at room temperature. Cu(MeCN)$_4$PF$_6$ (0.2220 g, 5.96 mmol) was added as a solid to the reaction mixture. It was crushed using a glass rod, while it is inside the reaction mixture, as the solubility of Cu(MeCN)$_4$PF$_6$ in Et_2O is poor. Immediate formation of an orange solid was seen. Reaction mixture was further stirred at room temperature for 3 hrs and filtered off to get an orange solid which was washed with pentane (2 mL × 3). This solid was re-dissolved in benzene (15 mL) and stirred for 10-15 min. Then it was filtered through a pad of celite and the celite was washed with benzene (2 mL × 6). Filtrate was completely evaporated to afford **10** as an orange solid. X-ray quality crystals were grown by slow evaporation of a concentrated solution of **10** in 1:1 mixture of toluene and benzene. Yield: 0.1534 g, 72 %. ^{1}H NMR (400 MHz, C_6D_6) δ 8.38 (s, 1H), 6.87 (s, 1H), 6.84 (s, 1H), 6.78 (s, 1H), 6.55 (s, 1H), 2.92 (s, 3H), 2.53 (s, 3H), 2.50 (s, 3H), 2.17 (s, 3H), 2.08 (s, 3H), 1.53 (s, 3H). ^{31}P NMR (162 MHz, C_6D_6) δ -74.39 (s). Anal. calcd. For $C_{76}H_{92}Cu_4N_4P_4$: C, 63.41; H, 6.44; N, 3.89. Found: C, 61.04, H,6.30; N, 3.44. (Repeated attempts gave consistent results implying incomplete combustion)

5.1.4   Experimental spectra and relevant data tables

1H NMR (CDCl3, 400 MHz) (Ph2P-C=N-Mes) (a)
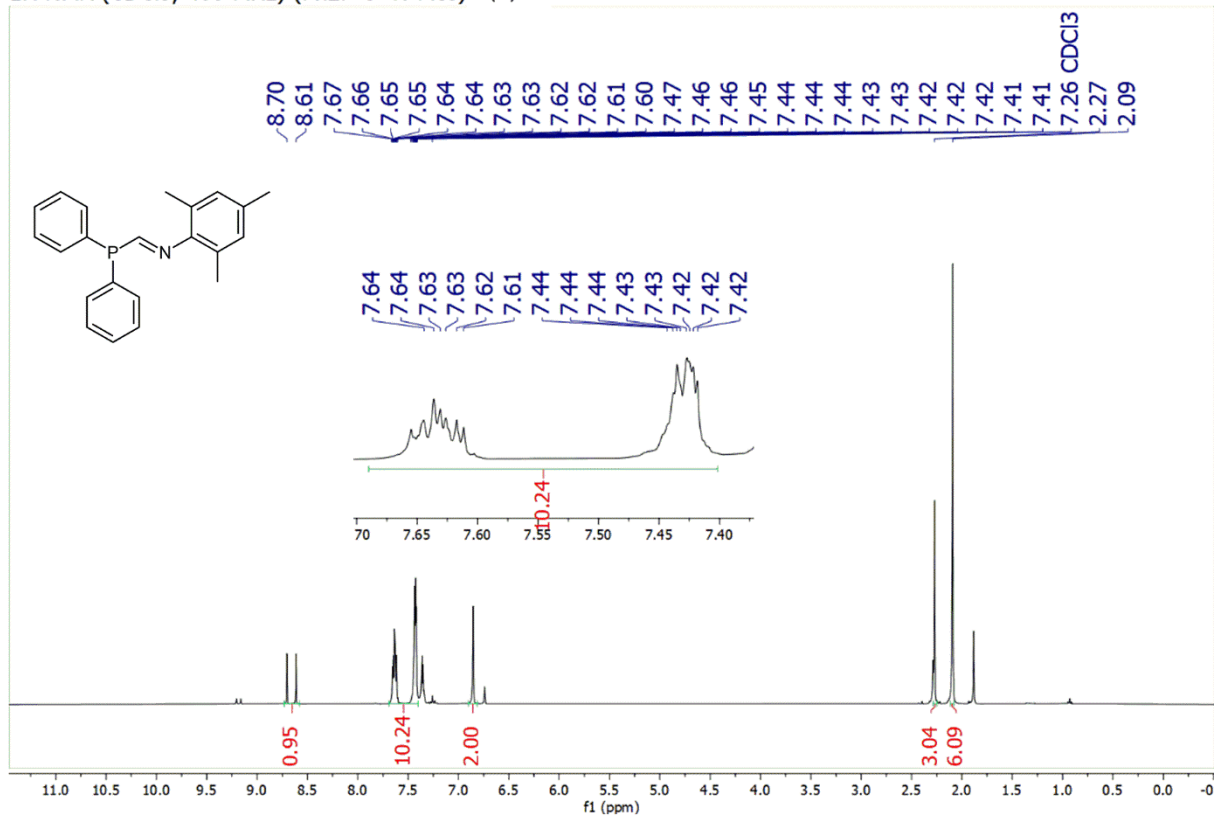
FIGURE S 1 ^{1}H NMR of (**a**). *E*-from ^{1}H NMR (400 MHz, CDCl3) δ 8.66 (d, *J* = 36.4 Hz, 1H), 7.69 – 7.39 (m, 10H), 6.85 (s, 2H), 2.27 (s, 3H), 2.09 (s, 6H). *Z*-from ^{1}H NMR (400 MHz, CDCl3) δ 9.18 (d, *J* = 17.3 Hz, 1H), 7.39 – 7.32 (m, 10H), 6.74 (s, 2H), 2.28 (s, 3H), 1.88 (s, 6H).

31P NMR (CDCl3, 400 MHz) (Ph2P-C=N-Mes)   (a)

−8.14
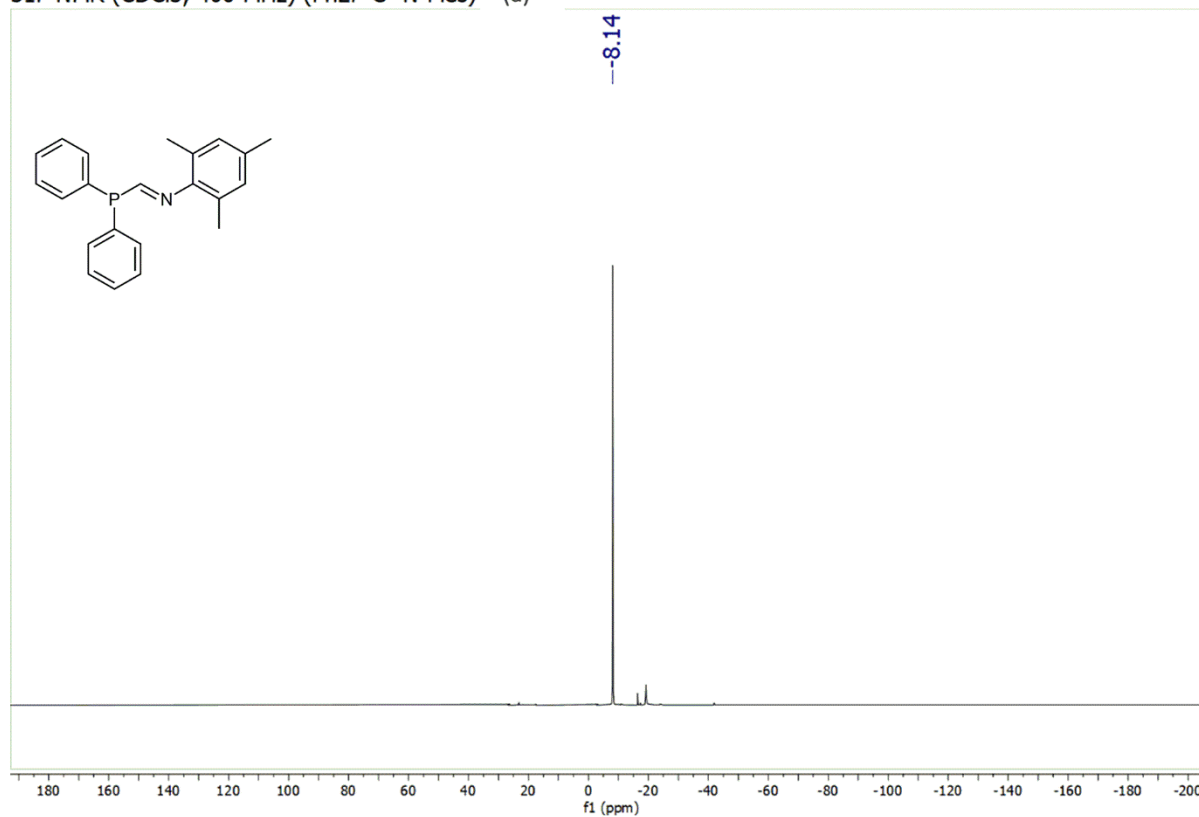
FIGURE S 2 ^{31}P{^{1}H} NMR of (**a**). ^{31}P{^{1}H} NMR (400 MHz, CDCl₃) δ -8.14.

1H NMR (CDCl3, 400 MHz) [Cu2(Ph2P-CH=NMes)2][(PF6)2]   (a')
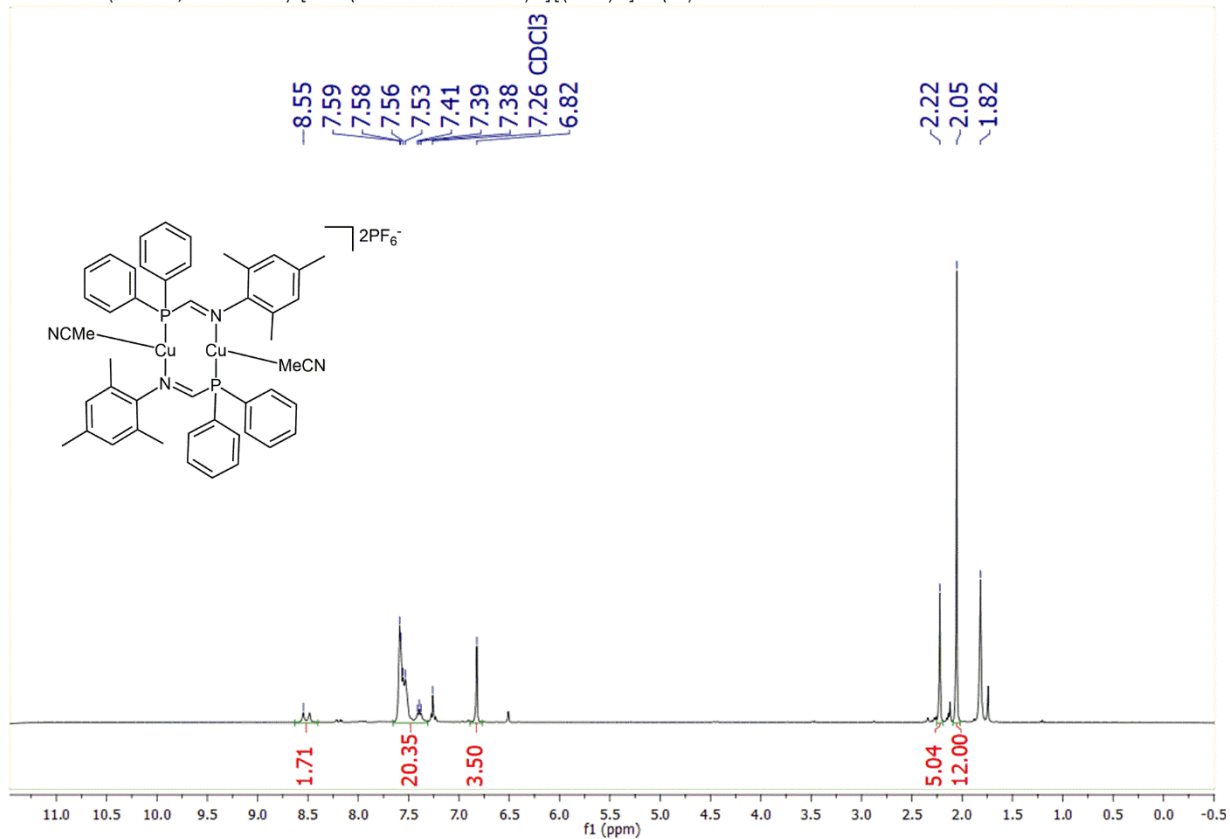
FIGURE S 3 ^{1}H NMR of Cu$_2$[Ph$_2$P(CH)=NMes]$_2$ (**a'**). ^{1}H NMR (400 MHz, CDCl$_3$) δ 8.55 (s, 2H), 7.65 – 7.31 (m, 20H), 6.82 (s, 4H), 2.22 (s, 6H), 2.05 (s, 12H), 1.82 (s, coordinated MeCN).

31P NMR (CDCl3, 400 MHz) [Cu2(Ph2P-CH=NMes)2][(PF6)2]   (a')
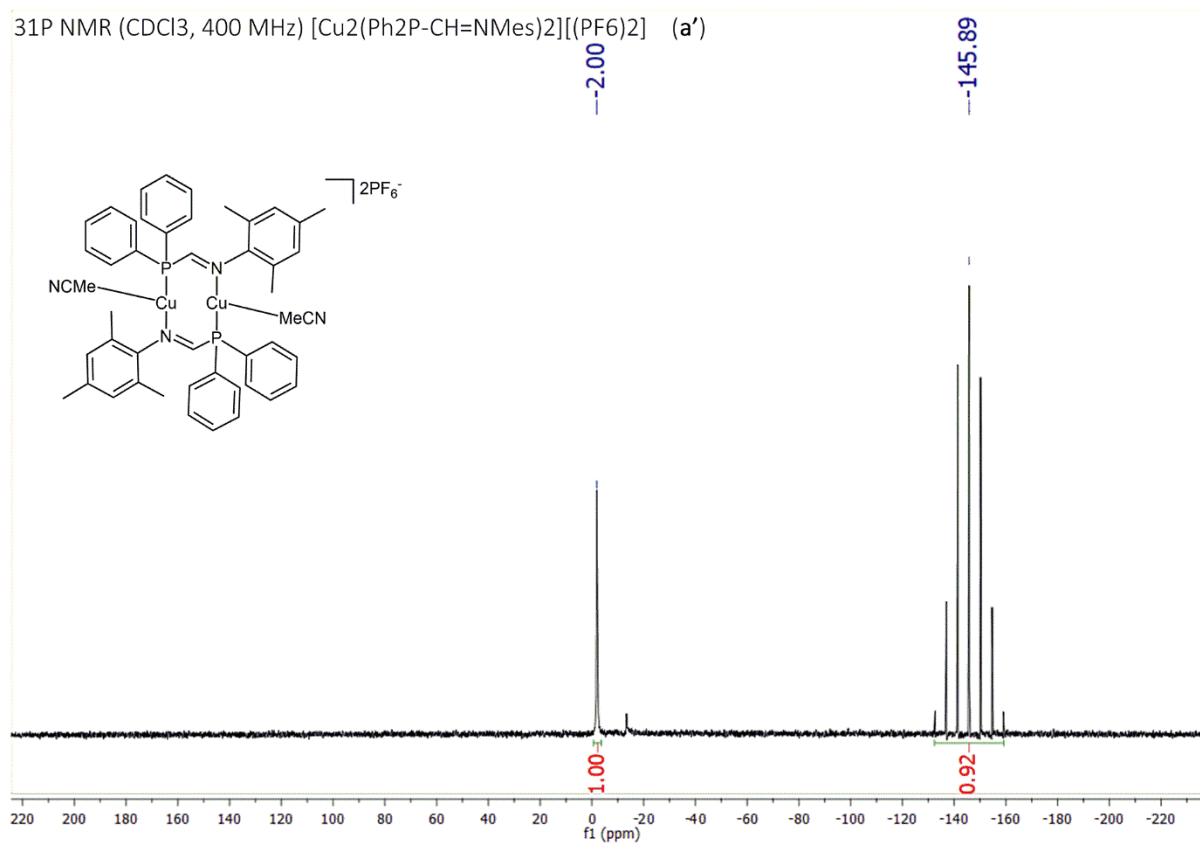
FIGURE S 4 ^{31}P{^{1}H} NMR of Cu$_2$[Ph$_2$P(CH)=NMes]$_2$ (**a'**). ^{31}P{^{1}H} NMR (400 MHz, CDCl$_3$) δ -2.00 (s), -145.89 (sept, PF$_6^-$).
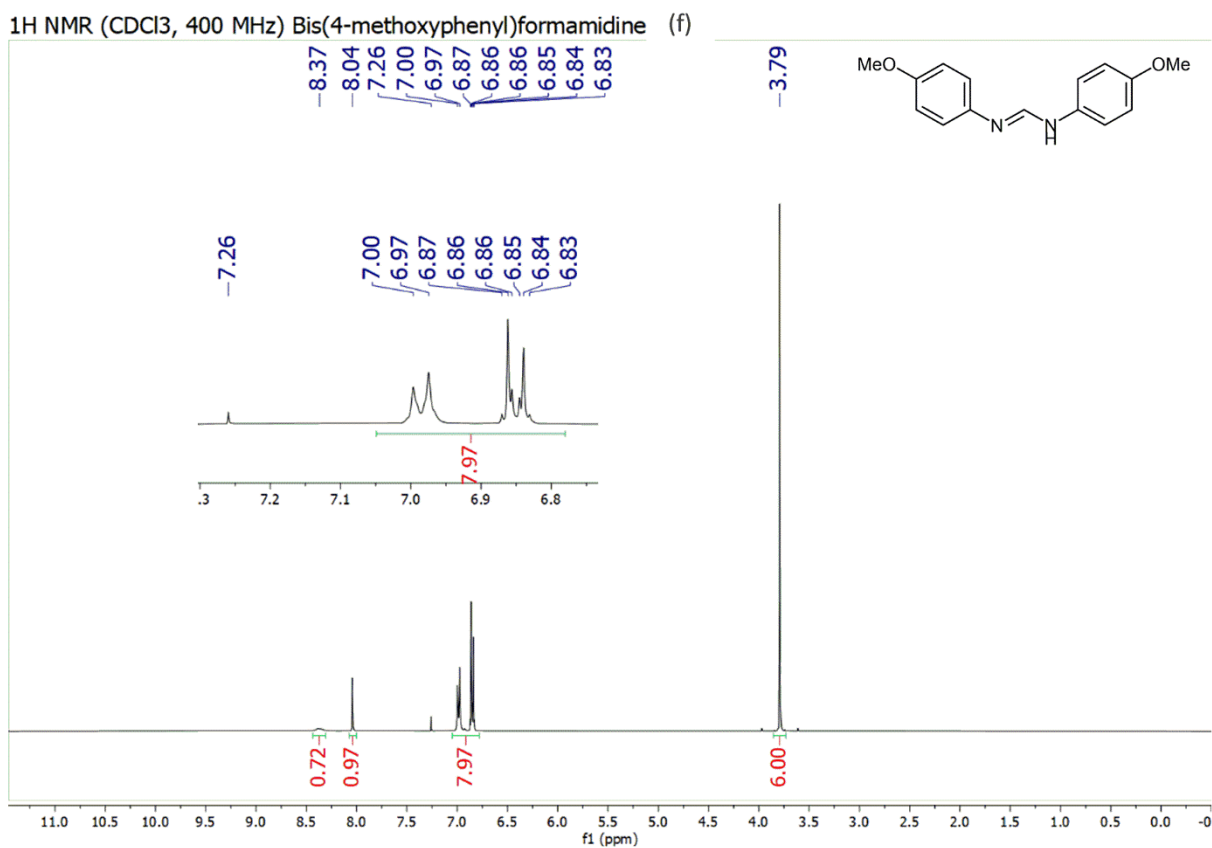
FIGURE S 5 ^{1}H NMR of bis(4-methoxyphenyl)formamidine (**f**). ^{1}H NMR (400 MHz, CDCl$_3$) δ 8.37 (s, 1H), 8.04 (s, 1H), 7.05 – 6.78 (m, 8H), 3.79 (s, 6H).

1H NMR (aceton-d6, 400 MHz) Bis(4-chlorophenyl) formamidine (g)
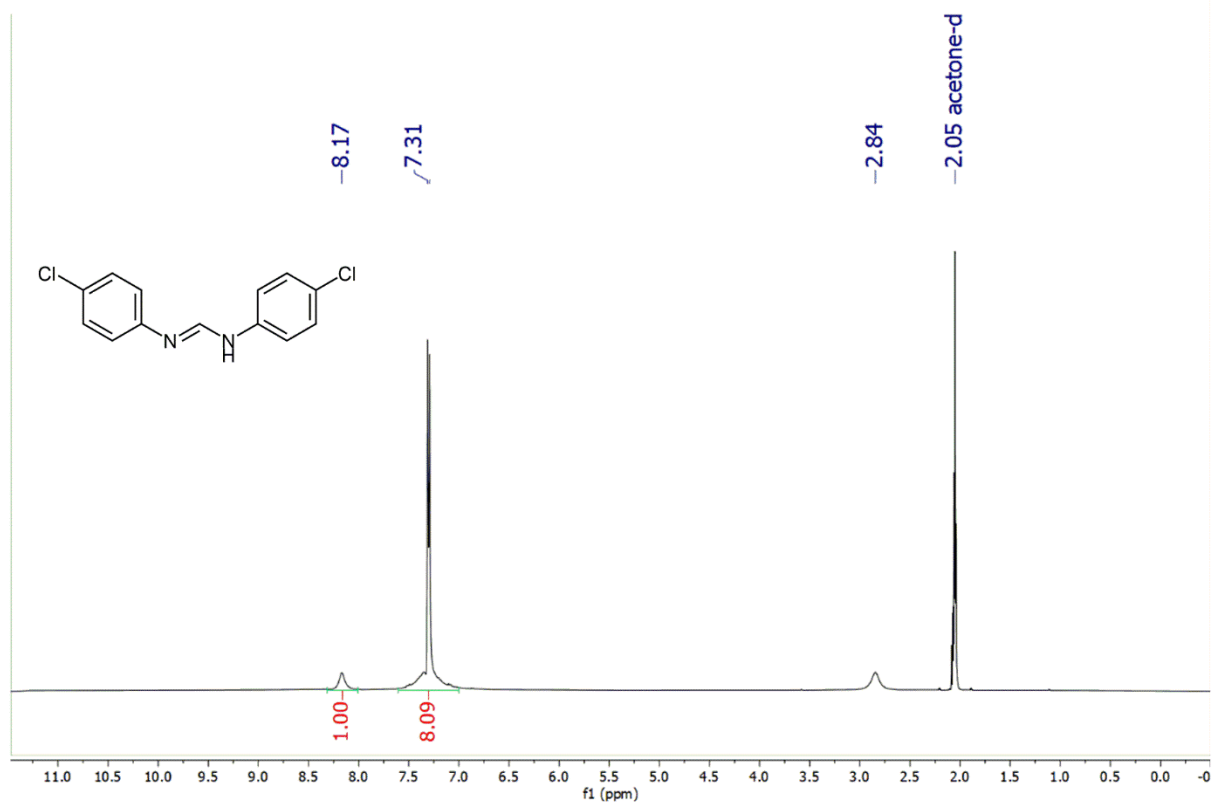
FIGURE S 6 ^{1}H NMR of bis(4-chlorophenyl)formamidine (**g**). ^{1}H NMR (400 MHz, CDCl$_3$) δ 8.17 (s, 1H), 7.31 (s, 8H), 2.84 (brs, residual H$_2$O).

1H NMR (CDCl3, 400 MHz) Bis(2,6-dimethylphenyl)formamidine (h)
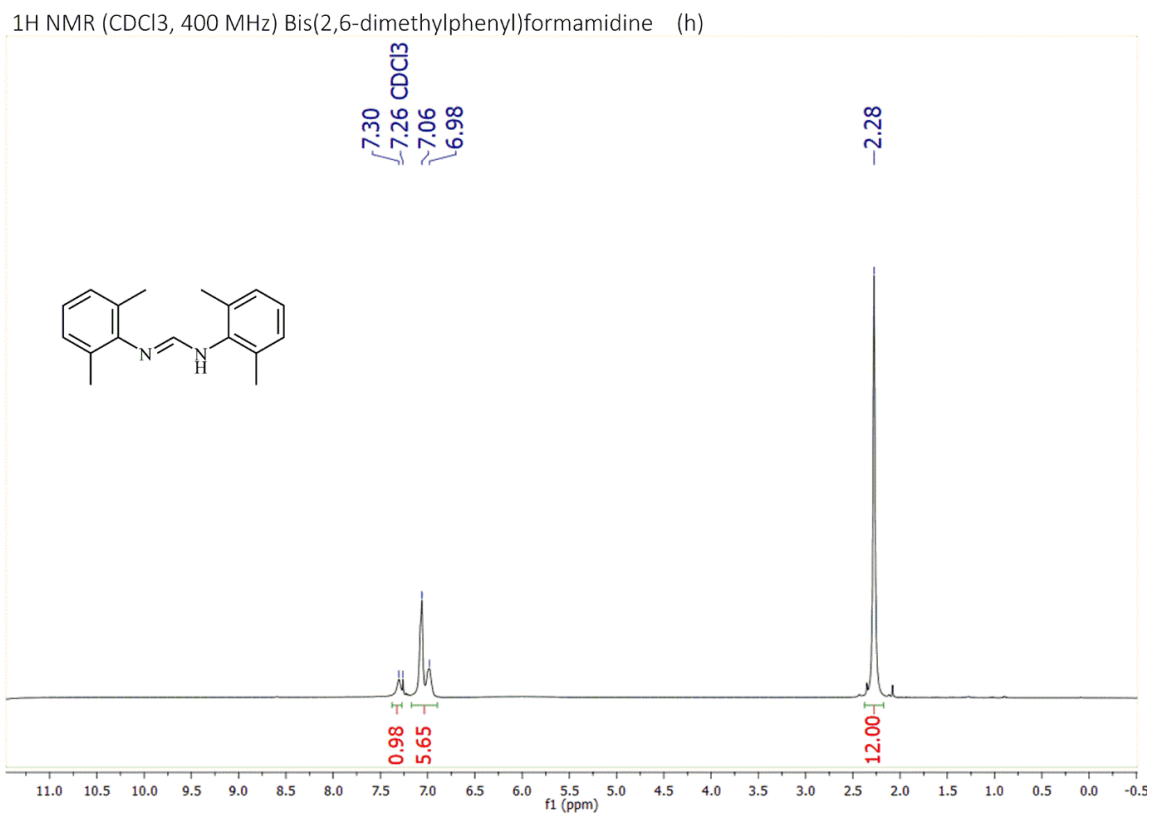
FIGURE S 7 [^1]H NMR of Bis(2,6-dimethylphenyl)formamidine (**h**). [^1]H NMR (400 MHz, CDCl$_3$) δ 7.30 (brs, 1H), 7.28 – 6.72 (m, 6H), 2.28 (s, 12H).
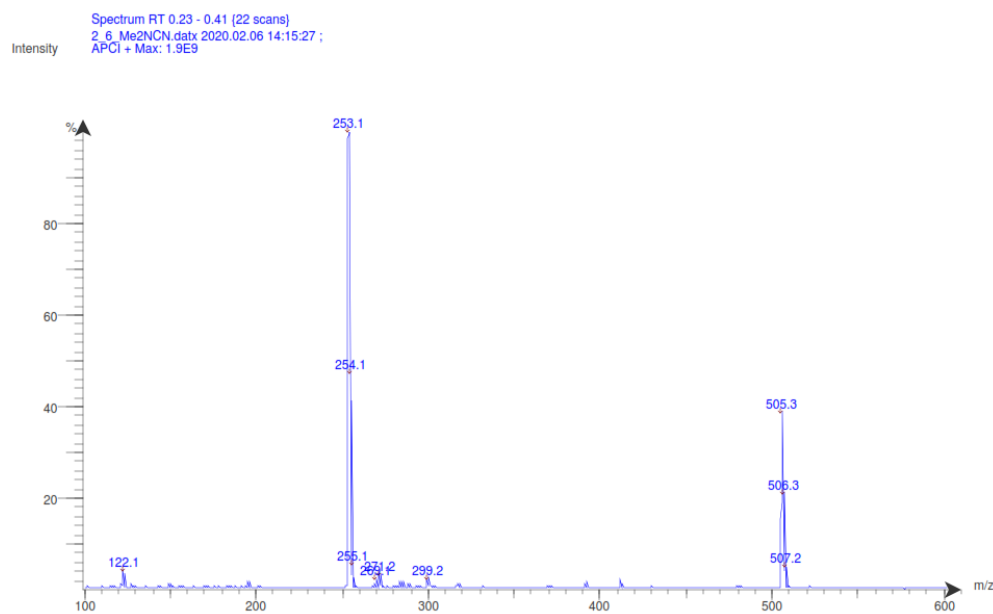
FIGURE S 8 APCI $^+$ mass spectrum of (**h**).

1H NMR (CDCl3, 400 MHz) Bis(4-chloro-2,6-dimethylphenyl)formamidine (i)
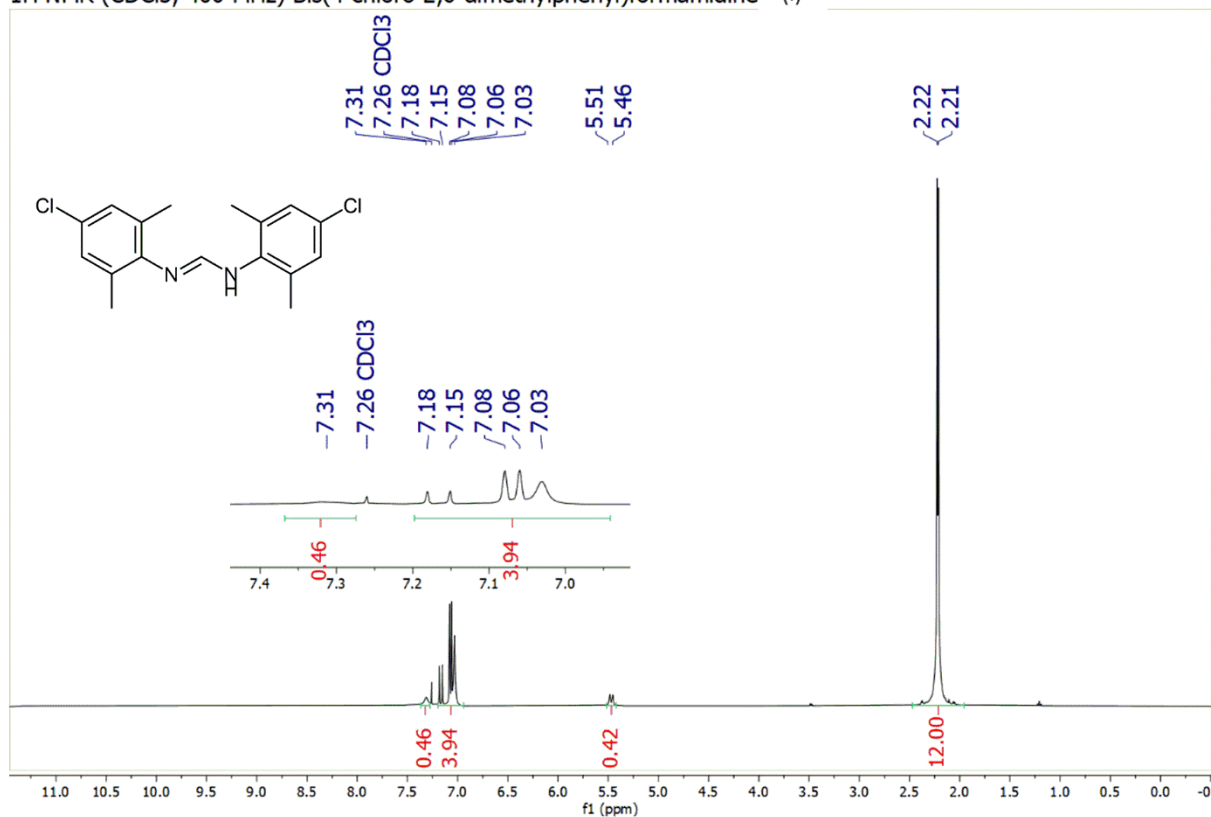
FIGURE S 9 ^{1}H NMR of bis(4-chloro-2,6-dimethylphenyl)formamidine (**i**). ^{1}H NMR (400 MHz, CDCl$_3$) δ 7.31 (brs, 1H), 7.20 – 6.98 (m, 4H), 2.22 (d, $J = 4.5$ Hz, 12H).

FIGURE S 10 APCI [+] mass spectrum of (**i**).

1H NMR (CDCl3, 400 MHz) Bis(4-methoxy-2-methylphenyl)formamidine (j)
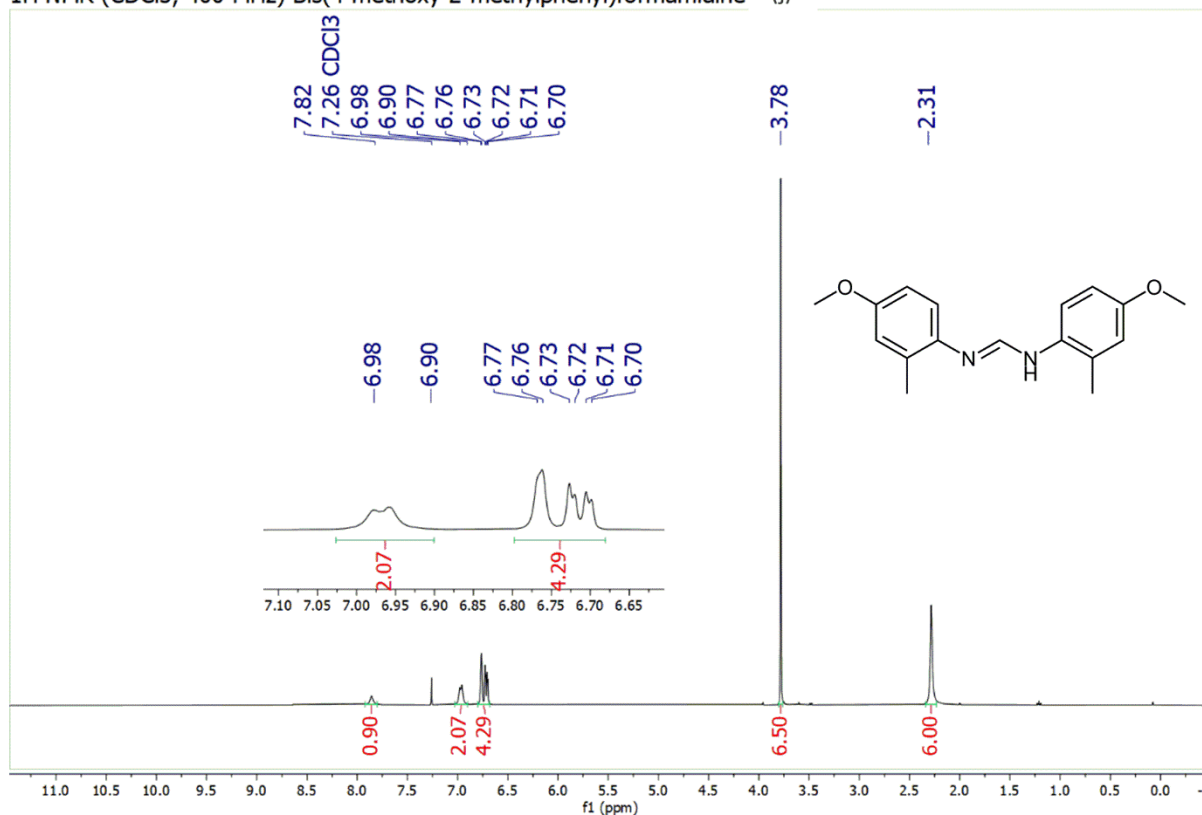
FIGURE S 11 ^{1}H NMR of bis(4-methoxy-2-methyphenyl)formamidine (**j**). ^{1}H NMR (400 MHz, CDCl$_3$) δ 7.82 (brs, 1H), 6.91 – 7.02 (m, 2H), 6.80 – 6.68 (m, 4H), 3.78 (s, 6H), 2.31 (s, 6H).

Spectrum RT 0.09 - 0.26 (44 scans) - Background Subtracted 0.01 - 0.07
Bis(4-methoxy-2-methylphenyl)formamidine.datx 2019.10.14 11:16:05 ;
APCI + Max: 1.7E8
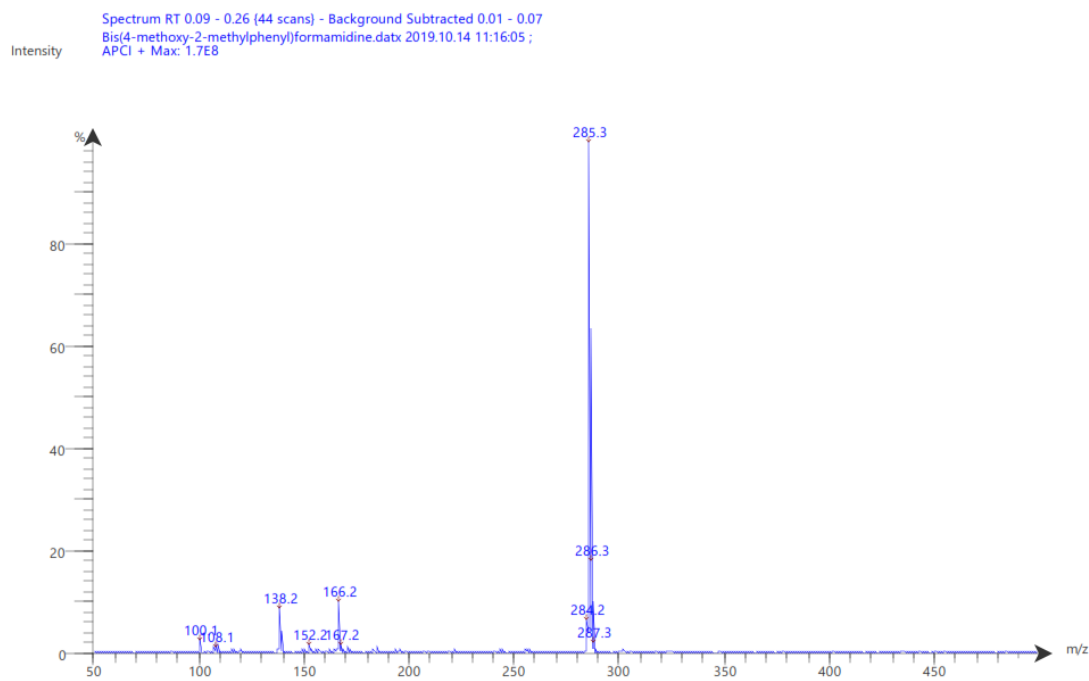
FIGURE S 12 APCI $^+$ mass spectrum of (**j**).

1H NMR (CDCl3, 400 MHz) Bis(2-methoxy-6-methylphenyl)formamidine (k)
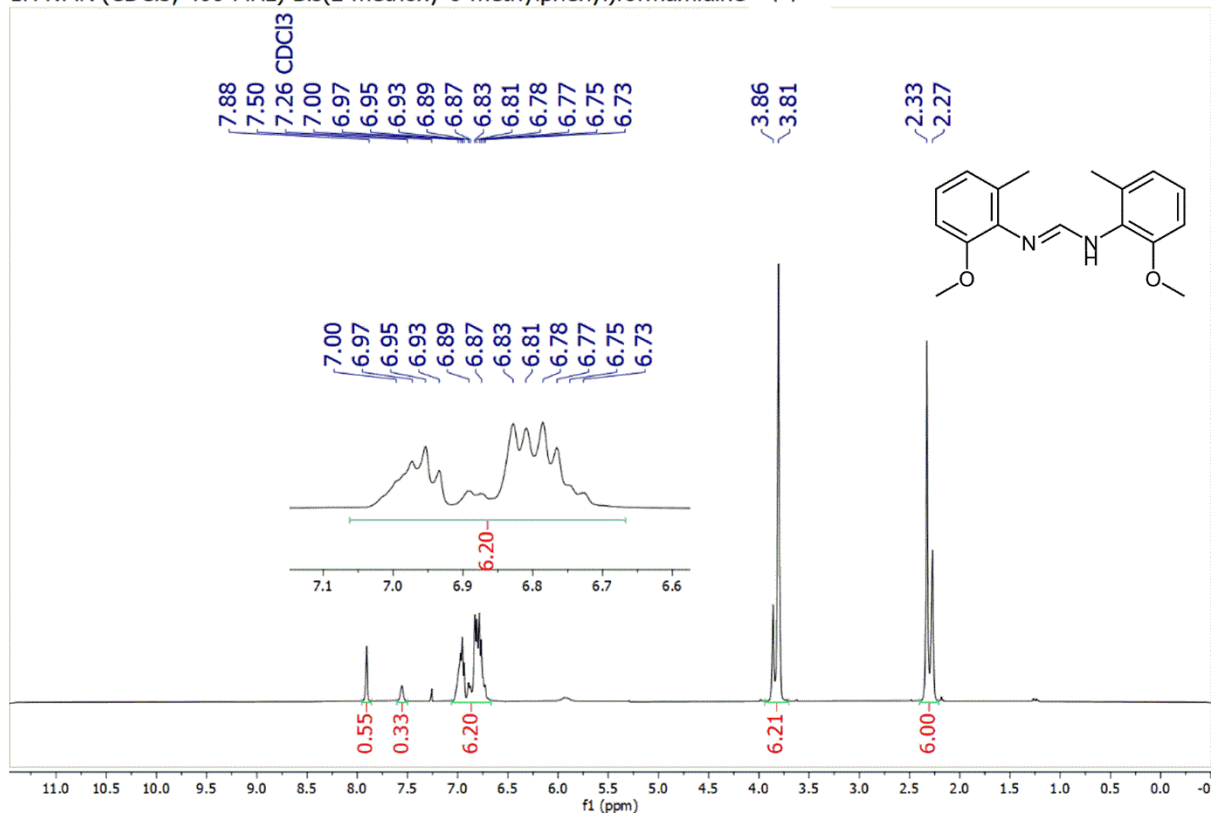
FIGURE S 13 ^{1}H NMR of bis(2-methoxy-6-methylphenyl)formamidine (**k**). ^{1}H NMR (400 MHz, CDCl₃) δ 7.88 (s, 1H), 7.56 (s, 1H), 7.04 – 6.70 (m, 6H), 3.90 – 3.70 (m, 6H), 2.37 – 2.22 (m, 6H).
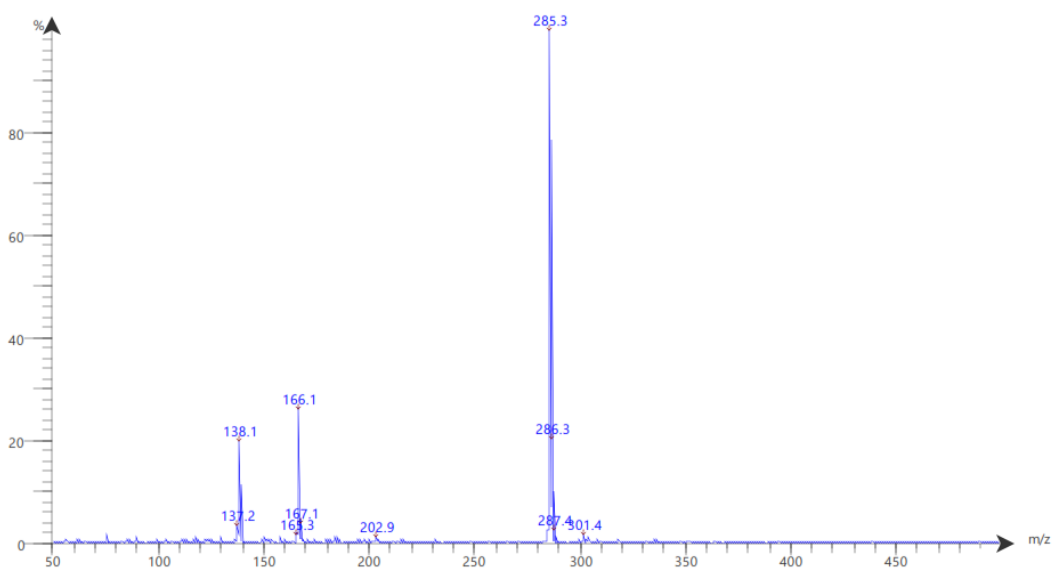
FIGURE S 14 APCI $^+$ mass spectrum of (**k**).

1H NMR (CDCl3, 400 MHz) Bis(2-chloro-6-methylphenyl)formamidine (l)
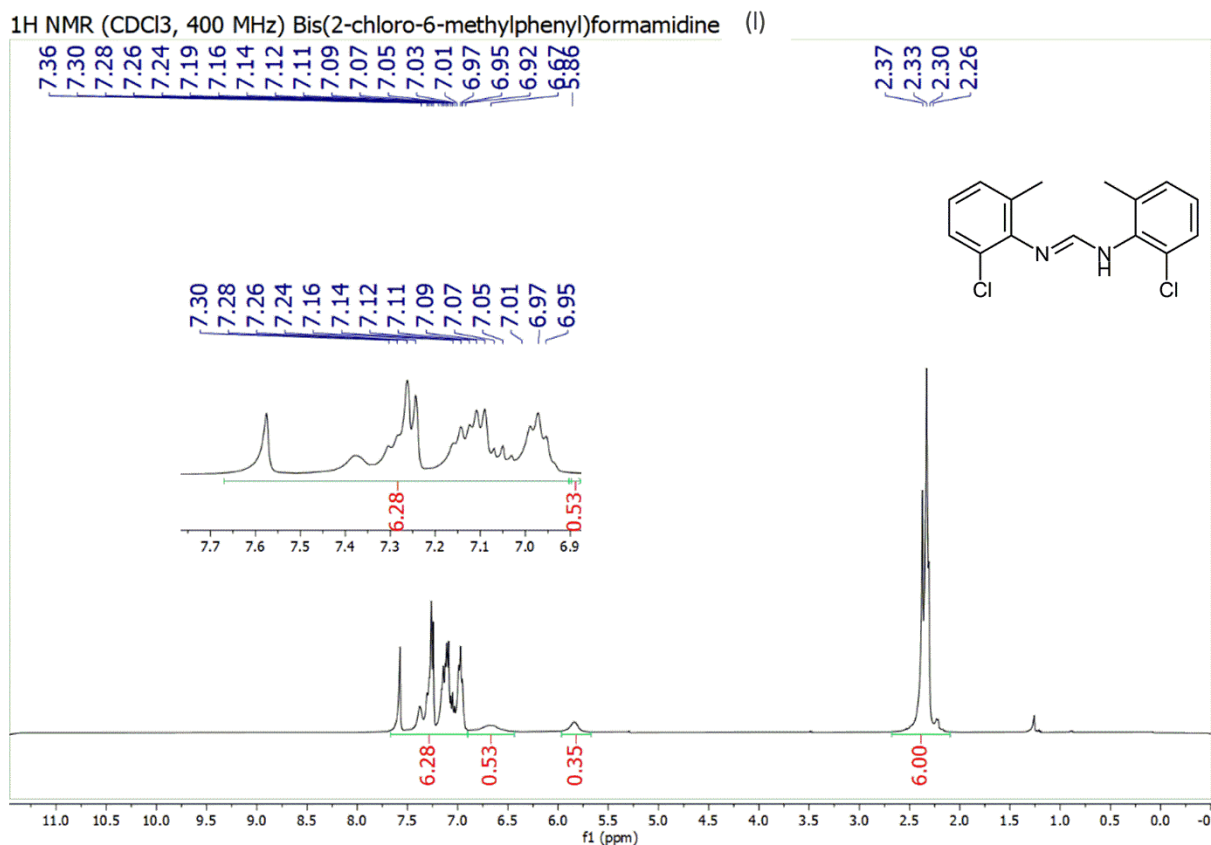
FIGURE S 15 ^{1}H NMR of bis(2-chloro-6-methylphenyl)formamidine (**l**). ^{1}H NMR (400 MHz, CDCl$_3$) δ 7.69 – 6.89 (m, 6H), 6.67 (brs, 1H), 5.86 (brs, 1H), 2.60 – 2.15 (m, 6H).

FIGURE S 16 APCI $^+$ mass spectrum of (**l**).

FIGURE S 17 ^{1}H NMR of bis(2,6-diisopropylphenyl)formamidine (**m**). ^{1}H NMR (400 MHz, CDCl$_3$) δ 7.29 – 7.01 (m, 6H), 5.55 (d, *J* = 11.9 Hz, 1H), 3.42 – 3.13 (m, 4H), 1.36 – 1.06 (m, 24H).
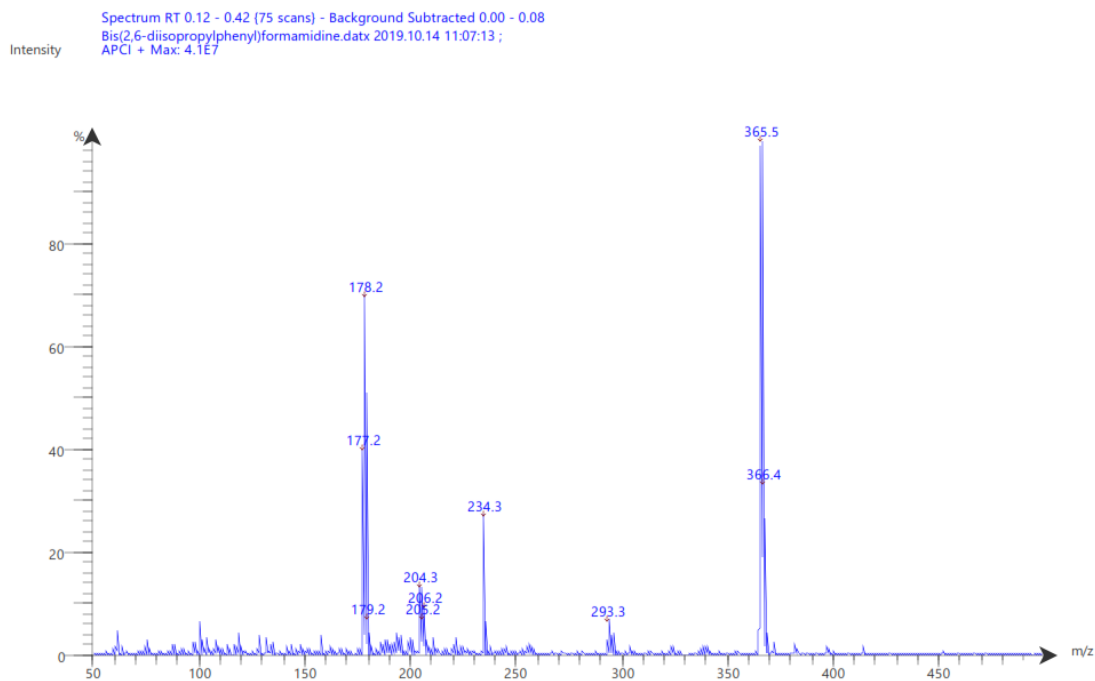
FIGURE S 18 APCI [+] mass spectrum of (**m**).

1H NMR (CDCl3, 400 MHz) [Cu2(Ph2P-CH=NMes)2][(PF6)2]   (h')
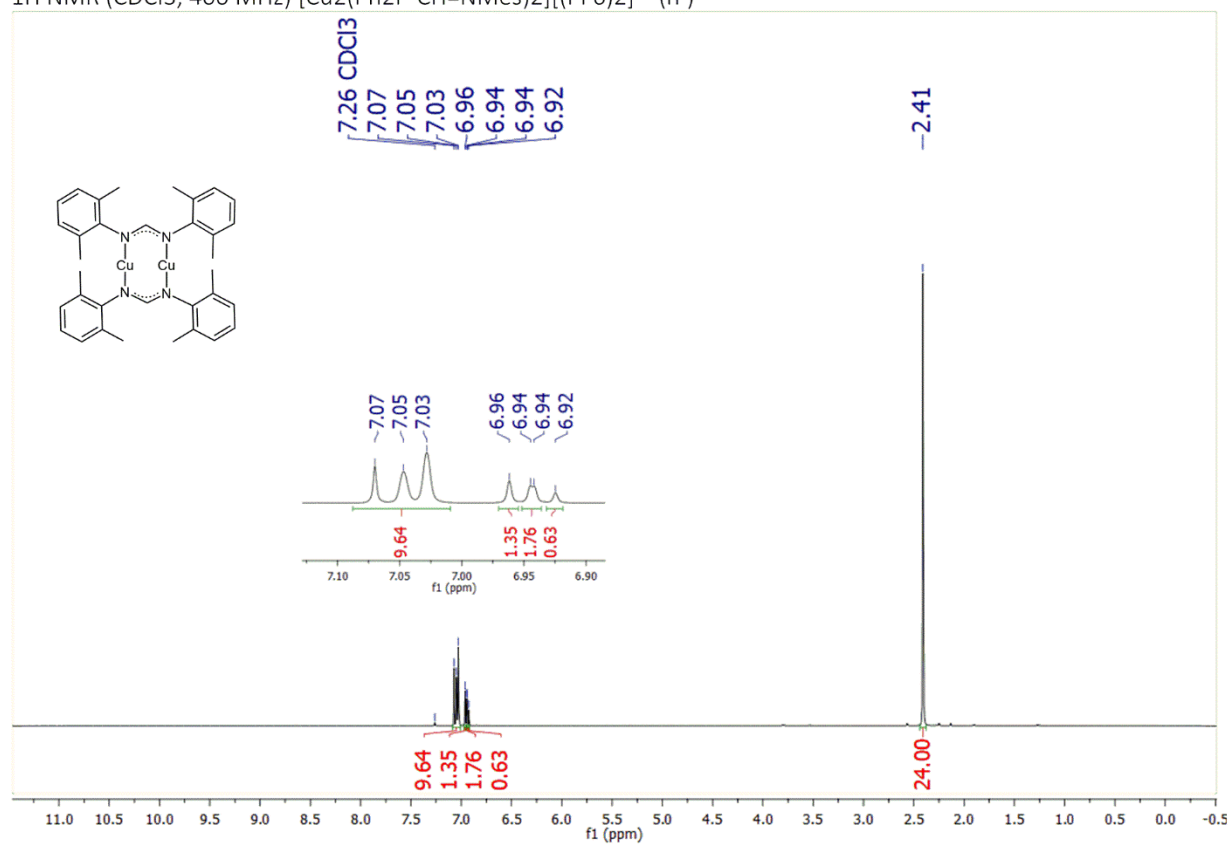
FIGURE S 19 ^{1}H NMR of Cu$_2$[Bis(2,6-dimethylphenyl)formamidinate]$_2$ (**h'**) ^{1}H NMR (400 MHz, CDCl$_3$) δ 7.09 – 7.01 (m, 10H), 6.96 (s, 1.4H), 6.94 (d, *J* = 1.2 Hz, 2H), 6.92 (s, 0.6H), 2.41 (s, 24H).

1H NMR (CDCl3, 400 MHz) Cu2[bis(4-chloro-2,6-dimethylphenyl)formamidinate]2 (i')

7.26 CDCl3
6.99
6.94
2.29

7.47
1.97
24.00

f1 (ppm)
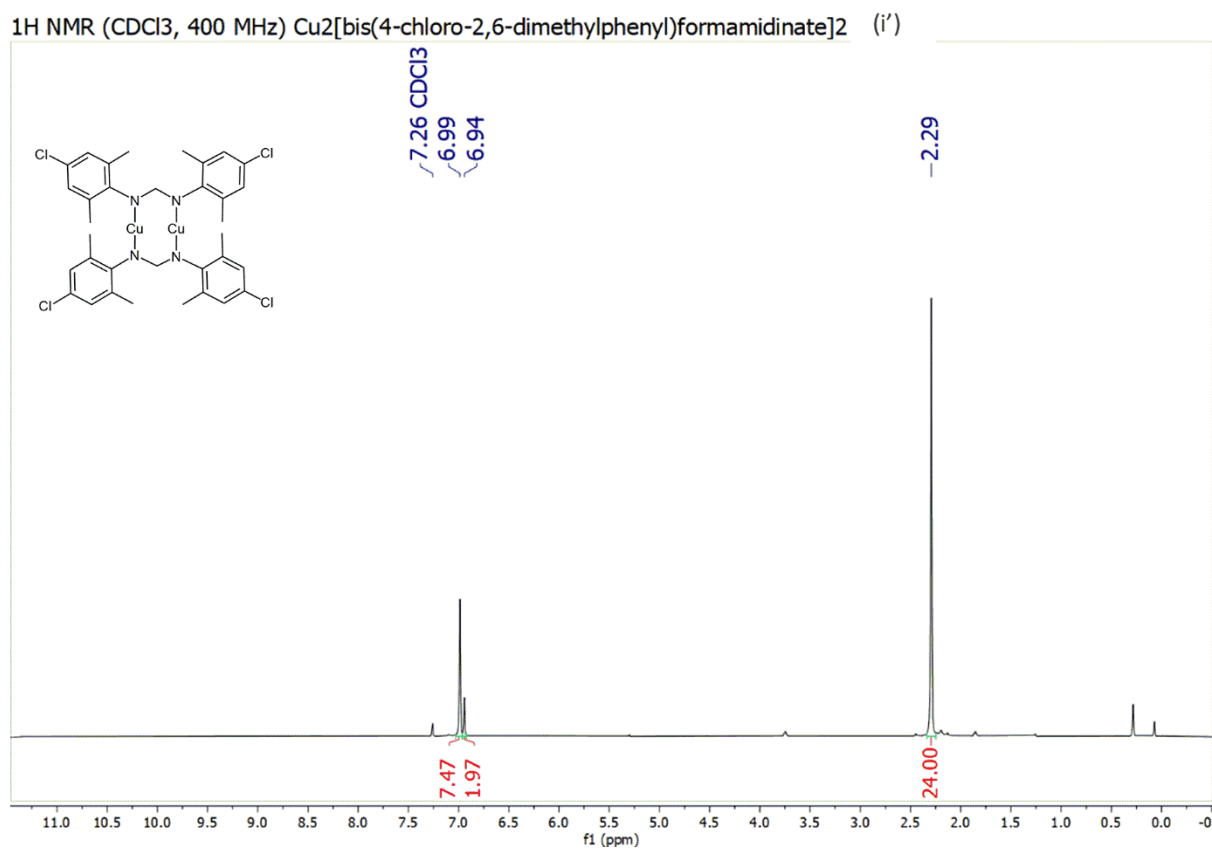
FIGURE S 20 ^{1}H NMR of Cu$_2$[bis(4-chloro-2,6-dimethylphenyl)formamidinate]$_2$ (**i'**). ^{1}H NMR (400 MHz, CDCl$_3$) δ 6.99 (s, 8H), 6.94 (s, 1H), 2.29 (s, 24H).

FIGURE S 21 ^{1}H NMR of Cu$_2$[bis(4-methoxy-2-methylphenyl)formamidinate]$_2$ (**j'**). ^{1}H NMR (400 MHz, CDCl$_3$) δ 7.53 (s, 2H), 6.85 (d, *J* = 8.4 Hz, 4H), 6.69 (d, *J* = 3.0 Hz, 4H), 6.66 – 6.61 (m, 4H), 3.75 (s, 12H), 2.39 (s, 12H), 0.28(s, residual HMDS).

1H NMR (CDCl3, 400 MHz) Cu2[bis(2-methoxy-6-methylphenyl)formamidinate]2 (k')
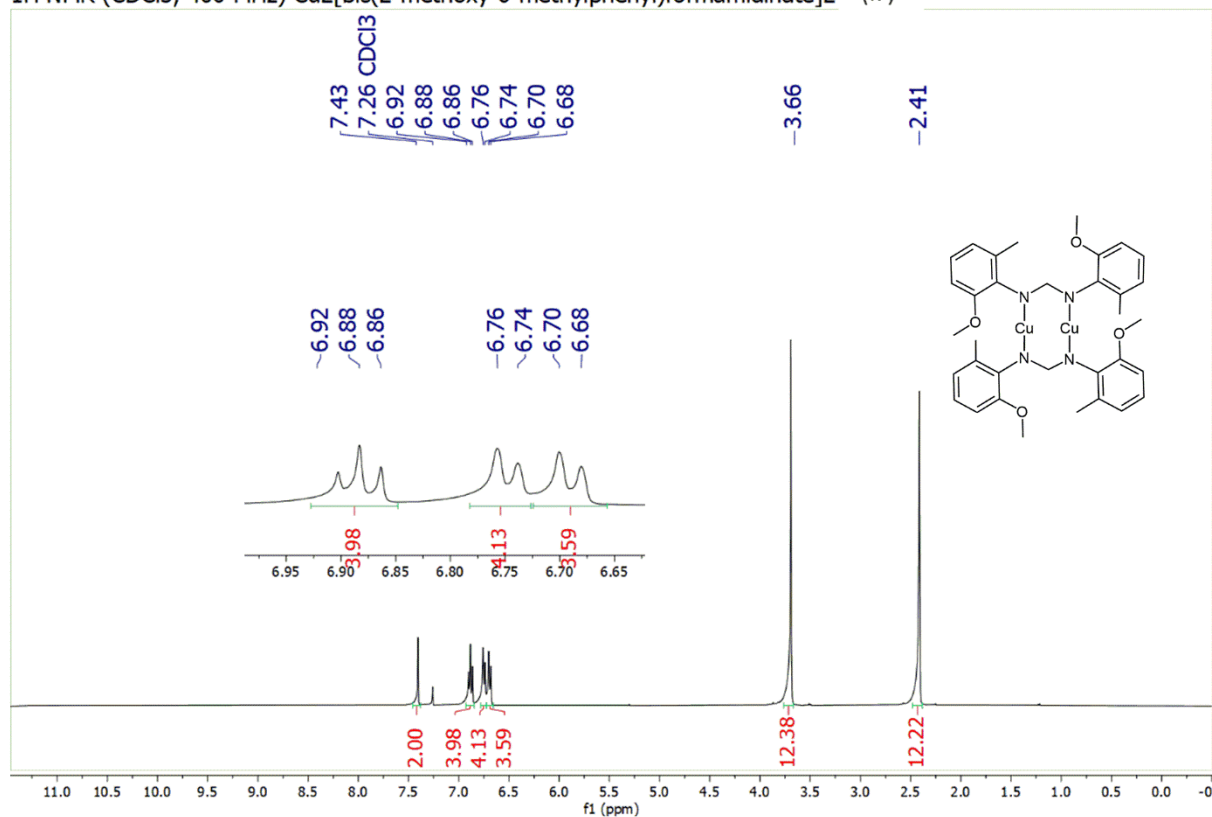
FIGURE S 22 ^{1}H NMR of Cu$_2$[bis(2-methoxy-6-methylphenyl)formamidinate]$_2$ (**k'**). ^{1}H NMR (400 MHz, CDCl$_3$) δ 7.43 (s, 2H), 6.88 (t, J = 8.0 Hz, 4H), 6.75 (d, J = 7.5 Hz, 4H), 6.69 (d, J = 8.0 Hz, 4H), 3.66 (s, 12H), 2.41 (s, 12H).

FIGURE S 23 ^{1}H NMR of Cu$_2$[bis(2-chloro-6-methylphenyl)formamidinate]$_2$ (**l'**). ^{1}H NMR (400 MHz, CDCl$_3$) δ 7.20 (d, $J = 7.9$ Hz, 4H), 7.18 (s, 2H), 7.06 (d, $J = 7.5$ Hz, 4H), 6.91 (t, $J = 7.8$ Hz, 4H), 2.42 (s, 12H).

FIGURE S 24 ^{1}H NMR of Cu$_2$[bis(2,6-diisopropylphenyl)formamidinate]$_2$ (**m'**).^{1}H NMR (400 MHz, CDCl$_3$) δ 7.09 – 7.02 (m, 14H), 3.61 (hept, J = 6.9 Hz, 8H), 1.26 (d, J = 6.9 Hz, 24H), 1.18 (d, J = 6.9 Hz, 24H).

1H NMR (Thf-d8, 400 MHz)
bis(tetrahydrofuran)lithium mesityl((mesitylphosphanylidene)(phenyl)methyl)amide
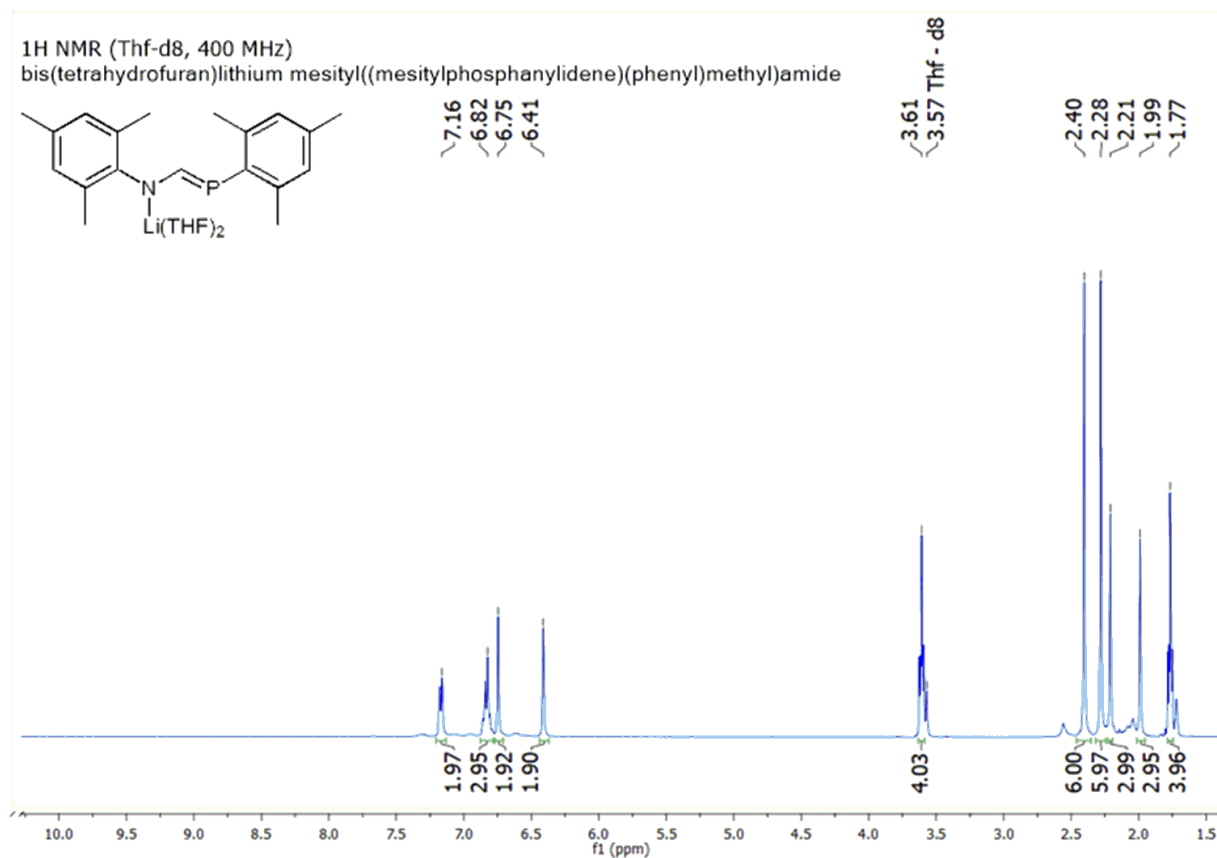
FIGURE S 25 ^{1}H NMR of bis(tetrahydrofuran)lithium mesityl((mesitylphosphanylidene)(phenyl)methyl)amide (**o**). ^{1}H NMR (400 MHz, THF-d8) δ 7.21 – 7.12 (m, 2H), 6.86 – 6.79 (m, 3H), 6.75 (s, 2H), 6.41 (s, 2H), 3.64 – 3.59 (m, 4H; THF), 2.40 (s, 6H), 2.28 (s, 6H), 2.21 (s, 3H), 1.99 (s, 3H), 1.79 – 1.74 (m, 4H; THF).

31P NMR (Thf-d8, 162 MHz)
bis(tetrahydrofuran)lithium mesityl
((mesitylphosphanylidene)(phenyl)methyl)amide
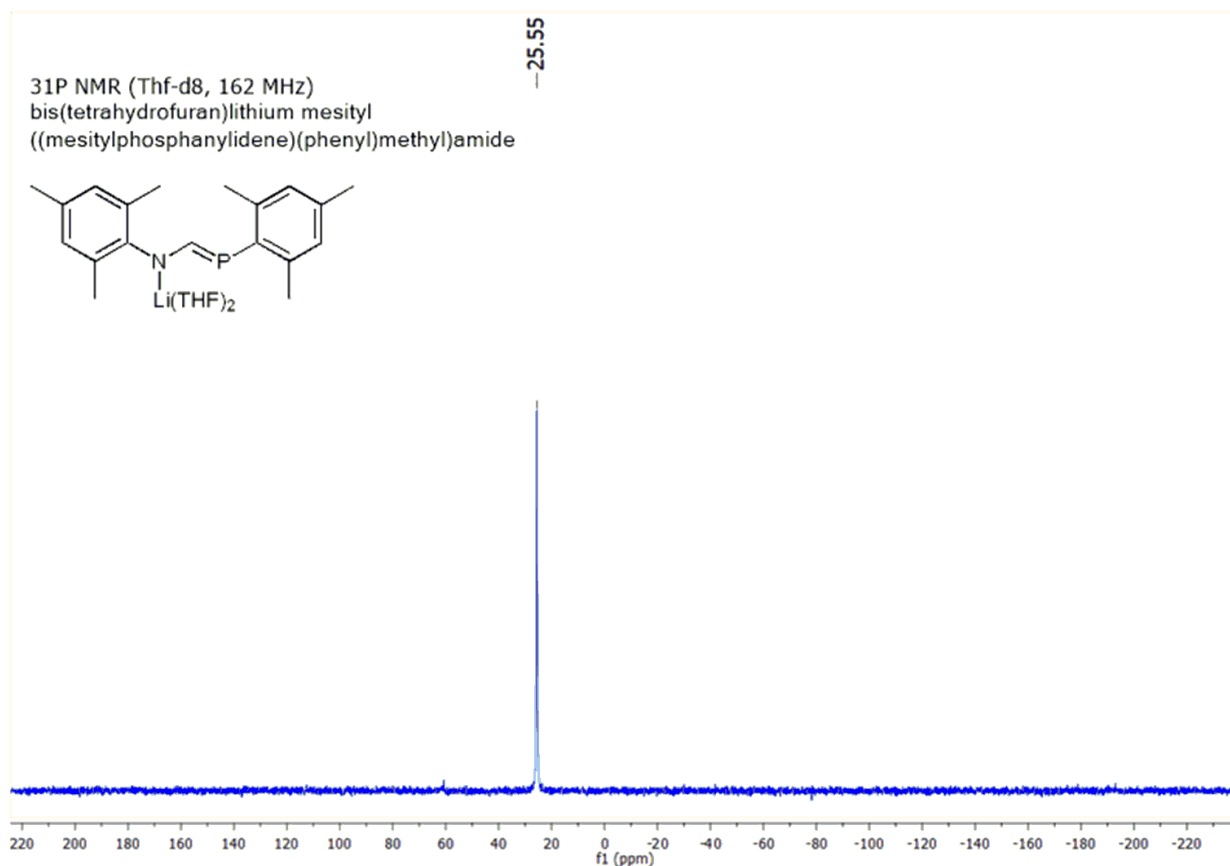
FIGURE S 26 ^{31}P{^{1}H} NMR of bis(tetrahydrofuran)lithium mesityl((mesitylphosphanylidene)(phenyl)methyl)amide (**o**). ^{31}P{^{1}H} NMR (162 MHz, THF-d8) δ 25.55 (s).
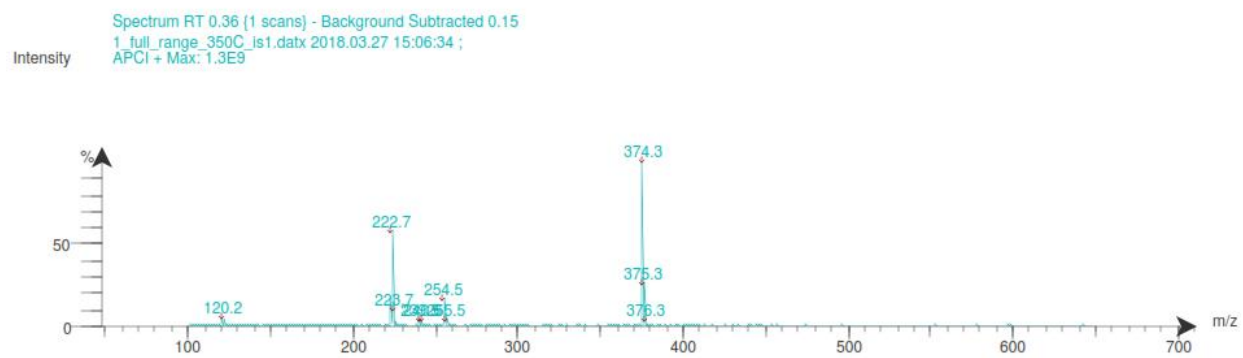
FIGURE S 27 Full range APCI^{+} mass spectrum of (**o**).
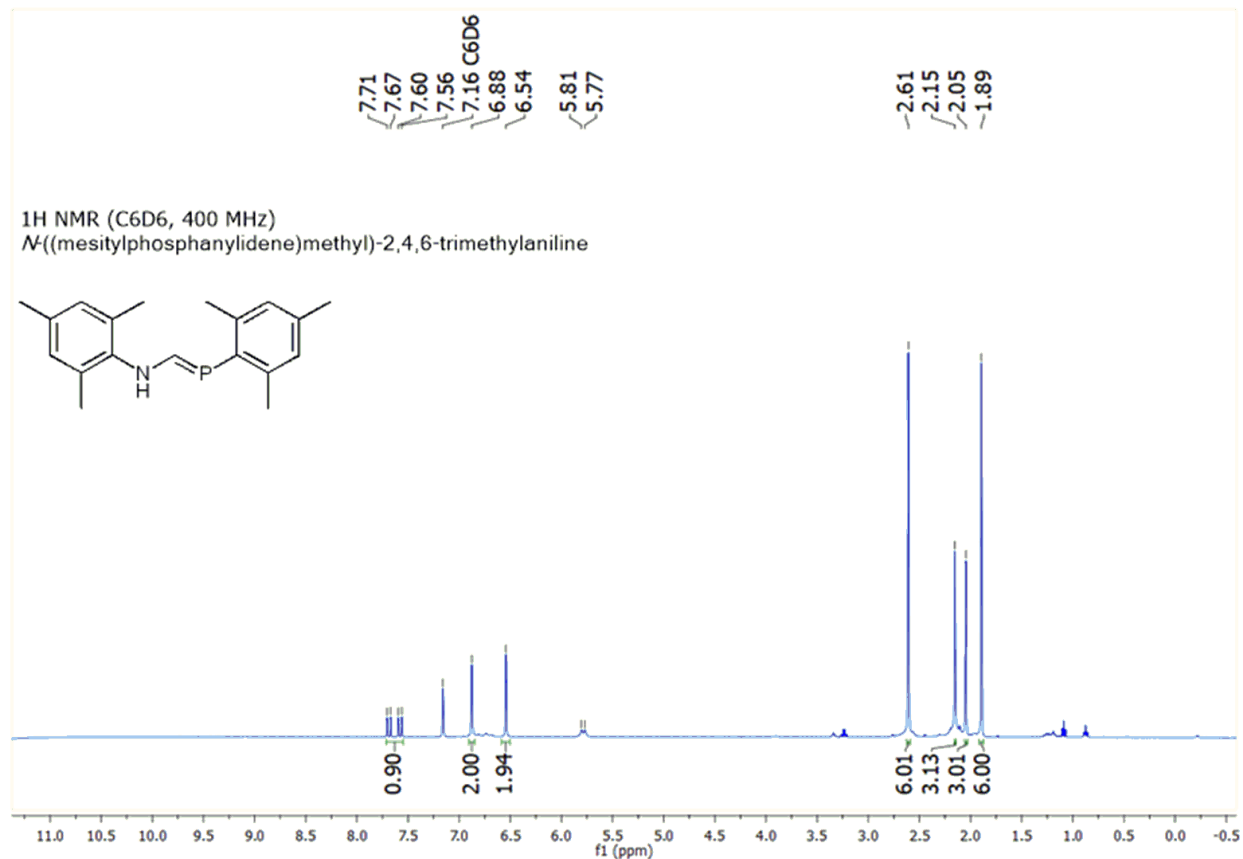
FIGURE S 28 ^{1}H NMR of *N*-((mesitylphosphanylidene)methyl)-2,4,6-trimethylaniline (**p**). ^{1}H NMR (400 MHz, C$_6$D$_6$) δ 7.63 (dd, *J* = 44.1, 13.9 Hz, 1H), 6.88 (s, 2H), 6.54 (s, 2H), 2.61 (s, 6H), 2.15 (s, 3H), 2.05 (s, 3H), 1.89 (s, 6H).

31P NMR (C6D6, 162 MHz)
N-((mesitylphosphanylidene)methyl)-2,4,6-trimethylaniline
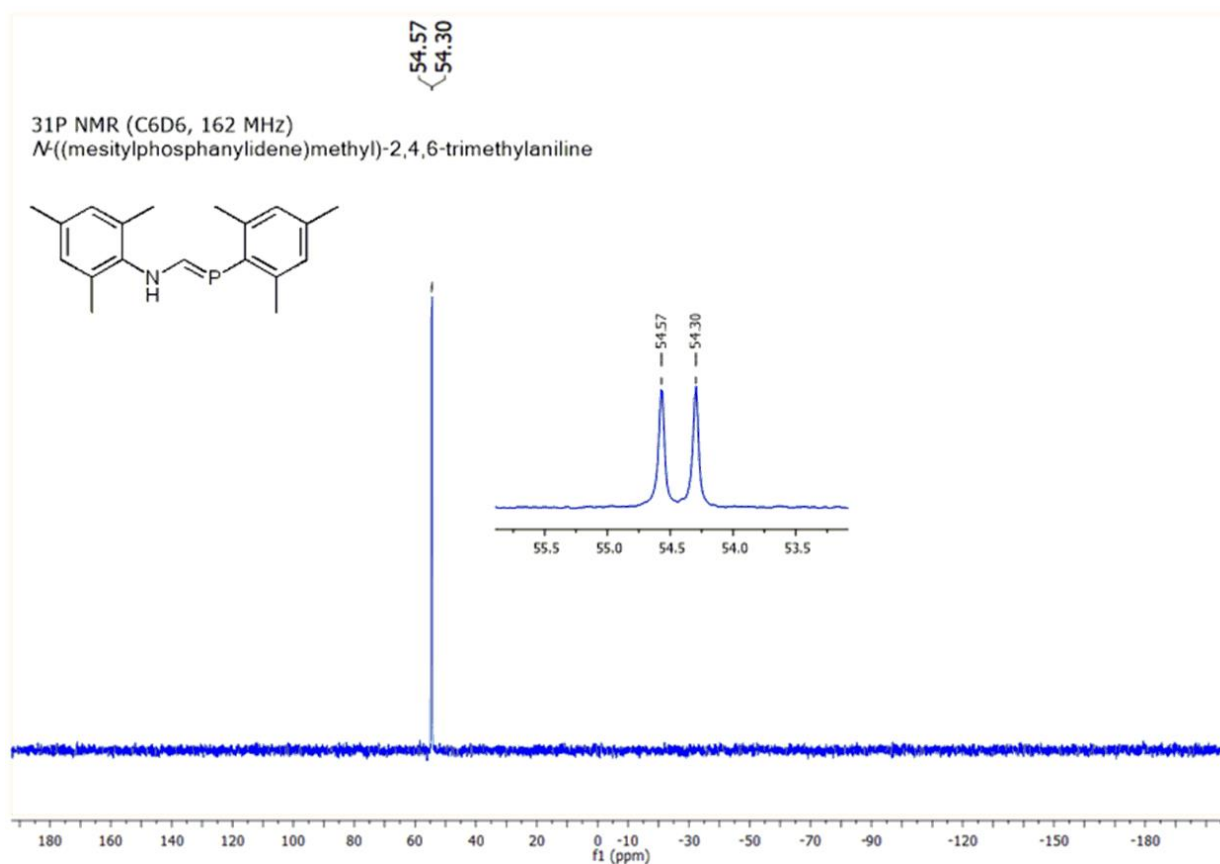
FIGURE S 29 ^{31}P{^{1}H} NMR of *N*-((mesitylphosphanylidene)methyl)-2,4,6-trimethylaniline (**p**). ^{31}P{^{1}H} NMR (162 MHz, C$_6$D$_6$) δ 54.43 (d, *J* = 44.2 Hz).
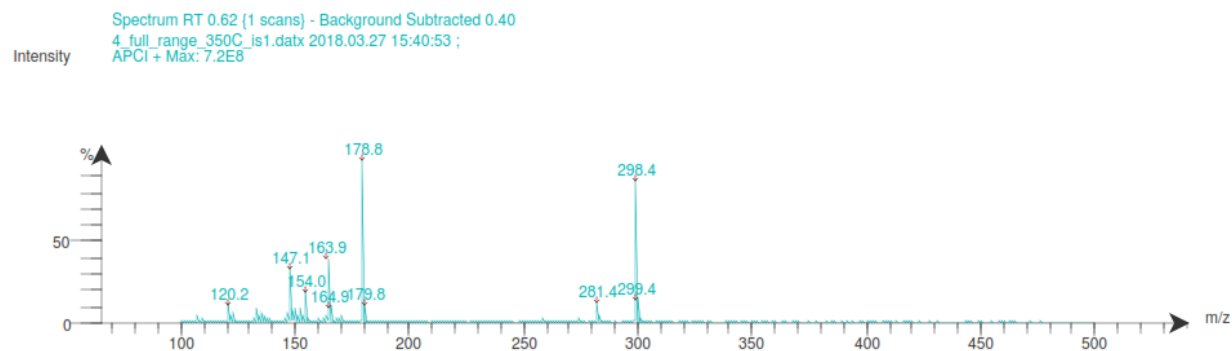
FIGURE S 30 Full range APCI$^+$ mass spectrum of (**p**).
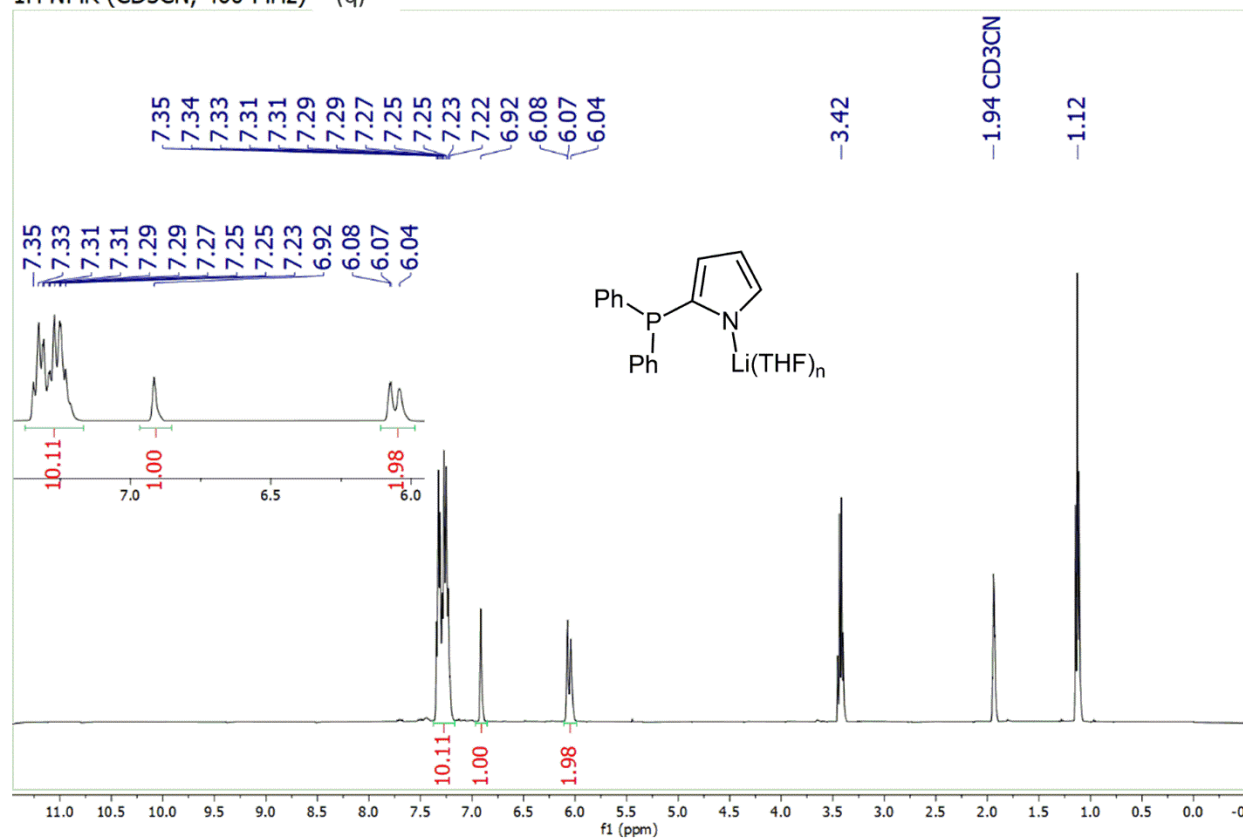
FIGURE S 31 ^{1}H NMR of (**q**). ^{1}H NMR (400 MHz, CD$_3$CN) δ 7.37 – 7.19 (m, 10H), 6.92 (s, 1H), 6.11 – 6.02 (m, 2H).

31P NMR (CD3CN, 400 MHz) (q)
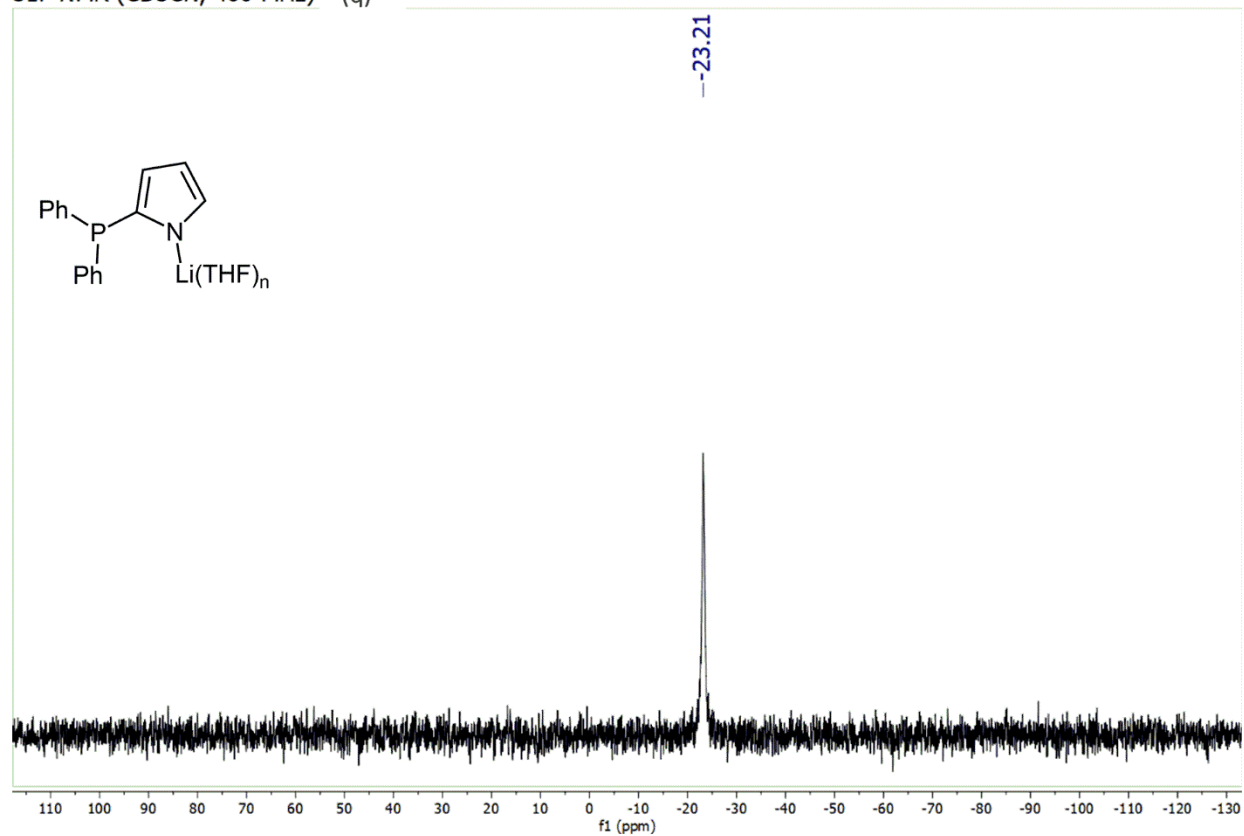
−23.21

FIGURE S 32 ^{31}P{^{1}H} NMR of (**q**). ^{31}P{^{1}H} NMR (400 MHz, CD$_3$CN) δ -23.21.

1H NMR (CD3CN, 400 MHz) (q')
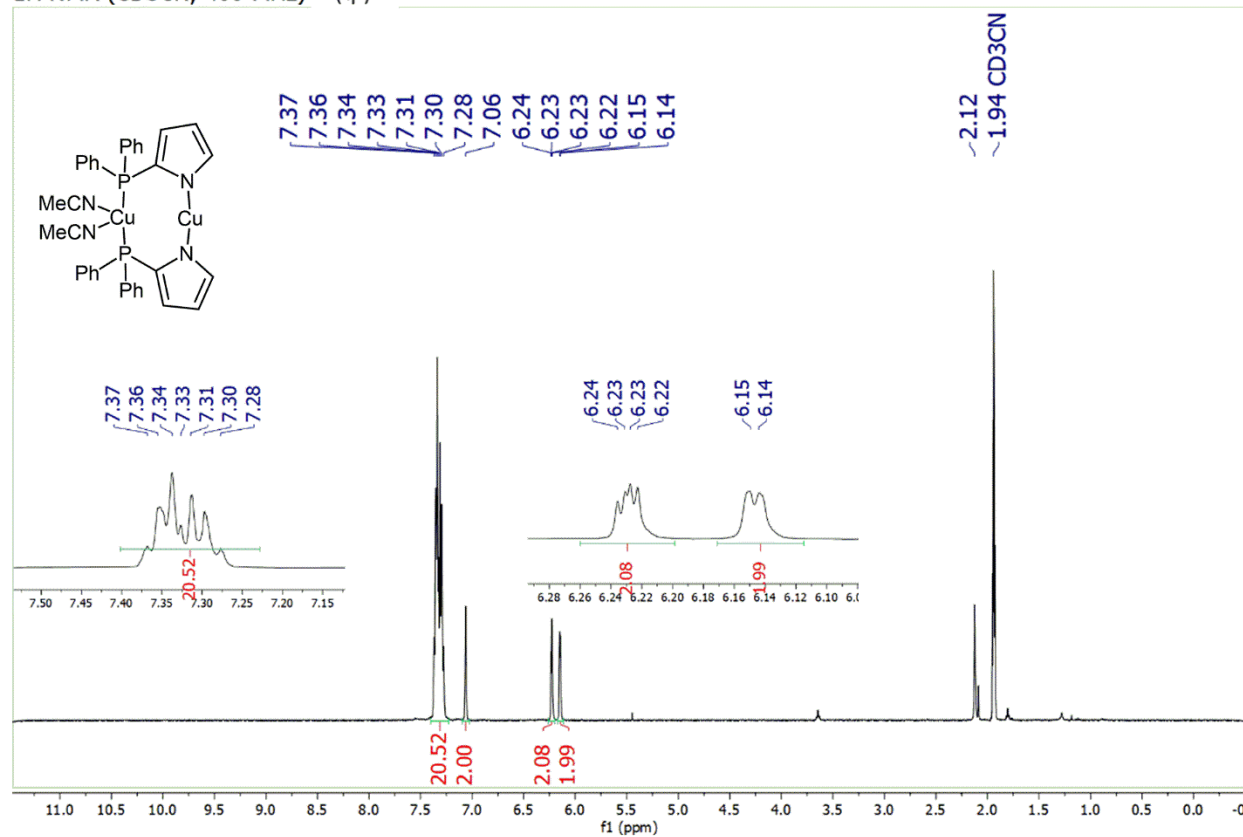
FIGURE S 33 ^{1}H NMR of (**q'**). ^{1}H NMR (400 MHz, CD$_3$CN) δ 7.39 – 7.25 (m, 20H), 7.06 (s, 2H), 6.23 (dd, *J* = 3.4, 2.0 Hz, 2H), 6.15 (d, *J* = 2.2 Hz, 2H), 2.12 (s, coordinated CH$_3$CN).
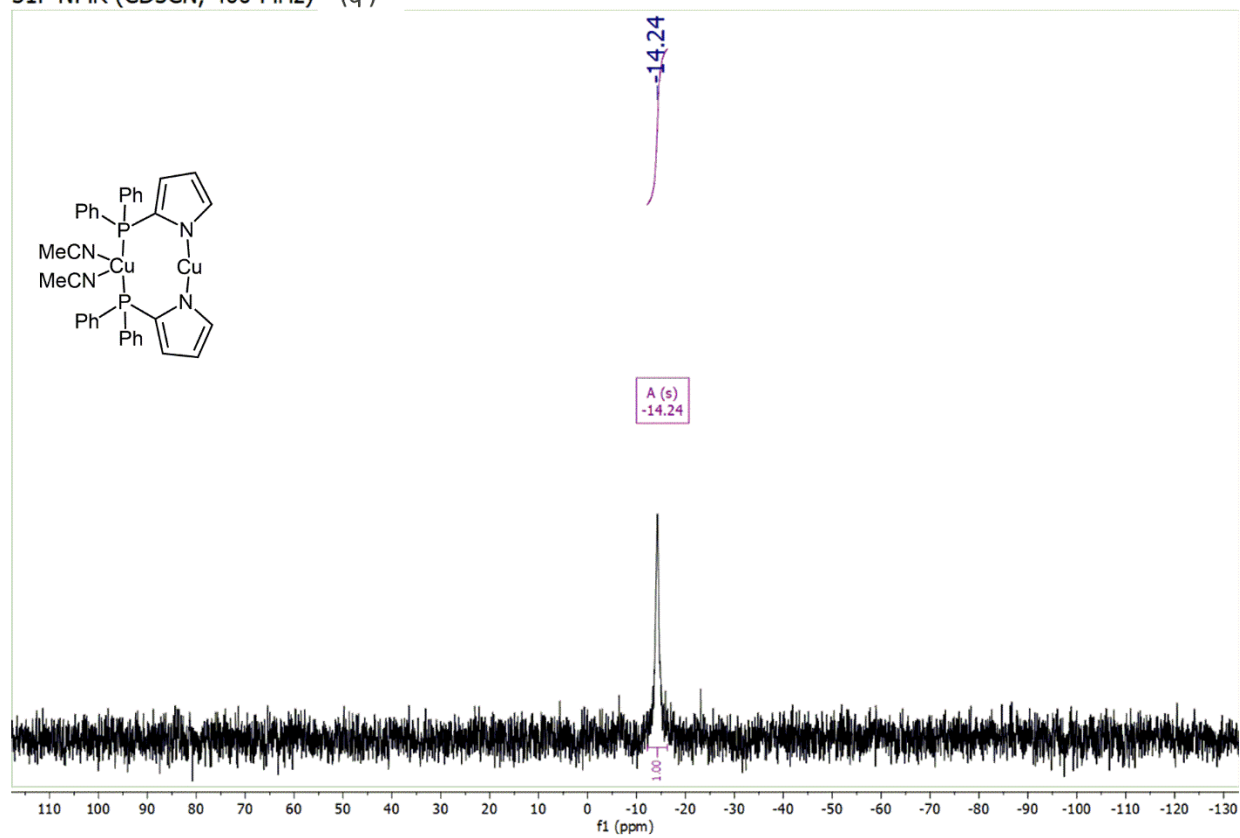
FIGURE S 34 ^{31}P{^{1}H} NMR of (**q'**). ^{31}P{^{1}H} NMR (400 MHz, CD$_3$CN) δ -14.24.
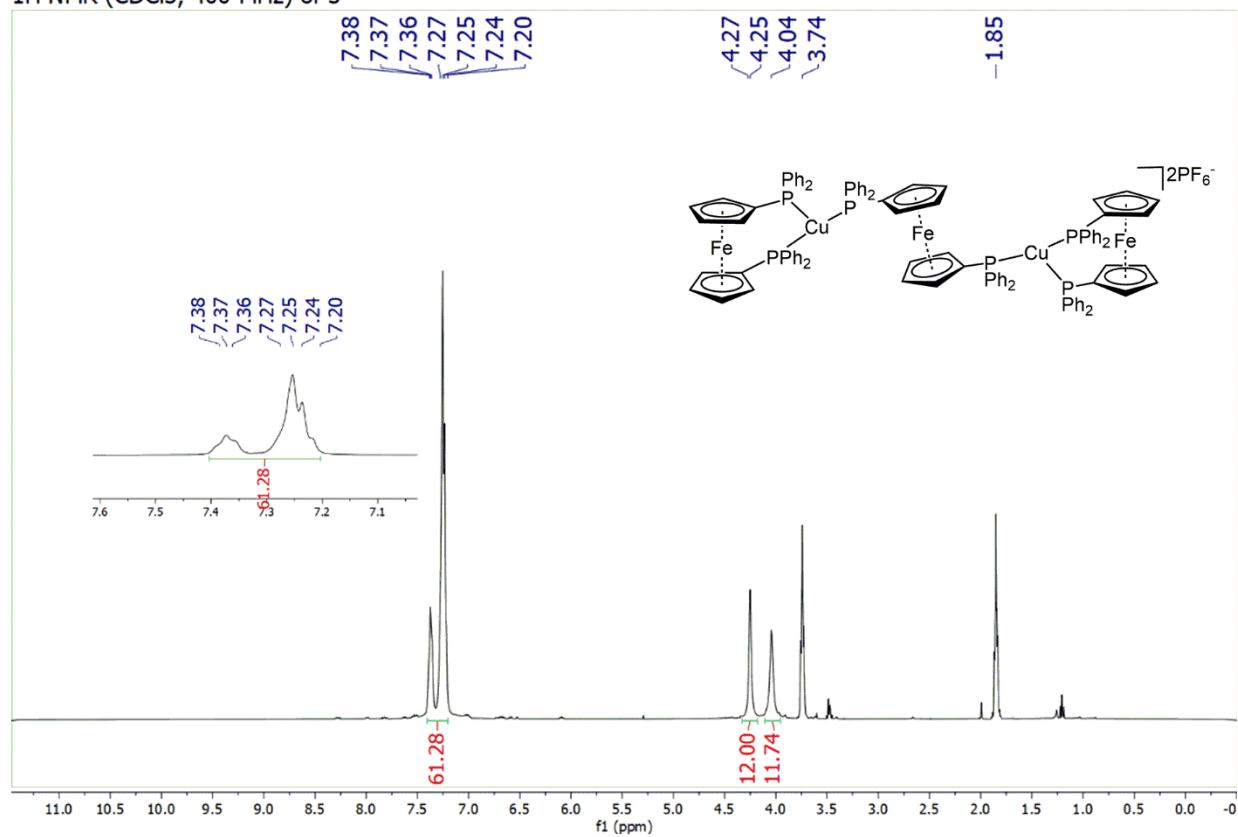
FIGURE S 35 ^{1}H NMR of **3**. ^{1}H NMR (400 MHz, CDCl$_3$) δ 7.47 – 7.15 (m, 60H), 4.25 (s, 12H), 4.04 (s, 12H), 3.74 (t, THF), 1.85 (q, THF).

31P NMR (CDCl3, 400 MHz) of 3
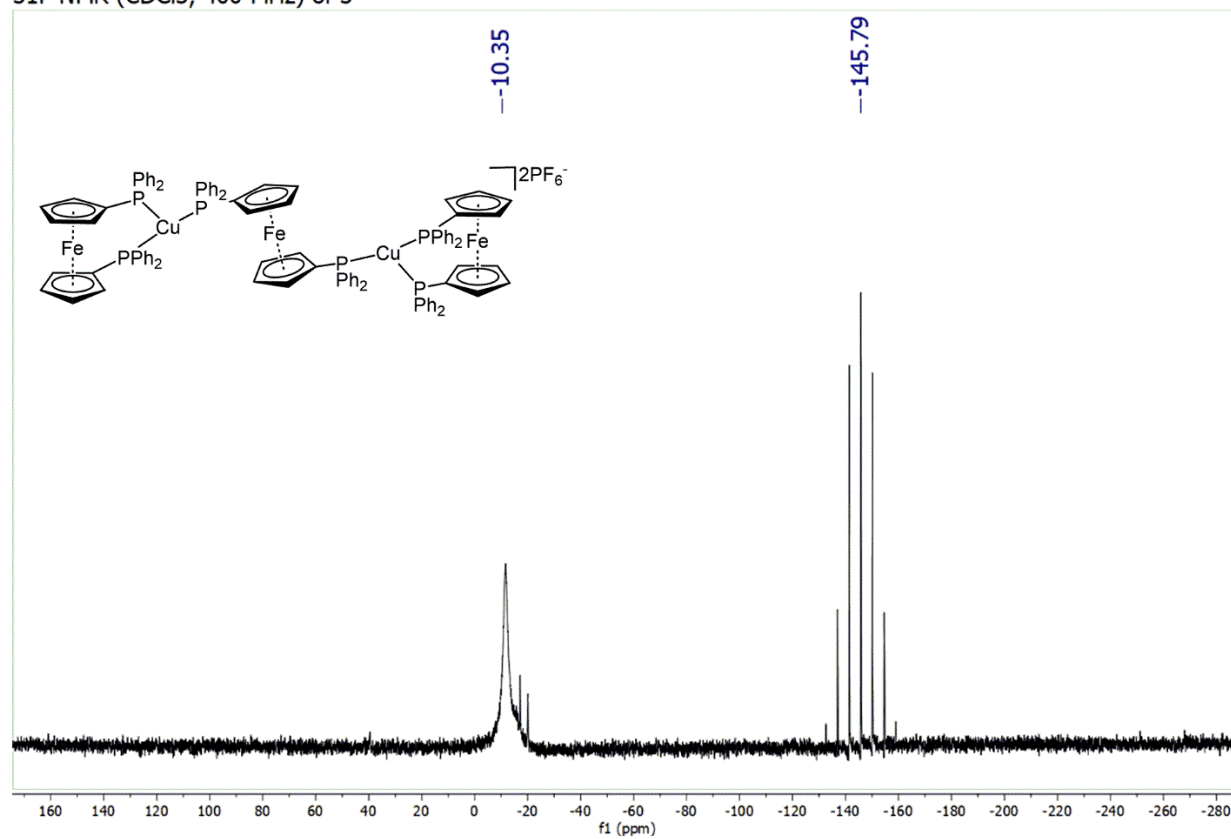
FIGURE S 36 ^{31}P{^{1}H} NMR of **3**. ^{31}P{^{1}H} NMR (400 MHz, CDCl$_3$) δ -10.35 (brs), -145.79 (sept, PF$_6$).
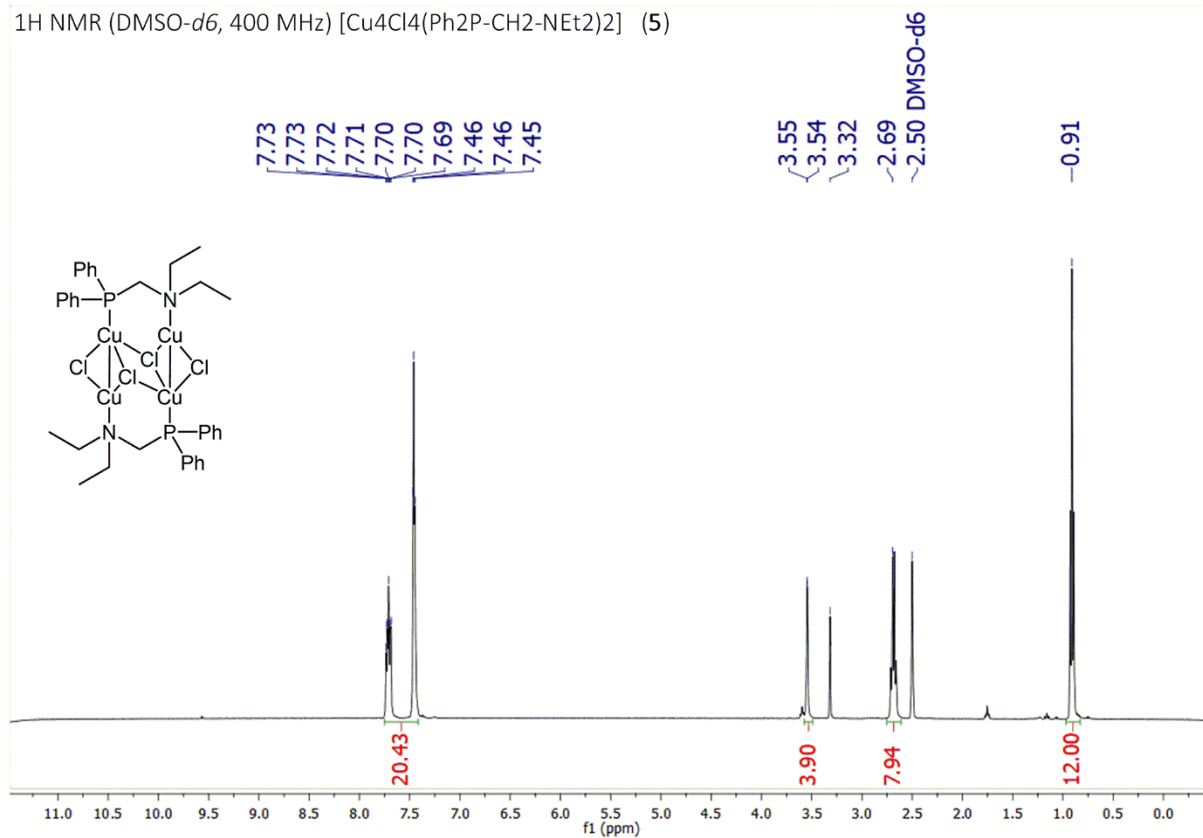
FIGURE S 37 ^{1}H NMR of **5**. ^{1}H NMR (400 MHz, DMSO-d_6) δ 7.75 – 7.42 (m, 20H), 3.55 (d, J = 1.7 Hz, 4H), 2.69 (q, 8H), 3.32 (s, residual H$_2$O in DMSO-d_6), 0.91 (t, 12H).

31P NMR (DMSO-*d6*, 400 MHz) [Cu4Cl4(Ph2P-CH2-NEt2)2] (**5**)
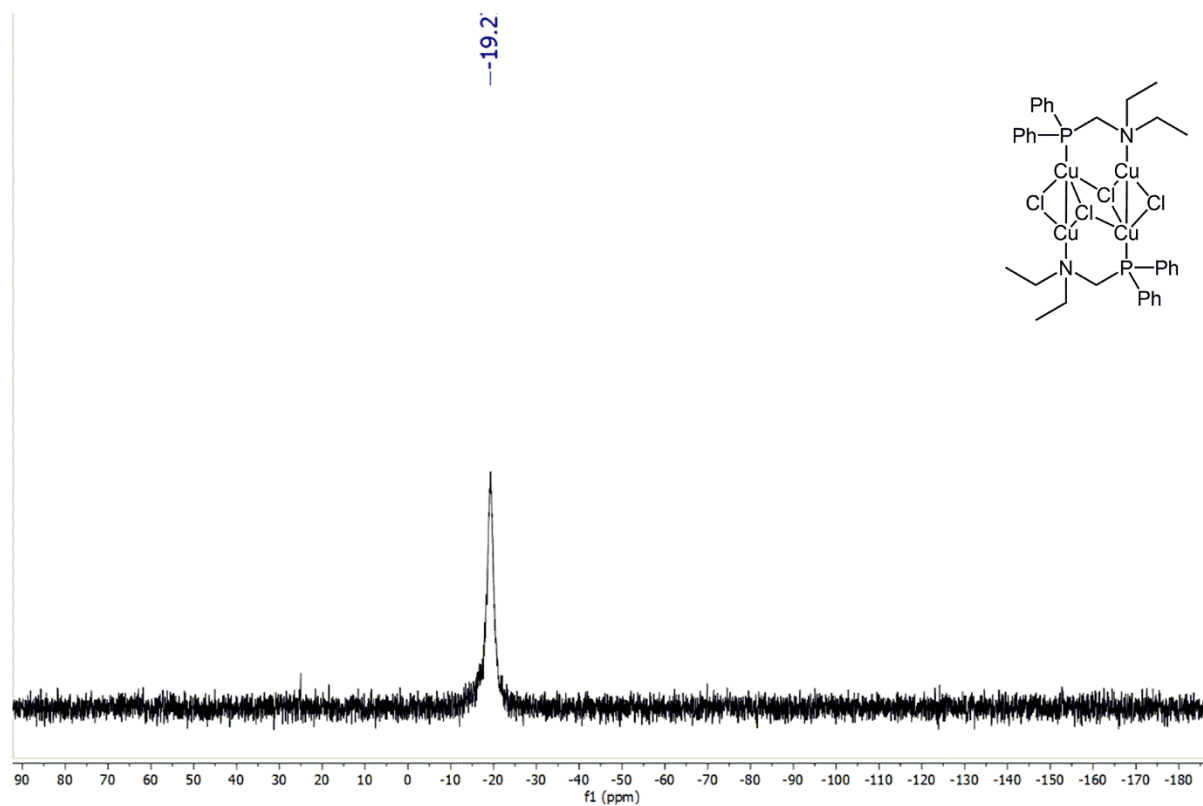
FIGURE S 38 ^{31}P{^{1}H} NMR of **5**. ^{31}P{^{1}H} NMR (400 MHz, DMSO-*d6*) δ -19.27.
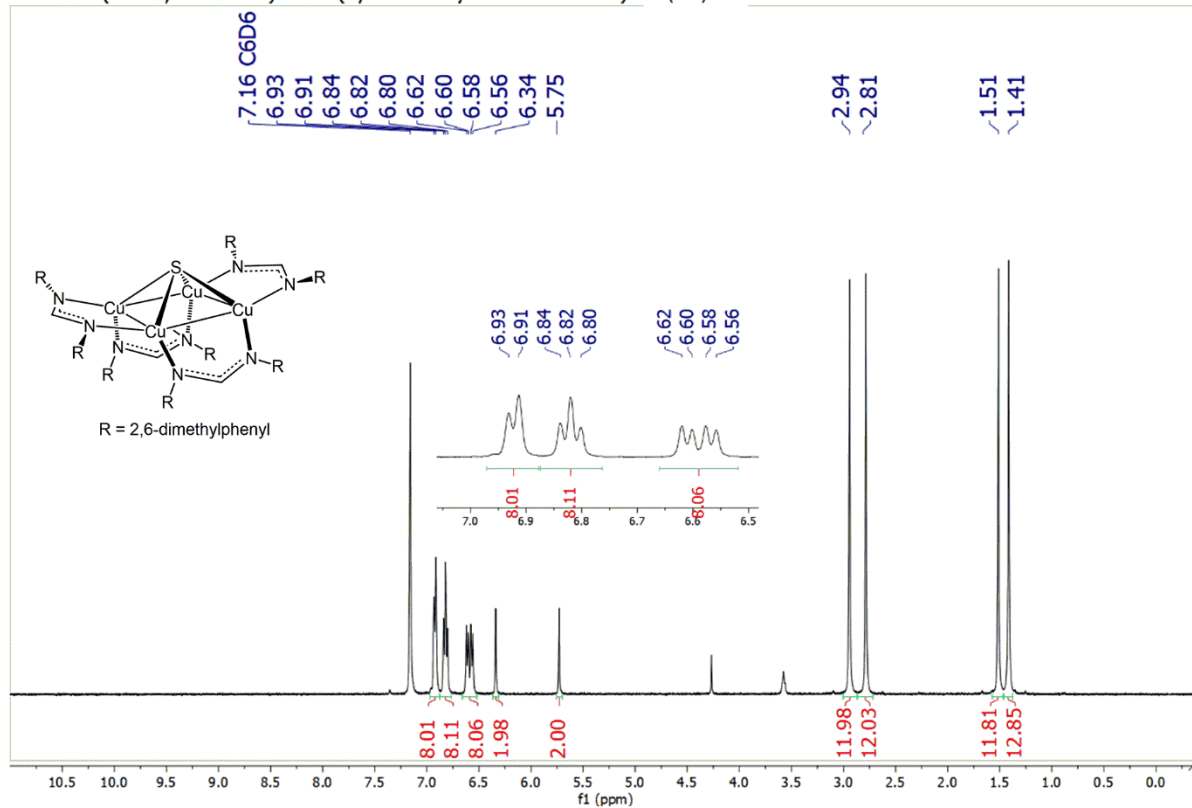
FIGURE S 39 ^{1}H NMR of **6h**. ^{1}H NMR (400 MHz, C_6D_6) δ 6.92 (d, J = 7.1 Hz, 8H), 6.82 (t, J = 7.5 Hz, 8H), 6.59 (dd, J = 17.3, 7.5 Hz, 8H), 6.34 (s, 2H), 5.75 (s, 2H), 2.94 (s, 12H), 2.79 (s, 12H), 1.51 (s, 12H), 1.41 (s, 12H).

1H NMR (Acetone-d6, 400 MHz) Cu4S[bis(2,6-dimethylphenyl)formamidinate]4 K(18-crown-6) (7h)
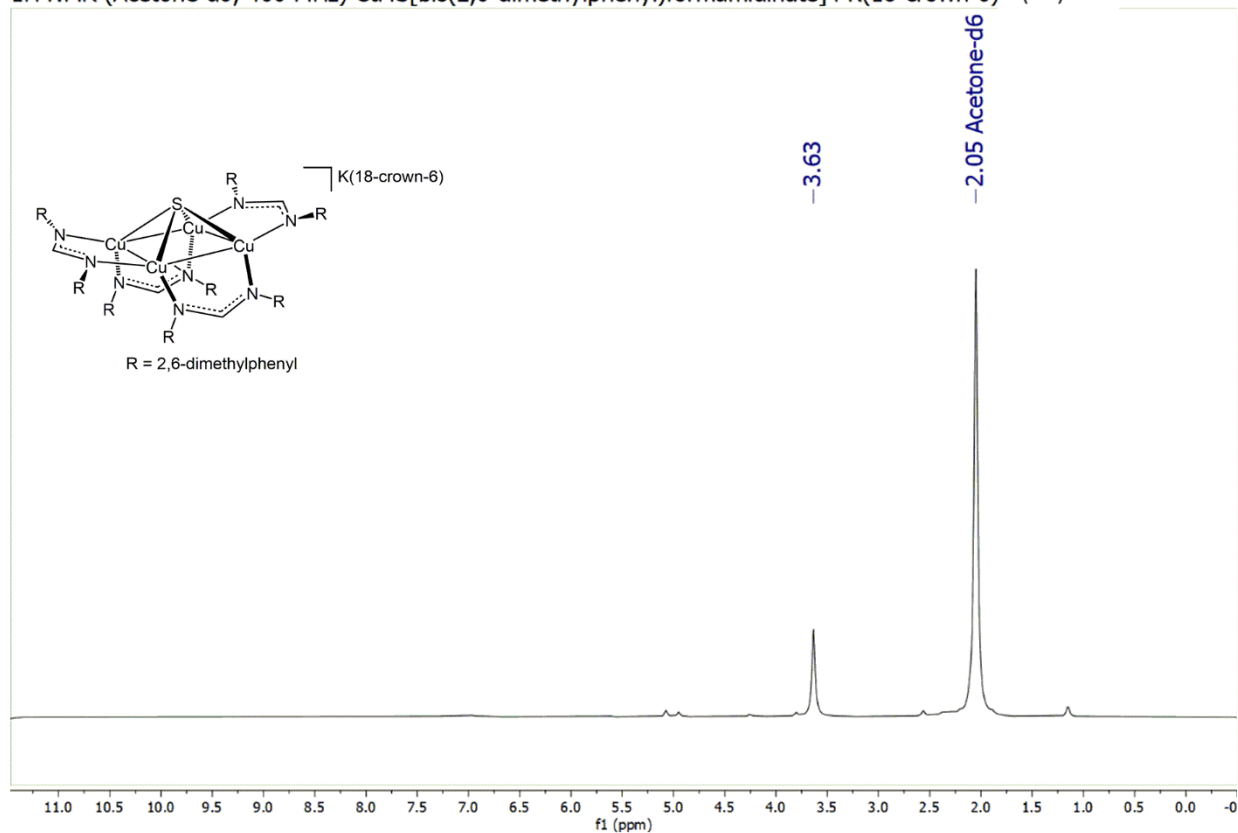
FIGURE S 40 ^{1}H NMR of **7h**. (^{1}H NMR (400 MHz, Acetone-d$_6$) δ 3.63 (s, 18-crown-6 -CH2-).
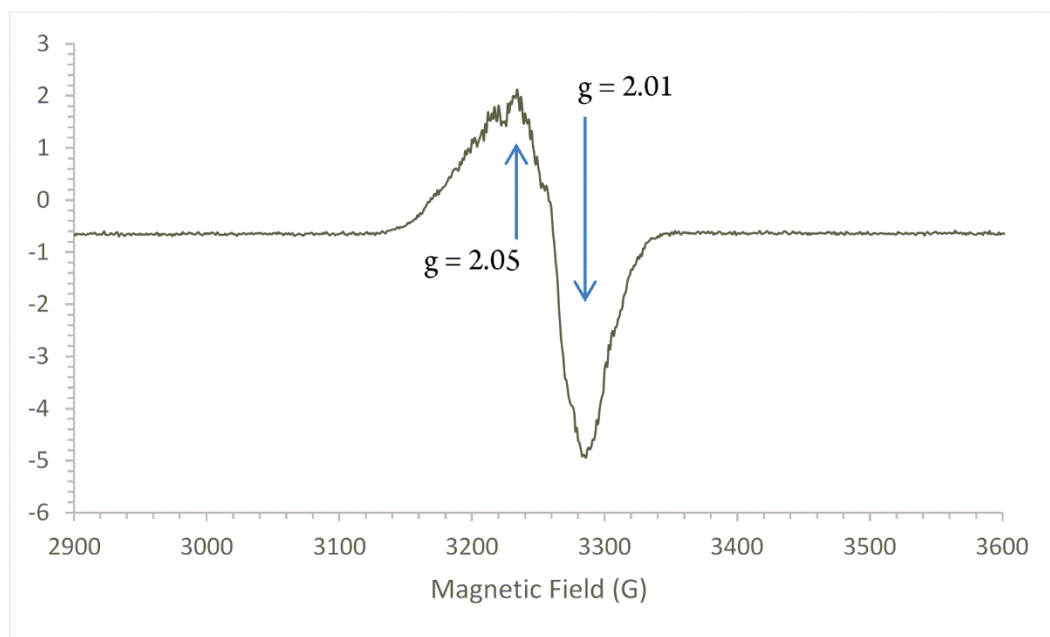
FIGURE S 41 X-band cw EPR spectrum of **7h** (5 mM, -195 ºC). Microwave frequency, 9.255 GHz; microwave power, 6 mW; scan time, 240 s; time constant, 0.03 s; field modulation amplitude, 1 mT. g=2.05 and 2.01.
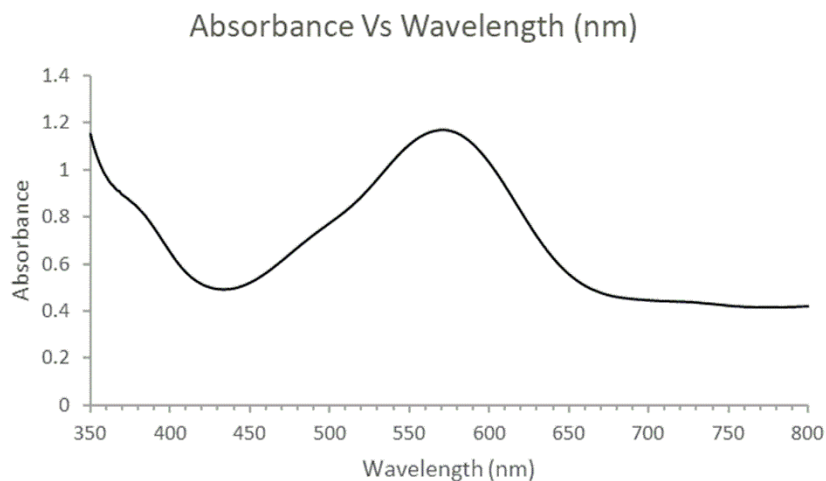
FIGURE S 42 Uv-Vis spectrum of 0.25 mM solution of **7h** in acetone. λ_{max} = 571 nm (ΔE = 210 kJ/mol, ε = 4680 M^{-1} cm^{-1})
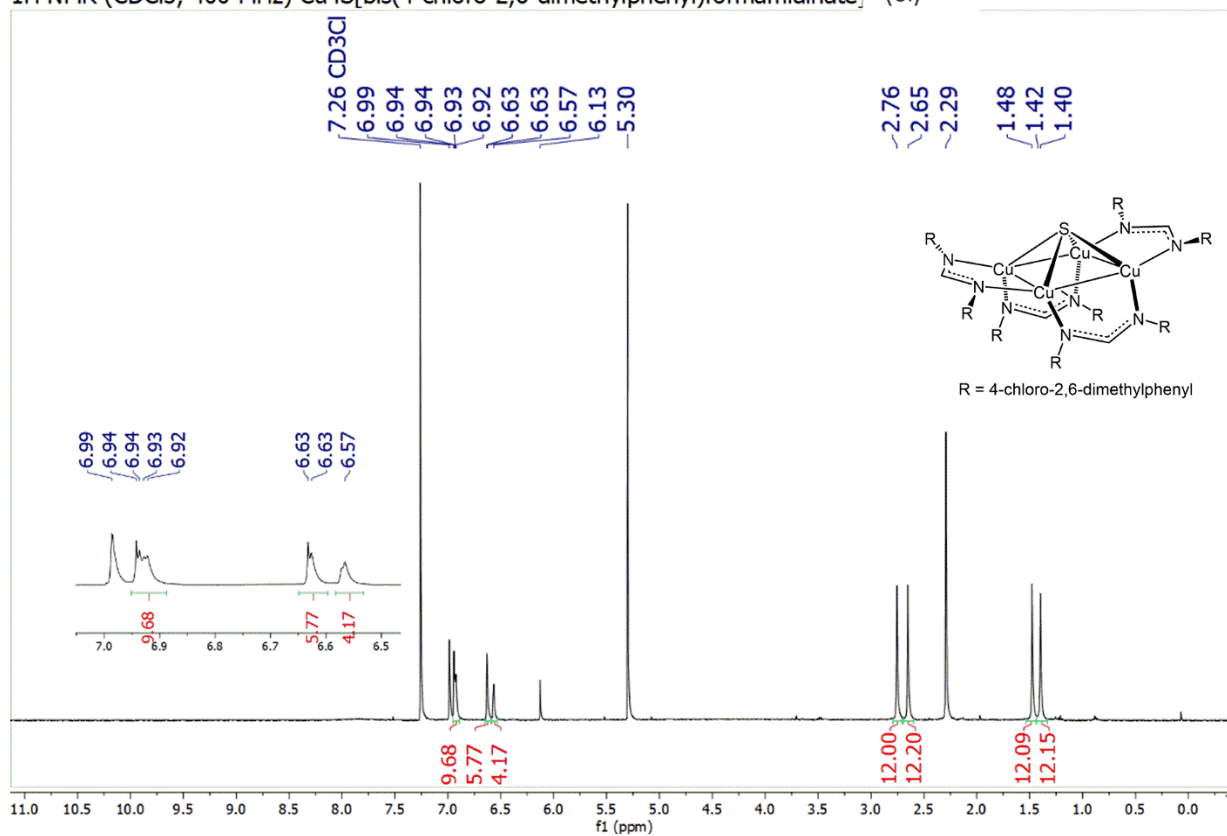
FIGURE S 43 ^{1}H NMR of **6i**. ^{1}H NMR (400 MHz, CDCl$_3$) δ 6.93 (dd, J = 5.6, 2.5 Hz, 10H), 6.63 (d, J = 2.7 Hz, 6H), 6.57 (s, 4H), 2.76 (s, 12H), 2.65 (s, 12H), 1.48 (s, 12H), 1.40 (s, 12H). residual precursor shows up at δ 6.99, δ 6.13 and δ 2.29.

1H NMR (CD2Cl2, 400 MHz) Cu4[bis(4-trifluoromethylphenyl)formamidinate]4 (8)

R = 4-trifluoromethylphenyl
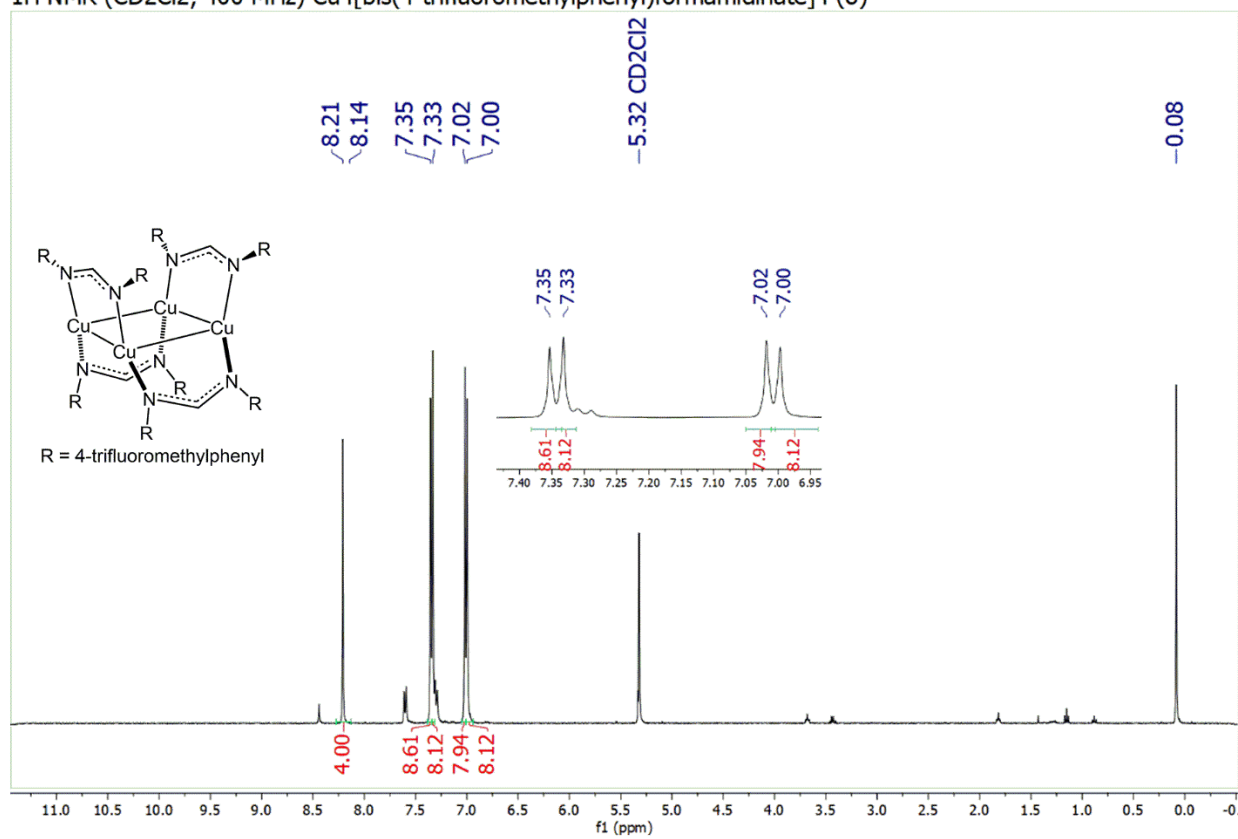
FIGURE S 44 ^{1}H NMR of **8**. ^{1}H NMR (400 MHz, CD$_2$Cl$_2$) δ 8.21 (s, 4H), 7.35 (s, 8H), 7.33 (s, 8H), 7.02 (s, 8H), 7.00 (s, 8H).

19F NMR (CD2Cl2, 400 MHz) Cu4[bis(4-trifluoromethylphenyl)formamidinate]4 (8)

R = 4-trifluoromethylphenyl
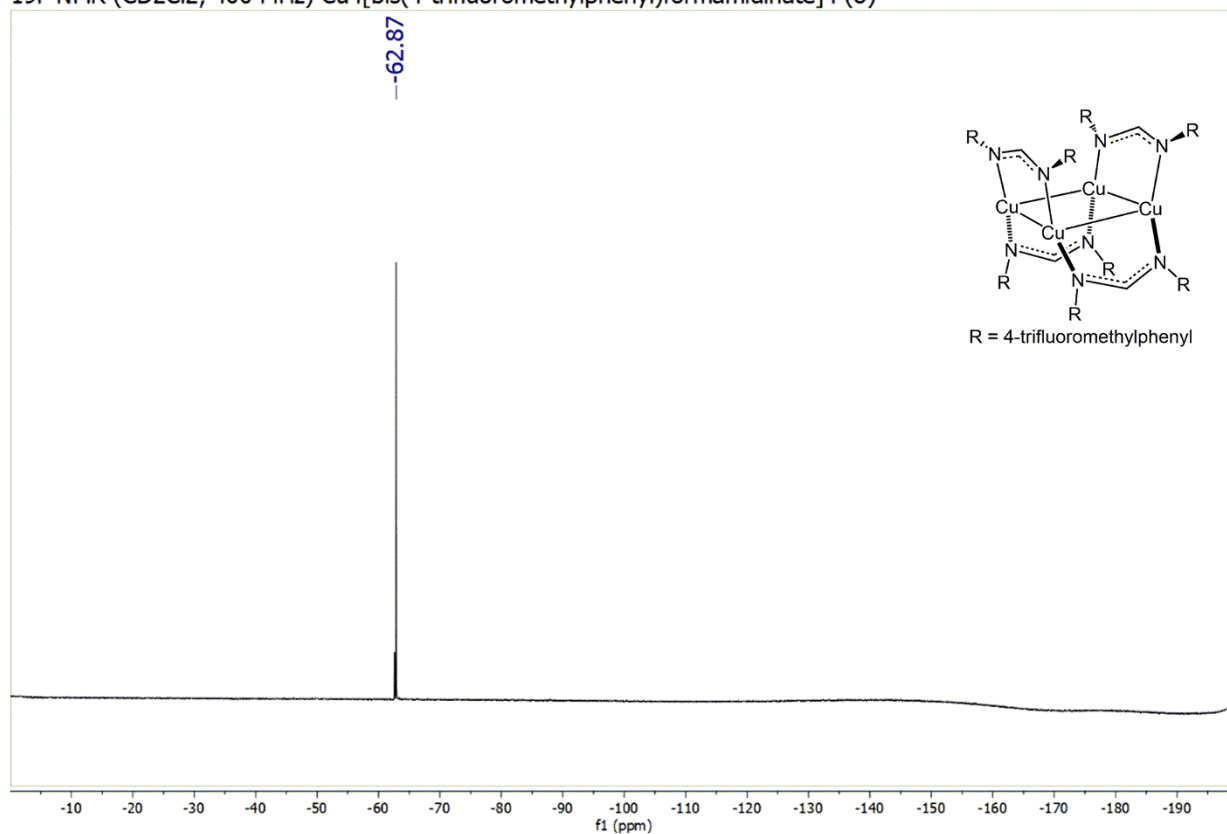
FIGURE S 45 ^{19}F{^{1}H} NMR of **8**. ^{19}F NMR (400 MHz, CD$_2$Cl$_2$) δ -62.87 (s, -CF$_3$).
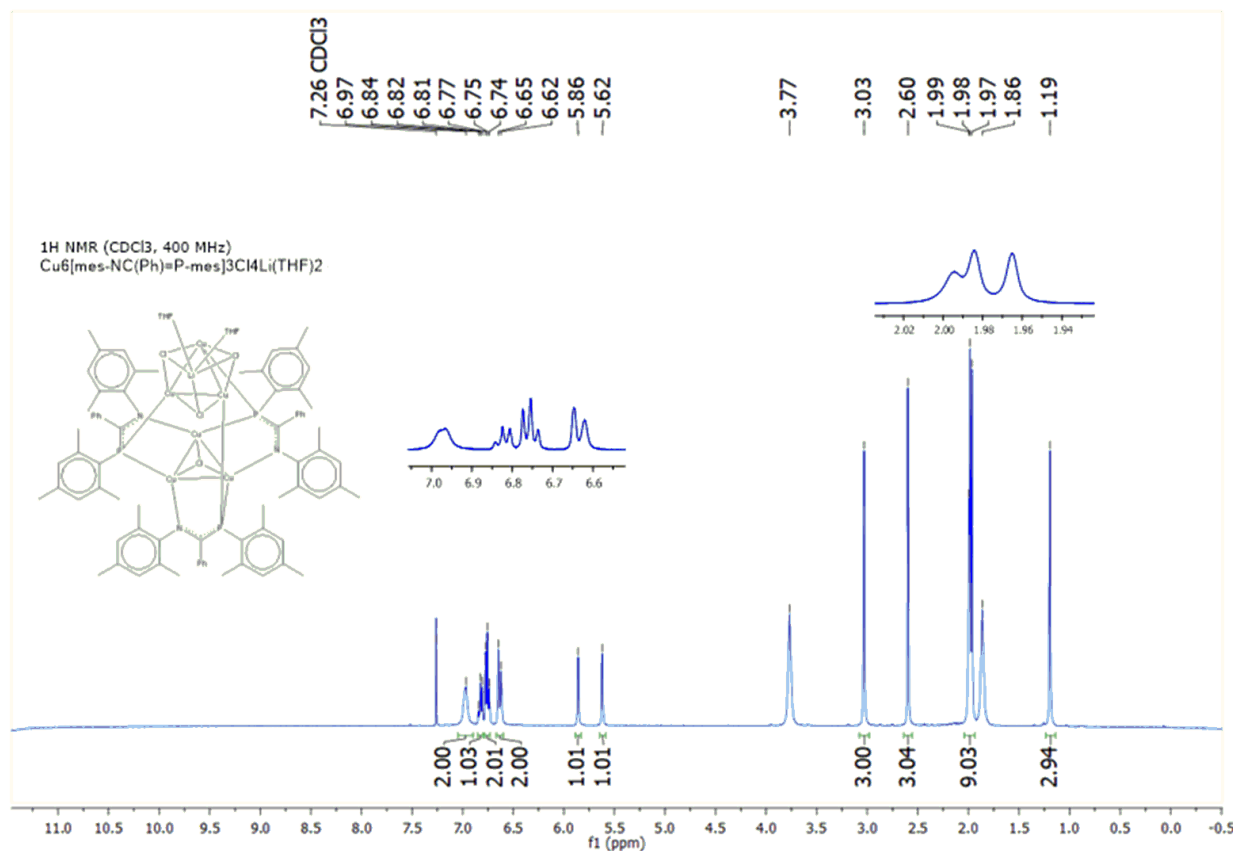
FIGURE S 46 ^{1}H NMR of complex **9**. ^{1}H NMR (400 MHz, CDCl$_3$) δ 6.97 (s, 2H), 6.82 (t, J = 7.2 Hz, 1H), 6.75 (t, J = 7.5 Hz, 2H), 6.65 (s, 1H), 6.62 (s, 1H), 5.86 (s, 1H), 5.62 (s, 1H), 3.77 (s, 4H; THF), 3.03 (s, 3H), 2.60 (s, 3H), 1.99 (s, 3H), 1.98 (s, 3H), 1.97 (s, 3H), 1.86 (s, 8H; THF), 1.19 (s, 3H).

31P NMR (CDCl3, 162 MHz)
Cu6[mes-NC(Ph)=P-mes]3Cl4Li(THF)2
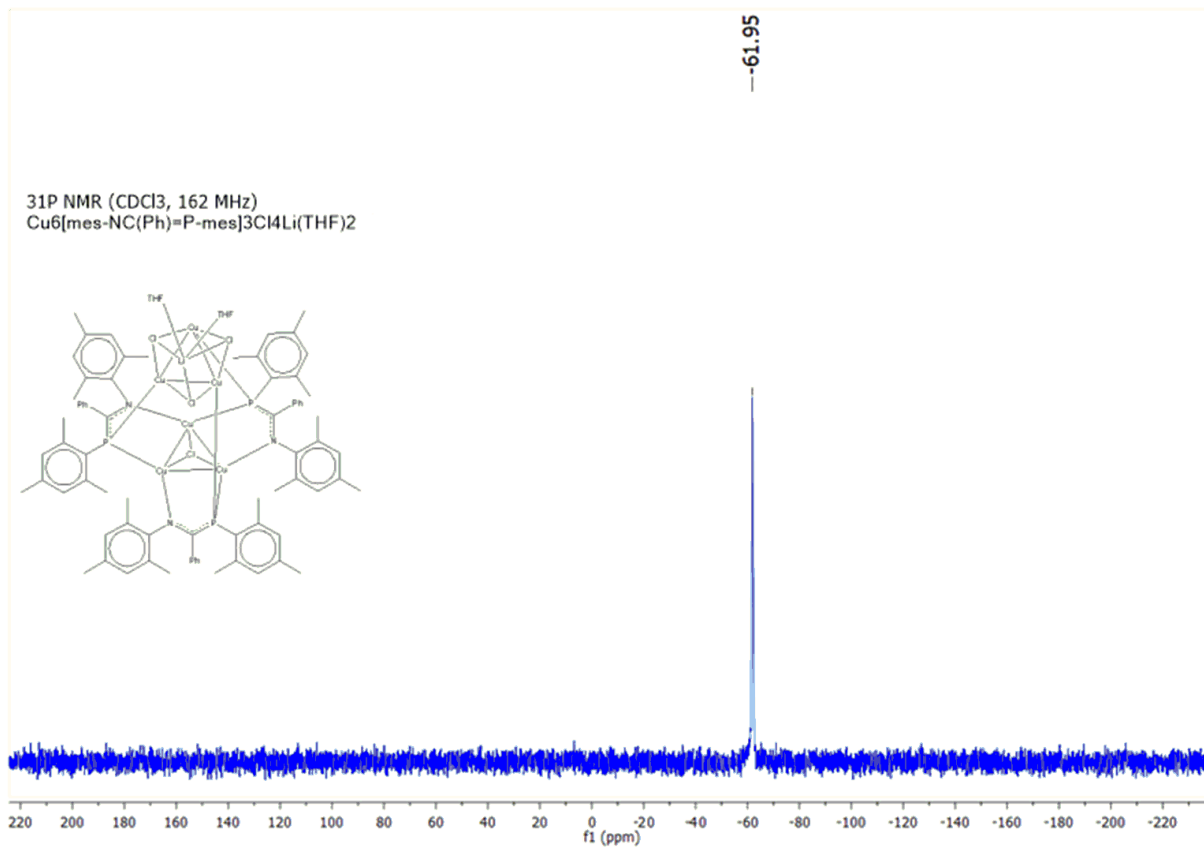
--61.95

FIGURE S 47 ^{31}P{^{1}H} NMR of complex **9**. ^{31}P{^{1}H} NMR (162 MHz, CDCl$_3$) δ -61.95 (s).

1H NMR (C6D6, 400 MHz)
Cu4[mes-N=CHP-mes]4 (5)
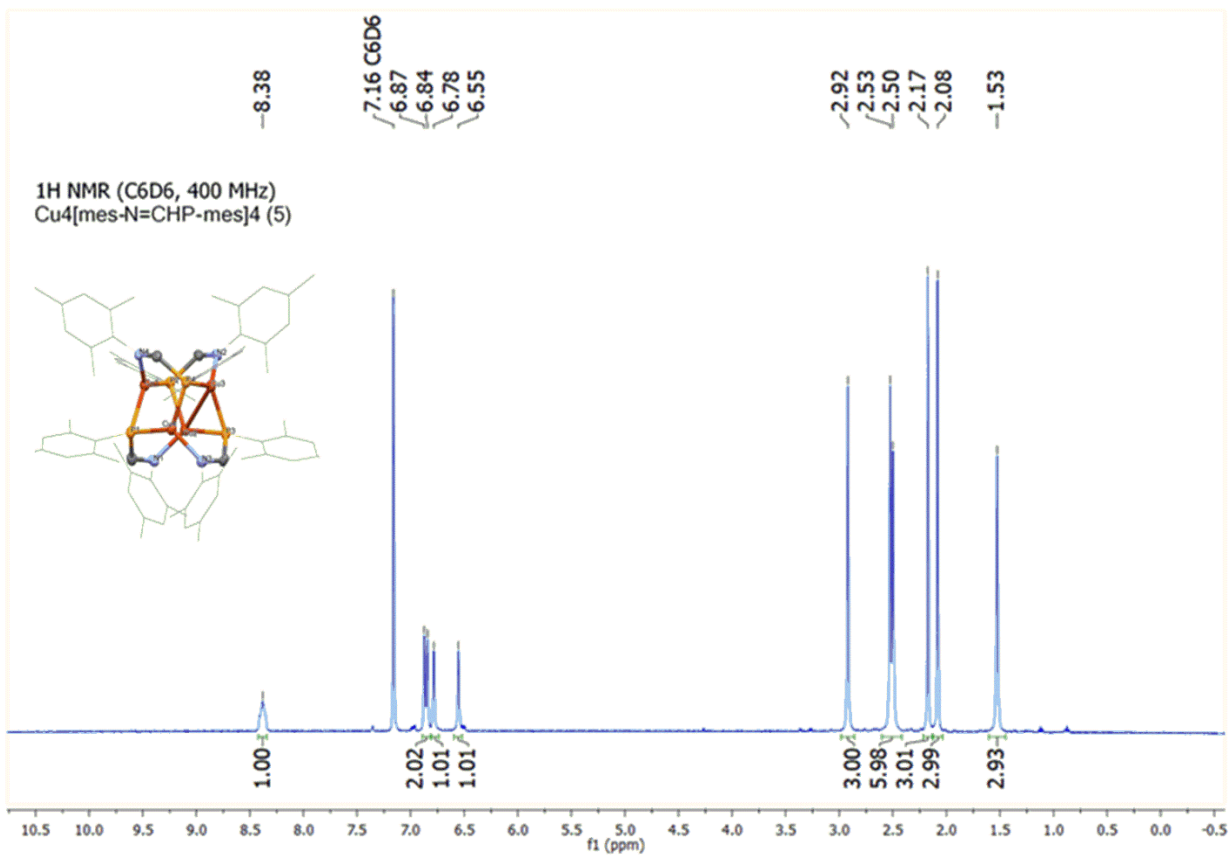
FIGURE S 48 ^{1}H NMR of complex **10**. ^{1}H NMR (400 MHz, C_6D_6) δ 8.38 (s, 1H), 6.87 (s, 1H), 6.84 (s, 1H), 6.78 (s, 1H), 6.55 (s, 1H), 2.92 (s, 3H), 2.53 (s, 3H), 2.50 (s, 3H), 2.17 (s, 3H), 2.08 (s, 3H), 1.53 (s, 3H).

31P NMR (C6D6, 162 MHz)
Cu4[mes-N=CHP-mes]4 (5)
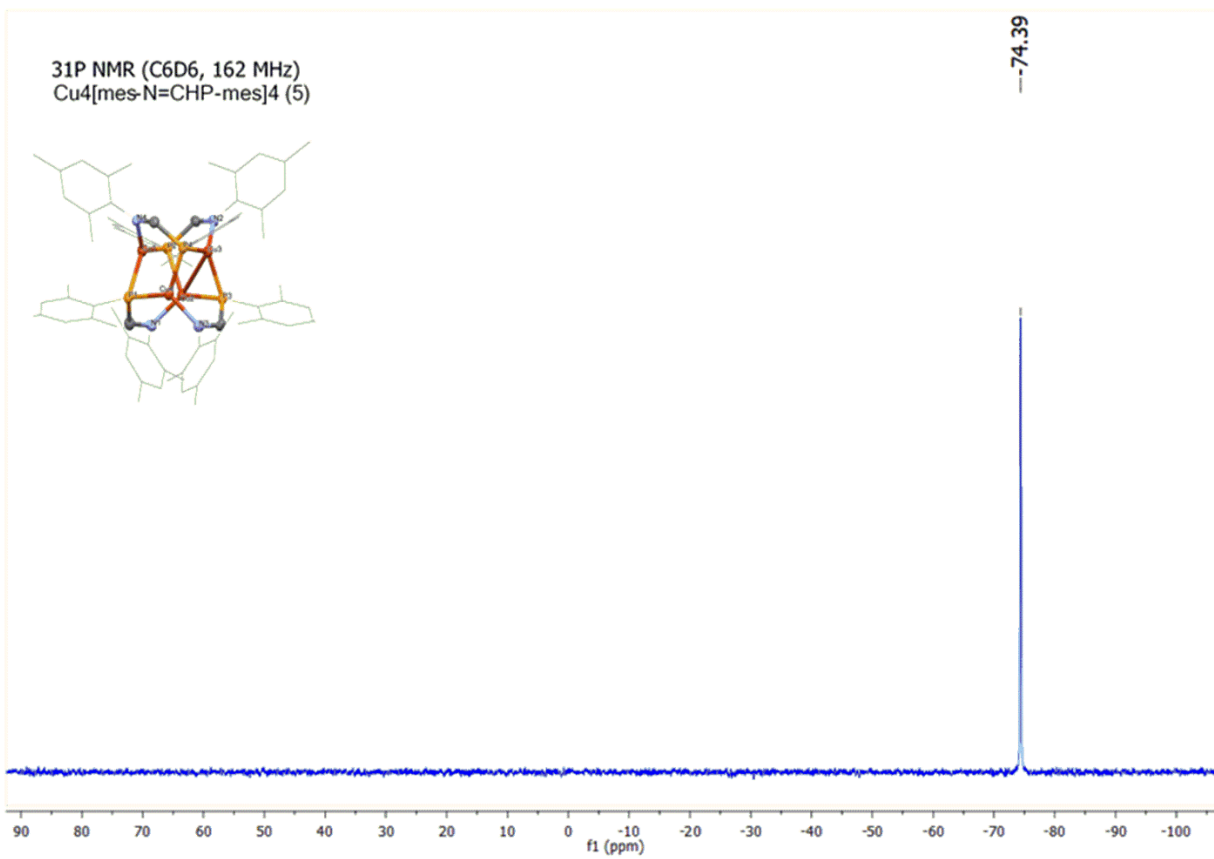
−−74.39

FIGURE S 49 ^{31}P{^{1}H} NMR of complex **10**. ^{31}P{^{1}H} NMR (162 MHz, C$_6$D$_6$) δ -74.39 (s).
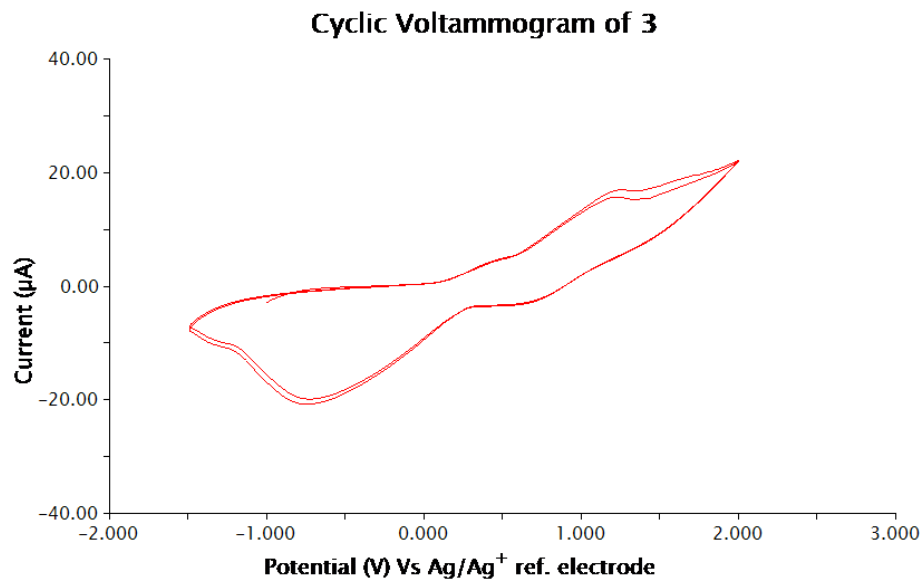
FIGURE S 50 Cyclic voltammogram of complex **9** (1.00x 10^{-3} M solution in 0.1 M Bu4NPF6/THF).
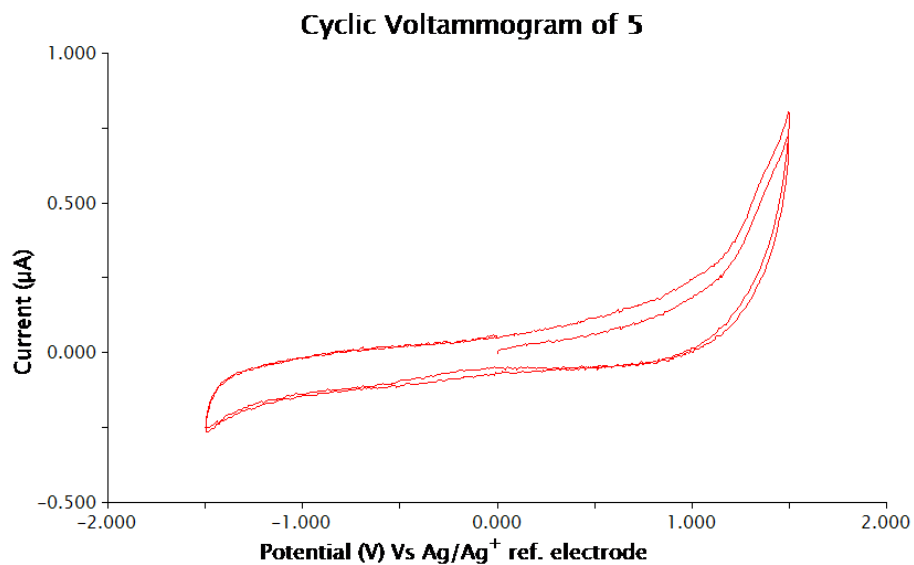
FIGURE S 51 Cyclic voltammogram of **10** (1.00 x 10^{-3} M solution in 0.1 M Bu4NPF6/THF).

UV-Vis spectroscopic analysis for the presence of trace amounts of 2-hole complexes.

The reactions between the precursors (**j'**, **k'**, **l'**, **m'** and **n'**) and S_8 were analyzed by UV-Vis spectrometry to prove (or disprove) the formation of corresponding 2-hole complexes. Intense purple color of a typical 2-hole complex results an absorbance around 560 cm^{-1}. All the reactions and preparations were carried out in a N_2 glove box.

A S_8 solution (0.5 eq) in toluene was added dropwise to a solution of precursor in THF. The resulted mixture was stirred for 3 days at 50 °C. Development of an intense purple color indicated the formation of the corresponding 2- hole complex. At the end, the solvent was completely evaporated leaving a dark solid. Small amount of solid was added with DCM (4 mL) and stirred for 15 min. It was filtered through a celite pipette into a UV-Vis cuvette fitted with a silicon septum cap. UV-Vis spectrum of each sample was recorded from 400 – 800 cm^{-1}.
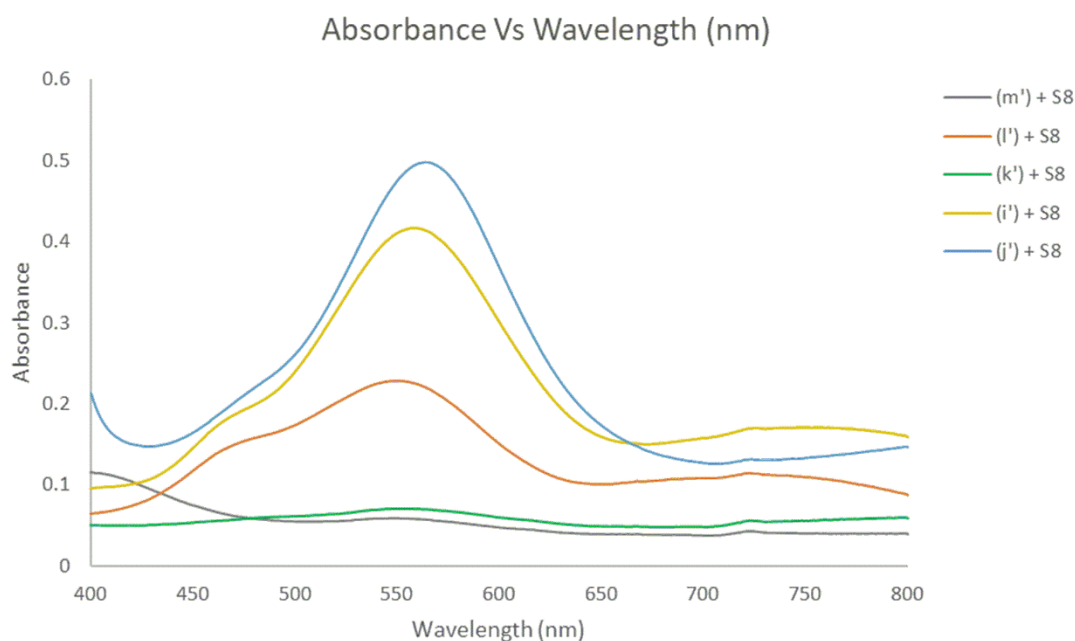
FIGURE S 52 The overlay of the graphs "Absorbance Vs Wavelength (nm)" for the reactions between precursors (**i'**, **j'**, **k'**, **l'** and **m'**) and S_8. **6i** (λ_{max} = 557 nm, ΔE = 215 kJ/mol), **6j** (λ_{max} = 564 nm, ΔE = 212 kJ/mol), **6l** (λ_{max} = 549 nm, ΔE = 218 kJ/mol). Absorption coefficients (ε) have not been given as the concentrations of the analyte in crude samples were not known.

Exact concentrations of the samples were unable to calculate as the reactions did not go to completion and the isolation of the pure 2-hole complexes was impossible. However, approximate dilutions were carried out to achieve a comparable absorbance (at λ_{max}) between the positive samples (samples that turned purple). The precursors **i'**, **j'** and

l' were able to reassemble in to a 2-hole complex while **k'** and **m'** were unable. This confirms that a steric factor greater than that of -CH$_3$ at the *ortho* positions (one or both) of the formamidinate ligand would destabilizes the formation of Cu$_4$(μ_4-S) assembly.

Structure refinement parameters

TABLE S 1 Sample and crystal data for complex (a')

Identification code	Cu2PCN2_a	
Empirical formula	C$_{52}$H$_{56}$Cu$_2$F$_{12}$N$_6$P$_4$	
Formula weight	1243.98 g/mol	
Temperature	100(2) K	
Wavelength	0.71073 Å	
Crystal size	0.210 x 0.280 x 0.760 mm	
Crystal system	monoclinic	
Space group	P 1 21/n 1	
Unit cell dimensions	a = 11.4946(6) Å	α = 90°
	b = 11.6650(6) Å	β = 102.3832(15)°
	c = 20.8075(10) Å	γ = 90°
Volume	2725.1(2) Å^3	
Z	2	
Density (calculated)	1.516 g/cm^3	
Absorption coefficient	0.981 mm^{-1}	
F(000)	1272	
Crystal size	0.21 x 0.28 x 0.76 mm^3	
Theta range for data collection	2.52 to 29.57°	
Index ranges	-15<=h<=15, -16<=k<=16, -28<=l<=28	
Reflections collected	43080	
Independent reflections	7611 [R(int) = 0.0685]	
Coverage of independent reflections	99.8%	
Absorption correction	Multi-scan	
Refinement method	Full-matrix least-squares on F^2	
Data / restraints / parameters	7611 / 0 / 348	
Goodness-of-fit on F^2	1.007	
Δ/σ$_{max}$	0.001	
Final R indices [5082 data; I>2σ(I)]	R1 = 0.0504, wR2 = 0.1367	
R indices (all data)	R1 = 0.0966, wR2 = 0.1694	
Largest diff. peak and hole	0.597 and -0.901 eÅ^{-3}	

TABLE S 2 Sample and crystal data for complex (**p'**)

Identification code	Cu2NP2_p	
Empirical formula	$C_{38}H_{32}Cu_2N_2P_2$	
Formula weight	705.67 g/mol	
Temperature	100(2) K	
Wavelength	0.71073 Å	
Crystal system	monoclinic	
Space group	P 1 21/c 1	
Unit cell dimensions	a = 19.2838(14) Å	$\alpha = 90°$
	b = 10.5574(8) Å	$\beta = 115.219(2)°$
	c = 17.5000(12) Å	$\gamma = 90°$
Volume	3223.2(4) Å^3	
Z	4	
Density (calculated)	1.454 g/cm^3	
Absorption coefficient	1.449 mm^{-1}	
F(000)	1448	
Crystal size	0.10 x 0.30 x 0.40 mm^3	
Theta range for data collection	2.25 to 26.16°	
Index ranges	-22<=h<=22, -11<=k<=12, -20<=l<=19	
Reflections collected	136240	
Independent reflections	5778 [R(int) = 0.1143]	
Coverage of independent reflections	89.7%	
Refinement method	Full-matrix least-squares on F^2	
Data / restraints / parameters	5778 / 0 / 399	
Goodness-of-fit on F^2	1.004	
Final R indices [4214 data; I>2σ(I)]	R1 = 0.0515, wR2 = 0.1191	
R indices (all data)	R1 = 0.0991, wR2 = 0.1451	
Largest diff. peak and hole	0.687 and -1.321 eÅ^{-3}	

TABLE S 3 Crystal data and structure refinement for complex **5**

Identification code	Cu4Cl4PCN2_5
Empirical formula	$C_{34} H_{44} Cl_4 Cu_2 N_2 P_2$
Formula weight	811.53 g/mol
Temperature	200(2) K
Wavelength	0.71073 Å
Crystal system	Monoclinic
Space group	C 1 2/c 1
Unit cell dimensions	a = 17.905(3) Å α = 90°
	b = 13.150(2) Å β = 101.137(6)°
	c = 16.242(2) Å γ = 90°
Volume	3752.2(11) Å^3
Z	4
Density (calculated)	1.437 g/cm^3
Absorption coefficient	1.530 mm^{-1}
F(000)	1672
Crystal size	0.11 x 0.17 x 0.32 mm^3
Theta range for data collection	2.19 to 26.73°
Index ranges	-22<=h<=20, -16<=k<=14, -19<=l<=15
Reflections collected	11468
Independent reflections	3752 [R(int) = 0.1168]
Coverage of independent reflections	94.2%
Absorption correction	Multi-scan
Max. and min. transmission	0.8500 and 0.6400
Refinement method	Full-matrix least-squares on F^2
Data / restraints / parameters	3752 / 0 / 210
Goodness-of-fit on F^2	1.165
Final R indices [I>2sigma(I)]	R1 = 0.0935, wR2 = 0.2220
R indices (all data)	R1 = 0.1349, wR2 = 0.2431
Largest diff. peak and hole	1.387 and -1.884 eÅ^{-3}

TABLE S 4 Crystal data and structure refinement for complex **7h**

Identification code	CHcryptand
Empirical formula	$C_{86}H_{112}Cu_4KN_{10}O_6S$
Formula weight	1707.17 g/mol
Temperature/K	100 (2) K
Crystal system	tetragonal
Space group	P43 21 2
Unit cell dimensions	a = 18.195 (2) $\alpha = 90°$
	b = 18.195 (2) $\beta = 90°$
	c = 58.198 (9) $\gamma = 90°$
Volume/Å^3	19267. (5)
Z	8
ρ_{calc}g/cm^3	1.177
μ/mm^{-1}	0.986
F(000)	7176
Crystal size/mm^3	0.2×0.1×0.1
Radiation	MoKα ($\lambda = 0.71073$ Å)
2Θ range for data collection/°	1.62 to 24.80
Index ranges	$-21 \le h \le 21, -20 \le k \le 20, -66 \le l \le 68$
Reflections collected	950792
Independent reflections	15757 [$R_{int} = 0.1945$]
Absorption correction	multi-scan
Refinement method	Full-matrix least-squares on F^2
Data/restraints/parameters	15757/2770/990
Goodness-of-fit on F^2	1.754
Final R indexes [I>=2σ (I)]	$R_1 = 0.0901$, w$R_2 = 0.2220$
Final R indexes [all data]	$R_1 = 0.1016$, w$R_2 = 0.2239$
Largest diff. peak/hole / e Å^{-3}	0.682/-1.047

TABLE S 5 Crystal data and structure refinement for **8**

Identification code	$Cu_4S(NCN-CF_3)_4$
Empirical formula	$C_{68}H_{52}N_8O_2F_{24}Cu_4$
Formula weight	1723.34
Temperature/K	100.00(10)
Crystal system	monoclinic
Space group	P2/c
Unit cell dimensions	a = 26.2035(2) α = 90°
	b = 8.37519(7) β = 100.0046(9)°
	c = 30.6475(3) γ = 90°
Volume/Å^3	6623.61(10)
Z	4
ρ_{calc}g/cm^3	1.728
μ/mm^{-1}	2.535
F(000)	3456.0
Crystal size/mm^3	0.3415 × 0.2793 × 0.1444
Radiation	CuKα (λ = 1.54184)
2Θ range for data collection/°	6.86 to 148.66
Index ranges	-32 ≤ h ≤ 32, -10 ≤ k ≤ 10, -36 ≤ l ≤ 38
Reflections collected	64797
Independent reflections	13309 [R_{int} = 0.0231, R_{sigma} = 0.0161]
Data/restraints/parameters	13309/0/957
Goodness-of-fit on F^2	1.033
Final R indexes [I>=2σ (I)]	R_1 = 0.0363, wR_2 = 0.0941
Final R indexes [all data]	R_1 = 0.0439, wR_2 = 0.1005
Largest diff. peak/hole / e Å^{-3}	0.87/-0.58

TABLE S 6 Crystal data and structure refinement for **9**

Identification code	neal1x4
Empirical formula	$C_{83}H_{97}LiN_3O_2P_3Cl_4Cu_6$
Formula weight	1791.52
Temperature/K	100.15
Crystal system	triclinic
Space group	P-1
a/Å	13.53456(18)
b/Å	13.7507(2)
c/Å	24.7864(4)
α/°	81.1953(12)
β/°	75.7315(12)
γ/°	65.3615(14)
Volume/Å^3	4057.01(11)
Z	2
ρ_{calc}g/cm^3	1.467
μ/mm^{-1}	3.849
F(000)	1844.0
Crystal size/mm^3	$0.216 \times 0.181 \times 0.053$
Radiation	CuKα (λ = 1.54184)
2Θ range for data collection/°	7.084 to 141.378
Index ranges	-16 ≤ h ≤ 16, -16 ≤ k ≤ 16, -30 ≤ l ≤ 30
Reflections collected	72560
Independent reflections	15263 [R_{int} = 0.0535, R_{sigma} = 0.0291]
Data/restraints/parameters	15263/0/947
Goodness-of-fit on F^2	1.032
Final R indexes [I>=2σ (I)]	R_1 = 0.0361, wR_2 = 0.0973
Final R indexes [all data]	R_1 = 0.0423, wR_2 = 0.1016
Largest diff. peak/hole / e Å^{-3}	0.64/-0.52
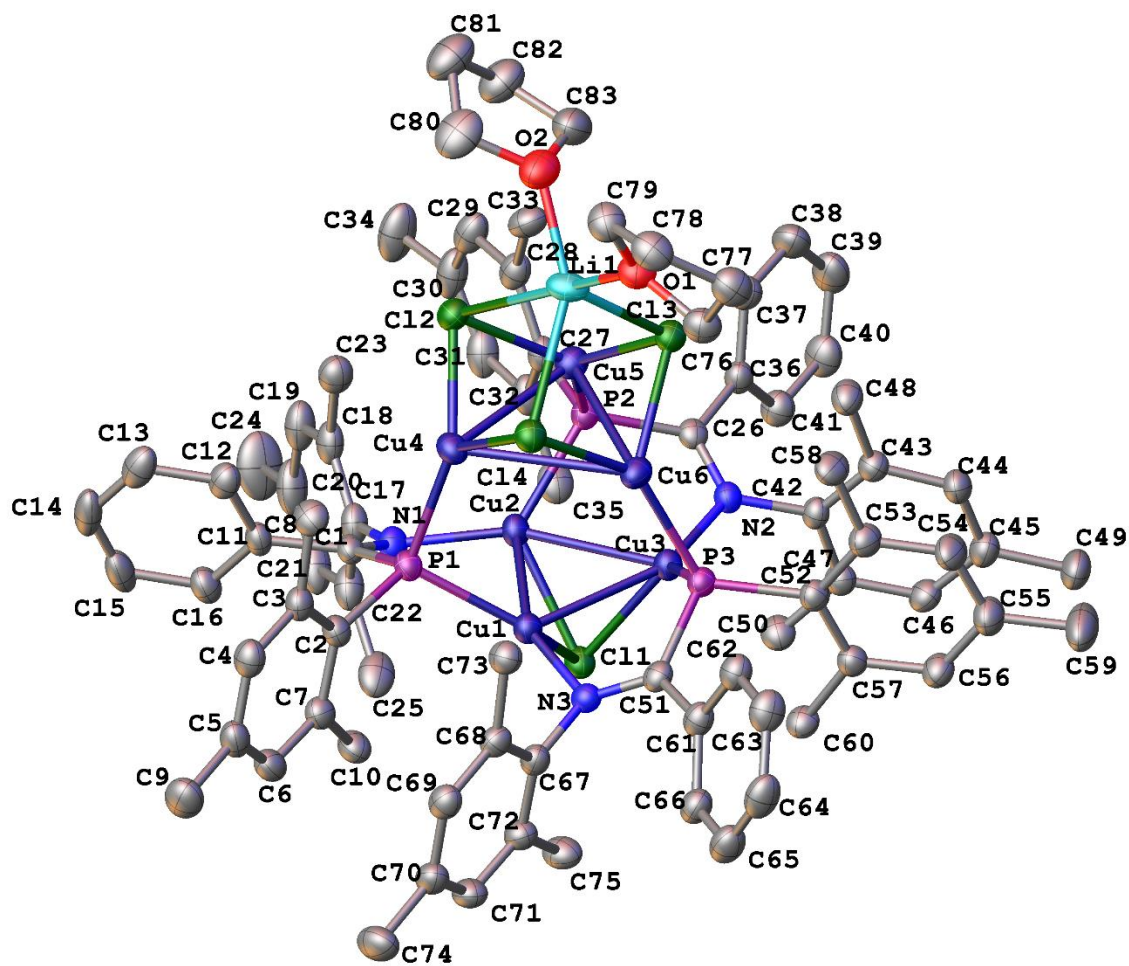
FIGURE S 53 Fully labeled ORTEP of **9** (50% probability ellipsoids). Hydrogen atoms have been omitted.
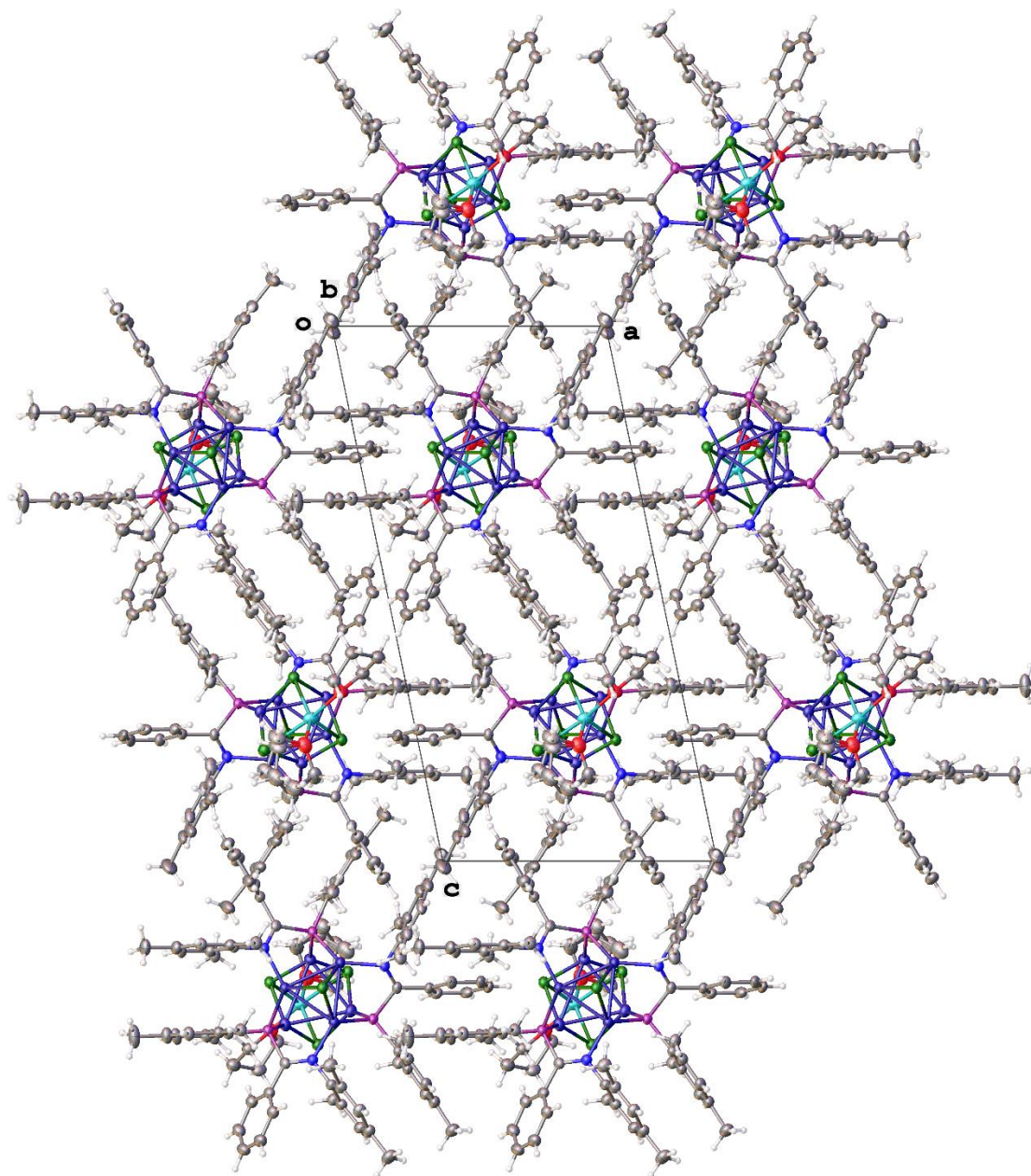
FIGURE S 54 Crystal packing of **9**. Mostly made by van-der-Waals forces (a limited stacking exists only between benzene rings C2…C7 through an inversion center).

TABLE S 7 Crystal data and structure refinement for **10**

Identification code	neal1y4
Empirical formula	$C_{76}H_{92}N_4P_4Cu_4$
Formula weight	1439.57
Temperature/K	100.15
Crystal system	monoclinic
Space group	Pn
a/Å	13.00013(17)
b/Å	12.77086(18)
c/Å	21.7987(3)
α/°	90
β/°	98.3082(15)
γ/°	90
Volume/Å^3	3581.11(9)
Z	2
ρ_{calc}g/cm^3	1.335
μ/mm^{-1}	2.512
F(000)	1504.0
Crystal size/mm^3	$0.173 \times 0.11 \times 0.057$
Radiation	CuKα (λ = 1.54184)
2Θ range for data collection/°	7.476 to 141.39
Index ranges	-15 ≤ h ≤ 15, -11 ≤ k ≤ 15, -26 ≤ l ≤ 25
Reflections collected	25529
Independent reflections	11248 [R_{int} = 0.0936, R_{sigma} = 0.0651]
Data/restraints/parameters	11248/2/818
Goodness-of-fit on F^2	1.062
Final R indexes [I>=2σ (I)]	R_1 = 0.0727, wR_2 = 0.2156
Final R indexes [all data]	R_1 = 0.0784, wR_2 = 0.2260
Largest diff. peak/hole / e Å^{-3}	1.34/-0.73
Flack parameter	0.16(5)
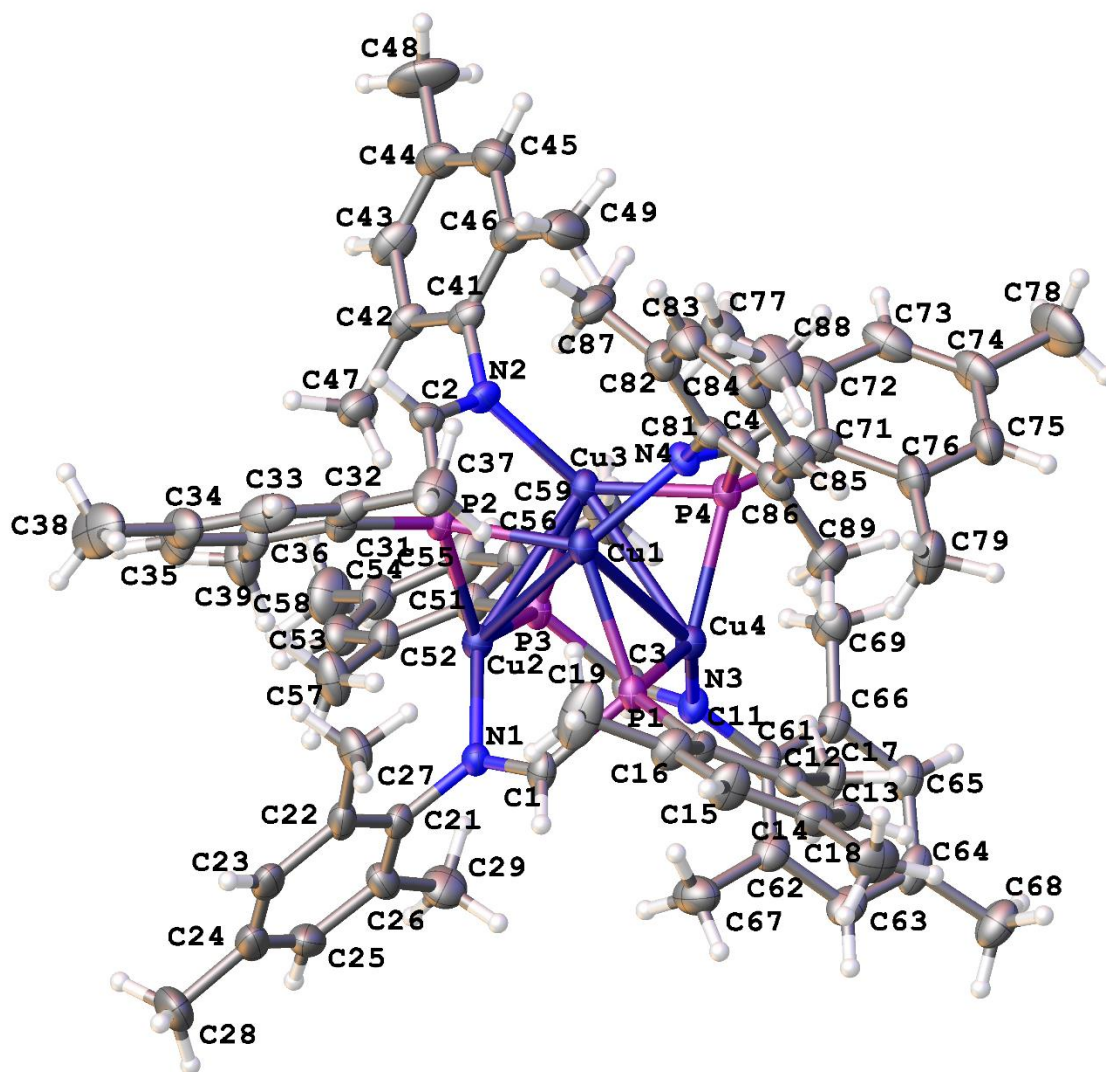
FIGURE S 55 Fully labeled ORTEP of **10** (50% probability ellipsoids). Hydrogen atoms have been omitted.
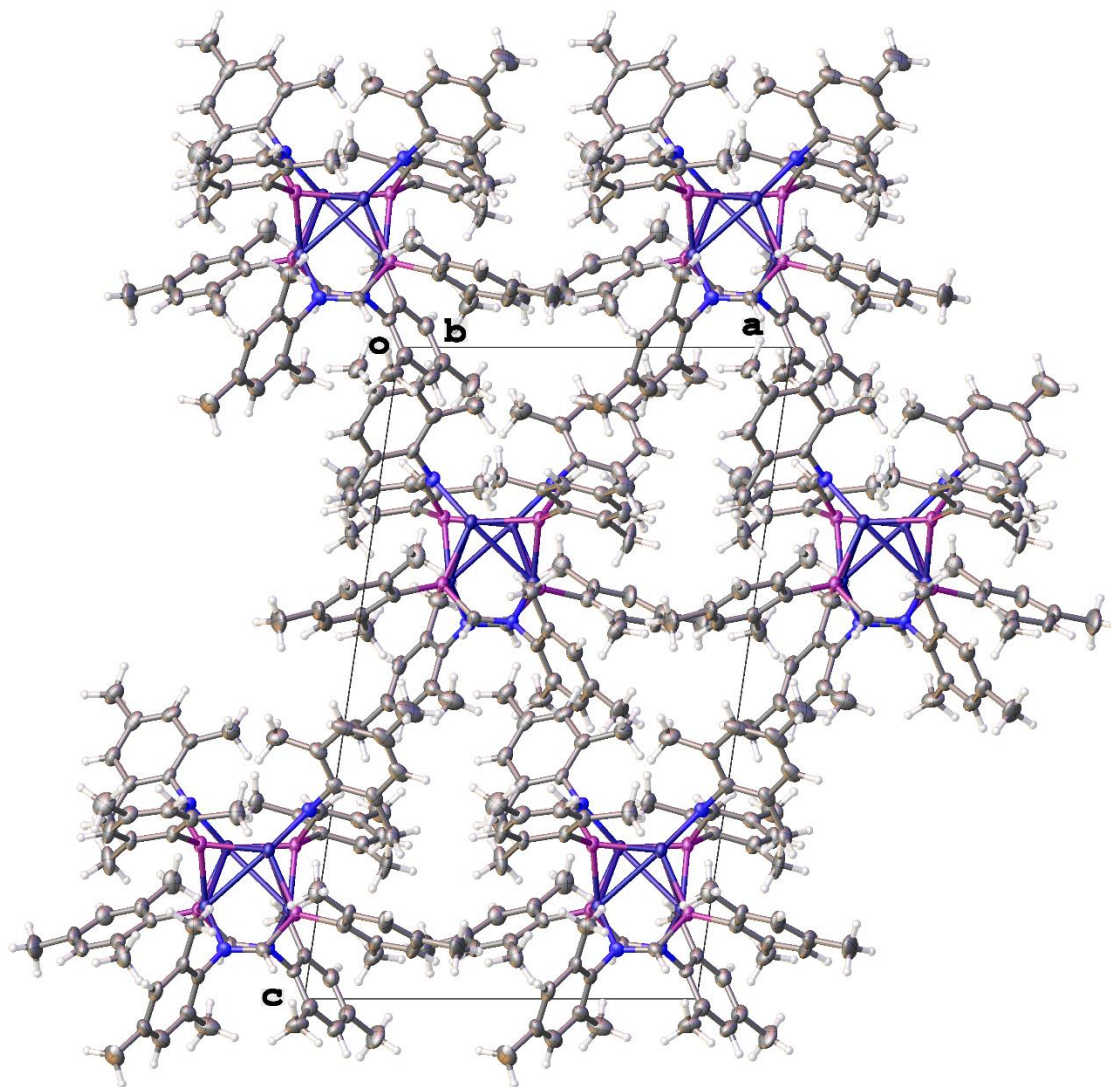
FIGURE S 56 Crystal packing of **10.** The crystal packing is discrete with the molecules joined only by van-der-Waals forces.

5.2   Supporting information for Chapter 3

Reproduced with the permission from Hsu, C.-W.; Rathnayaka, S. C.; Islam, S. M.; MacMillan, S. N.; Mankad, N. P. N₂O Reductase Activity of a [Cu₄S] Cluster in the 4Cu(I) Redox State Modulated by Hydrogen Bond Donors and Proton Relays in the Secondary Coordination Sphere. *Angew. Chemie Int. Ed.* **2020**, *59*, 627–631. RightsLink Printable License: Angewandte chemie international edition copyright 2011.

5.2.1   General Information and instrumentation

All solvents except methanol and acetone were purchased from commercial suppliers, purified under argon with a Glass Contour Solvent System built by Pure Process Technology, and stored in a N₂-filled glovebox over 4-Å molecular sieves. Methanol (extra dry) was purchased from Alfa Aesar and Acros, followed by the extra addition of 4-Å molecular sieves for storage in the glovebox. Acetone (extra dry) was purchase from Acros and treated with extra molecular sieves for further purification. Deuterated solvents were purified with 4-Å molecular sieves before use. All reactions were operated under N₂ with standard glovebox and Schlenk line techniques. Medical grade nitrous oxide was purchased from Praxair and passed through a Drierite column for delivery to reaction vessels.

NMR spectra for compound characterization were recorded at ambient temperature using Bruker Avance DPX-400. Chemical shifts are reported in ppm units relative to the residual signal of the solvent. The NearIR spectrum was collected with a Bruker Tensor II instrument using a 10-mm pathlength quartz cell. X-ray diffraction data for **2** (grown from MeOH/Et₂O) and **3** were collected on a Rigaku XtaLAB Synergy diffractometer coupled to a Rigaku Hypix detector with Cu Kα radiation (λ = 1.54184 Å), from a PhotonJet micro-focus X-ray source at 100 K. The diffraction images were processed and scaled using the CrysAlisPro software.[i] The structure was solved through intrinsic phasing using SHELXT[ii] and refined against F^2 on all data by full-matrix least squares with SHELXL[iii] following established refinement strategies.[iv] All non-hydrogen atoms were refined anisotropically. All hydrogen atoms bound to carbon were included in the model at geometrically calculated positions and refined using a riding model. Hydrogen atoms bound to nitrogen or oxygen were located in the difference Fourier synthesis and subsequently refined semi-freely with the help of distance restraints. The isotropic displacement parameters of all hydrogen atoms were fixed to 1.2 times the Ueq value of the atoms they are linked to (1.5 times for methyl groups). For **3**, a THF

solvent molecule was included in the unit cell but could not be satisfactorily modeled. Therefore, that solvent was treated as a diffuse contribution to the overall scattering without using specific atom positions by the solvent masking function in Olex2.[v] Details of the data quality and a summary of the residual values of the refinements are listed in **Tables S13** and **S14**. Synthesis of **1, 2** was based on the procedure of the reported literature.[vi] N_2 samples for calibration curve (upto 10 µL) were syringed using Hamilton gas tight syringe (10 µL, Model 1801 RN, Small Removable Needle, 26s gauge, 2 in, point style 2). Reaction and control head space gas samples (50 µL) were collected using Hamilton gas tight syringe (100 µL, Model 1710 SL SYR, customized Removable NDL (1 inch), 22s ga, 2 in, point style 2). GCMS data were collected using Agilent 5977B MSD sytem coupled to Agilent 7820A GC system with a CP-Molseieve 5A column (All the other instrument, column and inlet control parameters are povided in **Table S11** and **S12**. GCMS Data analysis was performed using Agilent MassHunter Analysis Navigator B.08.00 software.

Computational details

All the electronic structure calculations were carried out with Gaussian16.[vii] Input geometries for the dicationic portions of **1** and **2** were obtained from crystallographic coordinates, removing all co-crystallized anions and solvent molecules other than the one methanol molecule hydrogen bonded to **2**. Both single-point energy calculations and geometry optimizations were carried out at the B3LYP level of theory using the 6-31++G** basis set and PCM implicit solvation model for the MeOH solvent. The optimized structures were practically identical to the crystallographic coordinates regarding [Cu$_4$S] core structures, and so results from the single-point energy calculations are presented here. A depiction of the key occupied MO that changes between **1** and **2** is depicted in the main text at 0.04 isosurface value, and all other MOs near the HOMO level were very similar between the two compounds. NBO charges for the individual atoms within each [Cu$_4$S] core are shown in the main text. Comparison of the LUMO surfaces for the two compounds is presented below.

5.2.2   Solvent dependence of the reactions between complex **2** and N_2O

N_2O Reduction by {Cu$_4$(μ$_4$-S)[bis(diphenylphosphino)amine]$_4$}(PF$_6$)$_2$ (2) with the Addition of CoCp$_2$ (2 eq) in Methanol

In the glovebox, {Cu$_4$(μ$_4$-S)[bis(diphenylphosphino)amine]$_4$}(PF$_6$)$_2$ (**2**) (30 mg, 0.014 mmol), was added in a 100 mL vessel charged with dry MeOH (15 mL). While bubbling N_2O into the solution, a CoCp$_2$ solution (6 mg, 0.032 mmol in 1 mL dry MeOH) was added dropwise into the vessel over 2 minutes. After bubbling N_2O for an additional 5 minutes, the vessel was closed and kept stirring for one hour. Then the solvent was evaporated under vacuum and the compound was extracted in the following steps: First, use 5 mL (1 mL × 5) toluene, then 3 mL (1 mL × 3) THF to extract compounds (two batches) and filter the solution off to collect the filtrate. After the solvent removal of the filtrate *in vacuo*, use minimal acetone (0.5 mL × 6) to extract compounds from the collection of filtrates, then slowly evaporate the acetone. Finally, 3 mL (1 mL × 3) toluene was utilized to extract the dicopper complex **3**, followed by the collection of filtrates and the evaporation of toluene. Orange complex **3** was recrystallized at room temperature with slow diffusion of pentane into a THF solution, or at –20 °C in tetrahydrofuran layered with pentane. Recrystallization yield is 67% (12 mg, 0.009 mmol). ^{1}H NMR (400 MHz, acetone-d_6): δ 7.46 (br, 10 H, C$_6$H$_5$), 7.28 (br, 10 H, C$_6$H$_5$), 7.25–7.16 (m, 10 H, C$_6$H$_5$), 7.04–6.92 (m, 20 H, C$_6$H$_5$), 6.82–6.78 (m, 10 H, C$_6$H$_5$), 3.75 (s, 1 H, PPh$_2$–N(*H*)–PPh$_2$). ^{31}P NMR (162 MHz, acetone-d_6): δ 45.3 (dd, J = 51 Hz, 67 Hz, 4 P, *P*Ph$_2$–N–*P*Ph$_2$), 36.5 (m, 2 P, *P*Ph$_2$–N(H)–*P*Ph$_2$). Elemental analysis calculated (%) for **3**: C, 67.50; H, 4.80; N, 3.28; found: C, 67.15; H, 5.05; N, 3.21. To determine the NMR yield, 10 mg of **2** (0.005 mmol) and 2 mg of CoCp$_2$ (0.011 mmol) were utilized with the same protocol. After the N_2O reduction, the reaction solvent was evaporated under vacuum and 0.7 mL acetone-d_6 was added to extract compounds, followed by the filtration. The filtrate was mixed with 4 mg tri-*o*-tolylphosphine (0.013 mmol) as the internal standard (labeled as "IS" in the NMR spectra). The crude ^{1}H NMR shows the characteristic peaks of **3** overlapping with the internal standard. Based on the crude ^{31}P NMR (45 and 36 ppm, *P*Ph$_2$–N–*P*Ph$_2$ and *P*Ph$_2$–N(H)–*P*Ph$_2$ of **3** respectively), the yield of **3** is 90%.
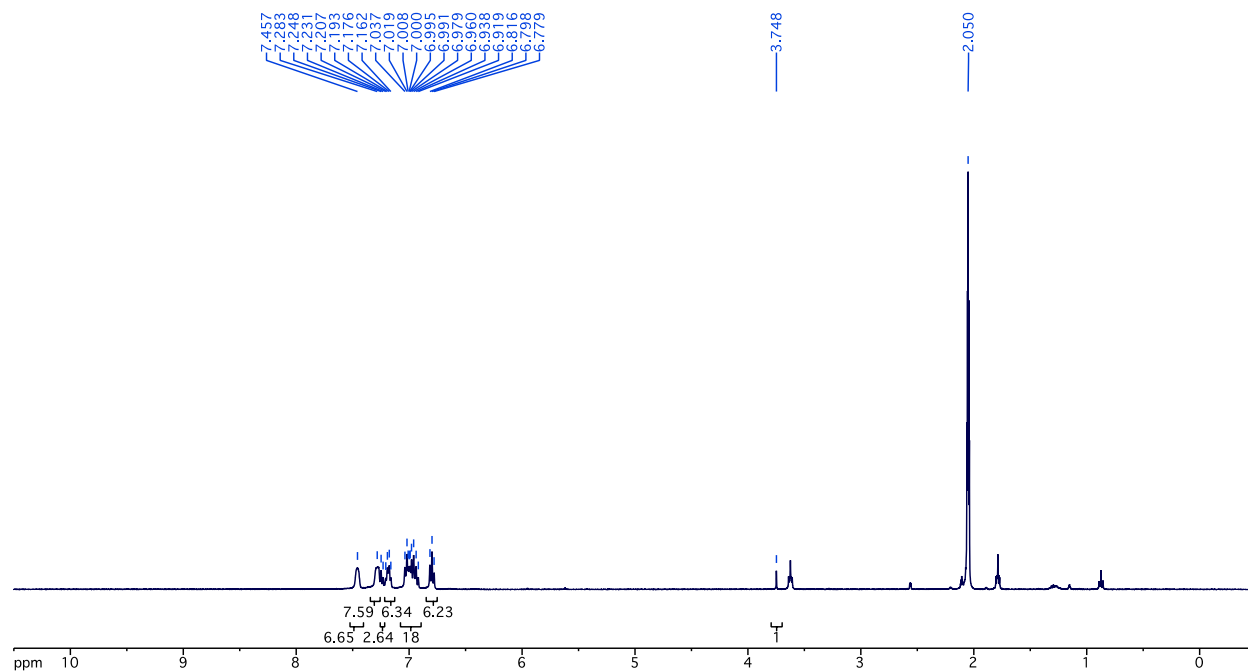
FIGURE S 57 ^{1}H NMR (400 MHz, acetone-d_6) spectrum of complex **3**.
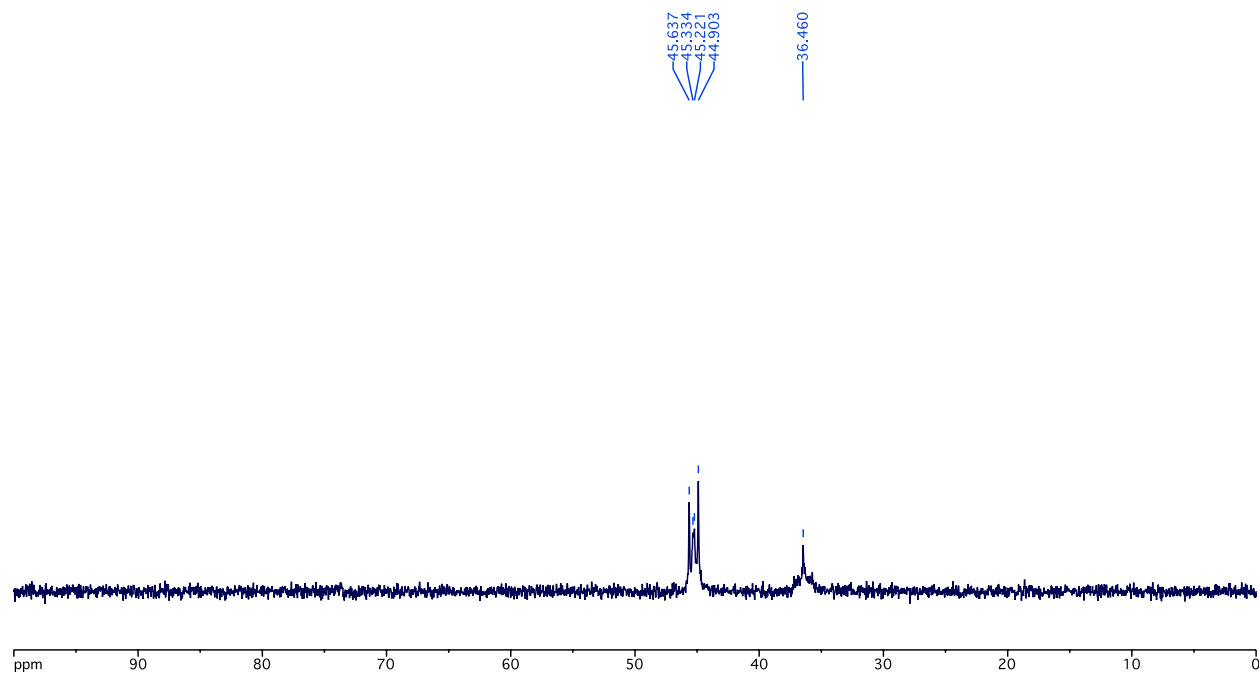
FIGURE S 58 ^{31}P {^{1}H} NMR (162 MHz, acetone-d_6) spectrum of complex **3.**
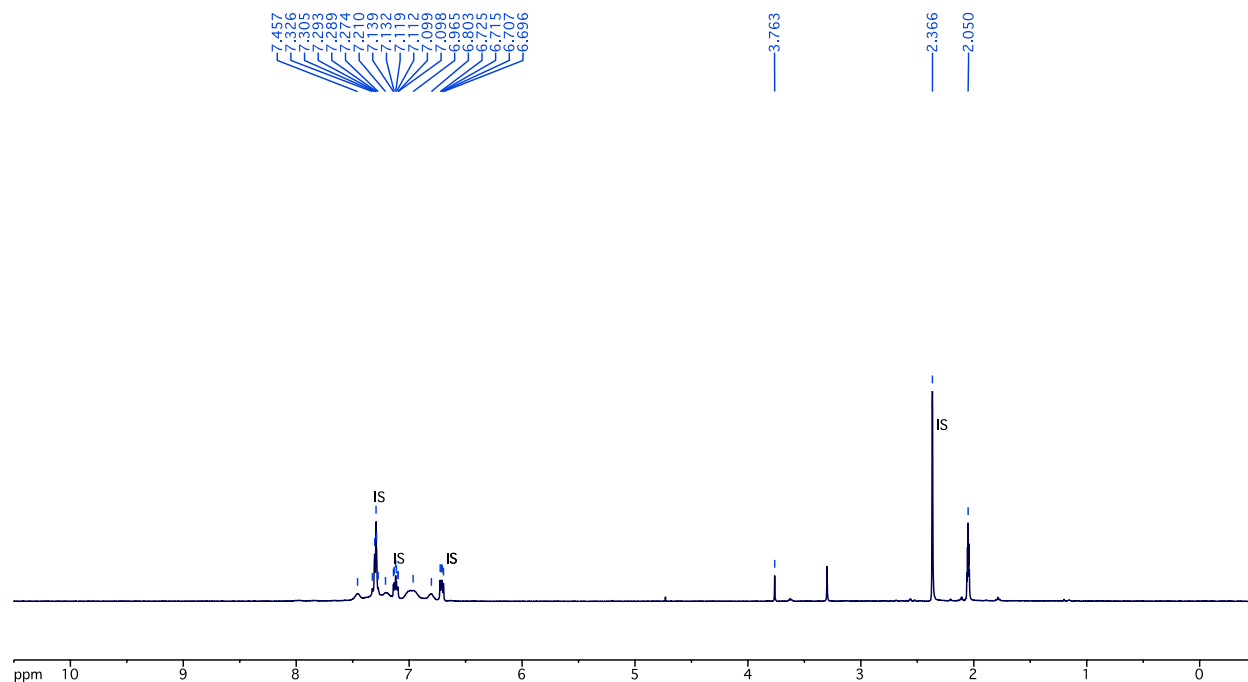
FIGURE S 59 ^{1}H NMR (400 MHz, acetone-d_6) spectrum of complex **3** - NMR yield.
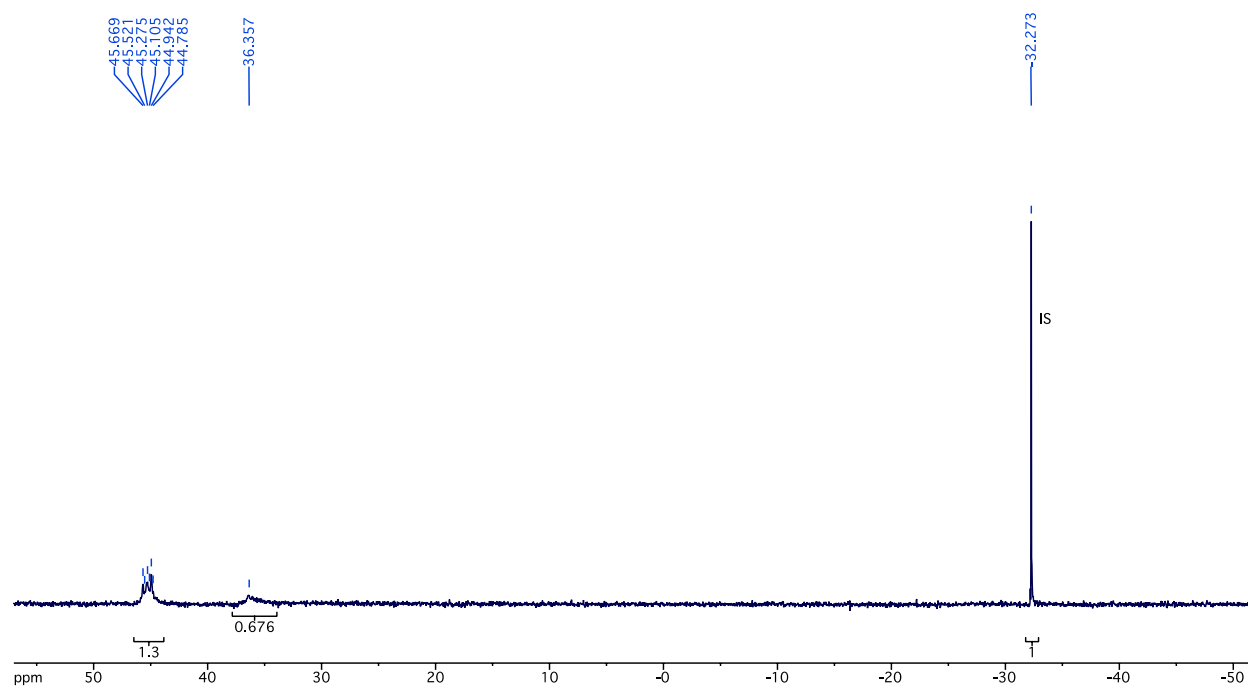
FIGURE S 60 ^{31}P {^{1}H} NMR (162 MHz, acetone-d_6) spectrum of complex **2** - NMR yield.

N₂O Reduction by {Cu₄(μ₄-S)[bis(diphenylphosphino)amine]₄}(PF₆)₂ (2) with the Addition of CoCp₂ (2 eq) in Acetone

In the glovebox, {Cu₄(μ₄-S)[bis(diphenylphosphino)amine]₄}(PF₆)₂ (**2**) (10 mg, 0.005 mmol) was added in a 20 mL sample vial charged with dry acetone (5 mL). While bubbling N₂O into the solution, a CoCp₂ solution (2 mg, 0.011 mmol in 1 mL dry acetone) was added dropwise into the vial over 2 minutes. After bubbling N₂O for another 5 minutes, the vial was closed and kept stirring for one hour. Then the solvent was evaporated under vacuum and 0.7 mL acetone-d_6 was added to extract compounds. After the filtration, the collected filtrate was mixed with 4 mg tri-*o*-tolylphosphine (0.013 mmol) as the internal standard (labeled as "IS" in the NMR spectra). The crude ¹H NMR shows the featuring peaks of **3** (δ 7.46, 7.28, 7.25–7.16, 7.04–6.92, and 6.82–6.78 from phenyls of **3**) overlapped with other unknown products and the internal standard. Based on the crude ³¹P NMR (45 and 37 ppm, PPh_2–N–PPh_2 and PPh_2–N(H)–PPh_2 of **3** respectively), the yield of **3** is 42%.
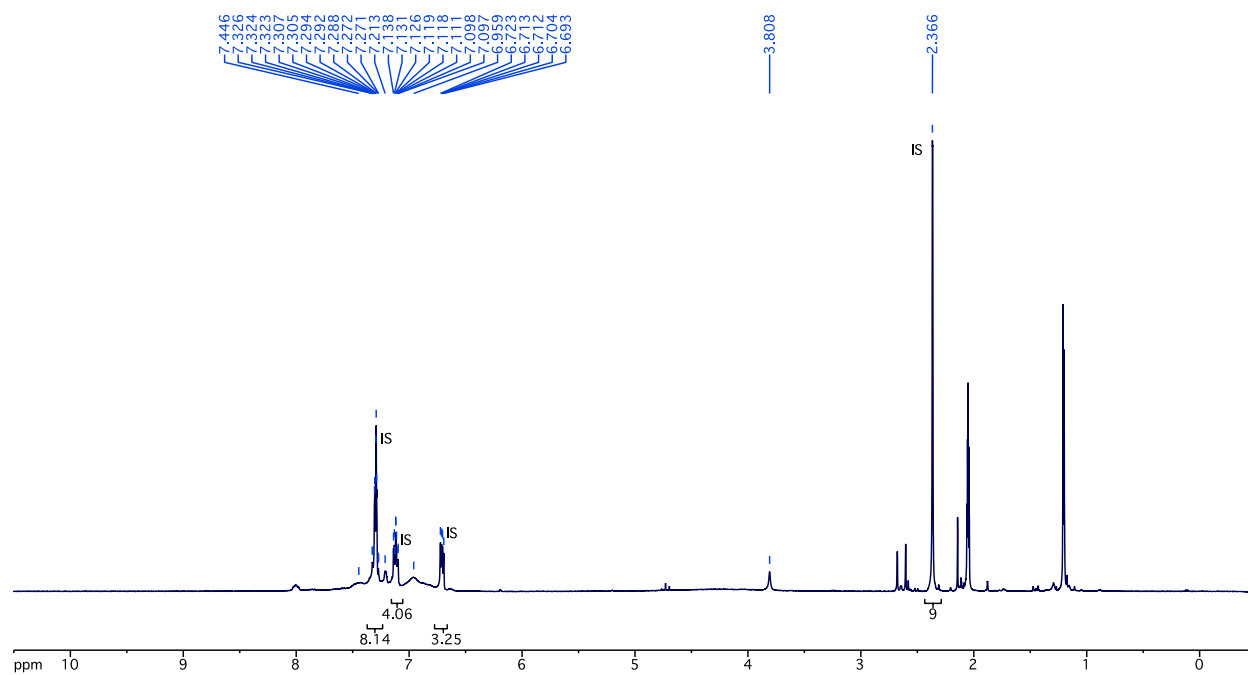
FIGURE S 61 Crude ¹H NMR (400 MHz, acetone-d_6) spectrum of N₂O reduction by complex **2** with the addition of CoCp₂ in acetone.
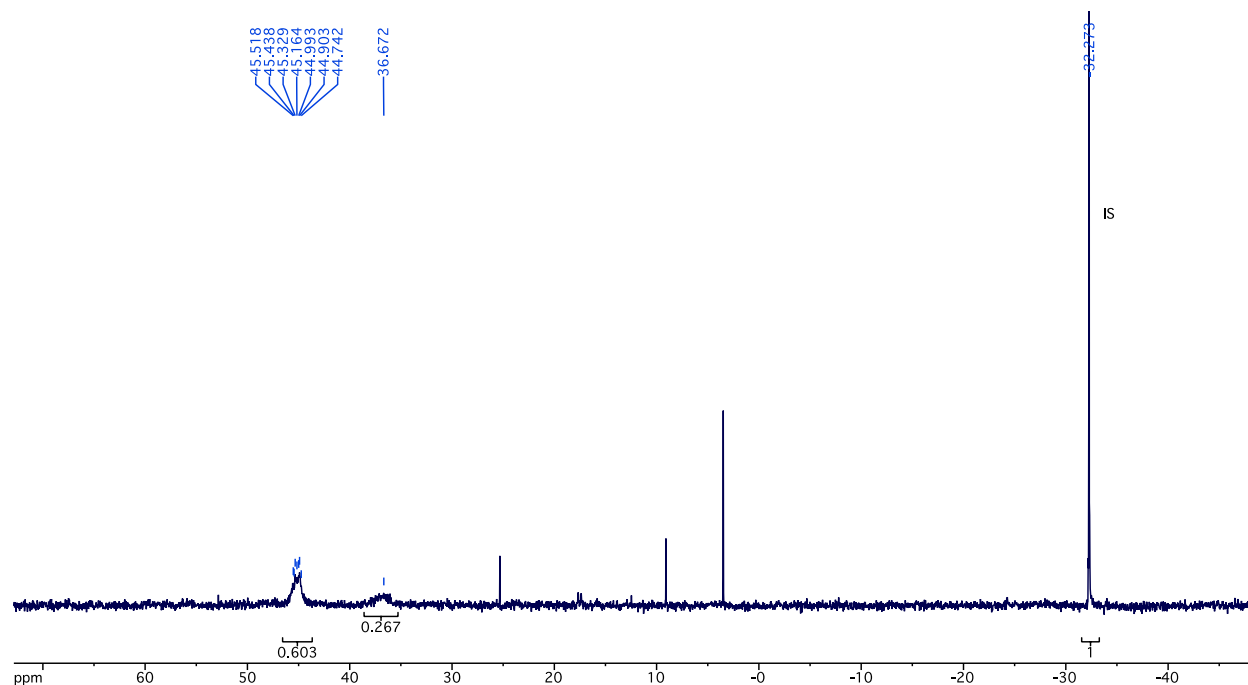
FIGURE S 62 Crude $^{31}P\{^1H\}$ NMR (162 MHz, acetone-d_6) spectrum of N$_2$O reduction by complex **2** with the addition of CoCp$_2$ in acetone.

The Reaction of {Cu$_4$(µ$_4$-S)[bis(diphenylphosphino)amine]$_4$}(PF$_6$)$_2$ (2) and N$_2$O with the Addition of CoCp$_2$ (2 eq) in Tetrahydrofuran

In the glovebox, {Cu$_4$(µ$_4$-S)[bis(diphenylphosphino)amine]$_4$}(PF$_6$)$_2$ (**2**) (30 mg, 0.014 mmol) was added in a 20 mL vial charged with 15 mL THF. While bubbling N$_2$O into the solution, a CoCp$_2$ solution (6 mg, 0.032 mmol in 1 mL THF) was added dropwise into the vial over 2 minutes. After bubbling N$_2$O for another 5 minutes, the vessel was closed and kept stirring for one hour. After the solvent removal in vacuum, use 5 mL (1 mL × 5) toluene to wash the mixture, then 4 mL (1 mL × 4) THF to extract the major product and collect the THF filtrate. Evaporate the THF and 30 mg crude compounds were obtained. Prepare the NMR sample using ~0.7 mL acetone-d_6 to dissolve the compounds and filter the solution into a vial charged with 5 mg tri-o-tolylphosphine (0.016 mmol) as the internal standard (labeled as "IS" in the NMR spectra). ^1H NMR (400 MHz, acetone-d_6): δ 7.42–7.08 (m, integral not determined due to peak overlap between phenyls from **2**, **2'** and the internal standard), 3.77 (s, N–H of **2'**). $^{31}P \{^1H\}$ NMR (162 MHz, acetone-d_6): δ 36.5 (s, PPh$_2$–N(H)–PPh$_2$ of **2**), 35.4 (s, PPh$_2$–N(H)–PPh$_2$ of **2'**). Based on the crude ^{31}P NMR, the major product is **2** in 38% yield with decomposed species **2'** in 48%.
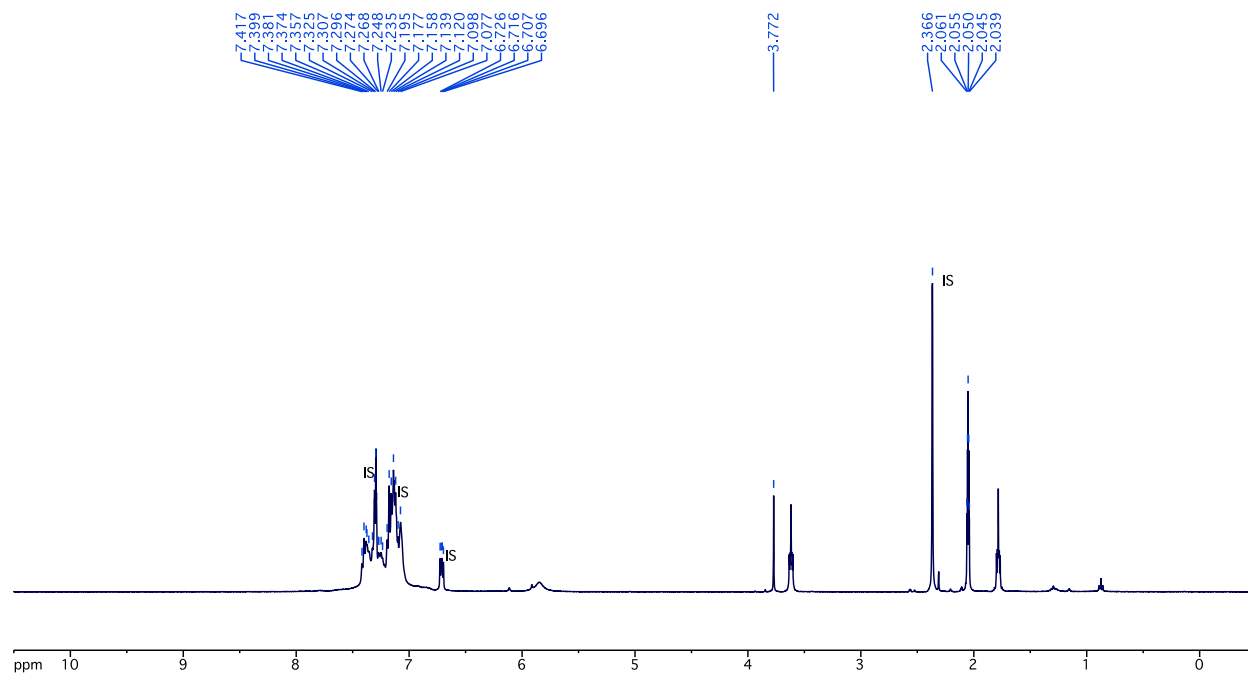
FIGURE S 63 Crude ^{1}H NMR (400 MHz, acetone-d_6) spectrum of the reaction between N$_2$O and complex **2** with the addition of CoCp$_2$ in tetrahydrofuran.
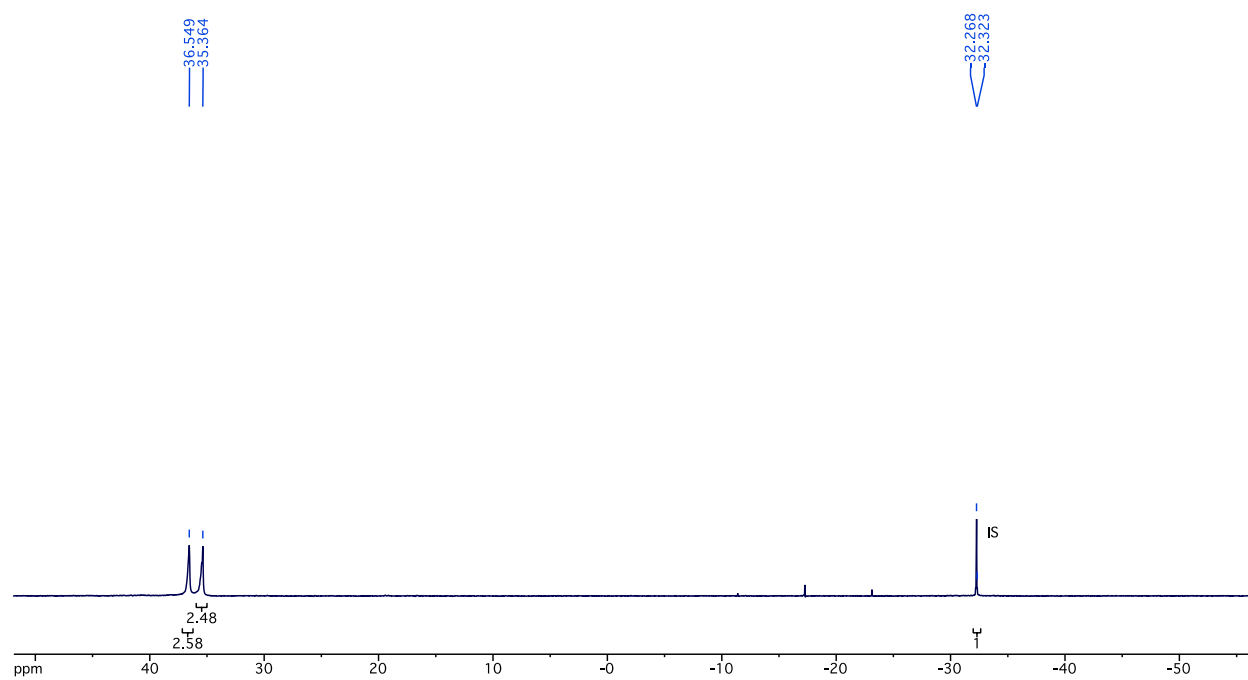
FIGURE S 64 Crude ^{31}P{^{1}H} NMR (162 MHz, acetone-d_6 spectrum of the reaction between N$_2$O and complex **2** with the addition of CoCp$_2$ in tetrahydrofuran.

The Reaction of {Cu$_4$(μ$_4$-S)[bis(diphenylphosphino)amine]$_4$}(PF$_6$)$_2$ (2) and N$_2$O with the Addition of CoCp$_2$ (2 eq) in Toluene

In the glovebox, 30 mg of {Cu$_4$(μ$_4$-S)[bis(diphenylphosphino)amine]$_4$}(PF$_6$)$_2$ (2) (0.014 mmol), was added in a 20 mL vial, charged with 15 mL toluene. With bubbling N$_2$O into the solution, the CoCp$_2$ solution (6 mg (0.032 mmol) of CoCp$_2$ in 1 mL toluene) was added dropwise into the vial for 2 minutes. After bubbling N$_2$O for 5 minutes, the vial was closed and kept stirring for one hour. After the solvent removal in vacuum, use 5 mL (1 mL × 5) toluene to wash the mixture, then 4 mL (1 mL × 4) THF to extract the major product and collect the THF filtrate. Evaporate the THF and 30 mg crude compounds were obtained. Prepare the NMR sample using ~0.7 mL acetone-d_6 to dissolve the compounds and filter the solution into a vial charged with 5 mg tri-o-tolylphosphine (0.016 mmol) as the internal standard (labeled as "IS" in the NMR spectra). ^{1}H NMR (400 MHz, acetone-d_6): δ 7.42–7.08 (m, integral not determined due to peak overlap between phenyls from **2, 2'** and the internal standard), 3.77 (s, N–H of **3**). ^{31}P {^{1}H} NMR (162 MHz, acetone-d_6): δ 36.6 (s, PPh$_2$–N(H)–PPh$_2$ of **2**), 35.4 (s, PPh$_2$–N(H)–PPh$_2$ of **2'**). Based on the ^{31}P NMR, the major product is **2** in 67% yield with decomposed species **2'** in 6%.
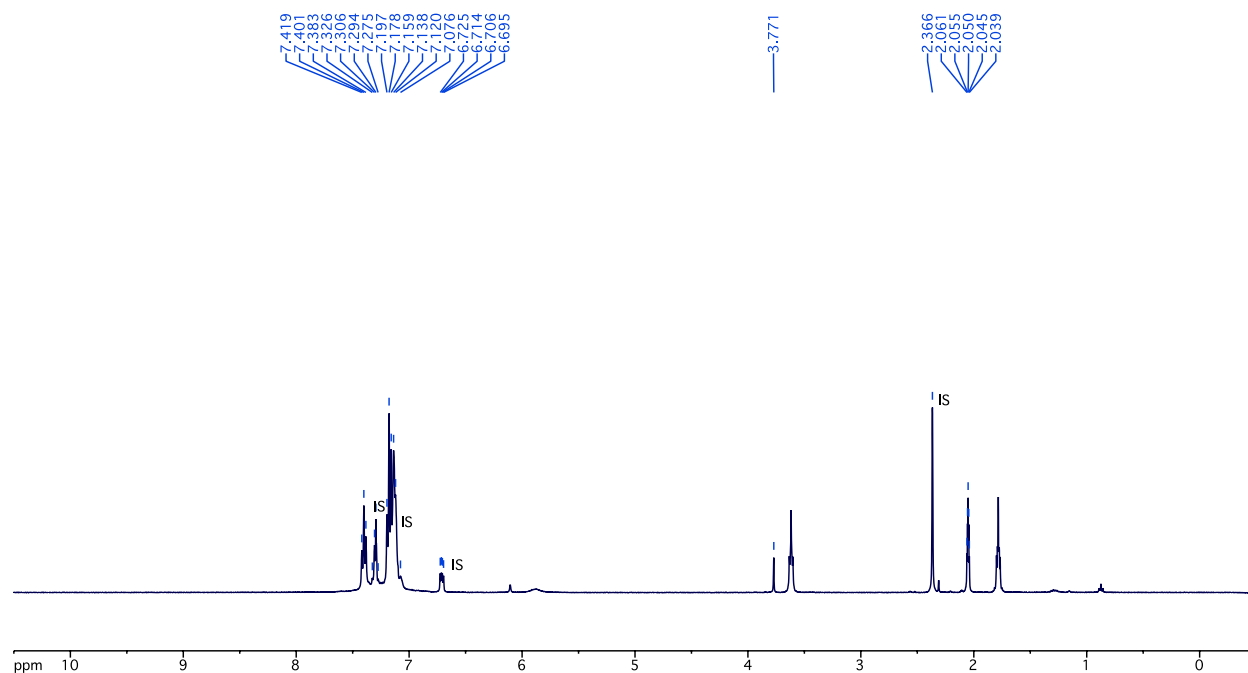
FIGURE S 65 Crude ^{1}H NMR (400 MHz, acetone-d_6) spectrum of the reaction between N$_2$O and complex **2** with the addition of CoCp$_2$ in toluene.
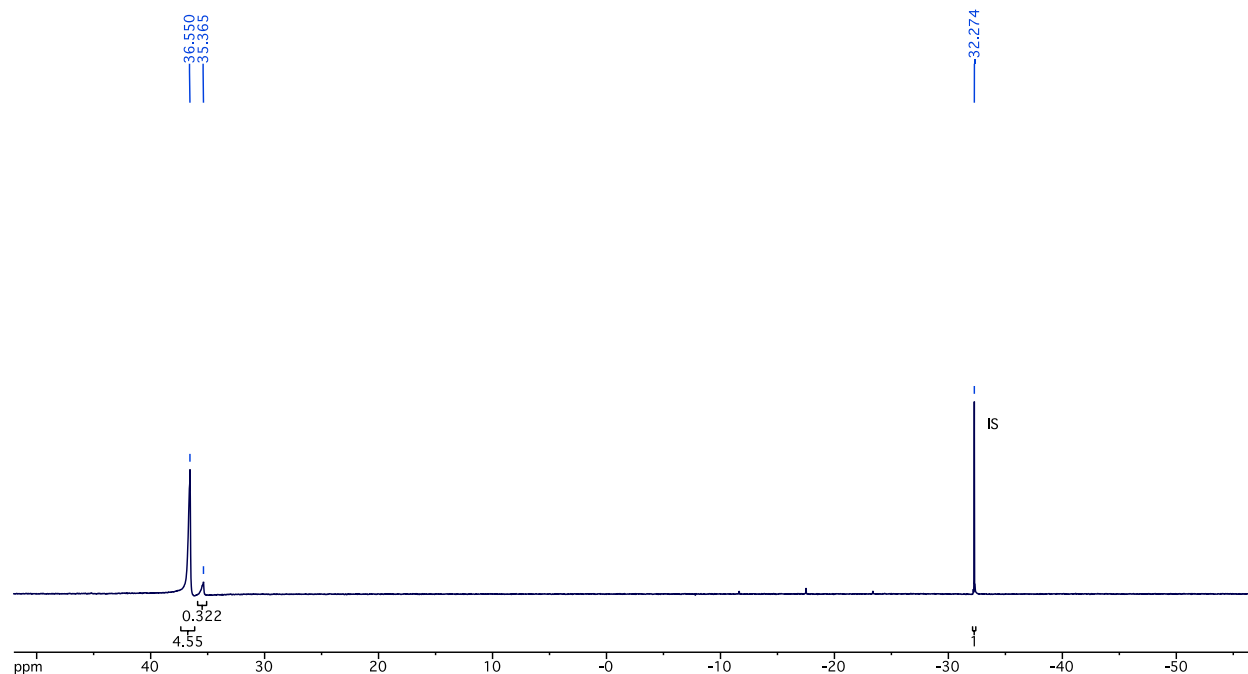
FIGURE S 66 Crude ^{31}P{^{1}H} NMR (162 MHz, acetone-d_6) spectrum of the reaction between N$_2$O and complex **2** with the addition of CoCp$_2$ in toluene.

The Reaction of {Cu$_4$(μ$_4$-S)[bis(diphenylphosphino)amine]$_4$}(PF$_6$)$_2$ (2) and N$_2$O with the Addition of CoCp$_2$ (2 eq) in Methanol-d_4

In the glovebox, 10 mg of {Cu$_4$(μ$_4$-S)[bis(diphenylphosphino)amine]$_4$}(PF$_6$)$_2$ (**2**) (0.005 mmol) and 2 mg CoCp$_2$ (0.011 mmol) was added in a Schlenk tube, charged with 1 mL MeOH-d_4. Bring the Schlenk tube out of the glovebox, followed by the freeze-pump-thaw technique three times to remove N$_2$ from the solvent. Warm up the tube to room temperature and refill it with N$_2$O. Keep the solution stirring for one hour and then bring the tube back to the glovebox for NMR sample preparation. Use 4 mg tri-o-tolylphosphine (0.013 mmol) as the internal standard for NMR yield calculation (labeled as "IS" in the NMR spectra). ^{1}H NMR (400 MHz, methanol-d_4): δ 7.32–7.00 (m, phenyls of **2**). ^{31}P {^{1}H} NMR (162 MHz, methanol-d_4): δ 36.3 (s, PPh$_2$–N(H)–PPh$_2$ of **2**). Based on the ^{31}P NMR, the major product is **2** (77% yield).
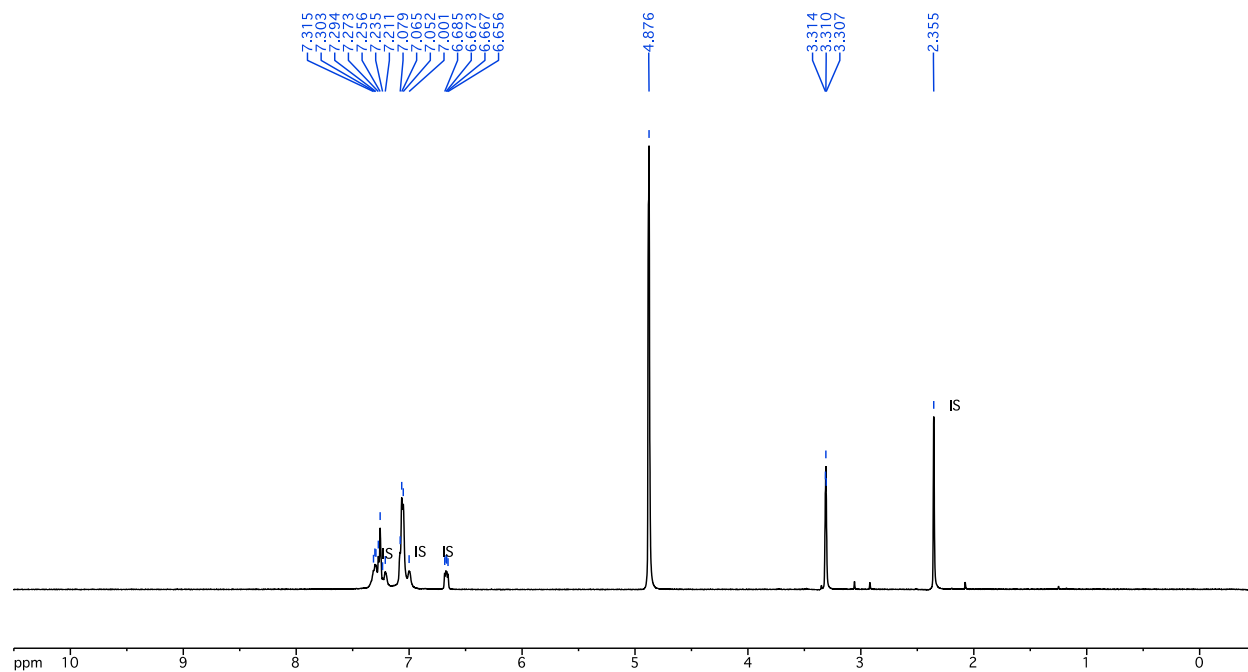
FIGURE S 67 Crude ^{1}H NMR (400 MHz, methanol-d_4) spectrum of the reaction between N_2O and complex **2** with the addition of $CoCp_2$ in methanol-d_4.
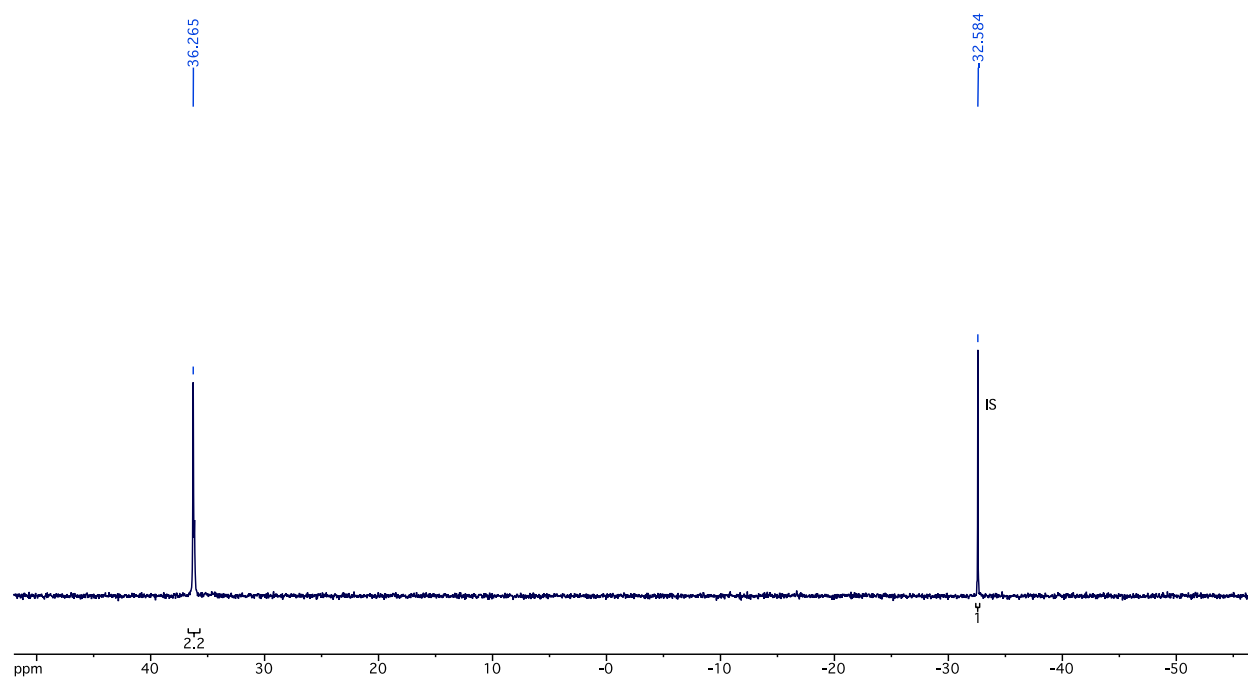
FIGURE S 68 Crude ^{31}P{^{1}H} NMR (162 MHz, methanol-d_4) spectrum of the reaction between N_2O and complex **2** with the addition of $CoCp_2$ in methanol-d_4.
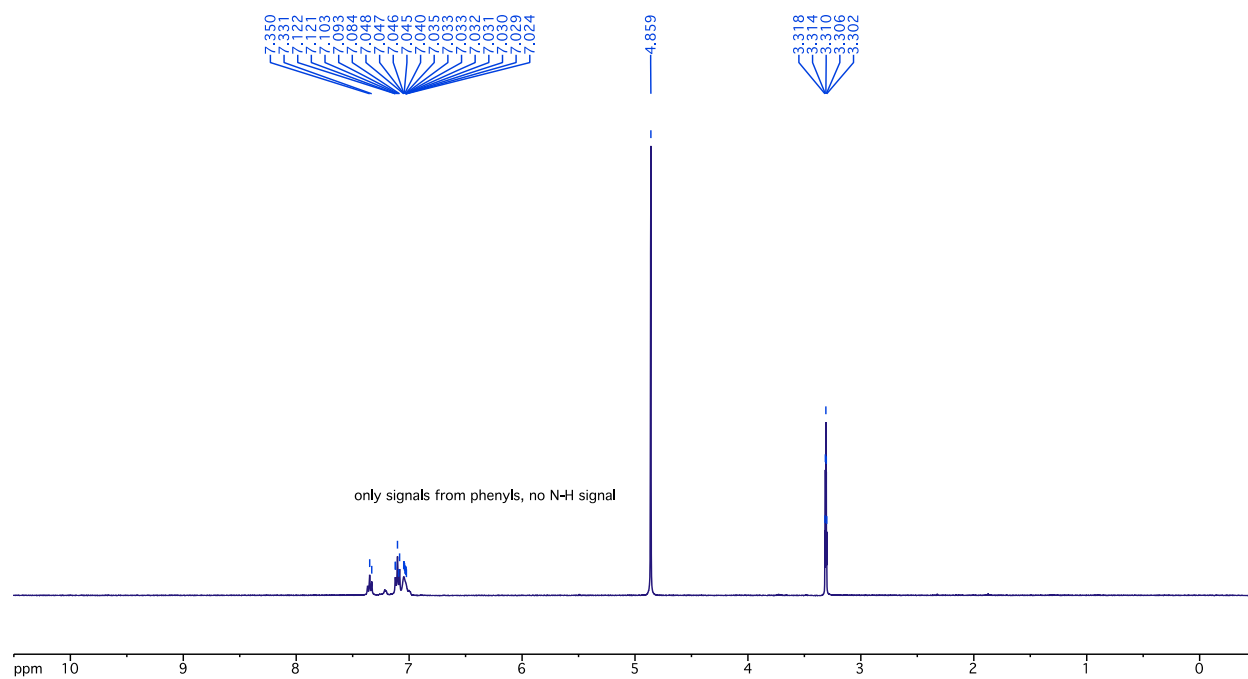
FIGURE S 69 ^{1}H NMR (400 MHz, MeOH-d_4) spectrum of {Cu$_4$(μ_4-S)[bis(diphenylphosphino)amine]$_4$}(PF$_6$)$_2$ (**2**).

5.2.3 Isolation of byproduct [CoCp$_2$]$^+$ and the relevant control experiments

Large Scale Reaction Between Cu$_4$S(dppa)$_4$(PF$_6$)$_2$[(CH$_3$)$_2$CO]$_2$ (2) and N$_2$O with CoCp$_2$ in MeOH to Isolate Possible by Byproducts.
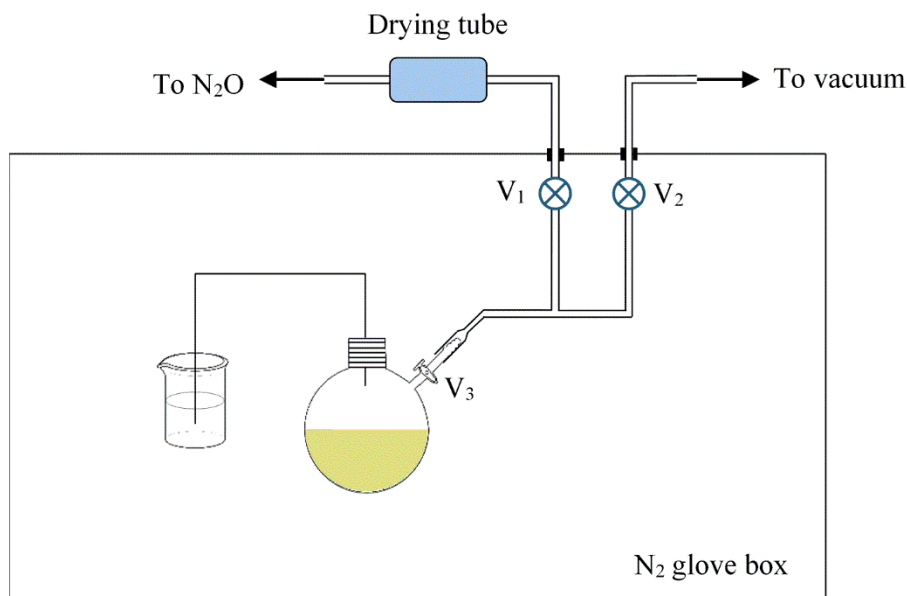
FIGURE S 70 Experimental setup for scaleup reaction between [Cu$_4$S(dppa)$_4$](PF$_6$)$_2$[(CH$_3$)$_2$CO]$_2$ (**2**) and N$_2$O with CoCp$_2$ in MeOH

Inside a N$_2$ filled glove box, Cu$_4$S(dppa)$_4$(PF$_6$)$_2$[(CH$_3$)$_2$CO]$_2$ (**2**) (1.0000 g, 0.4460 mmol) was dissolved in MeOH (20 mL) in a Schlenk flask fitted with a screw cap septum (Headspace screwTin cap with PTFE/ butyl septum). It was connected to a N$_2$O/ Vacuum line and to a MeOH bubbler through a cannula needle as shown above. N$_2$O was passed through a drying tube (CaSO$_4$, -10+20 Mesh) before it reaches the reaction mixture. N$_2$O line was purged with 3 vacuum-refill cycles keeping V$_3$ closed, before the headspace was opened to N$_2$O. CoCp$_2$ (0.1687 g, 0.8920 mmol) was dissolved in MeOH (20 mL) inside the glove box. It was added dropwise to the Cu$_4$S(dppa)$_4$(PF$_6$)$_2$[(CH$_3$)$_2$CO]$_2$ solution over 15 min while bubbling N$_2$O, resulting a red-brown solution. After the dropwise addition, N$_2$O was bubbled for 5 more min and the V$_3$ was closed. Cannular was removed and the septa was covered with a layer of silicon grease to assure a better seal. Reaction mixture was stirred for 3 hours at room temperature and was filtered to collect a yellow-brown precipitate. It was washed with pentane (4×2 mL) and vacuum dried. ^{1}H NMR in acetone-d_6 confirmed it to be complex **3** (**Figure S71**). ^{1}H NMR (500 MHz, Acetone-d_6) δ 7.46 (brs, 10H, C$_6$H$_5$), 7.33–7.13 (m,

20H, C$_6$H$_5$), 7.07–6.89 (m, 20H, C$_6$H$_5$), 6.84–6.74 (m, 10H, C$_6$H$_5$), 3.30 (s, residual methanol), 1.35–1.20 (m, residual

pentane), 0.87 (t, residual pentane).In addition, a sharp singlet was seen 5.92 ppm. In attempt to isolate this, the above

filtrate was reduced to half under vacuum and filtered off. Pentane (20 mL) was added to the filtrate, and the resulted

orange-brown precipitate was collected by filtration. It was rinsed with Et$_2$O (3×2 mL) and vacuum dried. ^{1}H and ^{31}P

NMR in acetone-d_6 confirmed the identity of this as [CoCp$_2$]PF$_6$ (**Figure S72 and Figure S73**). ^{1}H NMR (400 MHz,

Acetone-d_6) δ 5.92 (s, 10H, Cp$_2$) 3.40 (q, J = 7.0 Hz, residual Et$_2$O), 1.11 (t, J = 7.0 Hz, residual Et$_2$O). ^{31}P NMR (400

MHz, Acetone-d_6) δ -145.80 (s, PF$_6$).
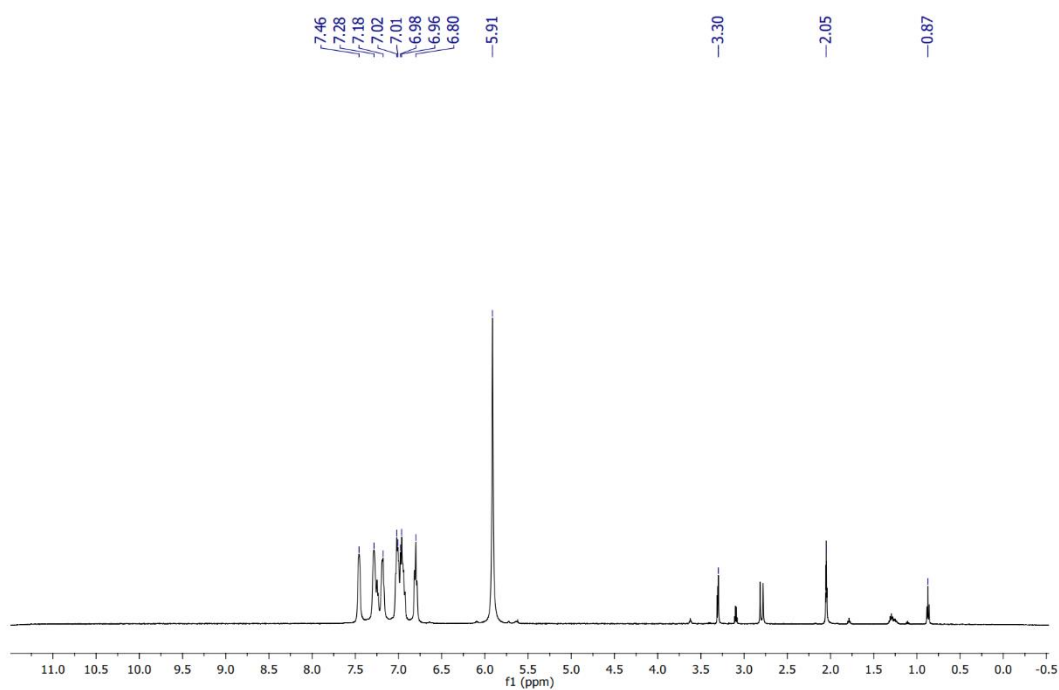
FIGURE S 71 ^{1}H NMR (400 MHz, Acetone-d_6) of complex **3** and [CoCp$_2$]PF$_6$.
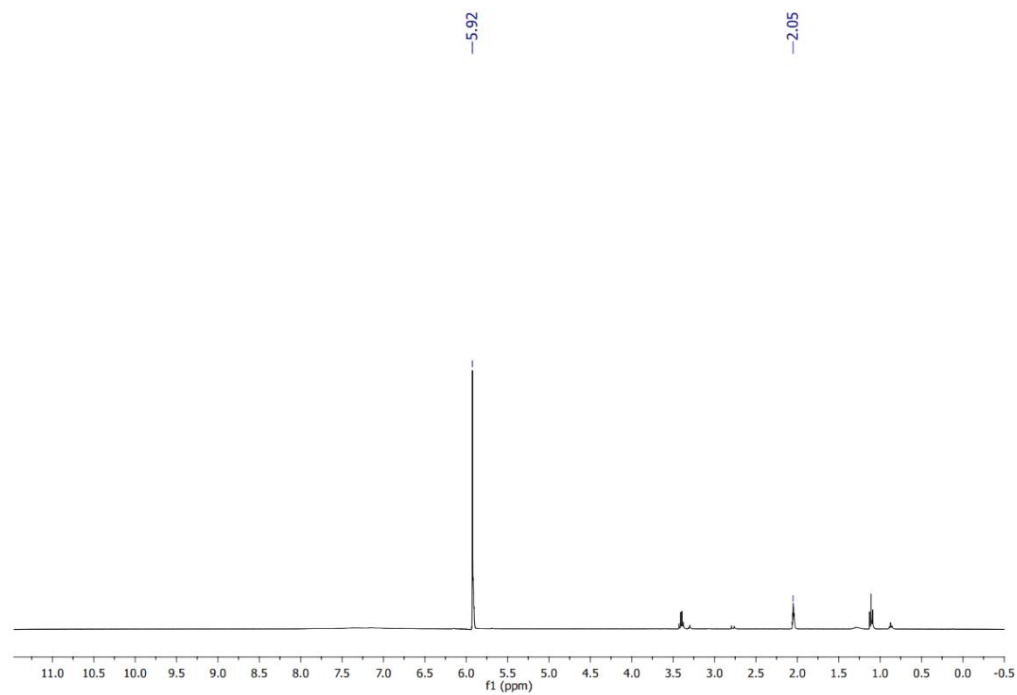
FIGURE S 72 ^{1}H NMR (400 MHz, Acetone-d_6) of [CoCp$_2$]PF$_6$.
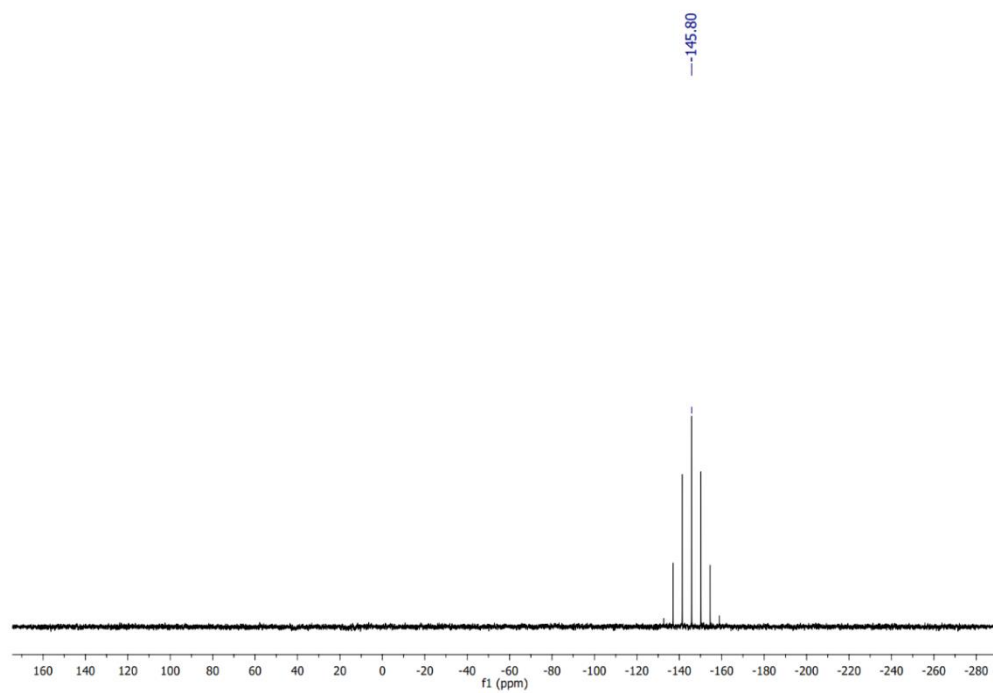
FIGURE S 73 ^{31}P{^{1}H} NMR (400 MHz, Acetone-d_6) of [CoCp$_2$]PF$_6$.

Control Experiment 1: The Reaction of {Cu$_4$(μ_4-S)[bis(diphenylphosphino)amine]$_4$}(PF$_6$)$_2$ (**2**) and N$_2$O in the absence of CoCp$_2$ in Methanol

In the glovebox, 30 mg of {Cu$_4$(μ_4-S)[bis(diphenylphosphino)amine]$_4$}(PF$_6$)$_2$ (**2**) (0.014 mmol), was added in a 20 mL vial, charged with 15 mL dry MeOH. With bubbling N$_2$O into the solution for 5 minutes, the vial was closed and kept stirring for one hour. After the solvent removal in vacuum, use 5 mL (1 mL × 5) toluene to wash the mixture, then 4 mL (1 mL × 4) THF to extract the major product and collect the THF filtrate. Evaporate the THF and 28 mg crude compounds were obtained. Prepare the NMR sample using ~0.7 mL acetone-d_6 to dissolve the compounds and filter the solution into a vial charged with 5 mg tri-o-tolylphosphine as the internal standard (labeled as "IS" in the NMR spectra). ^{1}H NMR (400 MHz, acetone-d_6): δ 7.42–7.08 (m, integral not determined due to peak overlap between phenyls from **2**, **2'** and the internal standard), 3.77 (s, N–H of **2'**). ^{31}P {^{1}H} NMR (162 MHz, acetone-d_6): δ 36.5 (s, PPh$_2$–N(H)–PPh$_2$ of **2**), 35.4 (s, PPh$_2$–N(H)–PPh$_2$ of **2'**). Based on the ^{31}P NMR, the major product is **2** in 60% yield with decomposed species **2'** in 15%.
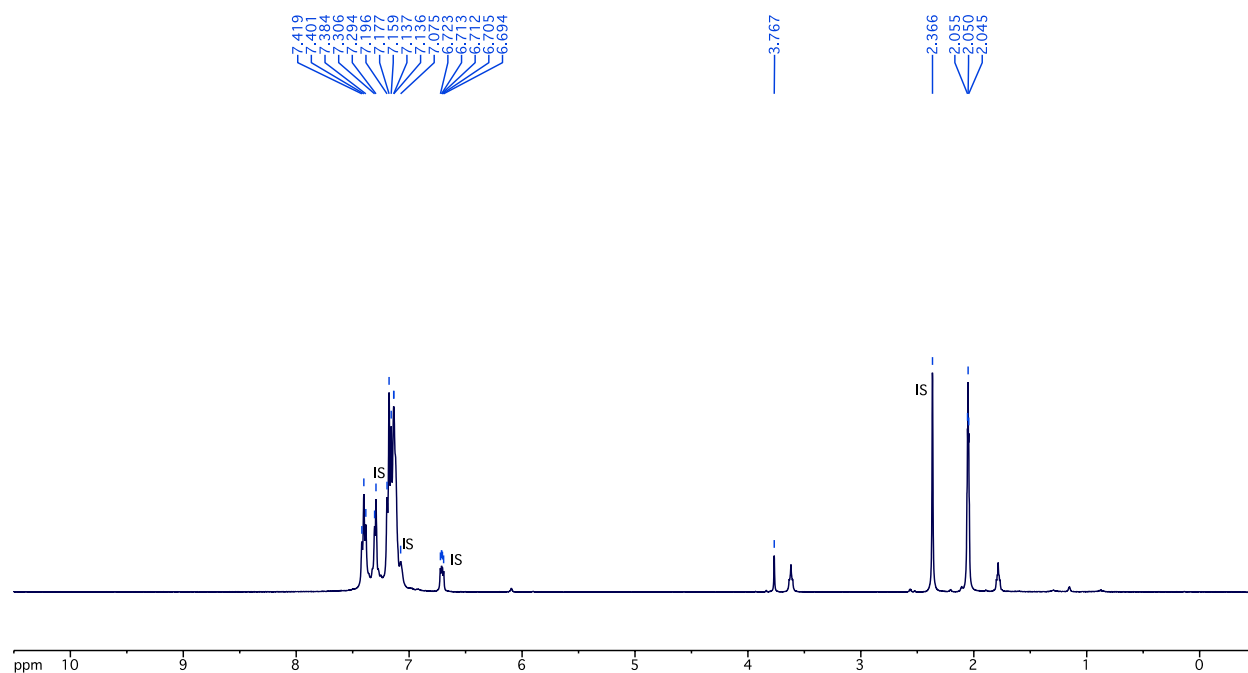
FIGURE S 74 Crude ^{1}H NMR (400 MHz, acetone-d_6) spectrum of the reaction between N$_2$O and complex **2** in MeOH without CoCp$_2$.
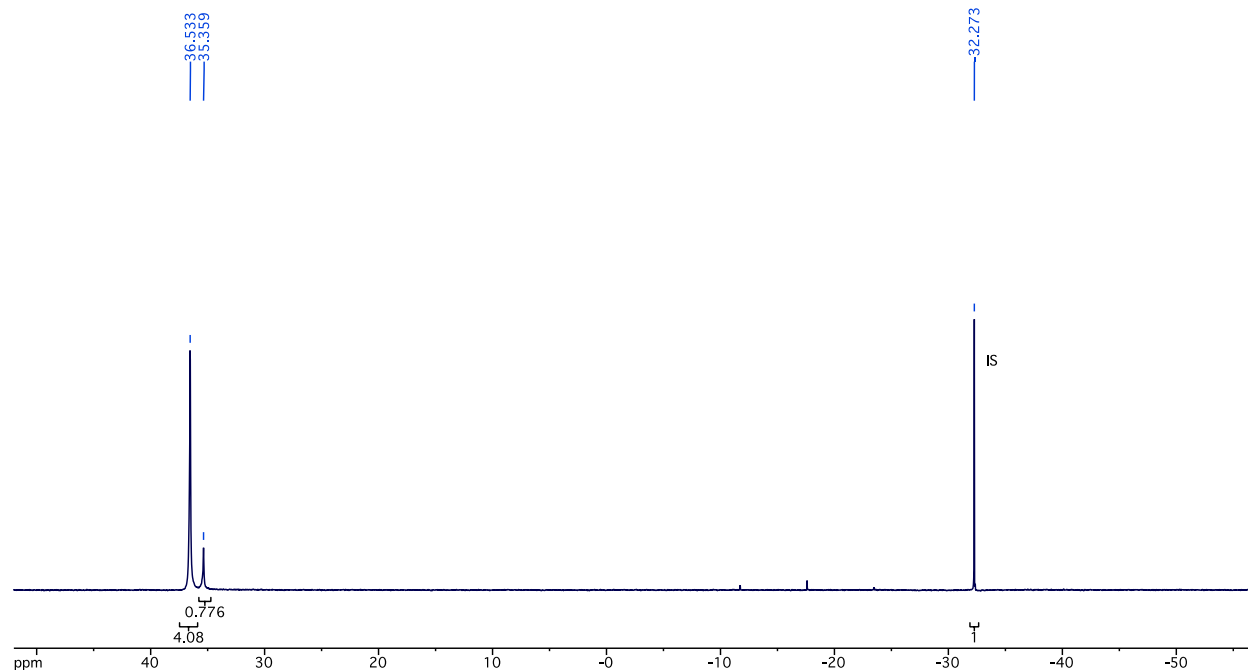
FIGURE S 75 Crude ^{31}P{^{1}H} NMR (162 MHz, acetone-d_6) spectrum of the reaction between N$_2$O and complex **2** in MeOH without CoCp$_2$.

Control Experiment 2: The Reaction of {Cu$_4$(μ$_4$-S)[bis(diphenylphosphino)amine]$_4$}(PF$_6$)$_2$ (**2**) and CoCp$_2$ (2 eq) in Methanol under N$_2$

In the glovebox, 30 mg of {Cu$_4$(μ$_4$-S)[bis(diphenylphosphino)amine]$_4$}(PF$_6$)$_2$ (**2**) (0.014 mmol), was added in a 20 mL vial, charged with 15 mL dry MeOH. The CoCp$_2$ solution (6 mg of CoCp$_2$ in 1 mL dry MeOH) was added dropwise into the vial for 2 minutes and the vial was closed and kept stirring for one hour. After the solvent removal in vacuum, use 5 mL (1 mL × 5) toluene to wash the mixture, then 4 mL (1 mL × 4) THF to extract the major product and collect the THF filtrate. Evaporate the THF and 30 mg crude compounds were obtained. Prepare the NMR sample using ~0.7 mL acetone-d_6 to dissolve the compounds and filter the solution into a vial charged with 5 mg tri-o-tolylphosphine as the internal standard (labeled as "IS" in the NMR spectra). ^{1}H NMR (400 MHz, acetone-d_6): δ 7.42–7.08 (m, integral not determined due to peak overlap between phenyls from **2**, **2'** and the internal standard), 3.77 (s, N–H of **2'**). ^{31}P {^{1}H} NMR (162 MHz, acetone-d_6): δ 36.6 (s, PPh$_2$–N(H)–PPh$_2$ of **2**), 35.4 (s, PPh$_2$–N(H)–PPh$_2$ of **2'**). Based on the ^{31}P-NMR, the major product is **2** in 54% yield with decomposed species **2'** in 25%.
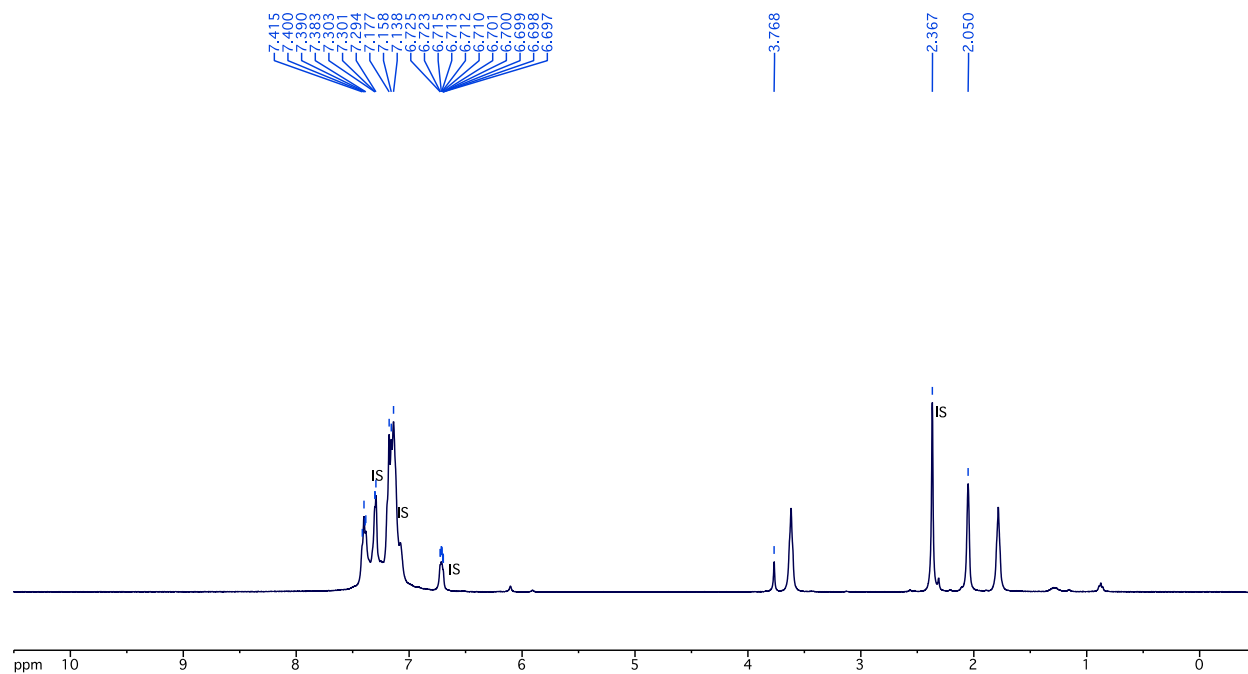
FIGURE S 76 Crude ^{1}H NMR (400 MHz, acetone-d_6) spectrum of the reaction between complex **2** and CoCp$_2$ in methanol under N$_2$.
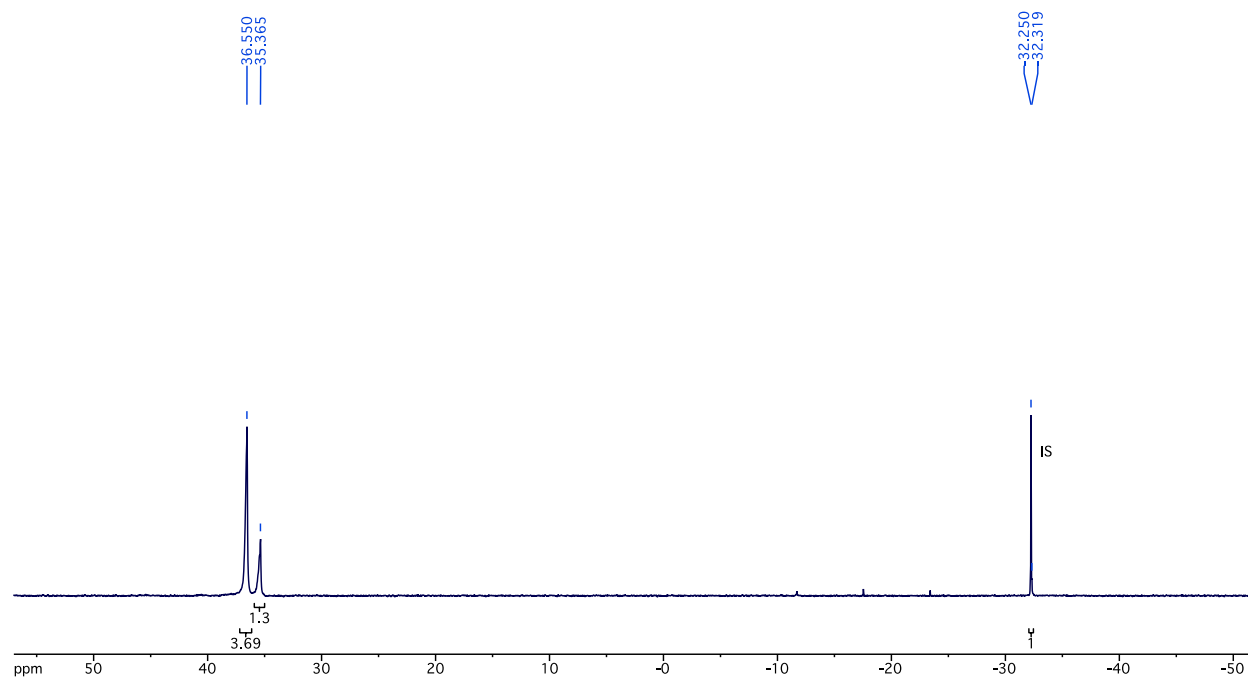
FIGURE S 77 Crude ^{31}P{^{1}H} NMR (162 MHz, acetone-d_6) spectrum of the reaction between complex **2** and CoCp$_2$ in methanol under N$_2$.

Control Experiment 3: Reaction of $CoCp_2$ and N_2O in Methanol in the absence of complex **2**.

Using a similar setup as **Figure S70**, a Schlenk flask was filled with N_2O. $CoCp_2$ (2 mg, 0.011 mmol) in 2 mL of methanol was added dropwise over 2-3 min. Schlenk flask was closed and reaction mixture was stirred for 1 hour at room temperature. At the end, solvent was completely evaporated, and NMR was taken in MeOD. No reaction was seen by NMR. ^1H NMR (400 MHz, MeOD) δ 4.84 (s, residual water in MeOD), 3.35 (s, residual MeOH), 3.31 (s, MeOD).
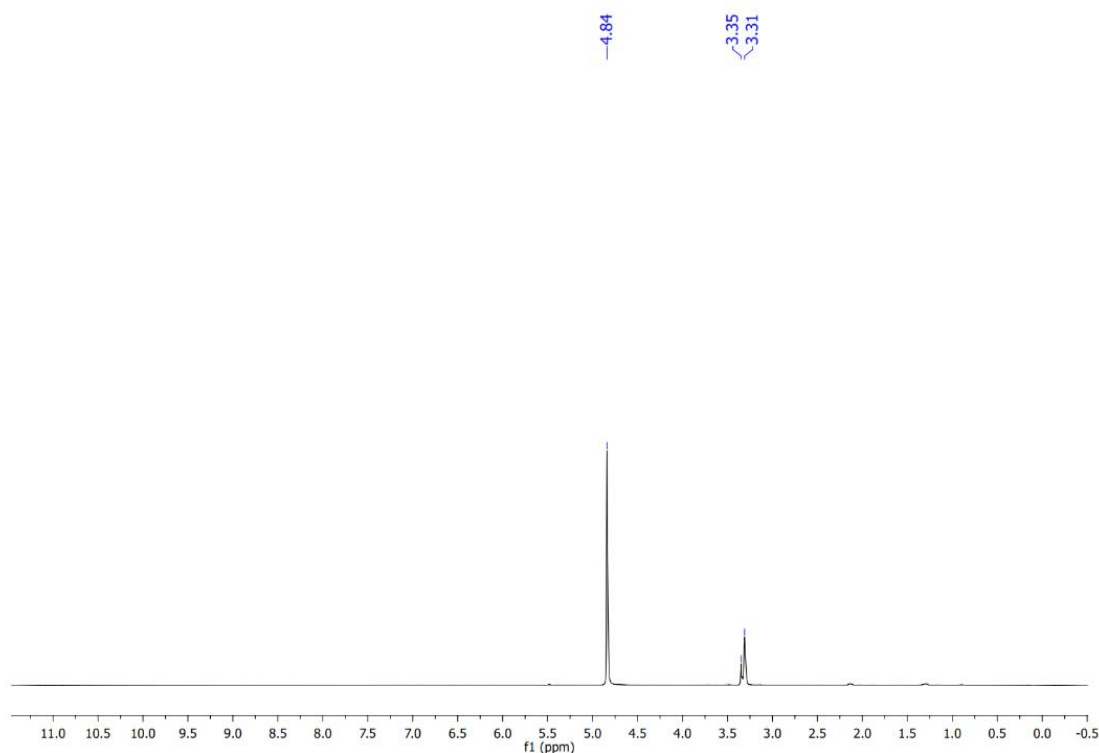
FIGURE S 78 ^1H NMR (400 MHz, MeOD) spectrum of the reaction of $CoCp_2$ and N_2O in Methanol in the absence of complex **2**.

Control Experiment 4: Reaction between complex **2** and N_2O in MeOH with only 1 equivalent of $CoCp_2$.

Using a similar setup as **Figure S70**, {$Cu_4(\mu_4\text{-}S)$[bis(diphenylphosphino)amine]$_4$}$(PF_6)_2$ (**2**) (20 mg, 0.010 mmol) in 1.5 mL of MeOH was added in to a Schlenk flask. Head space was filled with N_2O and $CoCp_2$ (2 mg, 0.011 mmol, 1 eq) in 1 mL of MeOH was added dropwise over 2-3 min. Schlenk flask was closed and reaction mixture was stirred for 1 hour at room temperature. At the end, solvent was completely evaporated and NMR was taken in acetone-d_6 using tri(o-tolyl)phosphine (12.2 mg, 0.04 mmol) as the internal standard. ^{31}P yield – 38 % of **3**, 44 % **2'** and 6 % of **2**. ^1H NMR (400 MHz, acetone-d_6) δ 7.74 – 6.46 (m, integral not determined due to peak overlap between aromatic hydrogens from **2, 2'** and the internal standard), 3.77 (s, N–H of **2'**), 2.36 (s, IS-CH_3), 2.05 (s, acetone-d_6). ^{31}P NMR (162 MHz, acetone-d_6) δ 46.33 – 43.26 (m, 4P, PPh_2–N⁻–PPh_2 of **2**), 36.53(s, PPh_2–N(H)–PPh_2 of **2**) 35.38 (s, PPh_2–N(H)–PPh_2 of **2'**), -32.22 (s, IS).
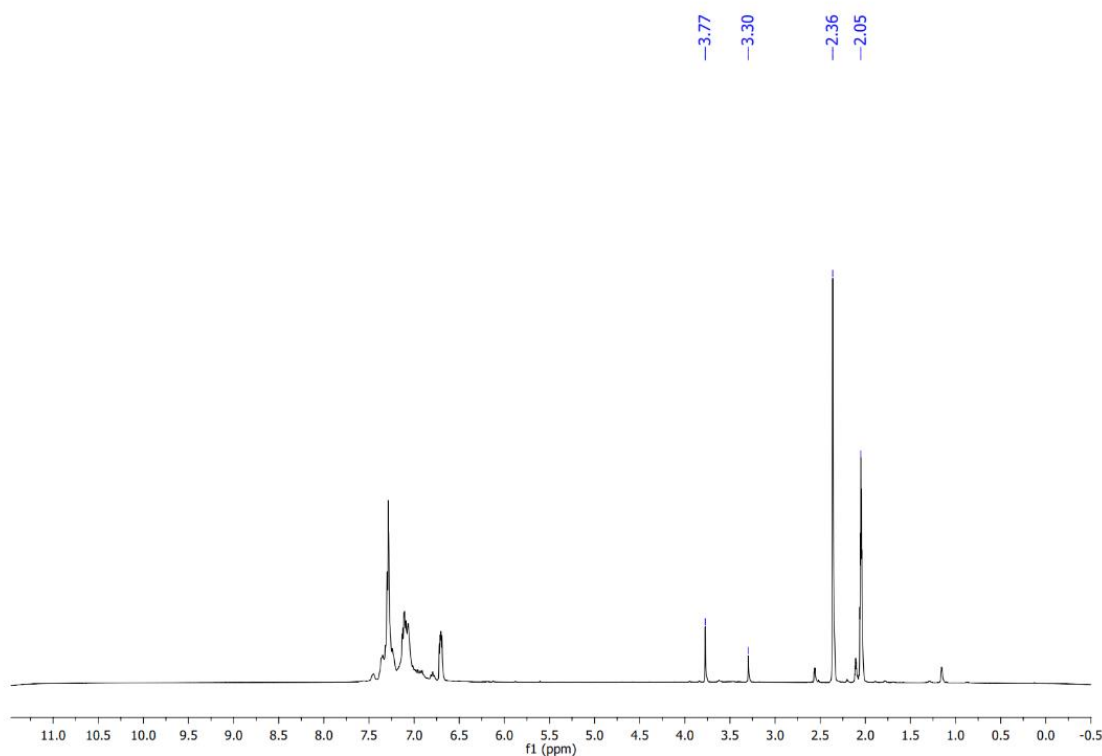
FIGURE S 79 Crude ^1H NMR (400 MHz, acetone-d_6) spectrum of the reaction between complex **2** and N_2O in MeOH with only 1 equivalent of $CoCp_2$.
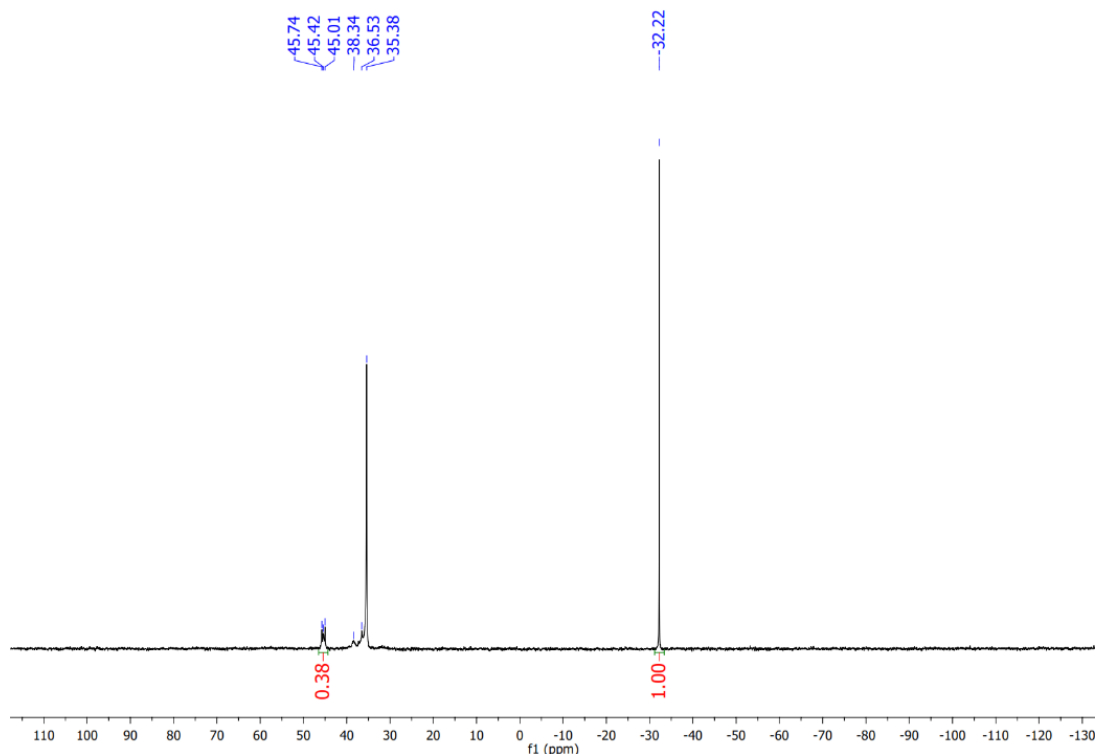
FIGURE S 80 Crude ^{31}P NMR (400 MHz, acetone-d_6) spectrum of the reaction of between complex **2** and N$_2$O in MeOH with only 1 equivalent of CoCp$_2$.

Control Experiment 5: Reaction between [Cu4(μ_4- S) (μ_2-dppm)$_4$](PF$_6$)$_2$ (**1**) and N$_2$O in MeOH with 2 eq of CoCp$_2$.

Using a similar setup as **Figure S70**, [Cu4(μ_4- S) (μ_2-dppm)$_4$](PF$_6$)$_2$ **1** (10.6 mg, 0.005 mmol) in 1.5 mL of aceton was added in to a schlenk flask. Head space was filled with N$_2$O and CoCp$_2$ (2 mg, 0.011 mmol, 2 eq) in 1 mL of acetone was added dropwise over 2-3 min. Schlenk flask was closed and reaction mixture was stirred for 1 hour at room temperature. At the end, solvent was completely evaporated and NMR was taken in acetone-d_6 using tri(o-tolyl)phosphine (12.2 mg, 0.04 mmol) as the internal standard. ^{31}P NMR confirms no reaction between **1** and N$_2$O under the tested conditions. ^{1}H NMR (400 MHz, aceton-d_6) δ 7.53 – 6.54 (m, integral not determined due to peak overlap between aromatic hydrogens from **1** and the IS), 3.53 (s, -CH$_2$- of **1**) 2.37 (s, IS-CH$_3$), 2.09 (s, residual aceton), 2.05 (s, acetone-d_6). ^{31}P NMR (400 MHz, acetone-d_6) δ -14.70 (s, PPh$_2$–CH$_2$–PPh$_2$ of **1**), -32.18 (s, IS).
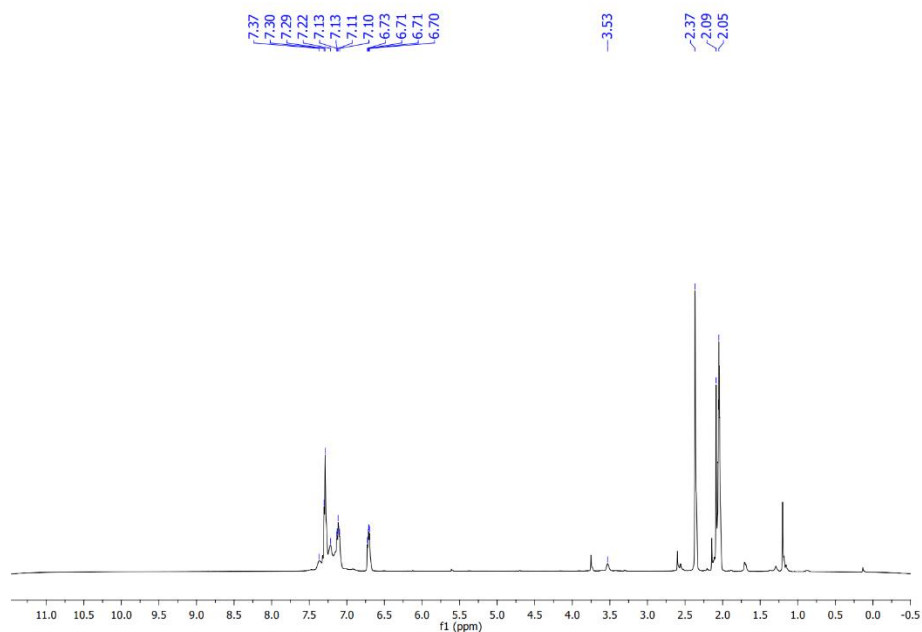
FIGURE S 81 Crude ^1H NMR (400 MHz, acetone-d_6) spectrum of the reaction between [Cu4(μ_4- S) (μ_2-dppm)$_4$](PF$_6$)$_2$ (**1**) and N$_2$O in MeOH with 2 eq of CoCp$_2$.
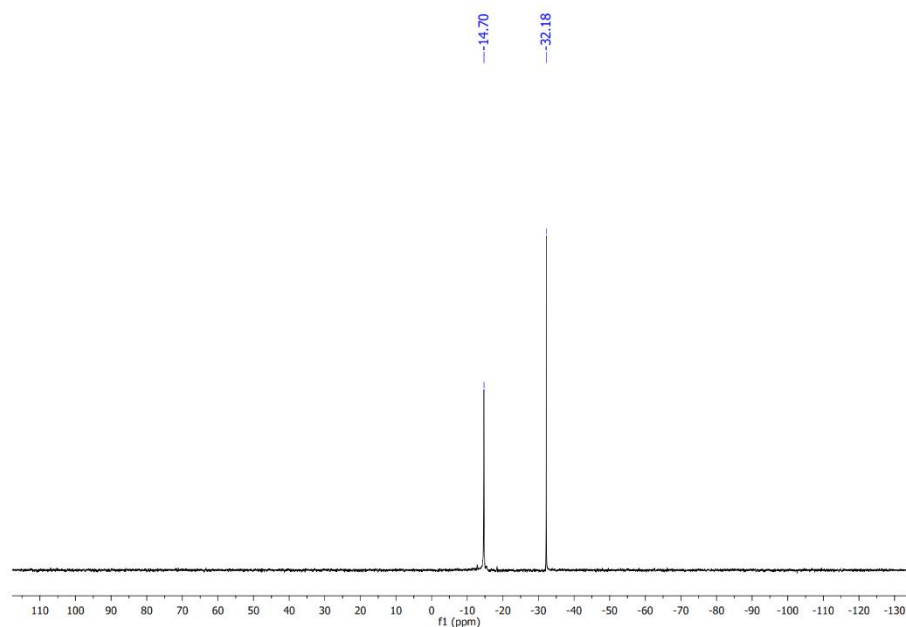
FIGURE S 82 Crude ^{31}P NMR (400 MHz, acetone-d_6) spectrum of the reaction between [Cu4(μ_4- S) (μ_2-dppm)$_4$](PF$_6$)$_2$ (**1**) and N$_2$O in MeOH with 2 eq of CoCp$_2$.

5.2.4 Qualitative analysis for water determination

Water Detection Using near-IR Spectrometry

A known near-IR assay was used to detect dilute water in methanol solution.[7,8] In a N_2 filled glovebox a screw cap Schlenk flask (15 mL, Headspace screwTin cap with PTFE/ butyl septum) was added with $Cu_4S(dppa)_4(PF_6)_2[(CH_3)_2CO]_2$ (**2**) (50 mg, 0.0024 mmol), dry acetone (2 mL) and a magnetic stir bar. An experimental setup given in **Figure S70** was used to connect the Schlenk flask to N_2O/ vacuum line. After purging the line with N_2O the head space was flushed with N_2O for 5 min. while open to N_2O, a solution of $CoCp_2$ (9.4 mg ,0.050 mmol) in dry acetone (2.5 mL) was added dropwise using a syringe into the solution of **2**. The Schlenk flask was closed and the connection needle to the bubbler was removed. The septum was secured with a layer of grease and the reaction mixture was stirred for 1 hour at room temperature. At the end, the reaction mixture was transferred to a 10-mm pathlength quartz cell and the near-IR spectrum was recorded. A control experiment was performed in a similar way in the absence of **2**. Similar analysis was repeated two more times.

TABLE S 8 Composition of the experiment and the controls of qualitative water detection.

Parameter	Control	Experiment
Compound **2**	-	50 mg
$CoCp_2$	9.4 mg	9.4 mg
Reaction gas	N_2O	N_2O
Total volume of acetone	4.5 mL	4.5 mL
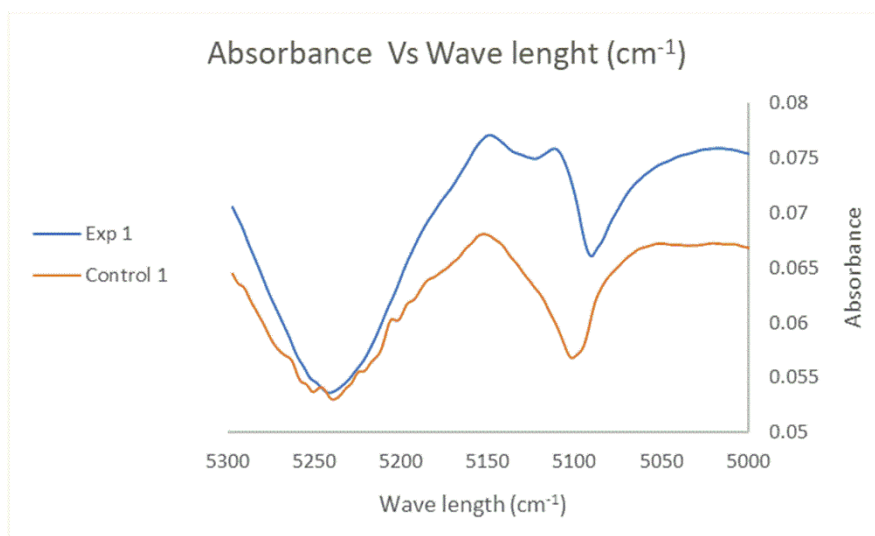
FIGURE S 83 The graph of Absorbance (at 5150 cm^{-1} for H_2O overtone) Vs Wavelength (cm^{-1}) for trace H_2O detection-Trial 1
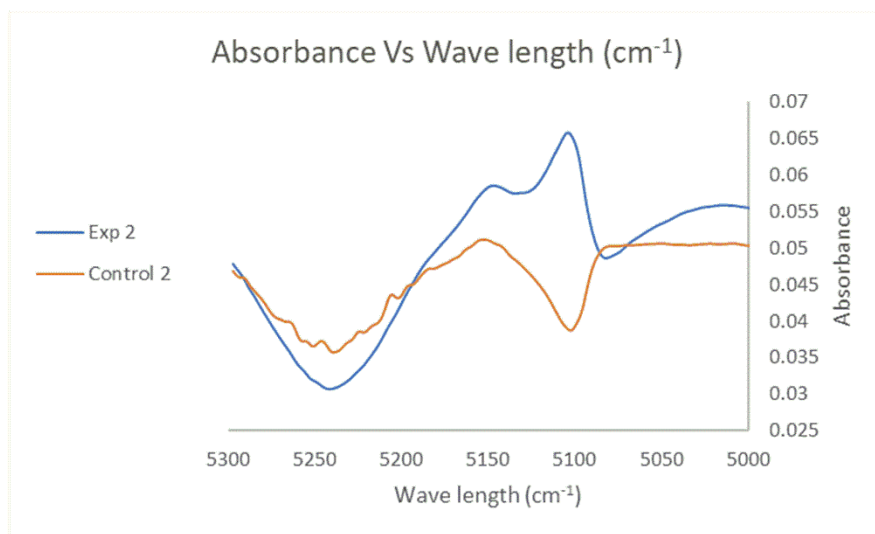
FIGURE S 84 The graph of Absorbance (at 5150 cm^{-1} for H_2O overtone) Vs Wavelength (cm^{-1}) for trace H_2O detection-Trial 2
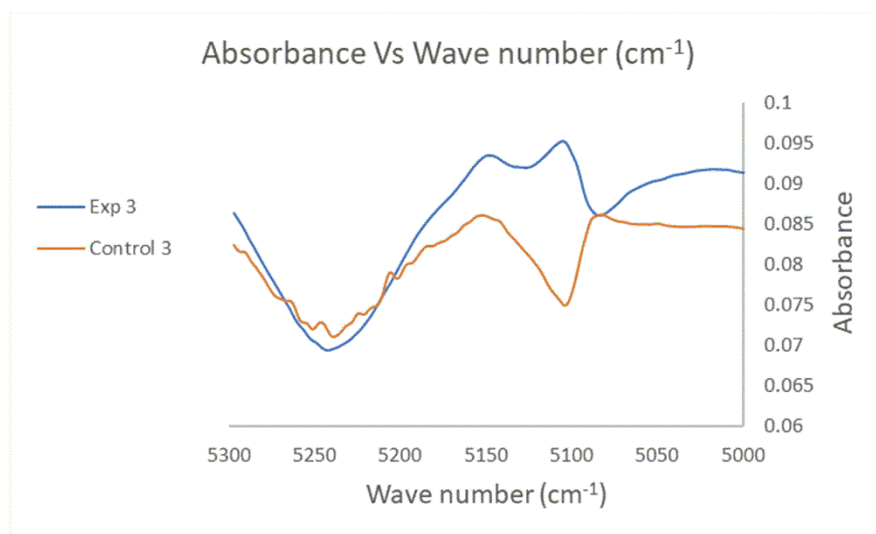
FIGURE S 85 The graph of Absorbance (at 5150 cm^{-1} for H_2O overtone) Vs Wavelength (cm^{-1}) for trace H_2O detection-Trial 3

Overtone peak for trace H_2O is sensitive to background moisture levels. However, the absorbance values (at 5150 cm^{-1}) for the experiments were found to be larger than that of controls repeatedly. Attempts to quantify produced H_2O were performed based on a calibration curve. However, they were inconclusive due to several issues with scaling up the reaction. First, poor solubility of $CoCp_2$ lowers the concentration of produced H_2O. Additionally, scaling up causes complex **3** to precipitate from the reaction mixture. This solid matter introduces random error in the near-IR base line and filtering the sample results in loss of H_2O. Lastly, higher concentrations of **2** give rise to interfering signals between 5000 – 5700 cm^{-1}.

5.2.5   Qualitative and quantitative determination of produced nitrogen

Quantification of Produced Nitrogen (N₂) by Headspace Analysis of the Reaction between [Cu₄S(dppa)₄](PF₆)₂[(CH₃)₂CO]₂ and N₂O with 2 eq of CoCp₂ in acetone.

Construction of a calibration curve: five Schlenk flasks fitted with screw cap septums (Headspace screwTin cap with PTFE/ butyl septum) were vacuum-refilled 3 times and filled with pure nitrogen. 2, 4, 6, 8 and 10 µL of pure N₂ samples were syringed separately from each flask and were introduced to GCMS (see **5.2.1** general information for syringe, GCMS instrument and method details). Peak area for each standard N₂ sample was recorded and plotted against the corresponding volume of N₂ to construct a calibration curve "Peak area Vs Volume of N₂ (µL)". Retention time for trace O₂ and N₂ are 6.2 and 8.1 respectively.
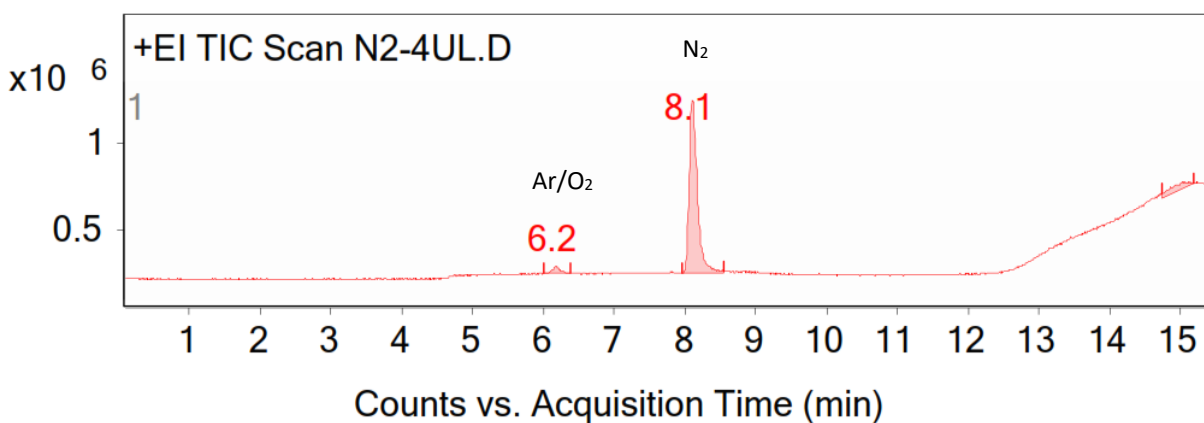
Integration Peak List

Peak	Start	RT	End	Height	Area	Area %
1	6	6.2	6.4	42700.71	339360.57	4.22
2	8	8.1	8.5	1011167.15	8047318.22	100
3	14.7	15	15.2	35251.74	732381.98	9.1

FIGURE S 86 The Total Ion Chromatogram (TIC) and the peak integration for 2 µL N₂ standard.
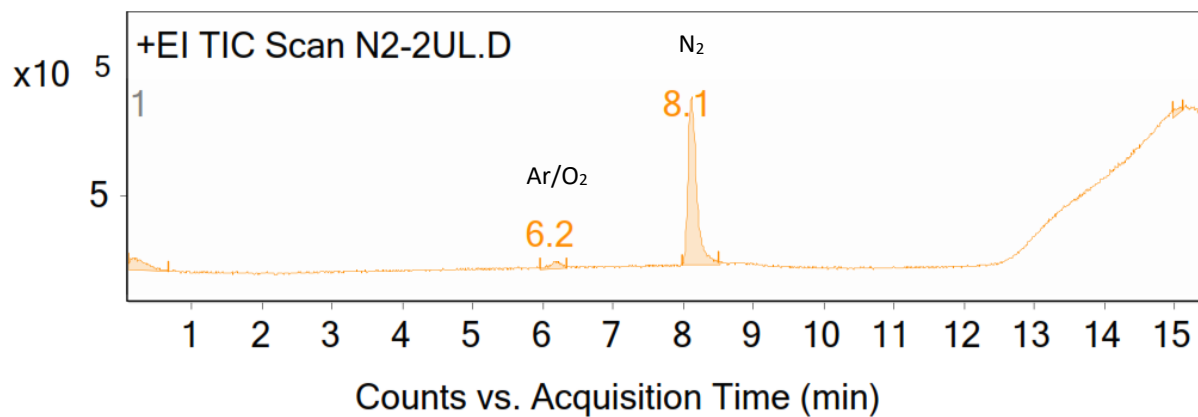
Integration Peak List

Peak	Start	RT	End	Height	Area	Area %
1	0.1	0.2	0.7	42842.38	689852.6	14
2	6	6.2	6.3	24228.27	246235.23	5
3	8	8.1	8.5	581257.89	4927980.5	100
4	15	15.1	15.1	20439.37	170978.43	3.47

FIGURE S 87 The Total Ion Chromatogram (TIC) and the peak integration for 4 μL N_2 standard.
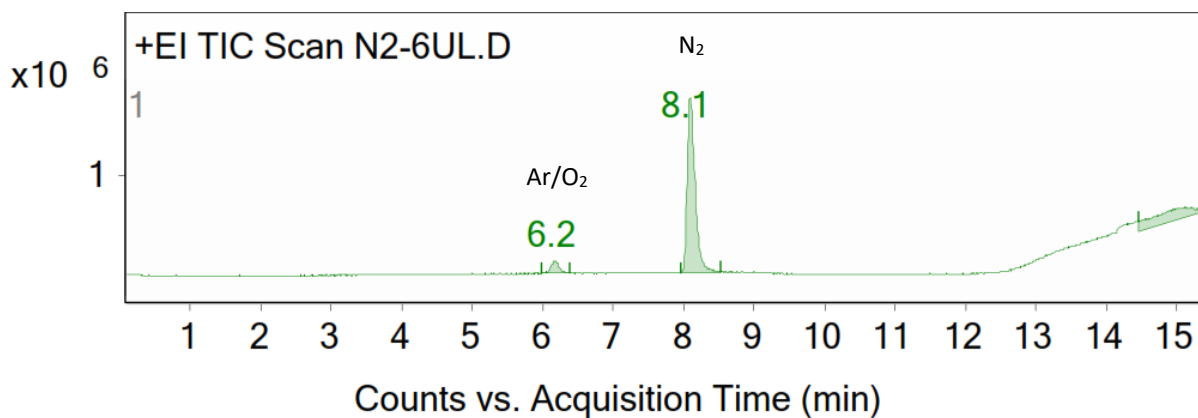
Integration Peak List

Peak	Start	RT	End	Height	Area	Area %
1	6	6.2	6.4	96777.18	793707.44	7.39
2	8	8.1	8.5	1370868.02	10738193.5	100
3	14.4	15.2	15.4	58007.05	3628890.17	33.79

FIGURE S 88 The Total Ion Chromatogram (TIC) and the peak integration for 6 μL N_2 standard.
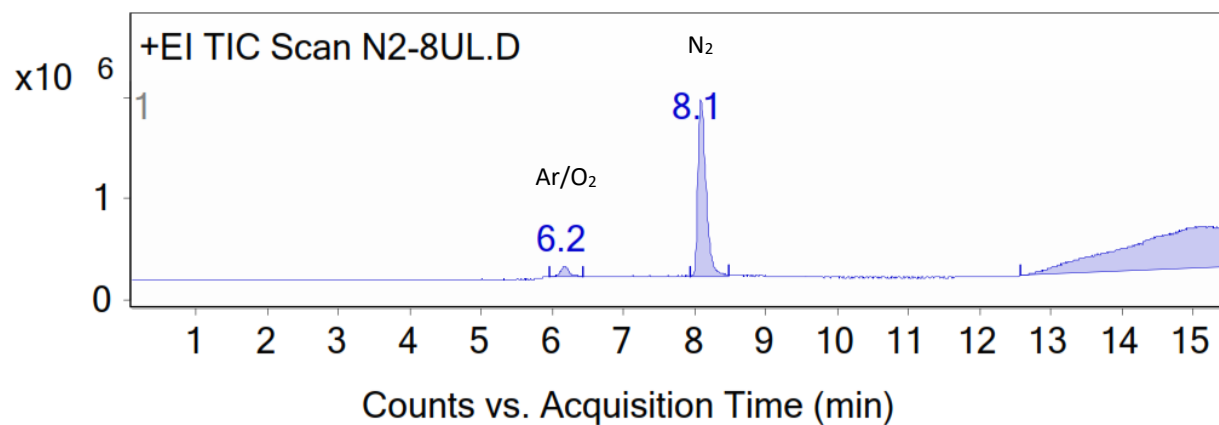
FIGURE S 89 The Total Ion Chromatogram (TIC) and the peak integration for 8 µL N_2 standard.
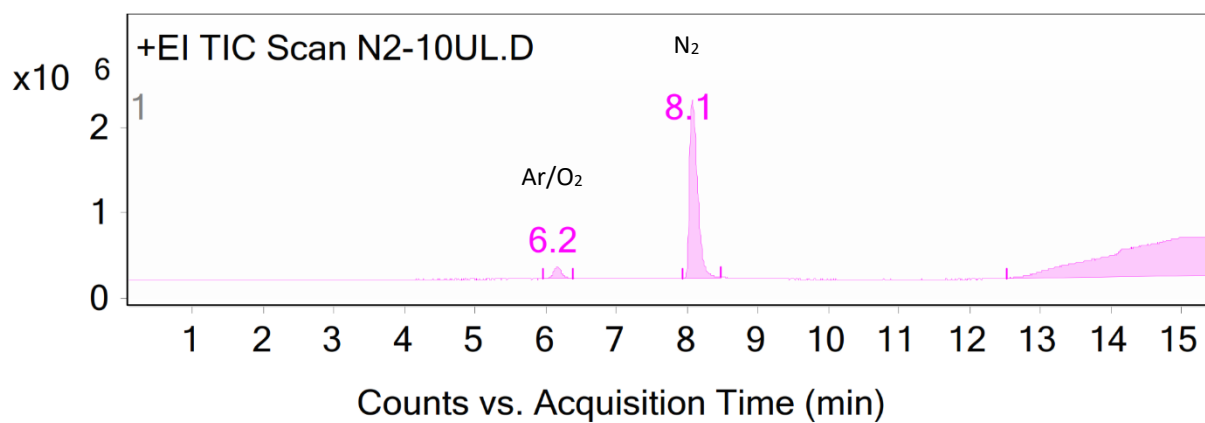
FIGURE S 90 The Total Ion Chromatogram (TIC) and the peak integration for 10 µL N_2 standard.

Headspace analysis of the reaction between [Cu₄S(dppa)₄](PF₆)₂[(CH₃)₂CO]₂ and N₂O with 2 eq of CoCp₂ in acetone.
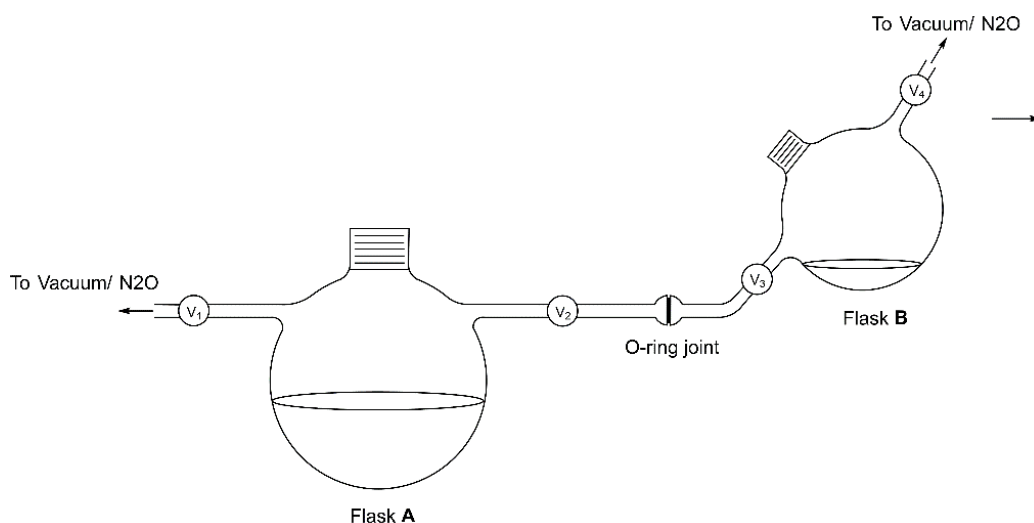
FIGURE S 91 Experimental setup used for headspace analysis.

An apparatus shown above was used for the analysis to minimize any background N₂ and to avoid the air oxidation of CoCp₂. In a N₂ filled glove box, flask **A** was charged with CoCp₂ (18.8 mg, 0.099 mmol) and acetone (40.0 mL). Similarly, flask **B** was added with Cu₄S(dppa)₄(PF₆)₂[(CH₃)₂CO]₂ (100 mg, 0.047 mmol), acetone (15.0 mL) and a magnetic stir bar. Both flasks were secured with screw cap (Headspace screwTin cap with PTFE/ butyl septum) and taken out of the glove box after closing the valves V₁, V₂, V₃ and V₄. Flasks were connected at the O-ring joint and were attached to Schlenk line streaming N₂O (at V₁ and V₃). Both solutions were frozen using liquid nitrogen and the valves V₁, V₂ and V₄ were open to vacuum for 5 min. Next, the corresponding main Schlenk line vacuum valves was closed and the solutions were thawed while keeping only V₃ closed. Then valves V₁, V₄ were closed and the corresponding main Schlenk line vacuum vales were open. Similarly, two more Free-pump-thaw (5 min each step) cycles were performed to remove remaining headspace gases and any dissolved gases (V₃ remains closed during this process). Both solutions were allowed to reach room temperature and flask **A** was open to N₂O (open V₁) for 20 min to facilitated N₂O dissolution in acetone. Then flask **B** was opened to N₂O using V₄ and closed it. While keeping V₄ closed and V₁, V₂, V₃ opened, the CoCp₂ solution was slowly poured into flask **B** by tilting the entire setup clockwise. Finally, the reaction mixture was detached at the O-ring and the Schlenk line, after closing V₃ (V₄ is already closed). Reaction mixture was stirred for 1 hour at room temperature and 50 μL of the headspace was

syringed (after flushing the needle 3 times with Ar) and analyzed using GCMS. Similarly, a separate control experiment was carried out in the absence of $Cu_4S(dppa)_4(PF_6)_2[(CH_3)_2CO]_2$ and the head space was analyzed in a similar manner. The whole experiment (both exp and control) was repeated two more times and the results were averaged. Retention times for Ar, N_2 and N_2O were 6.1, 8.1 and 9.5 min respectively.

Caution: With the limited head space volume, the thawing process must be done carefully while opening the head space to vacuum to prevent the Schlenk flask from exploding.

TABLE S 9 Composition of the experiment and the controls of headspace analysis for N_2 quantification.

Parameter	Control	Experiment
Compound **2**	-	100 mg
CoCp$_2$	0.0188 g	18.8 mg
Reaction gas	N_2O	N_2O
Total volume of acetone	55.0 mL	55.0 mL
Volume of Headspace	10.7 mL	10.7 mL

FIGURE S 92 Total Ion Chromatogram (TIC) and the peak integration of the headspace (50 μL) from the reaction between [Cu4(μ$_4$- S) (μ$_2$-dppa)$_4$](PF$_6$)$_2$ (**2**) and N$_2$O in acetone with 2 eq of CoCp$_2$ – Trial 1
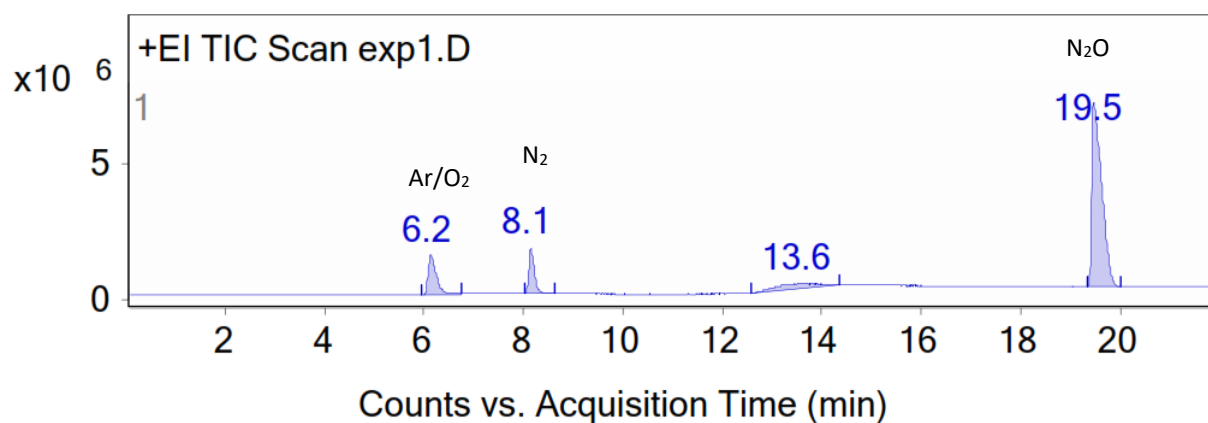
Integration Peak List

Peak	Start	RT	End	Height	Area	Area %
1	6	6.2	6.8	1423628.29	16475641.31	17.41
2	8	8.1	8.6	1682997.95	13337271.61	14.09
3	12.6	13.6	14.3	170098.85	11046719.46	11.67
4	19.3	19.5	20	6792785.29	94626730.67	100

FIGURE S 93 Total Ion Chromatogram (TIC) and the peak integration of the headspace (50 μL) from the control reaction – Trial 1
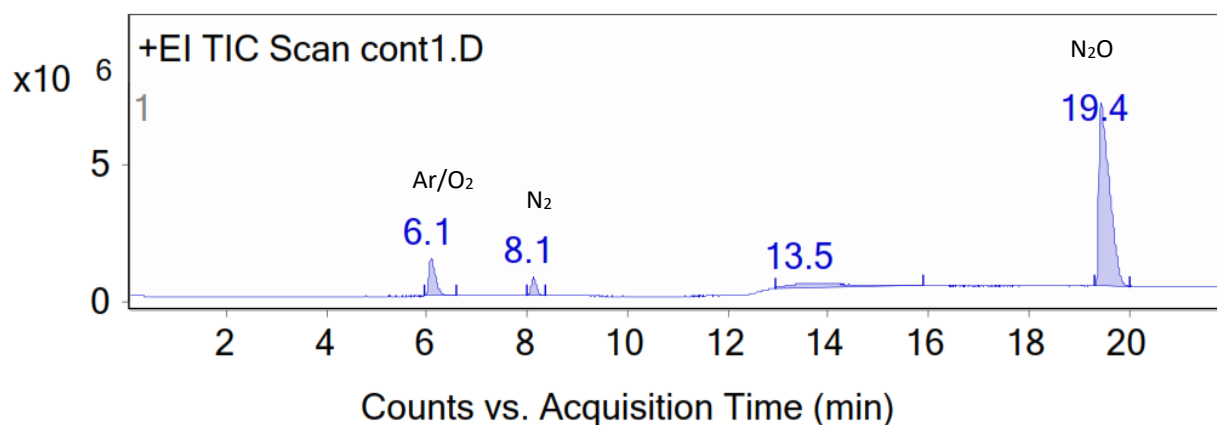
Integration Peak List

Peak	Start	RT	End	Height	Area	Area %
1	5.9	6.1	6.6	1361714.79	12998600.91	13.32
2	8	8.1	8.4	662187.85	4847753.36	4.97
3	12.9	13.5	15.9	151295.62	13590298.7	13.92
4	19.3	19.4	20	6692122.03	97615016.62	100

FIGURE S 94 Total Ion Chromatogram (TIC) and the peak integration of the headspace (50 μL) from the reaction between [Cu4(μ_4- S) (μ_2-dppa)$_4$](PF$_6$)$_2$ (**2**) and N$_2$O in acetone with 2 eq of CoCp$_2$ – Trial 2
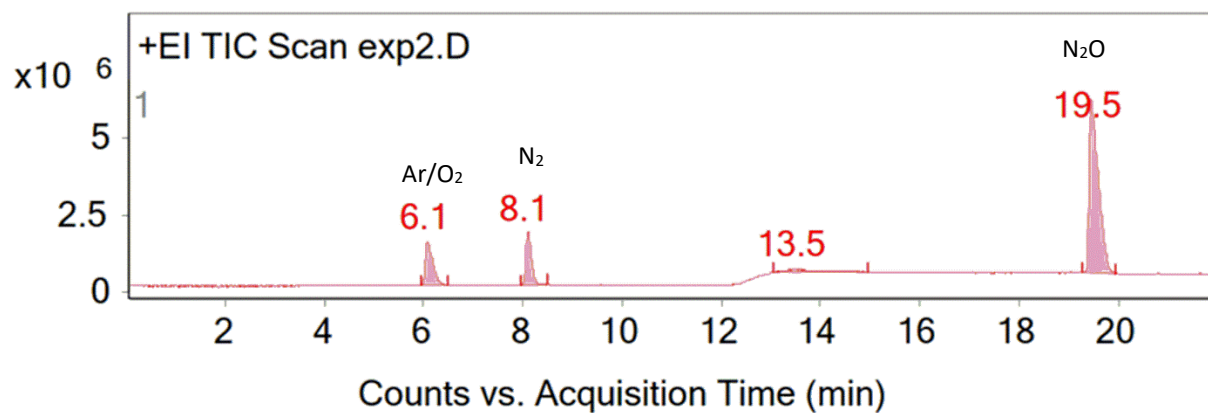
Integration Peak List

Peak	Start	RT	End	Height	Area	Area %
1	5.9	6.1	6.5	1402882.98	15333403.04	20.25
2	8	8.1	8.5	1647005.69	13538900.52	17.88
3	13	13.5	15	104301.5	6981589.85	9.22
4	19.3	19.5	19.9	5099499.09	75720431.44	100

FIGURE S 95 Total Ion Chromatogram (TIC) and the peak integration of the headspace (50 μL) from the control reaction – Trial 2
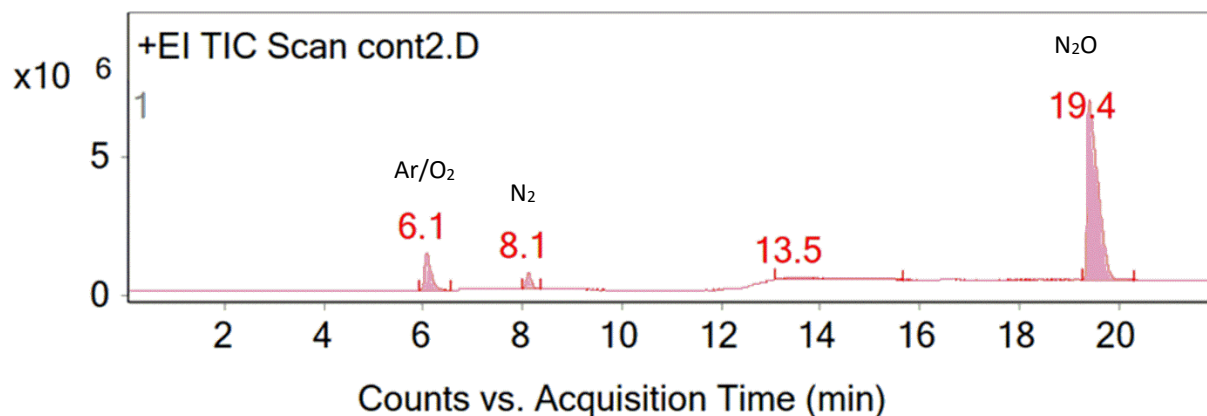
Integration Peak List

Peak	Start	RT	End	Height	Area	Area %
1	5.9	6.1	6.6	1325602.77	12659801.25	12.86
2	8	8.1	8.4	632987.75	4661892.49	4.73
3	13.1	13.5	15.7	82230.8	5157804.43	5.24
4	19.3	19.4	20.3	6571719.15	98456361.15	100

FIGURE S 96 Total Ion Chromatogram (TIC) and the peak integration of the headspace (50 µL) from the reaction between [Cu4(μ_4- S) (μ_2-dppa)$_4$](PF$_6$)$_2$ (**2**) and N$_2$O in acetone with 2 eq of CoCp$_2$ – Trial 3
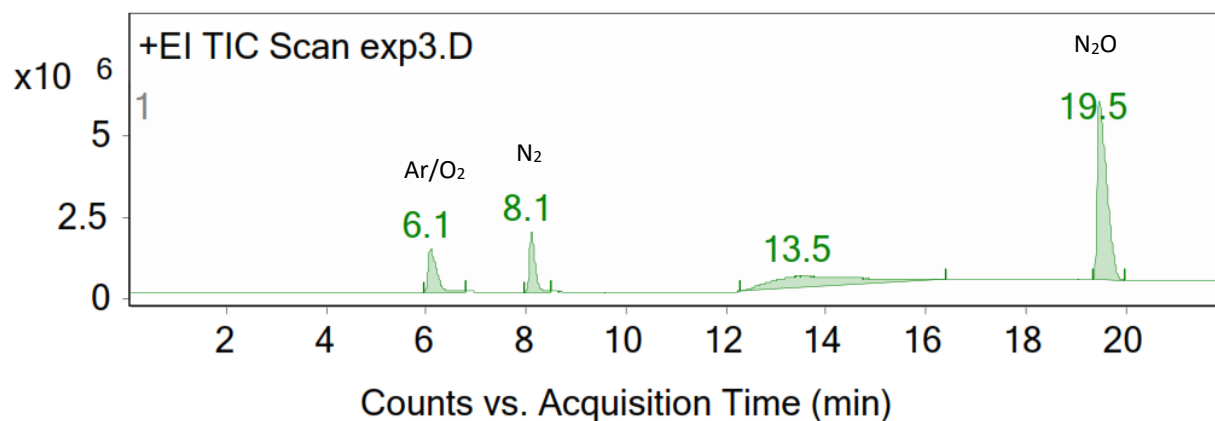
Integration Peak List

Peak	Start	RT	End	Height	Area	Area %
1	5.9	6.1	6.8	1237446.21	15461559.99	21.06
2	8	8.1	8.5	1759590.09	14550449.84	19.82
3	12.3	13.5	16.4	362509.09	45615068.51	62.14
4	19.3	19.5	20	5506292.48	73406645.5	100

FIGURE S 97 Total Ion Chromatogram (TIC) and the peak integration of the headspace (50 µL) from the control reaction – Trial 3
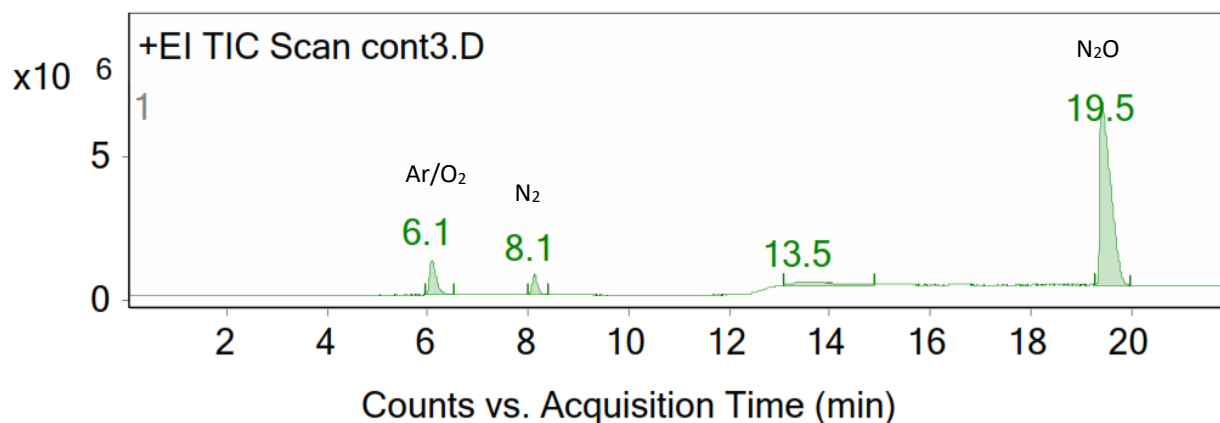
Integration Peak List

Peak	Start	RT	End	Height	Area	Area %
1	5.9	6.1	6.5	1189916.33	11141180.5	12.06
2	8	8.1	8.4	690897.94	5202349.13	5.63
3	13.1	13.5	14.9	89567.5	5961742.91	6.45
4	19.3	19.5	20	5144738.51	92397682.99	100

Data analysis for N_2 quantification

TABLE S 10 N_2 peak area for standards (2-10 µL), Controls and experiments.

Sample	N_2 peak area (integration)	
Standard 2 µL	4,927,980	
Standard 4 µL	8,047,318	
Standard 6 µL	10,738,193	
Standard 8 µL	13,689,632	
Standard 10 µL	16,387,675	
	Control	Experiment
Head space trial 1	4,847,753	13,337,271
Head space trial 2	4,661,892	13,538,900
Head space trial 3	5,202,349	14,550,449
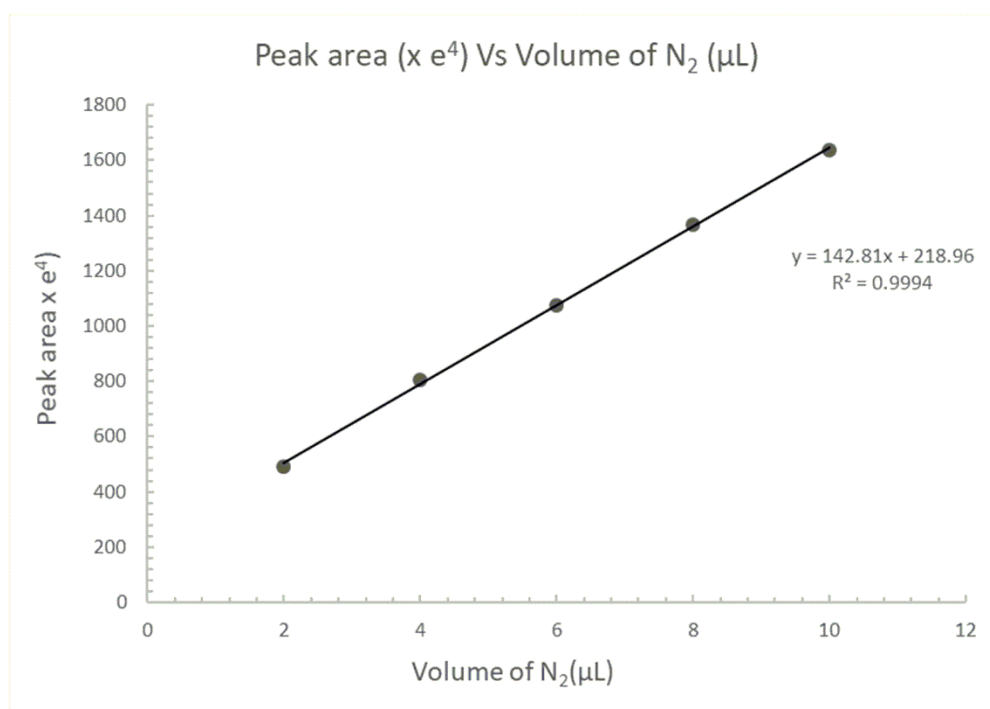
FIGURE S 98 The calibration curve "Peak area (x e^4) Vs volume of N_2 (µL)

Calculation for produce N₂ moles

Assumptions:

1. Room temperature and pressure do not change significantly over the course of entire analysis.

2. N₂ behave as an ideal gas

Calculations for headspace exp 1:

Moles of [Cu₄S(dppa)₄](PF₆)₂[(CH₃)₂CO]₂ (**2**)

$$= \frac{1\ mol}{2233.88\ g} \times 0.1000\ g$$

$$= 0.047\ mmol$$

N₂ peak area for the experiment $= 13{,}337{,}271$

N₂ peak are for the control experiment $= 4{,}847{,}753$

Peak area for produced N₂ from the reaction $= 13{,}337{,}271 - 4{,}847{,}753$

$$= 8{,}489{,}518$$

Produced N₂ volume in 50 μL of the headspace $= 4.4\ \mu L$

(by interpolating from the calibration curve)

Produced N₂ volume in total 10.7 mL of headspace

$$= \frac{4.4\ \mu L}{50\ \mu L} \times 10.7\ mL$$

$$= 0.94\ mL$$

Produced N₂ moles from the reaction

(using PV = nRT)

$$= \frac{PV}{RT}$$

$$= \frac{1\ atm \times 0.94 \times 10^{-3}\ L}{0.082\ L.atm.K^{-1}.mol^{-1} \times 298\ K}$$

$$= 0.038\ mmol$$

[Cu₄S(dppa)₄](PF₆)₂[(CH₃)₂CO]₂ (**2**) : N₂ $= 0.047 : 0.038$

N₂ yield (reference to **2**) $= 81\ \%$

Calculations for headspace exp 2:

Moles of $[Cu_4S(dppa)_4](PF_6)_2[(CH_3)_2CO]_2$ (**2**)

$$= \frac{1\ mol}{2233.88\ g} \times 0.1000\ g$$

$$= 0.047\ mmol$$

N$_2$ peak area for the experiment

$$= 13,538,900$$

N$_2$ peak are for the control experiment

$$= 4,661,892$$

Peak area for produced N$_2$ from the reaction

$$= 13,538,900 - 4,661,892$$

$$= 8,877008$$

Produced N$_2$ volume in 50 μL of the headspace

(by interpolating from the calibration curve)

$$= 4.6\ \mu L$$

Produced N$_2$ volume in total 10.7 mL of headspace

$$= \frac{4.6\ \mu L}{50\ \mu L} \times 10.7\ mL$$

$$= 0.98\ mL$$

Produced N$_2$ moles from the reaction

(using PV = nRT)

$$= \frac{PV}{RT}$$

$$= \frac{1\ atm \times 0.98 \times 10^{-3}\ L}{0.082\ L.atm.K^{-1}.mol^{-1} \times 298\ K}$$

$$= 0.040\ mmol$$

$[Cu_4S(dppa)_4](PF_6)_2[(CH_3)_2CO]_2$ (**2**) : N$_2$

$$= 0.047 : 0.040$$

N$_2$ yield (reference to **2**)

$$= 85\ \%$$

Calculations for headspace exp 3:

Moles of $[Cu_4S(dppa)_4](PF_6)_2[(CH_3)_2CO]_2$ (**2**)	$= \dfrac{1\ mol}{2233.88\ g} \times 0.1000\ g$
	$= 0.047\ mmol$
N_2 peak area for the experiment	$= 14{,}550{,}449$
N_2 peak are for the control experiment	$= 5{,}202{,}349$
Peak area for produced N_2 from the reaction	$= 14{,}550{,}449 - 5{,}202{,}349$
	$= 9{,}348{,}100$
Produced N_2 volume in 50 µL of the headspace (by interpolating from the calibration curve)	$= 5.0\ \mu L$
Produced N_2 volume in total 10.7 mL of headspace	$= \dfrac{5.0\ \mu L}{50\ \mu L} \times 10.7\ mL$
	$= 1.07\ mL$
Produced N_2 moles from the reaction (using PV = nRT)	$= \dfrac{PV}{RT}$
	$= \dfrac{1\ atm \times 1.07 \times 10^{-3}\ L}{0.082\ L.atm.K^{-1}.mol^{-1} \times 298\ K}$
	$= 0.043\ mmol$
$[Cu_4S(dppa)_4](PF_6)_2[(CH_3)_2CO]_2$ (**2**) : N_2	$= 0.047 : 0.043$
N_2 yield (reference to **2**)	$= 91\ \%$

Average N_2 yield (reference to **2**)	$= 86\ \%$
Standard deviation	$= \sqrt{\dfrac{\sum_{i=1}^{3}(x_i - \bar{x})^2}{n-1}}$
	$= \pm 5$

x_i = N_2 yield for ith headspace exp

$\bar{x}$ = Average N_2 yield

n = 3

Produced N_2 yield (reference to **2**) from the reaction	$= 86\ (\pm 5)\ \%$

Qualitative N_2 detection using labeled $^{15}N2O$

Headspace analysis of $^{15}N_2O$ labeled experiment

Inside a N_2 filled glovebox a Schlenk flask was added with $Cu_4S(dppa)_4(PF_6)_2[(CH_3)_2CO]_2$ (10 mg, 0.0047 mmol), $CoCp_2$ (1.88 mg, 0.0099 mmol), acetone (5 mL) and a magnetic stir bar. Flask was secured with a screw cap (Headspace screwTin cap with PTFE/ butyl septum) and taken out. Using a T-joint the flask was connected to both Schlenk line and a $^{15}N_2O$ tank. Three freeze-pump-thaw cycles (5 min each step) were performed before opening the headspace to $^{15}N_2O$. Then the Schlenk flask was closed and the reaction mixture was stirred at room temperature for 1 hour. 50 μL of the headspace was syringed (after flushing the needle 3 times with Ar) and analyzed using GCMS. Similarly, a control experiment was carried out in the absence of $Cu_4S(dppa)_4(PF_6)_2[(CH_3)_2CO]_2$ and a 50 μL aliquot was introduced to GCMS. Retention times of $^{15}N_2$ and $^{15}N_2O$ were 8.1 and 19.6 min respectively (Same as N_2 and N_2O). Therefore, the Extracted Ion Chromatograms (EIC) for m/z = 30 were used to evaluate the corresponding $^{15}N_2$ peak areas for the experiment and the control.

TABLE S 11 Composition of experiment and control of $^{15}N_2O$ labeled headspace analysis.

Parameter	Control	Experiment
Compound **2**	-	10 mg
$CoCp_2$	1.88 mg	1.88 mg
Reaction gas	$^{15}N_2O$	$^{15}N_2O$
Total volume of acetone	5 mL	5 mL
Volume of Headspace	10 mL	10 mL
$^{15}N_2$ Peak area	199331	498864
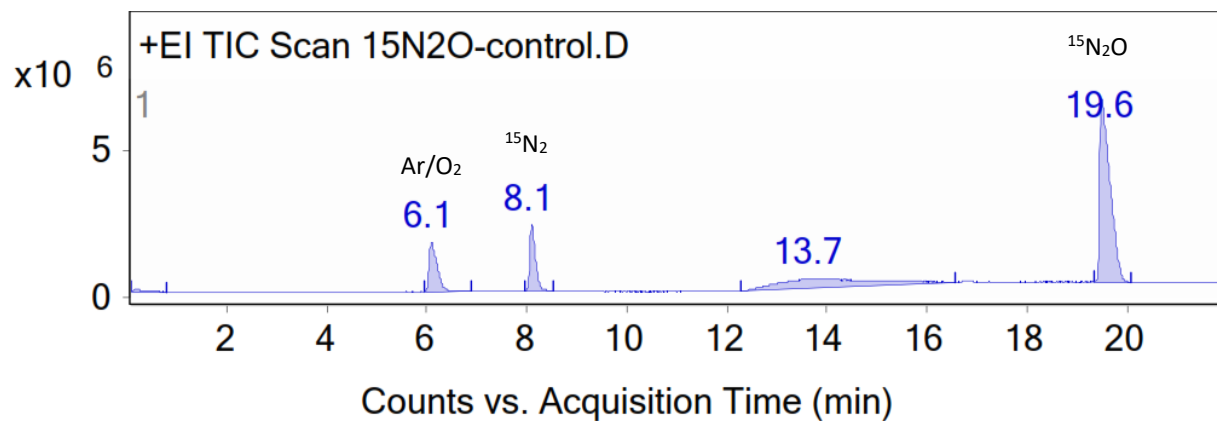
Integration Peak List

Peak	Start	RT	End	Height	Area	Area %
1	0.1	0.2	0.8	72229.82	1394759.32	1.55
2	5.9	6.1	6.9	1685771.77	19426664.63	21.65
3	8	8.1	8.5	2267970.65	18390694.65	20.49
4	12.3	13.7	16.6	303182.16	39909596.51	44.47
5	19.3	19.6	20.1	5197914.58	89735036.64	100

FIGURE S 99 Total Ion Chromatogram (TIC) and the peak integration of the headspace (50 µL) from the $^{15}N_2O$ labeled control experiment.
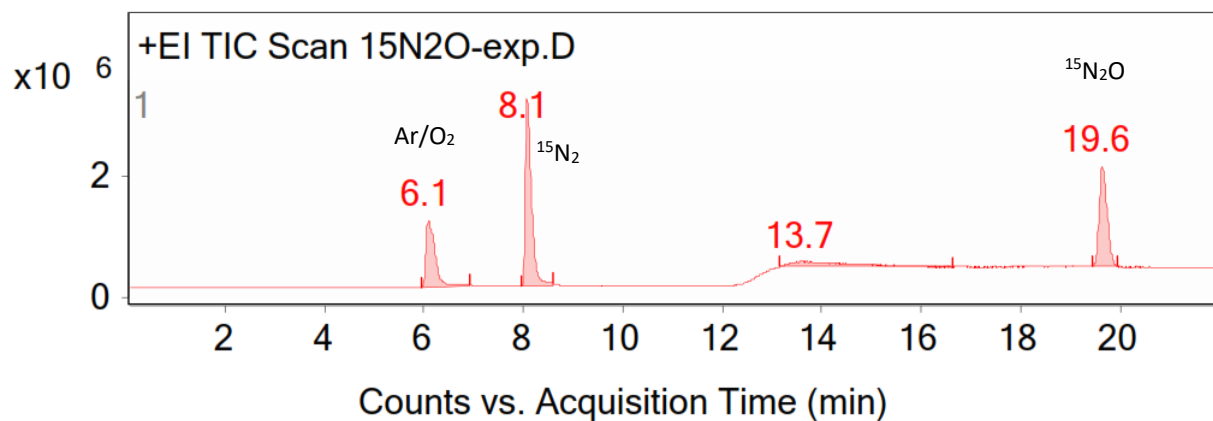
Integration Peak List

Peak	Start	RT	End	Height	Area	Area %
1	5.9	6.1	6.9	1091626.89	14144891.32	52.95
2	8	8.1	8.6	2855928.32	26712083.42	100
3	13.2	13.7	16.6	88529	6945683.32	26
4	19.4	19.6	19.9	1651334	18495800.9	69.24

FIGURE S 100 Total Ion Chromatogram (TIC) and the peak integration of the headspace (50 µL) from the reaction between [Cu4(μ_4- S) (μ_2-dppa)4](PF$_6$)$_2$ (**2**) and $^{15}N_2O$ in acetone with 2 eq of CoCp$_2$.

FIGURE S 101 Extracted Ion Chromatogram (EIC) and the peak integration of the headspace (50 μL) from the $^{15}N_2O$ labeled control experiment.
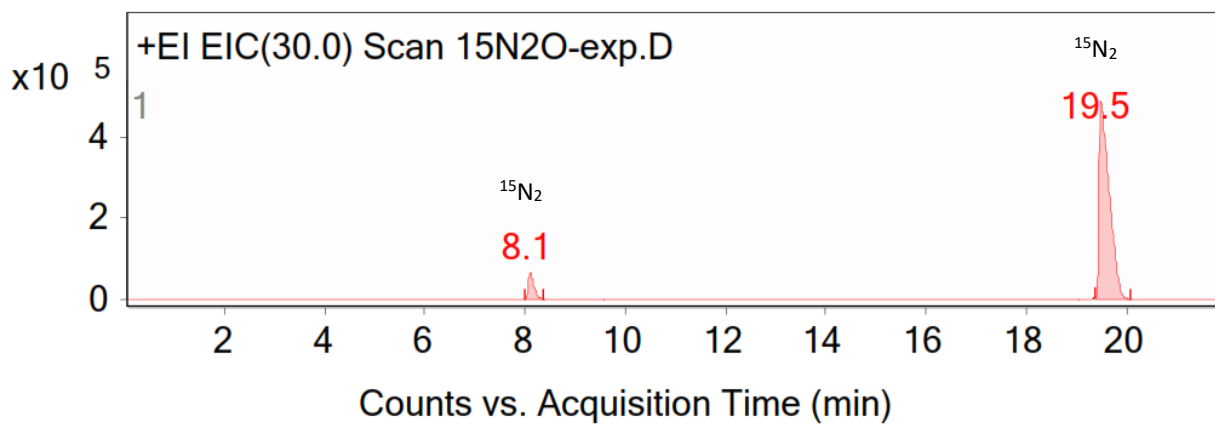
FIGURE S 102 Extracted Ion Chromatogram (EIC) and the peak integration of the headspace (50 μL) from the reaction between $[Cu4(\mu_4\text{-}S)(\mu_2\text{-dppa})_4](PF_6)_2$ (**2**) and $^{15}N_2O$ in acetone with 2 eq of $CoCp_2$.
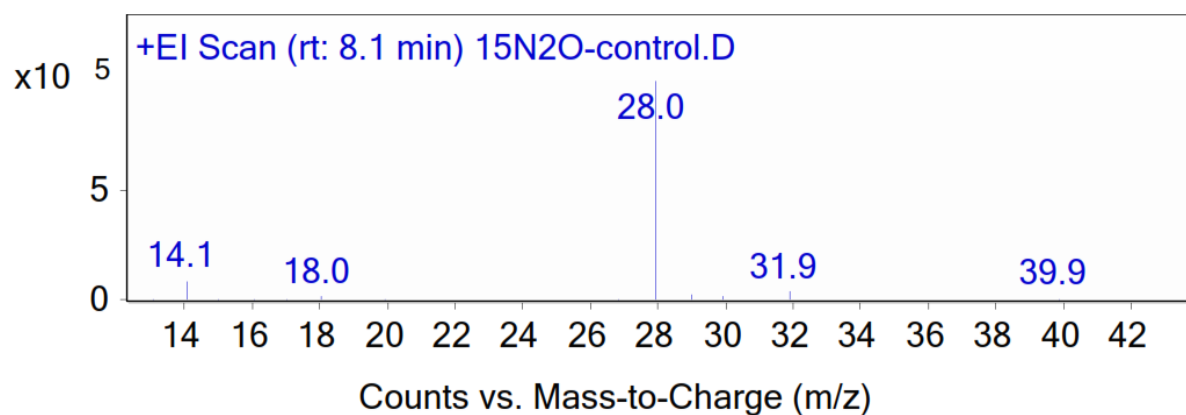
FIGURE S 103 Mass spectrum at retention time: 8.1 min of the EIC of the $^{15}N_2O$ labeled control experiment.
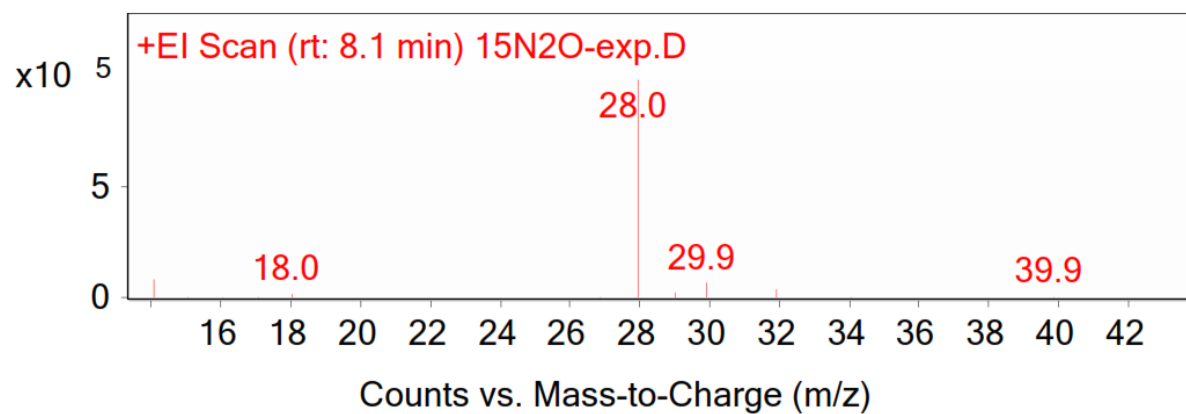
FIGURE S 104 Mass spectrum at retention time: 8.1 min of the EIC of the $^{15}N_2O$ labeled experiment

TABLE S 12 MS Parameter report

Single Quadrupole Acquisition Method - MS Parameters Report

Method file	D:\MassHunter\GCMS\1\methods\SureshN2O.m
Tune file	ATUNE.U
Ion source	EI
Source temperature (°C)	250
Quad temperature (°C)	150
Fixed Electron energy (eV)	70.0
Acquisition Type	Scan
Stop time (min)	650.00
Solvent delay (min)	0.00
Trace Ion Detection	False
Gain Factor	1
EM Saver	False
EM Saver Limit	N/A

Scan Time Segments

Time	Start Mass	End Mass	Threshold	Scan Speed
0.00	9	839	150	1,562 [N=2]
15.50	9	839	150	1,562 [N=2]

Timed Events

Time	Type of Event	Parameter

Real-Time Plots

Type of Plot	Label	Low Mass	High Mass
Spectrum	N/A	N/A	N/A
Base Peak	N/A	N/A	N/A
Extracted Ion	Scan 1-1	9	839

TABLE S 13 Instrument Control Parameters

```
INSTRUMENT CONTROL PARAMETERS:    Agilent 5977B MSD System
---------------------------------------------------------------

  D:\MassHunter\GCMS\1\methods\SureshN2O.m
     Mon Sep 23 18:16:02 2019

Control Information
------- -----------

Sample Inlet            : GC
Injection Source        : Manual
Mass Spectrometer       : Enabled


 No Sample Prep method has been assigned to this method.



GC
GC Summary
Run Time                            22 min
Post Run Time                       3 min

Oven
Equilibration Time                  0.2 min
Max Temperature                     320 °C
Maximum Temperature Override        Disabled
Slow Fan                            Disabled
Temperature
Setpoint                            On
(Initial)                           50 °C
Hold Time                           2 min
Post Run                            50 °C
Program
#1 Rate                             20 °C/min
#1 Value                            220 °C
#1 Hold Time                        0 min
#2 Rate                             40 °C/min
#2 Value                            300 °C
#2 Hold Time                        9.5 min



Front SSZ Inlet He
Mode                                Split
Heater                              On     250 °C
Pressure                            On     1.2 psi
Gas Saver                           Off
Split Ratio                         20 :1
Split Flow                          4.0835 mL/min

Thermal Aux 1 (MSD Transfer Line)
Temperature
Setpoint                            On
(Initial)                           300 °C
Post Run                            0 °C
```

```
Column
Column Outlet Pressure              0 psi
Column #1
Column Information                  Agilent CP7533
CP-Molsieve 5Å
Temperature Range                   -60 °C–350 °C (350 °C)
Dimensions                          25 m x 250 µm x 30 µm


In                                  Front SSZ Inlet He
Out                                 MSD
(Initial)                           50 °C
Pressure                            1.2 psi
Flow                                0.20417 mL/min
Average Velocity                    18.04 cm/sec
Holdup Time                         2.3097 min
Flow
Setpoint                            Off
(Initial)                           0.20417 mL/min
Post Run                            1 mL/min



Valve 1
Name                                ?
Type                                Gas Sampling Valve
GSV Loop Volume                     1 mL
Load Time                           0.5 min
Inject Time                         0.5 min
```

5.2.6   Crystal structure refinement parameters for complex 2 and 3

TABLE S 14 Crystal Data and Structure Refinement of complex **2**

Empirical formula	C207 H210 Cu8 F24 N8 O6 P20 S2
Formula weight	4553.66
Temperature	100.00(10) K
Wavelength	1.54184 Å
Crystal system	Monoclinic
Space group	$P\ 1\ 21/n\ 1$
Unit cell dimensions	a = 13.51084(4) Å $\alpha = 90°$.
	b = 52.87594(16) Å $\beta = 93.2500(3)°$.
	c = 14.51261(4) Å $\gamma = 90°$.
Volume	10351.11(5) Å^3
Z	2
Density (calculated)	1.461 mg/m^3
Absorption coefficient	3.192 mm^{-1}
F(000)	4672
Crystal size	$0.118 \times 0.108 \times 0.069$ mm^3
Theta range for data collection	3.162 to 74.502°.
Index ranges	$-16 \leq h \leq 16, -66 \leq k \leq 65, -18 \leq l \leq 18$
Reflections collected	446459
Independent reflections	21151 [R(int) = 0.0488]
Completeness to theta	67.684° 100.0 %
Absorption correction	Gaussian
Max. and min. transmission	1.000 and 0.607
Refinement method	Full-matrix least-squares on F^2
Data / restraints / parameters	21151 / 391 / 1269
Goodness-of-fit on F^2	1.099
Final R indices [I>2sigma(I)]	R$_1$ = 0.0551, wR$_2$ = 0.1446
R indices (all data)	R$_1$ = 0.0563, wR$_2$ = 0.1454
Extinction coefficient	n/a
Largest diff. peak and hole	2.107 and -1.761 eÅ^{-3}

TABLE S 15 Crystal Data and Structure Refinement of complex **3**

Empirical formula	C74 H65 Cu2 N3 O0.50 P6
Formula weight	1317.19
Temperature	100.00(10) K
Wavelength	1.54184 Å
Crystal system	Triclinic
Space group	P-1
Unit cell dimensions	a = 13.14300(10) Å $\quad \alpha = 86.1510(10)°$.
	b = 13.59950(10) Å $\quad \beta = 81.3720(10)°$.
	c = 21.57920(10) Å $\quad \gamma = 62.1960(10)°$.
Volume	3373.10(5) Å^3
Z	2
Density (calculated)	1.297 mg/m^3
Absorption coefficient	2.466 mm^{-1}
F(000)	1364
Crystal size	0.202 × 0.167 × 0.128 mm^3
Theta range for data collection	3.674 to 77.947°.
Index ranges	$-16 \leq h \leq 16, -17 \leq k \leq 17, -24 \leq l \leq 27$
Reflections collected	149824
Independent reflections	14367 [R(int) = 0.0424]
Completeness to theta	67.684° 100.0 %
Absorption correction	Gaussian
Max. and min. transmission	1.000 and 0.480
Refinement method	Full-matrix least-squares on F^2
Data / restraints / parameters	14367 / 66 / 796
Goodness-of-fit on F^2	1.043
Final R indices [I>2sigma(I)]	R$_1$ = 0.0354, wR$_2$ = 0.0932
R indices (all data)	R$_1$ = 0.0370, wR$_2$ = 0.0944
Extinction coefficient	n/a
Largest diff. peak and hole	0.716 and -0.707 eÅ^{-3}

5.2.7   References

i.   *CrysAlisPro*; Rigaku OD, The Woodlands, TX, 2015.

ii.   Sheldrick, G. M. *Acta Cryst*. **2015**, *A71*, 3.

iii.   Sheldrick, G.M. *Acta Cryst*. **2008**, *A64*, 112.

iv.   Müller, P. *Crystallography Reviews* **2009**, *15*, 57.

v.   1Dolomanov, O.V.; Bourhis, L.J.; Gildea, R.J.; Howard, J.A.K.; Puschmann, H. *J. Appl. Cryst*. **2009**, 42, 339.

vi.   Johnson, B. J.; Lindeman, S. V.; Mankad, N. P. *Inorg. Chem*. **2014**, *53*, 10611.

      (a) Bonner, O. D.; Choi, Y. S. *J. Phys. Chem*. **1974**, *78*, 1723; (b) Bonner, O. D.; Choi, Y. S. *J. Phys. Chem*. **1974**, *78*, 1727.

vii.   Galinski, E. A.; Stein, M.; Amendt, B.; Kinder, M. *Comp. Biochem. Physiol. A* **1997**, *117*, 357.

viii.   Frisch, M.J., Trucks, G.W., Schlegel, H.B., Scuseria, G.E., Robb, M.A., Cheeseman, J.R., Scalmani, G., Barone, V., Mennucci, B. G., Petersson, A., Nakatsuji, H., Caricato, M., Li, X., Hratchian, H.P., Izmaylov, A.F., Bloino, J., Zheng, G., Sonnenberg, J.L., Hada, M., Ehara, Toyota, M. K., Fukuda, R., Hasegawa, J., Ishida, M., Nakajima, T., Honda, Y., Kitao, O., Nakai, H., Vreven, T., Montgomery Jr., J.A., Peralta, J.E., Ogliaro, F., Bearpark, M., Heyd, J.J., Brothers, E., Kudin, K.N., Staroverov, V.N., Kobayashi, R., Normand, J., Raghavachari, Rendell, K. A., Burant, J.C., Iyengar, S.S., Tomasi, J., Cossi, M., Rega, N., Millam, J.M., Klene, M., Knox, J.E., Cross, J.B., Bakken, V., Adamo, C., Jaramillo, J., Gomperts, R., Stratmann, R.E., Yazyev, O., Austin, A.J., Cammi, R., Pomelli, C., Ochterski, J.W., Martin, R.L., Morokuma, K., Zakrzewski, V.G., Voth, G.A., Salvador, P., Dannenberg,J.J., Dapprich, S., Daniels, A.D., Farkas,O., Foresman, J.B., Ortiz, J.V., Cioslowski, J. and Fox, D.J. Gaussian 09, Revision A.02, Gaussian, Inc., Wallingford, CT, 2009.

5.3   Supporting information for Chapter 4

Reprinted with the permission from Rathnayaka, S. C.; Islam, S. M.; DiMucci, I. M.; MacMillan, S. N.; Lancaster, K. M.; Mankad, N. P. Probing the Electronic and Mechanistic Roles of the µ 4 -Sulfur Atom in a Synthetic Cu Z Model System. *Chem. Sci.* **2020**, *11*, 3441–3447. Copyrights 2020 Royal Society of Chemistry.

5.3.1   General remarks

All solvents except acetone were purchased from commercial suppliers, purified under argon with a Glass Contour Solvent System built by Pure Process Technology, and stored in a N_2-filled glovebox over 4-Å molecular sieves. Acetone (extra dry) was purchase from Acros and also treated with extra molecular sieves for further purification. Deuterated solvents were degassed and purified with 4-Å molecular sieves before use. All reactions were operated under N_2 with standard glovebox and Schlenk line techniques unless otherwise indicated. Medical grade nitrous oxide was purchased from Praxair and passed through a Drierite column for delivery to reaction vessels.

Instrument specifications

NMR spectra for compound characterization were recorded at ambient temperature using a Bruker Avance DPX-400 spectrometer. Chemical shifts are reported in ppm units relative to the residual signal of the solvent. Synthesis of the 1-hole and 2-hole [Cu$_4$S] clusters was based on literature procedures.[1] N_2 samples for calibration curves were syringed using a Hamilton gas tight syringe (10 µL, Model 1801 RN, Small Removable Needle, 26s gauge, 2 in, point style 2). Reaction and control head space gas samples (50 µL) were collected using Hamilton gas tight syringe (100 µL, Model 1710 SL SYR, customized Removable NDL(1 inch), 22s ga, 2 in, point style 2). GCMS data were collected using Agilent 5977B MSD sytem coupled to Agilent 7820A GC system with a CP-Molseieve 5A column (see Tables S3-S6 for other instrument, column and inlet control parameters). GCMS data analysis was performed using Agilent MassHunter Analysis Navigator B.08.00 software.

5.3.2   Quantification of Produced N_2 by Headspace Analysis of the Reaction between $[Cu_4(\mu_4\text{-}S)(\mu_2\text{-}2,4,6\text{-}$
trimethylphenylformamidinate)$_4$][K(18-crown-6)] (1-hole) and N_2O in acetone.

Construction of a calibration curve

Five Schlenk flasks fitted with screw-cap septa (Headspace screwTin cap with PTFE/ butyl septum) were vacuum-refilled 3 times and filled with pure nitrogen. 2, 4, 6, 8 and 10 µL of pure N_2 samples were syringed separately from each flask and were injected into the GCMS. Peak area for each standard N_2 sample was recorded and plotted against the corresponding volume of N_2 to construct a calibration curve "Peak area Vs Volume of N_2 (µL)". Retention time for O_2 (trace) and N_2 are 4.3 and 6.1 min respectively.
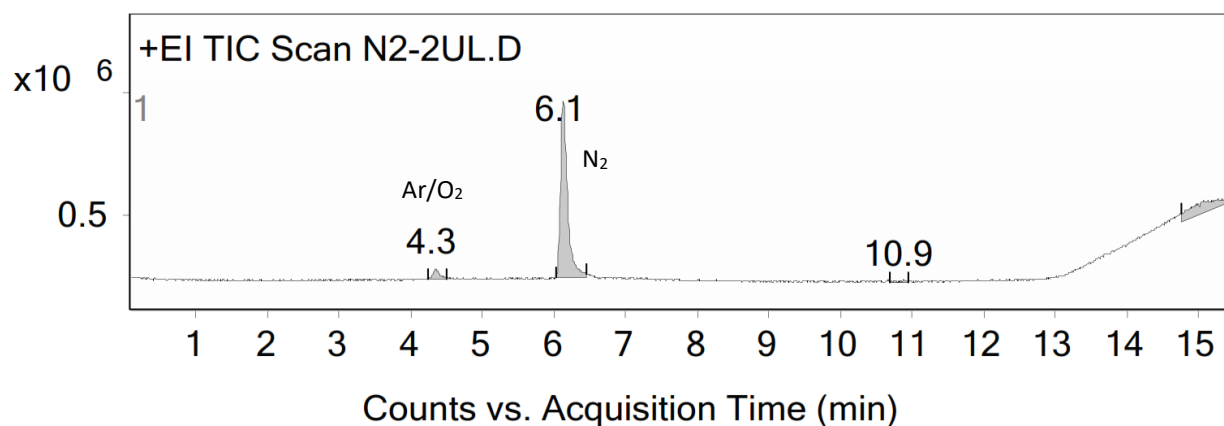
Integration Peak List

Peak	Start	RT	End	Height	Area	Area %
1	4.2	4.3	4.5	41590.73	263341.39	5.3
2	6	6.1	6.5	718399.34	4965640.6	100
3	10.7	10.9	10.9	9736.76	65628.54	1.32
4	14.8	15.3	15.4	31036.05	1306016.5	26.3

FIGURE S 105 The Total Ion Chromatogram (TIC) and the peak integration for 2 µL N_2 standard.
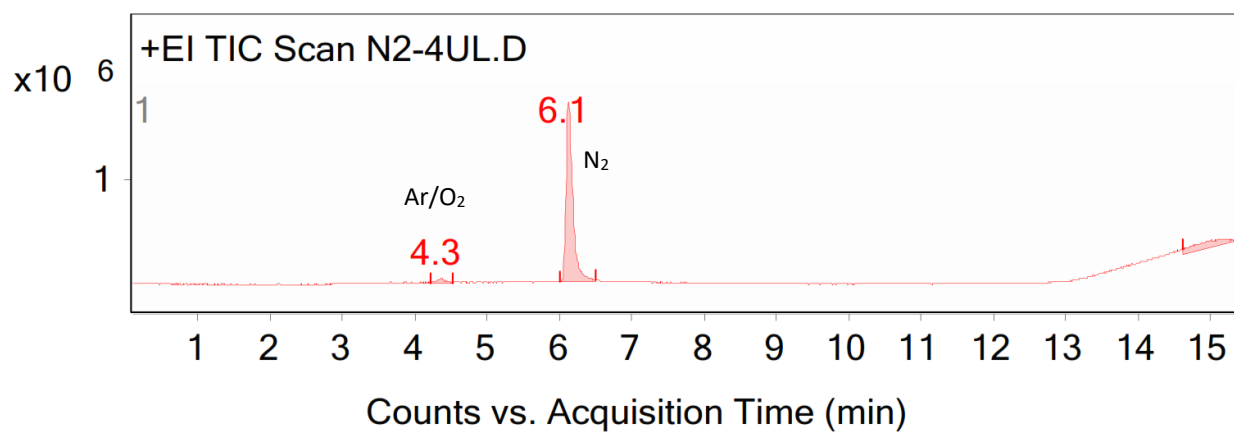
FIGURE S 106 The Total Ion Chromatogram (TIC) and the peak integration for 4 μL N_2 standard.
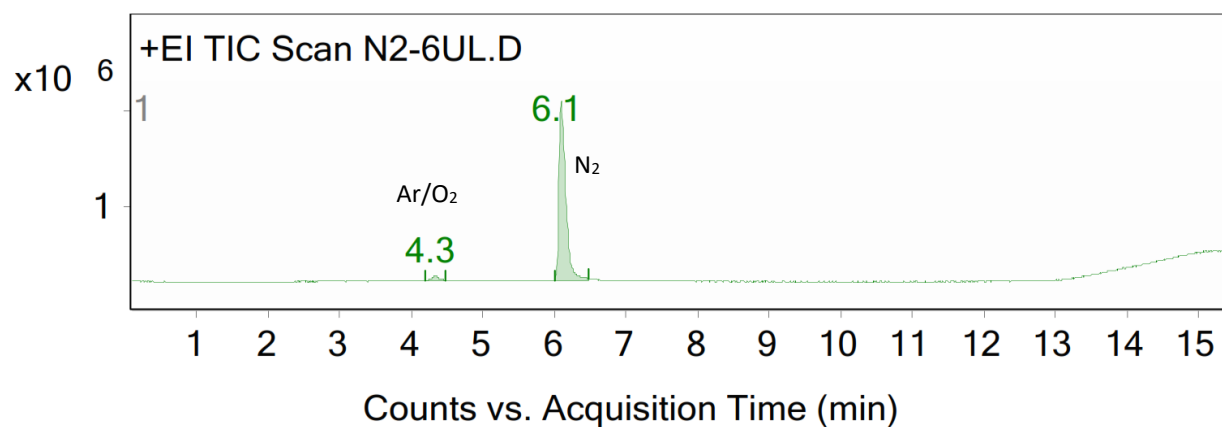
FIGURE S 107 The Total Ion Chromatogram (TIC) and the peak integration for 6 μL N_2 standard.

FIGURE S 108 The Total Ion Chromatogram (TIC) and the peak integration for 8 μL N₂ standard.
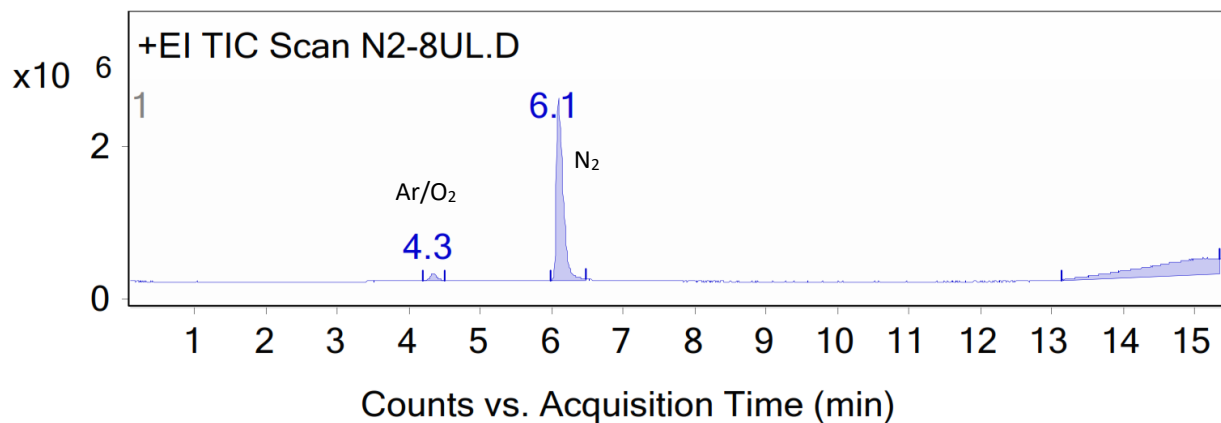
Integration Peak List

Peak	Start	RT	End	Height	Area	Area %
1	4.2	4.3	4.5	93396.29	647698.25	4.13
2	6	6.1	6.5	2403337.82	15482161.84	98.64
3	13.1	15.2	15.3	219968.1	15696028.35	100

FIGURE S 109 The Total Ion Chromatogram (TIC) and the peak integration for 10 μL N₂ standard.
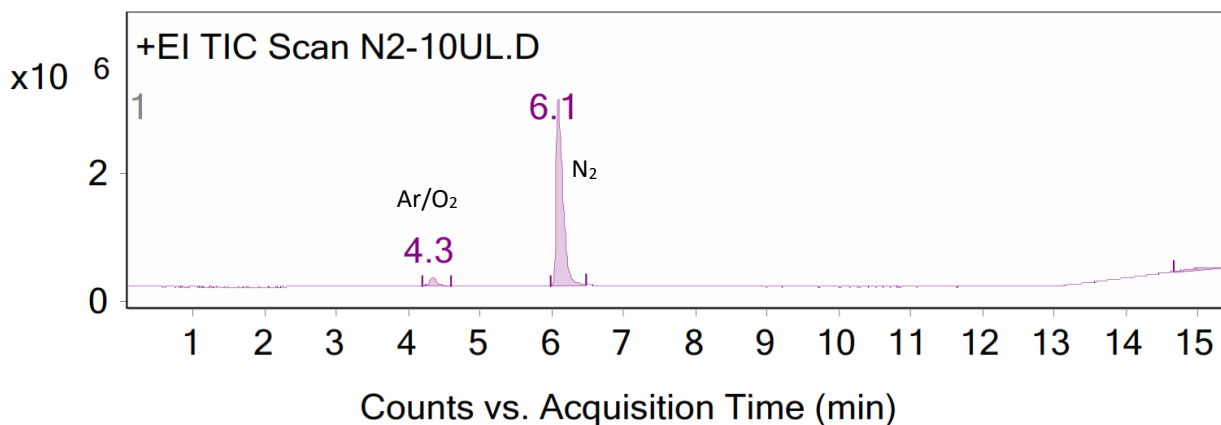
Integration Peak List

Peak	Start	RT	End	Height	Area	Area %
1	4.2	4.3	4.6	141987.09	970282.76	5.12
2	6	6.1	6.5	2914764.09	18934075.64	100
3	14.7	15.2	15.4	33154.09	1445020.29	7.63

Headspace analysis of the reaction
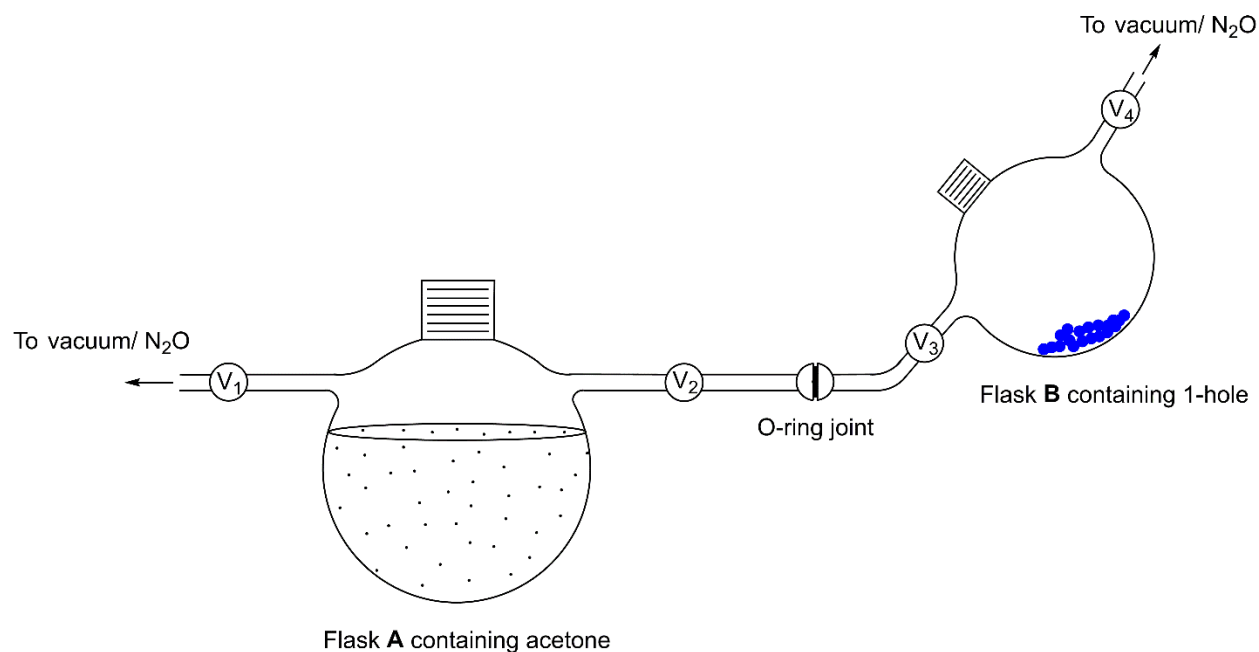
FIGURE S 110 Experimental setup used for headspace analysis.

The apparatus shown above (**Figure S110**) was used for the analysis to minimize any background N_2 and to avoid any air oxidation of the 1-hole cluster. In a N_2 filled glove box, flask **A** was charged with 55.0 mL of acetone and a magnetic stir bar. Similarly, flask **B** was charged with [Cu$_4$(μ_4-S)(μ_2-2,4,6-trimethylphenylformamidinate)$_4$] [K(18-crown-6)] (1-hole) (148.9 mg, 0.087 mmol) and a magnetic stir bar. Both flasks were secured with screw-cap septa (Headspace screwTin cap with PTFE/ butyl septum), and then flask **B** was then connected to a vacuum line and evacuated for 30 min. Both flasks were taken out of the glove box after closing the valves V_1, V_2, V_3 and V_4. Flasks were connected at the O-ring joint and were attached to Schlenk line (N_2O/vacuum) at V_1 and V_4. Acetone in flask **A** was frozen using liquid nitrogen and the headspace was evacuated by opening valves V_1, V_2, V_3 and V_4 to vacuum for 5 min. Next, V_1 and V_4 were closed and the acetone was allowed to thaw. During the thawing process, V_4 was opened to vacuum (for 3 sec) occasionally to release any buildup pressure. Then V_2 was closed and acetone in flask **A** was frozen again while keeping V_4 open to vacuum. Similarly, two more freeze-pump-thaw cycles were performed to remove remaining headspace gases and any dissolved gases. After the final cycle, acetone was allowed to reach room temperature for 20 min and V_2 was closed and V_4 was opened to vacuum. Headspace of Flask **A** was filled with N_2O

by opening V_1 to N_2O. V_1 was then closed and the acetone was stirred for 30 min allowing N_2O to equilibrate. Then, the space between V_2 and V_4 was filled with N_2O by opening V_4 to N_2O. Finally, V_4 was closed and the acetone in flask **A** was transferred into flask **B** by tilting the entire setup clockwise, while keeping V_1 open to N_2O. Once all the acetone was transferred, V_1 and V_3 were closed and the flask **B** was detached at the O-ring and from the Schlenk line. The reaction mixture was stirred for 4 h at -78 °C and allowed to reach room temperature over 1 h. A 50-μL portion of the headspace was syringed (after flushing the needle 3 times with Ar) and analyzed using GCMS. Retention times for Ar, N_2 and N_2O were 4.3, 6.1 and 14.9 min respectively. H_2O from the CP-molsieve 5A column began to elute around 12.3 min. The reaction mixture was taken back into the glove box and filtered through a fine frit to recover the produced 2-hole. Solid on the frit was rinsed with 2×10 mL of acetone and 10 mL of Et_2O. The dark residue was completely dried under vacuum and NMR was taken in CD_2Cl_2 (**Figure S118**). Filtrate was completely evaporated, and NMR was taken in acetone-d_6 (**Figure S119**). A separate control experiment was carried out in the absence of 1-hole and the head space was analyzed in a similar manner. The whole experiment (both exp and control) was repeated two more times and the results were averaged.

Caution: With the limited head space volume, the thawing process must be done carefully while opening the head space to vacuum occasionally to prevent the Schlenk flask/ setup from exploding.

TABLE S 16 Details of experiment and control runs of headspace analysis.

Parameter		Experiment	Control
1-hole		148.9 mg	-
Reaction gas		N_2O	N_2O
Total volume of reaction flask **B**		65.7 mL	65.5 mL
Total volume of acetone		55.0 mL	54.8 mL
Volume of Headspace		10.7 mL	10.7 mL
Recovered 2-hole	Trial 1	0.0477 g	N/A
	Trial 2	0.0679 g	
	Trial 2	0.0507 g	
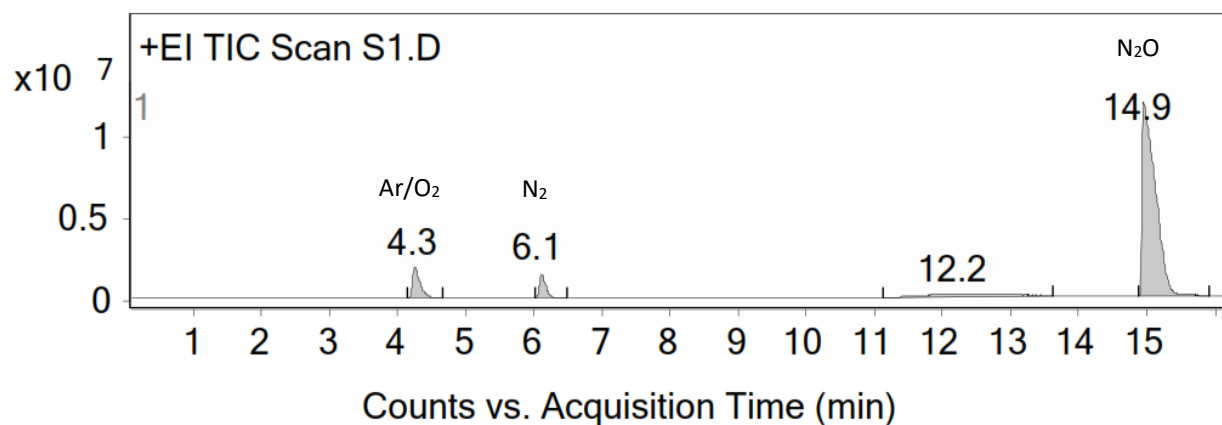
Integration Peak List

Peak	Start	RT	End	Height	Area	Area %
1	4.1	4.3	4.7	1854138.41	14809365.81	9.35
2	6	6.1	6.5	1480061.6	9328899.21	5.89
3	11.1	12.2	13.6	136005.82	11511281.87	7.27
4	14.9	14.9	15.9	11791901.95	158371163.73	100

FIGURE S 111 Total Ion Chromatogram (TIC) and the peak integration of the headspace (50 μL) from the reaction between 1-hole and N_2O in acetone – Trial 1
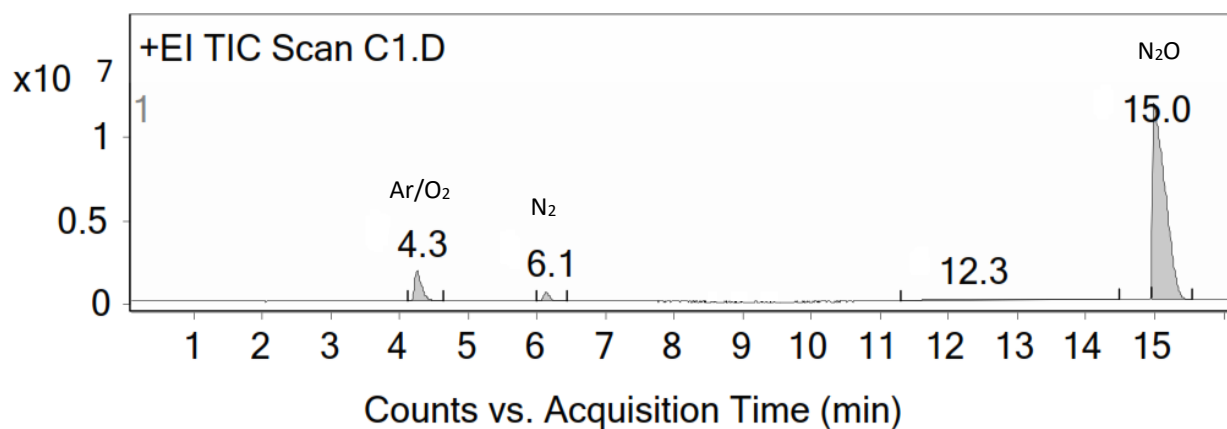
Integration Peak List

Peak	Start	RT	End	Height	Area	Area %
1	4.1	4.3	4.6	1760896.17	13580475.57	9.18
2	6	6.1	6.4	592103.9	3701271.78	2.5
3	11.3	12.3	14.5	117155.62	11468083.8	7.76
4	14.9	15	15.6	11708257.9	147877861.22	100

FIGURE S 112 Total Ion Chromatogram (TIC) and the peak integration of the headspace (50 μL) from the control reaction – Trial 1

Integration Peak List

Peak	Start	RT	End	Height	Area	Area %
1	4.2	4.3	4.8	1619286.58	13022682.39	9.23
2	6	6.1	6.5	1620249.44	10470446	7.42
3	11	12.1	13.7	142052.64	12330752.89	8.74
4	14.9	14.9	15.5	11285538.93	141150950.34	100
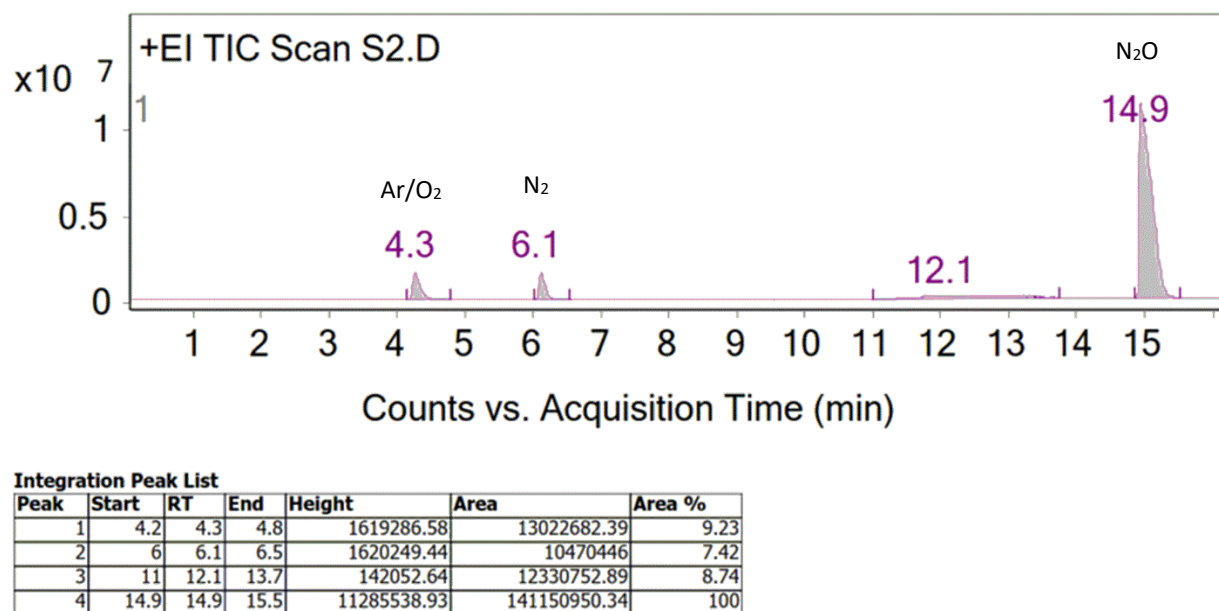
FIGURE S 113 Total Ion Chromatogram (TIC) and the peak integration of the headspace (50 μL) from the reaction between 1-hole and N_2O in acetone – Trial 2

Integration Peak List

Peak	Start	RT	End	Height	Area	Area %
1	4.1	4.2	4.8	1154788.66	9846659.58	6.9
2	6	6.1	6.4	706874.39	4343091.95	3.04
3	11.1	12.1	14	128114.95	11585254.9	8.11
4	14.9	14.9	15.5	11455672.39	142771694.92	100
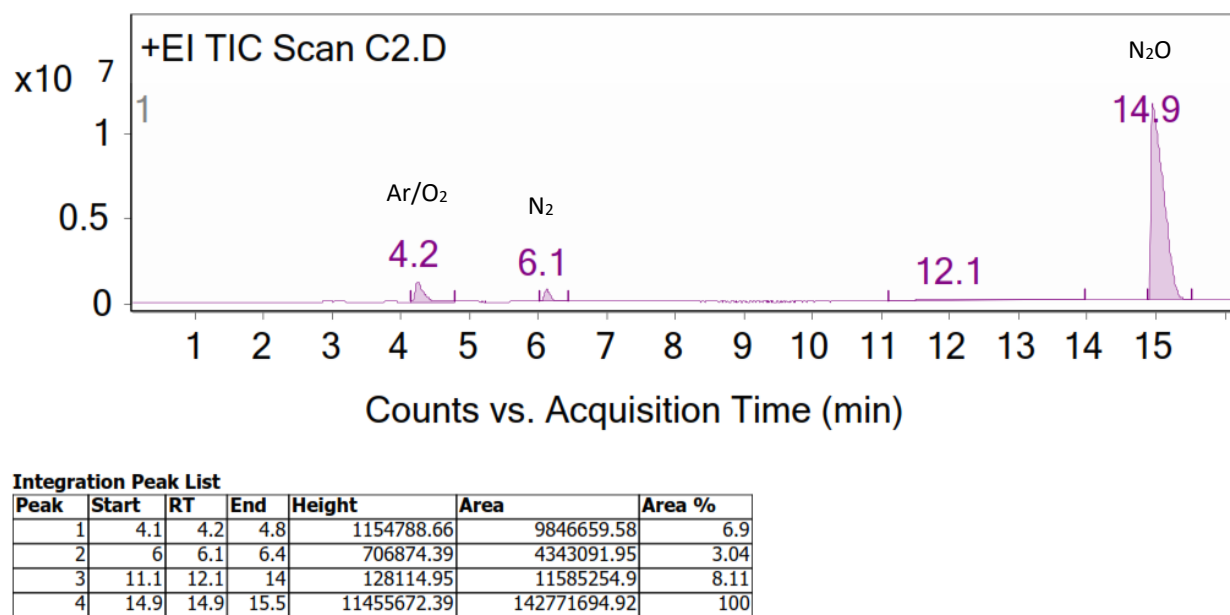
FIGURE S 114 Total Ion Chromatogram (TIC) and the peak integration of the headspace (50 μL) from the control reaction – Trial 2

FIGURE S 115 Total Ion Chromatogram (TIC) and the peak integration of the headspace (50 µL) from the reaction between 1-hole and N_2O in acetone – Trial 3
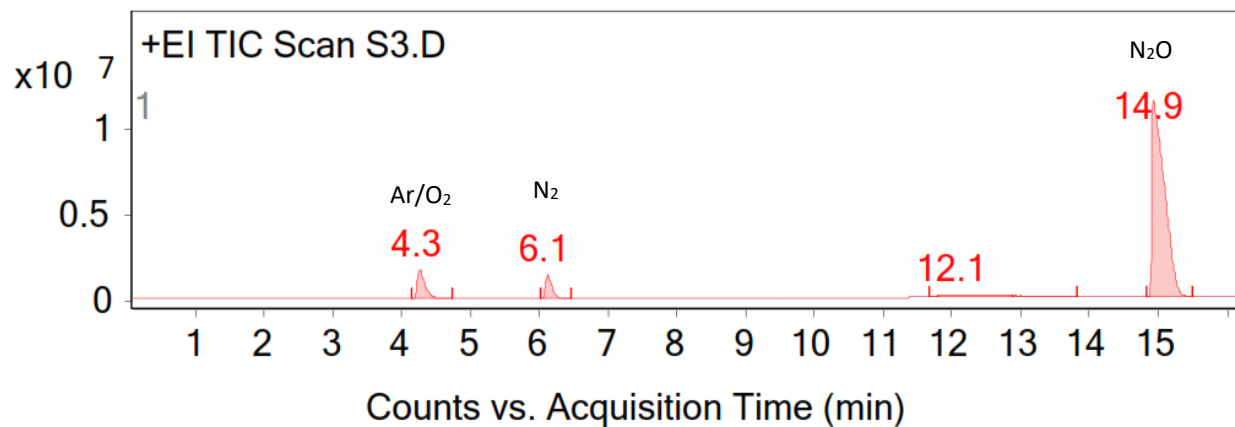
Integration Peak List

Peak	Start	RT	End	Height	Area	Area %
1	4.1	4.3	4.7	1692061.81	13930292.04	9.79
2	6	6.1	6.5	1328445.76	8994435.01	6.32
3	11.7	12.1	13.8	51318.33	3433487.06	2.41
4	14.8	14.9	15.5	11321683.11	142288175.79	100

FIGURE S 116 Total Ion Chromatogram (TIC) and the peak integration of the headspace (50 µL) from the control reaction – Trial 3
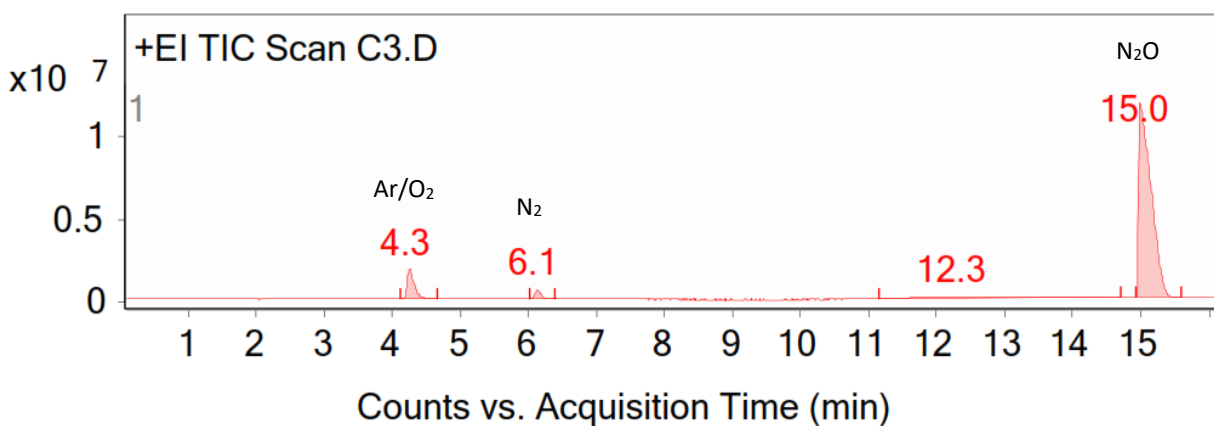
Integration Peak List

Peak	Start	RT	End	Height	Area	Area %
1	4.1	4.3	4.7	1765110.59	13859762.11	9.3
2	6	6.1	6.4	590501.95	3657080.5	2.45
3	11.2	12.3	14.7	129757.5	13863590.69	9.3
4	14.9	15	15.6	11759648.25	148998148.69	100

Data analysis

TABLE S 17 N_2 peak area for standards (2-10 µL), Controls and experiments.

Sample	N_2 peak area (integration)	
Standard 2 µL	4,965,640	
Standard 4 µL	8,755,552	
Standard 6 µL	12,117,721	
Standard 8 µL	15,482,161	
Standard 10 µL	18,934,075	
	Experiment	Control
Head space trial 1	9,328,899	3,701,271
Head space trial 2	10,470,446	4,343,091
Head space trial 3	8,994,435	3,657,080
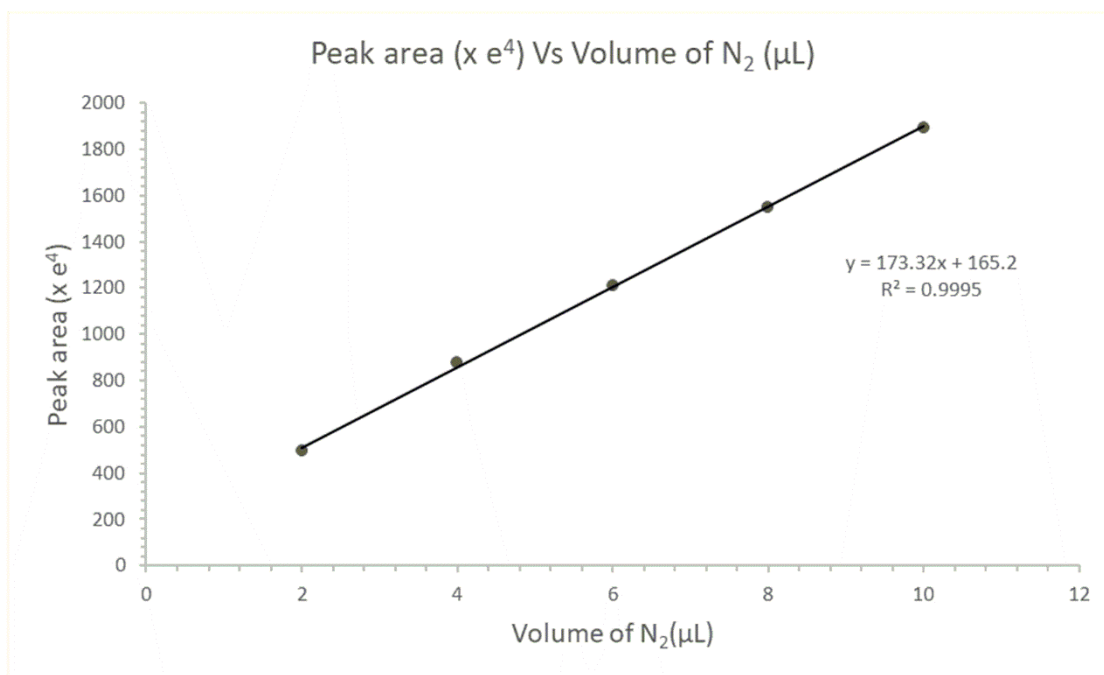
FIGURE S 117 The calibration curve "Peak area (x e^4) Vs volume of N_2 (µL)

Calculation for produced N_2 per mole of 1-hole

Assumptions:

1. Room temperature and pressure do not change significantly over the course of entire analysis.

2. N_2 behaves as an ideal gas

Calculations for headspace exp 1:

Moles of 1-hole complex	$= \dfrac{1\ mol}{1707.29\ g} \times 0.1489\ g$
	$= 0.087\ mmol$
N_2 peak area for the experiment	$= 9{,}328{,}899$
N_2 peak are for the control experiment	$= 3{,}701{,}271$
Peak area for produced N_2 from the reaction	$= 9{,}328{,}899 - 3{,}701{,}271$
	$= 5{,}627{,}628$
Produced N_2 volume in 50 µL of the headspace (by interpolating from the calibration curve)	$= 2.29\ \mu L$
Produced N_2 volume in total 10.7 mL of headspace	$= \dfrac{2.29\ \mu L}{50\ \mu L} \times 10.7\ mL$
	$= 0.49\ mL$
Produced N_2 moles from the reaction (using PV = nRT)	$= \dfrac{PV}{RT}$
	$= \dfrac{1\ atm \times 0.49 \times 10^{-3}\ L}{0.082\ L.atm.K^{-1}.mol^{-1} \times 298\ K}$
	$= 0.020\ mmol$
Recovered 2-hole weight	$= 0.0477\ g$
Produced 2-hole	$= 0.034\ mmol$
Consumed 1-hole	$= 0.034\ mmol$
1-hole : N_2	$= 0.034 : 0.020$
	$= 1 : 0.59$
Yield of 2-hole	$= 39\ \%$

Calculations for headspace exp 2:

Moles of 1-hole	$= \dfrac{1 \; mol}{1707.29 \; g} \times 0.1489 \; g$
	$= 0.087 \; mmol$
N_2 peak area for the experiment	$= 10{,}470{,}446$
N_2 peak are for the control experiment	$= 4{,}343{,}091$
Peak area for produced N_2 from the reaction	$= 10{,}470{,}446 - 4{,}343{,}091$
	$= 6{,}127{,}355$
Produced N_2 volume in 50 µL of the headspace (by interpolating from the calibration curve)	$= 2.58 \; \mu L$
Produced N_2 volume in total 10.7 mL of headspace	$= \dfrac{2.58 \; \mu L}{50 \; \mu L} \times 10.7 \; mL$
	$= 0.55 mL$
Produced N_2 moles from the reaction (using PV = nRT)	$= \dfrac{PV}{RT}$
	$= \dfrac{1 \; atm \times 0.55 \times 10^{-3} \; L}{0.082 \; L.atm.K^{-1}.mol^{-1} \times 298 \; K}$
	$= 0.022 \; mmol$
Recovered 2-hole weight	$= 0.0642 \; g$
Produced 2-hole	$= 0.046 \; mmol$
Consumed 1-hole	$= 0.046 \; mmol$
1-hole : N_2	$= 0.046 : 0.022$
	$= 1 : 0.48$
Yield of 2-hole	$= 53 \; \%$

Calculations for headspace exp 3:

Moles of 1-hole	$= \dfrac{1\ mol}{1707.29\ g} \times 0.1489\ g$
	$= 0.087\ mmol$
N_2 peak area for the experiment	$= 8{,}994{,}435$
N_2 peak are for the control experiment	$= 3{,}657{,}080$
Peak area for produced N_2 from the reaction	$= 8{,}994{,}435 - 3{,}657{,}080$
	$= 5{,}337{,}355$
Produced N_2 volume in 50 µL of the headspace (by interpolating from the calibration curve)	$= 2.13\ \mu L$
Produced N_2 volume in total 10.7 mL of headspace	$= \dfrac{2.13\ \mu L}{50\ \mu L} \times 10.7\ mL$
	$= 0.46 mL$
Produced N_2 moles from the reaction (using PV = nRT)	$= \dfrac{PV}{RT}$
	$= \dfrac{1\ atm \times 0.46 \times 10^{-3}\ L}{0.082\ L.atm.K^{-1}.mol^{-1} \times 298\ K}$
	$= 0.019\ mmol$
Recovered 2-hole weight	$= 0.0507\ g$
Produced 2-hole	$= 0.036\ mmol$
Consumed 1-hole	$= 0.036\ mmol$
1-hole : N_2	$= 0.036 : 0.019$
	$= 1 : 0.52$
Yield of 2-hole	$= 41\ \%$

Average N_2 moles produced per 1 mole of 1-hole = 0.53 mol

Standard deviation $= \sqrt{\dfrac{\sum_{i=1}^{3}(x_i-\bar{x})^2}{n-1}}$

x_i = N_2 moles per 1 mole of 1-hole for the ith headspace exp
$\bar{x}$ = Average N_2 moles produced per 1 mole of 1-hole
n = 3

$= \pm 0.06$

Produced N_2 moles per 1 mole of 1-hole = 0.53 (± 0.06) mol
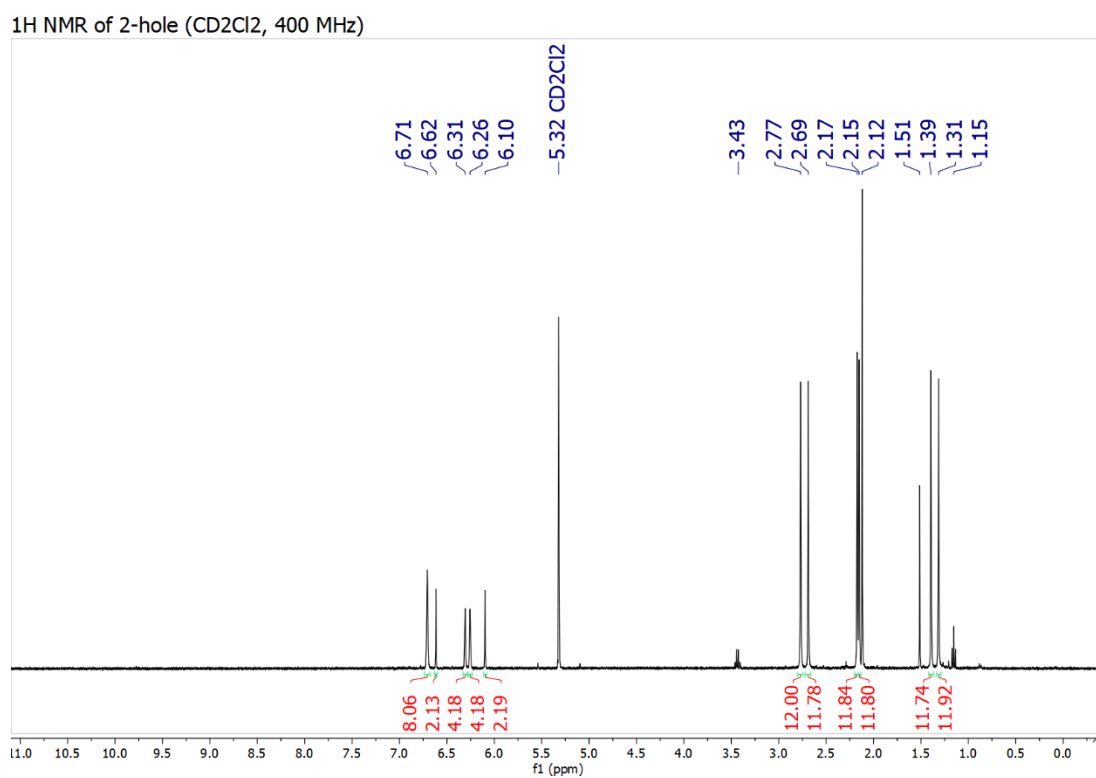
FIGURE S 118 ^{1}H Sample NMR of the 2-hole recovered. ^{1}H NMR (400 MHz, CD$_2$Cl$_2$) δ 6.71 (s, 8H, Ar CH), 6.62 (s, 2H, NC(H)N), 6.31 (s, 4H, Ar CH), 6.26 (s, 4H, Ar CH), 6.10 (s, 2H, NC(H)N), 2.77 (s, 12H, Ar CH3), 2.69 (s, 12H, Ar CH3), 2.17 (s, 12H, Ar CH3), 2.15 (s, 12H, Ar CH3), 2.12 (s, residual acetone), 1.51 (s, residual H$_2$O), 1.39 (s, 12H, Ar CH3), 1.31 (s, 12H, Ar CH3), 3.43 (q, residual Et$_2$O), 1.15 (t, residual Et$_2$O)
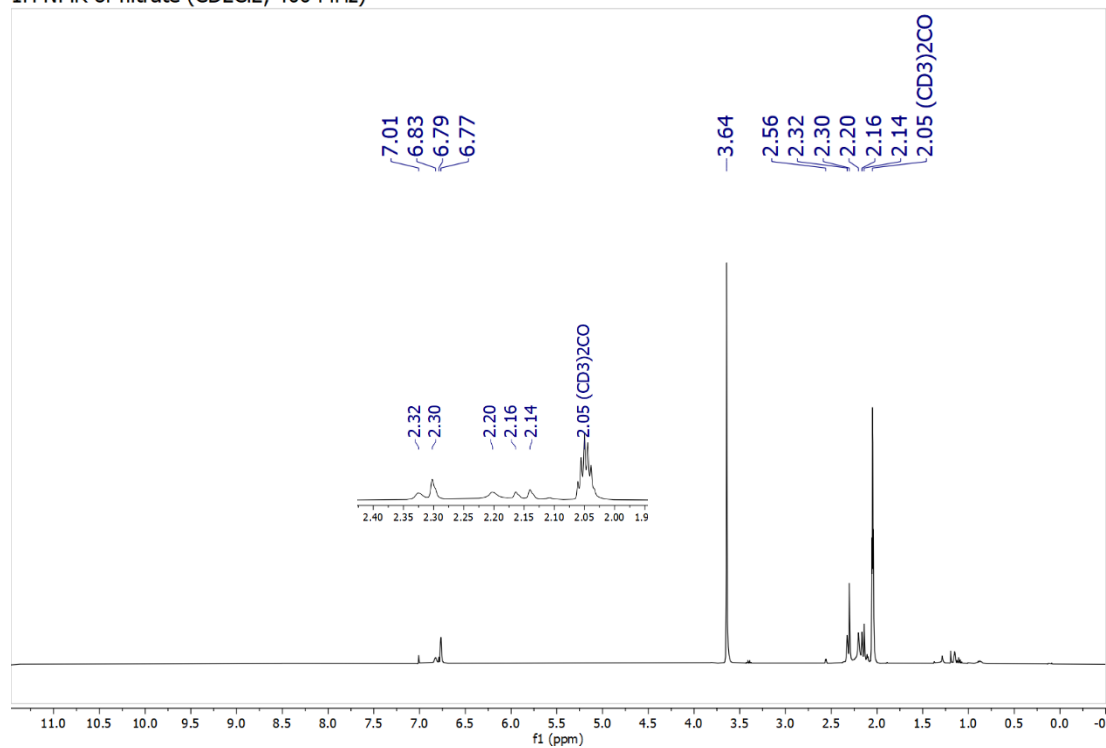
FIGURE S 119 Sample ^{1}H NMR of the filtrate collected. ^{1}H NMR (400 MHz, CD$_2$Cl$_2$) δ 3.64 (s, 18-crown-6), 2.05 (aceton-d_6). Characteristic peaks for Cu$_2$(NCN)$_2$ precursor were located at δ 7.01, 6.79, 2.30 and 2.20 overlapping with unidentified byproducts.

TABLE S 18 MS parameter report for calibration.

Single Quadrupole Acquisition Method - MS Parameters Report

Method file	D:\MassHunter\GCMS\1\methods\SureshNitrogent.m
Tune file	ATUNE.U
Ion source	EI
Source temperature (°C)	250
Quad temperature (°C)	150
Fixed Electron energy (eV)	70.0
Acquisition Type	Scan
Stop time (min)	650.00
Solvent delay (min)	0.00
Trace Ion Detection	False
Gain Factor	1
EM Saver	False
EM Saver Limit	N/A

Scan Time Segments

Time	Start Mass	End Mass	Threshold	Scan Speed
0.00	9	839	150	1,562 [N=2]
15.50	9	839	150	1,562 [N=2]

Timed Events

Time	Type of Event	Parameter

Real-Time Plots

Type of Plot	Label	Low Mass	High Mass
Spectrum	N/A	N/A	N/A
Base Peak	N/A	N/A	N/A
Extracted Ion	Scan 1-1	9	839

Self-Cleaning Ion Source Parameters

Mode	No Cleaning

TABLE S 19 Instrumental control parameters for standard samples (calibration).

```
INSTRUMENT CONTROL PARAMETERS:    Agilent 5977B MSD System
----------------------------------------------------------

   D:\MassHunter\GCMS\1\methods\SureshNitrogent.m
      Thu Nov 21 12:13:57 2019

Control Information
------- -----------

Sample Inlet            : GC
Injection Source        : Manual
Mass Spectrometer       : Enabled


  No Sample Prep method has been assigned to this method.


GC
GC Summary
Run Time                              15.5 min
Post Run Time                         3 min

Oven
Equilibration Time                    0.2 min
Max Temperature                       320 °C
Maximum Temperature Override          Disabled
Slow Fan                              Disabled
Temperature
Setpoint                              On
(Initial)                             50 °C
Hold Time                             2 min
Post Run                              50 °C
Program
#1 Rate                               20 °C/min
#1 Value                              300 °C
#1 Hold Time                          1 min



Front SSZ Inlet He
Mode                                  Split
Heater                                On    250 °C
Pressure                              On    1.2 psi
Gas Saver                             Off
Split Ratio                           20 :1
Split Flow                            4.0835 mL/min

Thermal Aux 1 (MSD Transfer Line)
Temperature
Setpoint                              On
(Initial)                             300 °C
Post Run                              0 °C


Column
Column Outlet Pressure                0 psi
Column #1
Column Information                    Agilent CP7533
CP-Molsieve 5Å
Temperature Range                     -60 °C-350 °C (350 °C)
Dimensions                            25 m x 250 µm x 30 µm
In                                    Front SSZ Inlet He
Out                                   MSD
(Initial)                             50 °C


Pressure                              1.2 psi
Flow                                  0.20417 mL/min
Average Velocity                      18.04 cm/sec
Holdup Time                           2.3097 min
Flow
Setpoint                              Off
(Initial)                             0.20417 mL/min
Post Run                              1 mL/min
```

TABLE S 20 MS parameter report for N_2 quantification experiments and controls.

Single Quadrupole Acquisition Method - MS Parameters Report

Method file	D:\MassHunter\GCMS\1\methods\SureshN2O.m
Tune file	ATUNE.U
Ion source	EI
Source temperature (°C)	250
Quad temperature (°C)	150
Fixed Electron energy (eV)	70.0
Acquisition Type	Scan
Stop time (min)	650.00
Solvent delay (min)	0.00
Trace Ion Detection	False
Gain Factor	1
EM Saver	False
EM Saver Limit	N/A

Scan Time Segments

Time	Start Mass	End Mass	Threshold	Scan Speed
0.00	9	839	150	1,562 [N=2]
15.50	9	839	150	1,562 [N=2]

Timed Events

Time	Type of Event	Parameter

Real-Time Plots

Type of Plot	Label	Low Mass	High Mass
Spectrum	N/A	N/A	N/A
Base Peak	N/A	N/A	N/A
Extracted Ion	Scan 1-1	9	839

Self-Cleaning Ion Source Parameters

Mode	No Cleaning

TABLE S 21 Instrumental control parameters for N_2 quantification experiments and controls.

```
INSTRUMENT CONTROL PARAMETERS:    Agilent 5977B MSD System
--------------------------------------------------------------

    D:\MassHunter\GCMS\1\methods\SureshN2O.m
        Thu Nov 21 12:17:10 2019

Control Information
------- -----------


Sample Inlet              : GC
Injection Source          : Manual
Mass Spectrometer         : Enabled


  No Sample Prep method has been assigned to this method.


GC
GC Summary
Run Time                             16.25 min
Post Run Time                        3 min

Oven
Equilibration Time                   0.2 min
Max Temperature                      320 °C
Maximum Temperature Override         Disabled
Slow Fan                             Disabled
Temperature
Setpoint                             On
(Initial)                            50 °C
Hold Time                            2 min
Post Run                             50 °C
Program
#1 Rate                              20 °C/min
#1 Value                             150 °C
#1 Hold Time                         0 min
#2 Rate                              40 °C/min
#2 Value                             300 °C
#2 Hold Time                         5.5 min



Front SSZ Inlet He
Mode                                 Split
Heater                               On    250 °C
Pressure                             On    1.2 psi
Gas Saver                            Off
Split Ratio                          20 :1
Split Flow                           4.0835 mL/min

Thermal Aux 1 (MSD Transfer Line)
Temperature
Setpoint                             On
(Initial)                            300 °C
Post Run                             0 °C



Column
Column Outlet Pressure               0 psi
Column #1
Column Information                   Agilent CP7533
CP-Molsieve 5Å
Temperature Range                    -60 °C—350 °C (350 °C)
Dimensions                           25 m x 250 µm x 30 µm

In                                   Front SSZ Inlet He
Out                                  MSD
(Initial)                            50 °C
Pressure                             1.2 psi
Flow                                 0.20417 mL/min
Average Velocity                     18.04 cm/sec
Holdup Time                          2.3097 min
Flow
Setpoint                             Off
(Initial)                            0.20417 mL/min
Post Run                             1 mL/min
```

5.3.3   Computational Details for Optimization of Reactive Intermediate Structures

All the electronic structure calculations were carried out with Gaussian16.[2] The geometries were fully optimized at the B3LYP level of theory using the 6-31G(d) basis set. Frequencies were calculated for all structures to ensure the absence of imaginary frequencies for energy minima. The optimized XYZ coordinates are provided below.
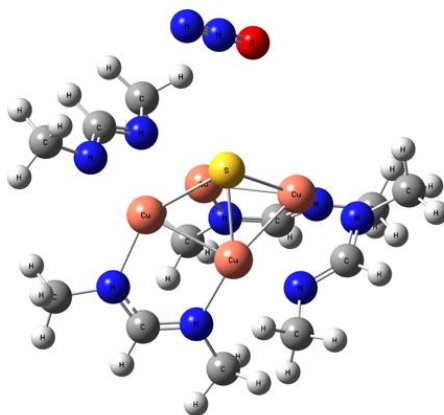
FIGURE S 120 $[Cu_4S(NCN)_4]^- + N_2O$ reactant

(Sum of electronic and thermal Free Energies= -8056.123923 Hartrees)

Center Number	Atomic Number	Atomic Type	Coordinates (Angstroms)		
			X	Y	Z
1	29	0	1.657760	-1.006228	-0.145533
2	16	0	-0.084767	-0.420511	-1.511342
3	7	0	3.310365	-0.570623	-1.173112
4	7	0	2.637751	1.670610	-1.179631
5	6	0	3.468181	0.697096	-1.504028
6	1	0	4.365554	0.962465	-2.095663
7	29	0	-1.573370	1.090212	-0.665257
8	7	0	-3.351214	0.189890	-0.675782
9	7	0	-2.485437	-1.442186	0.760724
10	6	0	-3.456923	-0.914550	0.038126
11	1	0	-4.433547	-1.435786	0.030363
12	29	0	-0.591586	-0.721877	0.656028

13	7	0	0.110119	-0.776851	2.473078
14	7	0	2.111394	-1.627766	1.635654
15	6	0	1.323805	-1.265286	2.634628
16	1	0	1.705495	-1.378955	3.665160
17	29	0	0.815173	1.283646	-0.385236
18	7	0	0.480304	2.714408	0.891126
19	7	0	-1.717299	2.857983	0.127375
20	6	0	-0.715297	3.269483	0.887202
21	1	0	-0.890675	4.130383	1.557014
22	6	0	-4.474344	0.540966	-1.516515
23	1	0	-4.770990	1.589668	-1.364395
24	1	0	-4.231649	0.432397	-2.586012
25	1	0	-3.834752	-2.985952	1.344666
26	1	0	-2.112820	-3.430170	1.353893
27	1	0	-2.761271	-2.401468	2.631856
28	6	0	-0.600073	-0.324481	3.649024
29	1	0	-0.709951	0.770833	3.650969
30	1	0	-1.613981	-0.745544	3.680326
31	1	0	-0.088593	-0.609423	4.584941
32	6	0	3.412187	-2.163927	1.982197
33	1	0	4.214427	-1.565094	1.529013
34	1	0	3.583645	-2.183372	3.072585
35	1	0	3.532552	-3.194997	1.614517
36	6	0	4.266847	-1.516503	-1.701493
37	1	0	5.112646	-1.024840	-2.215098
38	1	0	4.689937	-2.144759	-0.902715
39	1	0	3.800820	-2.202136	-2.427972
40	6	0	2.987608	3.004675	-1.619474
41	1	0	3.087641	3.697022	-0.769339
42	1	0	3.940654	3.030655	-2.177325
43	1	0	2.211381	3.424852	-2.276628
44	6	0	1.445109	3.190715	1.858053
45	1	0	1.635685	2.434880	2.635403

46	1	0	2.409162	3.400358	1.376260
47	1	0	1.112872	4.113691	2.364529
48	6	0	-2.961668	3.594258	0.223168
49	1	0	-2.911799	4.412849	0.962176
50	1	0	-3.238864	4.043810	-0.743382
51	1	0	-3.786355	2.930149	0.516916
52	7	0	-1.464493	-3.606168	-1.715601
53	7	0	-2.235795	-3.240037	-2.460056
54	8	0	-0.659023	-4.023242	-0.941303
55	1	0	-5.363410	-0.084734	-1.320375
56	6	0	-2.816524	-2.609833	1.551403
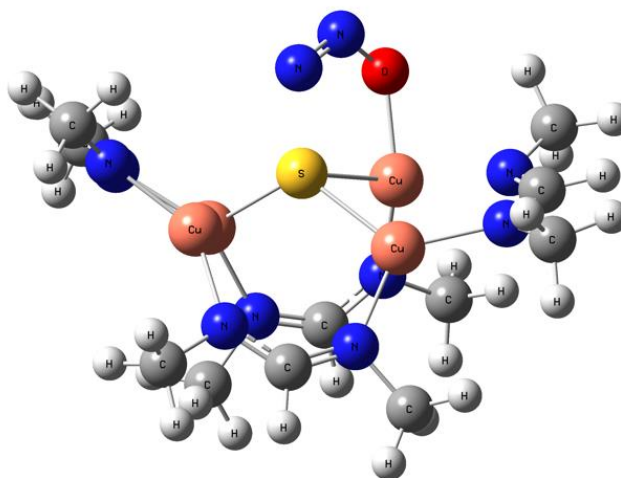
FIGURE S 121 $[Cu_4S(NCN)_4 \cdot N_2O]^-$ (Intermediate $[\mathbf{A}]^-$)

(Sum of electronic and thermal Free Energies= -8056.089054 Hartrees)

| Center | Atomic | Atomic | Coordinates (Angstroms) | | |
| Number | Number | Type | X | Y | Z |

| 1 | 29 | 0 | 1.748073 | -1.200321 | 0.053598 |
| 2 | 16 | 0 | -0.166276 | -0.379237 | -0.886533 |

3	7	0	3.681464	-0.937406	-0.352092
4	7	0	3.202753	1.220786	-1.134240
5	6	0	4.006638	0.183694	-0.967578
6	1	0	5.030874	0.260451	-1.374708
7	29	0	-2.206976	0.825488	-0.684920
8	7	0	-3.646248	-0.303734	-1.236558
9	7	0	-3.092219	-1.893194	0.384371
10	6	0	-3.816969	-1.468042	-0.636699
11	1	0	-4.625947	-2.122265	-1.002384
12	29	0	-1.520230	-0.928824	0.899167
13	7	0	-0.578469	-0.305691	2.442670
14	7	0	1.697274	-0.848898	1.990082
15	6	0	0.700100	-0.389412	2.739822
16	1	0	0.983693	-0.039649	3.748115
17	29	0	1.343790	1.230237	-0.578684
18	7	0	0.499051	2.678160	0.418184
19	7	0	-1.851977	2.560426	0.016066
20	6	0	-0.746327	3.107244	0.501828
21	1	0	-0.890077	4.057176	1.050795
22	6	0	-4.473869	-0.031939	-2.396351
23	1	0	-4.999363	0.928518	-2.289539
24	1	0	-3.869262	0.030583	-3.312787
25	1	0	-5.236072	-0.813066	-2.558509
26	6	0	-3.439345	-3.183641	0.949422
27	1	0	-4.277501	-3.662441	0.414883
28	1	0	-2.586571	-3.875410	0.910249
29	1	0	-3.729664	-3.091175	2.007286
30	6	0	-1.410219	0.387947	3.416305
31	1	0	-1.815746	1.314349	2.987642
32	1	0	-2.264556	-0.235999	3.711320
33	1	0	-0.852185	0.657666	4.329817
34	6	0	2.979148	-0.959884	2.677622
35	1	0	3.774086	-0.514737	2.072536

36	1	0	2.966568	-0.459898	3.659548
37	1	0	3.250770	-2.013242	2.852082
38	6	0	4.622023	-2.036620	-0.399179
39	1	0	5.582936	-1.745000	-0.855810
40	1	0	4.836779	-2.414385	0.612290
41	1	0	4.208802	-2.871512	-0.980226
42	6	0	3.769986	2.371364	-1.813321
43	1	0	3.809220	3.253985	-1.155627
44	1	0	4.796129	2.183538	-2.173648
45	1	0	3.161877	2.652270	-2.684381
46	6	0	1.458097	3.430477	1.216926
47	1	0	1.864598	2.812504	2.030752
48	1	0	2.310830	3.755336	0.606654
49	1	0	1.012681	4.330016	1.678039
50	6	0	-3.049566	3.383787	0.147428
51	1	0	-2.867218	4.301559	0.734785
52	1	0	-3.429625	3.697010	-0.836535
53	1	0	-3.857011	2.826872	0.639455
54	7	0	0.665077	-2.478618	-2.249101
55	7	0	-0.213487	-1.603639	-2.262770
56	8	0	1.581950	-2.549159	-1.294610
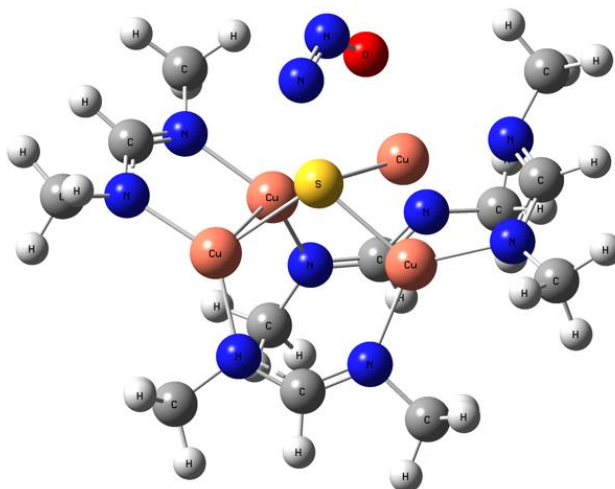
FIGURE S 122 $[Cu_4S(NCN)_4 \cdot N_2O]^{2-}$ (intermediate $[\mathbf{A}]^{2-}$)

(Sum of electronic and thermal Free Energies= -8056.023196 Hartrees)

Center Number	Atomic Number	Atomic Type	Coordinates (Angstroms)		
			X	Y	Z

1	29	0	1.322767	-1.153420	0.155424
2	16	0	-0.156893	-0.134094	-1.277041
3	7	0	3.334411	-1.121662	-0.519332
4	7	0	3.319902	1.150009	-1.069111
5	6	0	3.886636	-0.053383	-1.036662
6	1	0	4.897792	-0.148126	-1.493189
7	29	0	-2.114703	0.841058	-0.641773
8	7	0	-3.678631	-0.289004	-0.915928
9	7	0	-2.638024	-1.981529	0.313289
10	6	0	-3.588752	-1.540140	-0.477937
11	1	0	-4.371431	-2.255011	-0.802749
12	29	0	-1.112327	-0.828649	0.787722
13	7	0	-0.560596	-0.204115	2.534246
14	7	0	1.613863	-0.931015	2.106210
15	6	0	0.698847	-0.387947	2.886468
16	1	0	1.004331	-0.056420	3.899723

17	29	0	1.430966	1.266626	-0.571586
18	7	0	0.574186	2.875000	0.170149
19	7	0	-1.802888	2.639910	-0.006855
20	6	0	-0.679436	3.263758	0.322006
21	1	0	-0.815721	4.259458	0.794515
22	6	0	-4.805966	0.024103	-1.758878
23	1	0	-5.421988	0.838638	-1.336629
24	1	0	-4.484912	0.363515	-2.757650
25	1	0	-5.478055	-0.843231	-1.913859
26	6	0	-2.606202	-3.398649	0.598092
27	1	0	-3.445642	-3.947892	0.127513
28	1	0	-1.666819	-3.836687	0.235574
29	1	0	-2.653063	-3.585632	1.684177
30	6	0	-1.398505	0.552047	3.432073
31	1	0	-1.674105	1.527451	3.000307
32	1	0	-2.341986	0.020037	3.635213
33	1	0	-0.911437	0.750067	4.407949
34	6	0	2.910334	-1.158345	2.703230
35	1	0	3.701096	-0.830166	2.017966
36	1	0	3.041741	-0.622894	3.664974
37	1	0	3.089624	-2.230913	2.906370
38	6	0	4.046944	-2.367926	-0.665219
39	1	0	4.991578	-2.267982	-1.239309
40	1	0	4.306805	-2.797900	0.318512
41	1	0	3.412919	-3.108313	-1.170685
42	6	0	4.120090	2.219125	-1.612284
43	1	0	4.399504	2.969253	-0.848238
44	1	0	5.066255	1.858641	-2.064366
45	1	0	3.577717	2.769251	-2.397971
46	6	0	1.558882	3.803002	0.701861
47	1	0	2.167910	3.328771	1.485160
48	1	0	2.258419	4.136434	-0.079322
49	1	0	1.100179	4.710345	1.144594

50	6	0	-3.015786	3.388740	0.274754
51	1	0	-2.814516	4.373102	0.745516
52	1	0	-3.593696	3.581040	-0.643518
53	1	0	-3.679248	2.829739	0.950586
54	7	0	0.133604	-2.766047	-1.934426
55	7	0	-0.345226	-1.719586	-2.386161
56	8	0	0.769492	-2.863990	-0.781492
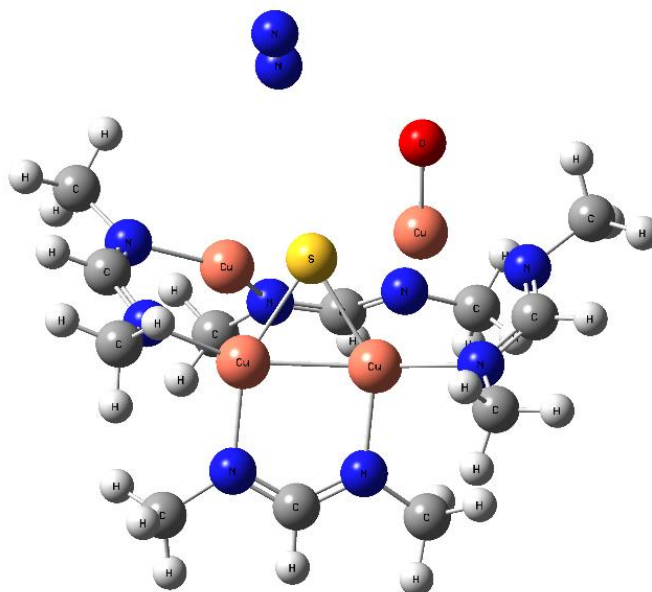
FIGURE S 123 $[Cu_4S(NCN)_4O]^-$ + N_2 (less favor [**B**]$^-$)

(Sum of electronic and thermal Free Energies= -8056.115109 Hartrees)

| Center | Atomic | Atomic | Coordinates (Angstroms) | | |
| Number | Number | Type | X | Y | Z |

1	29	0	-1.866880	1.326090	-0.154469
2	16	0	0.159632	0.505993	-1.184041
3	7	0	-3.659293	0.428143	-0.509013
4	7	0	-2.671468	-1.597804	-1.105371

5	6	0	-3.680063	-0.741693	-1.102629
6	1	0	-4.604284	-1.039234	-1.634830
7	29	0	1.434563	-1.108839	-0.494053
8	7	0	3.144828	-0.637913	-1.333167
9	7	0	3.259772	1.376033	-0.144295
10	6	0	3.735330	0.498108	-1.007632
11	1	0	4.704864	0.720829	-1.484218
12	29	0	1.505811	1.143135	0.603113
13	7	0	0.658252	1.130699	2.318642
14	7	0	-1.668005	1.015811	1.799898
15	6	0	-0.625570	1.008857	2.613969
16	1	0	-0.856636	0.883906	3.687156
17	29	0	-0.878925	-1.242516	-0.361607
18	7	0	-0.639228	-2.799877	0.773375
19	7	0	1.672571	-2.743424	0.531657
20	6	0	0.568519	-3.266609	1.030760
21	1	0	0.658231	-4.140788	1.699277
22	6	0	3.733042	-1.430335	-2.391182
23	1	0	3.851173	-2.477759	-2.078446
24	1	0	3.098499	-1.432336	-3.290761
25	1	0	4.727871	-1.058090	-2.688589
26	6	0	4.075449	2.545332	0.126810
27	1	0	4.998144	2.563562	-0.477880
28	1	0	3.521326	3.469085	-0.088459
29	1	0	4.371234	2.588801	1.186021
30	6	0	1.563586	1.033671	3.456440
31	1	0	2.226258	0.161574	3.364102
32	1	0	2.206950	1.922090	3.523161
33	1	0	1.025502	0.938939	4.416556
34	6	0	-2.962143	0.902958	2.465371
35	1	0	-3.565987	0.125246	1.988368
36	1	0	-2.860618	0.662936	3.536178
37	1	0	-3.530193	1.843039	2.390403

38	6	0	-4.836787	1.263390	-0.626866
39	1	0	-5.673937	0.741212	-1.122471
40	1	0	-5.189074	1.585196	0.365503
41	1	0	-4.604575	2.169971	-1.198951
42	6	0	-2.809664	-2.784850	-1.923809
43	1	0	-2.442717	-3.671249	-1.388235
44	1	0	-3.858754	-2.974480	-2.208406
45	1	0	-2.226491	-2.713430	-2.856151
46	6	0	-1.746944	-3.369451	1.518926
47	1	0	-2.027430	-2.738334	2.376575
48	1	0	-2.631278	-3.444338	0.878209
49	1	0	-1.512626	-4.374597	1.907276
50	6	0	2.929206	-3.398087	0.829744
51	1	0	2.822253	-4.171736	1.608555
52	1	0	3.357228	-3.886489	-0.060058
53	1	0	3.670179	-2.668935	1.180946
54	7	0	0.449869	4.348448	-0.726679
55	7	0	0.563679	4.521653	-1.812363
56	8	0	-1.911549	2.505144	-1.408863
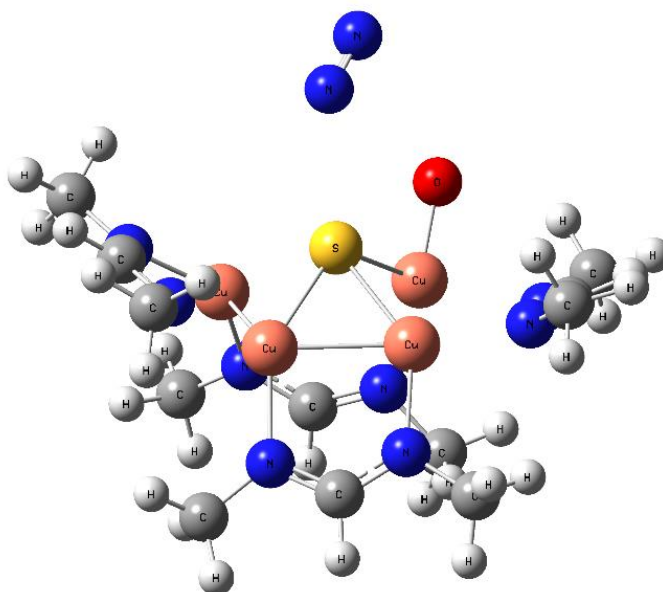
FIGURE S 124 [Cu$_4$S(NCN)$_4$·O]$^{2-}$ + N$_2$ (intermediate [**B**]$^{2-}$)

(Sum of electronic and thermal Free Energies= -8056.041476 Hartrees)

Center	Atomic	Atomic	Coordinates (Angstroms)		
Number	Number	Type	X	Y	Z

1	29	0	-1.504517	1.340190	0.188459
2	16	0	0.079577	0.551729	-1.162060
3	7	0	-3.573409	0.766194	0.228671
4	7	0	-3.100901	-1.146100	-1.047440
5	6	0	-3.873125	-0.127497	-0.684204
6	1	0	-4.852566	-0.028289	-1.206320
7	29	0	1.246061	-1.152783	-0.379468
8	7	0	3.010522	-1.163529	-1.353607
9	7	0	3.510282	1.008666	-0.642985
10	6	0	3.764587	-0.083106	-1.346917
11	1	0	4.686554	-0.088381	-1.965004
12	29	0	1.848248	1.098984	0.347019
13	7	0	1.259378	1.315599	2.160675

14	7	0	-1.029803	0.662984	2.023352
15	6	0	0.102866	0.893015	2.657556
16	1	0	0.090927	0.712887	3.753342
17	29	0	-1.129371	-1.252801	-0.623302
18	7	0	-0.989698	-3.029869	0.239576
19	7	0	1.224744	-2.664946	0.870419
20	6	0	0.096483	-3.341380	0.929578
21	1	0	0.051321	-4.221436	1.602897
22	6	0	3.443069	-2.265871	-2.174751
23	1	0	3.570439	-3.184629	-1.578338
24	1	0	2.698892	-2.502397	-2.952408
25	1	0	4.405874	-2.070385	-2.688751
26	6	0	4.425174	2.114528	-0.805874
27	1	0	5.273233	1.871675	-1.476865
28	1	0	3.919540	2.996959	-1.228591
29	1	0	4.851563	2.430577	0.160822
30	6	0	2.241231	1.705260	3.155201
31	1	0	3.206762	1.213457	2.972082
32	1	0	2.430925	2.792146	3.137706
33	1	0	1.926414	1.450893	4.188425
34	6	0	-2.031894	-0.051364	2.797461
35	1	0	-2.054628	-1.117568	2.524330
36	1	0	-1.837469	0.009648	3.885231
37	1	0	-3.025778	0.351410	2.586314
38	6	0	-4.502786	1.858290	0.393629
39	1	0	-5.447782	1.711494	-0.167483
40	1	0	-4.770772	1.996732	1.456837
41	1	0	-4.019319	2.778892	0.035509
42	6	0	-3.583323	-1.932747	-2.158192
43	1	0	-3.508670	-3.012731	-1.950414
44	1	0	-4.643139	-1.720621	-2.401731
45	1	0	-3.003087	-1.752012	-3.080001
46	6	0	-2.116303	-3.925759	0.390679

47	1	0	-3.044398	-3.345115	0.449392
48	1	0	-2.222305	-4.616849	-0.466684
49	1	0	-2.047687	-4.554248	1.299863
50	6	0	2.299861	-3.071175	1.740504
51	1	0	2.107458	-4.040442	2.241627
52	1	0	3.240028	-3.169552	1.176867
53	1	0	2.485877	-2.325556	2.531182
54	7	0	-0.059986	4.495306	-1.271857
55	7	0	-0.564977	5.386399	-1.704436
56	8	0	-1.811470	2.697947	-0.822496
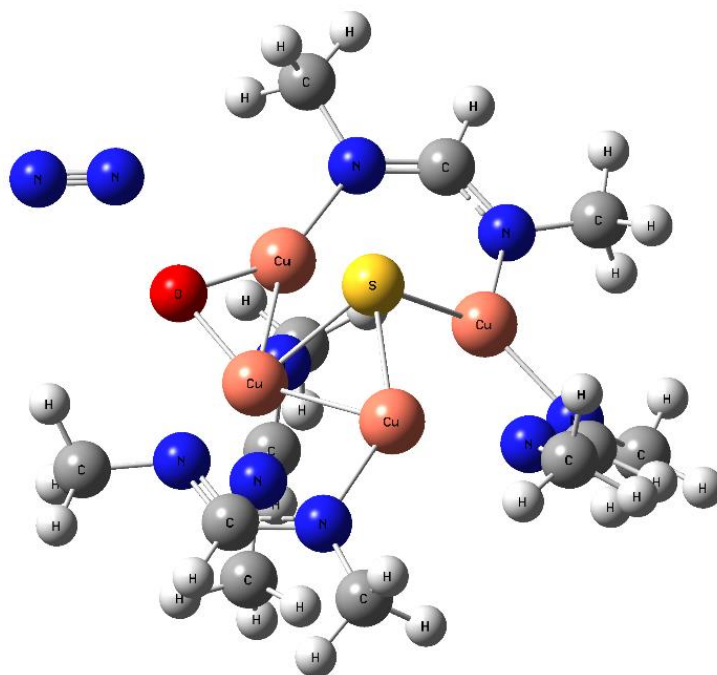
FIGURE S 125 $[Cu_4S(NCN)_4(\mu\text{-}O)]^{2-} + N_2$ (intermediate $[\mathbf{C}]^{2-}$)

(Sum of electronic and thermal Free Energies= -8056.063793 Hartrees)

| Center | Atomic | Atomic | Coordinates (Angstroms) | | |
| Number | Number | Type | X | Y | Z |

| 1 | 29 | 0 | 1.494333 | -1.474961 | -0.129385 |

2	16	0	0.144482	0.061156	-1.364978
3	7	0	3.310142	-0.924946	-0.658720
4	7	0	3.230421	1.405356	-0.277368
5	6	0	3.832210	0.283008	-0.642156
6	1	0	4.889787	0.369274	-0.973486
7	29	0	-1.726052	0.954971	-0.605614
8	7	0	-3.498452	0.492734	0.069930
9	7	0	-2.947542	-1.772287	0.148362
10	6	0	-3.801754	-0.794228	0.265412
11	1	0	-4.847724	-1.031265	0.558270
12	29	0	-0.936072	-1.210276	0.118057
13	7	0	-0.627287	-0.941671	2.191970
14	7	0	1.690451	-1.233489	1.954290
15	6	0	0.602344	-0.992396	2.660886
16	1	0	0.738965	-0.805832	3.752454
17	29	0	1.282483	1.601855	-0.205348
18	7	0	0.419944	3.271050	0.322435
19	7	0	-1.632555	2.961851	-0.826321
20	6	0	-0.710774	3.692865	-0.223364
21	1	0	-0.911420	4.787293	-0.161228
22	6	0	-4.584148	1.427011	0.265641
23	1	0	-4.225452	2.331636	0.775432
24	1	0	-5.046817	1.764940	-0.682428
25	1	0	-5.403339	1.006695	0.880186
26	6	0	-3.389437	-3.110873	0.441693
27	1	0	-4.479482	-3.174807	0.640090
28	1	0	-3.156489	-3.787010	-0.392997
29	1	0	-2.861258	-3.513864	1.319231
30	6	0	-1.675981	-0.667490	3.137986
31	1	0	-2.254268	0.221954	2.843125
32	1	0	-2.400783	-1.499497	3.196748
33	1	0	-1.298766	-0.493352	4.167506
34	6	0	2.945317	-1.196067	2.653922

35	1	0	3.618635	-0.433144	2.232483
36	1	0	2.832638	-0.972359	3.735602
37	1	0	3.482856	-2.160469	2.582939
38	6	0	4.130464	-1.977239	-1.218233
39	1	0	5.156078	-1.634120	-1.459937
40	1	0	4.219325	-2.822985	-0.519707
41	1	0	3.688803	-2.379430	-2.143248
42	6	0	4.083734	2.572470	-0.242850
43	1	0	4.235231	2.944934	0.786169
44	1	0	5.091909	2.384943	-0.667113
45	1	0	3.641106	3.402638	-0.813342
46	6	0	1.071887	4.231156	1.190156
47	1	0	0.984310	3.943455	2.251714
48	1	0	2.145613	4.298613	0.971848
49	1	0	0.645760	5.252016	1.098229
50	6	0	-2.590458	3.710008	-1.608316
51	1	0	-2.633631	4.782438	-1.325785
52	1	0	-2.359053	3.677067	-2.688475
53	1	0	-3.601160	3.298338	-1.492708
54	7	0	-0.282202	-3.853145	-2.390377
55	7	0	-0.565774	-4.909578	-2.193544
56	8	0	0.163804	-2.694146	-0.156844
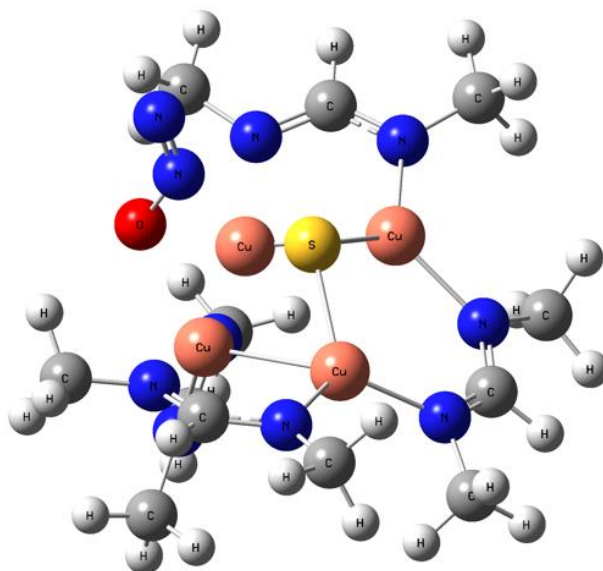
FIGURE S 126 Less favorable [Cu$_4$S(NCN)$_4$(μ-1,2 N$_2$O)]$^-$ isomer

(Sum of electronic and thermal Free Energies= -8056.004321 Hartrees)

Center	Atomic	Atomic	Coordinates (Angstroms)		
Number	Number	Type	X	Y	Z

1	29	0	1.286556	-1.082346	0.236256
2	16	0	0.000379	0.148080	-1.346530
3	7	0	3.177252	-1.496237	-0.375422
4	7	0	3.632380	0.764965	-0.747404
5	6	0	3.975584	-0.519854	-0.734678
6	1	0	5.009063	-0.776153	-1.053079
7	29	0	-1.728009	1.194206	-0.461643
8	7	0	-3.631220	0.768041	-0.747206
9	7	0	-3.178740	-1.493926	-0.376673
10	6	0	-3.975920	-0.516377	-0.735361
11	1	0	-5.009649	-0.771298	-1.054032
12	29	0	-1.288153	-1.082632	0.236154
13	7	0	-1.167898	-1.243204	2.208156
14	7	0	1.166407	-1.242907	2.208327

15	6	0	-0.000777	-1.266175	2.822048
16	1	0	-0.000860	-1.305439	3.932253
17	29	0	1.729678	1.193541	-0.462058
18	7	0	1.196950	2.914646	0.347050
19	7	0	-1.194107	2.915042	0.347646
20	6	0	0.001571	3.409585	0.622518
21	1	0	0.001875	4.379902	1.164950
22	6	0	-4.656745	1.699630	-1.149562
23	1	0	-4.918720	2.406647	-0.342004
24	1	0	-4.332531	2.316684	-2.004099
25	1	0	-5.597070	1.197454	-1.453494
26	6	0	-3.692320	-2.838079	-0.471315
27	1	0	-4.719710	-2.882731	-0.887605
28	1	0	-3.044916	-3.457335	-1.109102
29	1	0	-3.715981	-3.328691	0.516740
30	6	0	-2.343720	-1.261415	3.044463
31	1	0	-2.972689	-0.374670	2.870299
32	1	0	-2.979403	-2.137406	2.830389
33	1	0	-2.103052	-1.288282	4.126706
34	6	0	2.342146	-1.261054	3.044738
35	1	0	2.971006	-0.374201	2.870738
36	1	0	2.101375	-1.288093	4.126953
37	1	0	2.977967	-2.136921	2.830593
38	6	0	3.689374	-2.841026	-0.468758
39	1	0	4.716547	-2.887268	-0.885414
40	1	0	3.712917	-3.330596	0.519830
41	1	0	3.041013	-3.460261	-1.105580
42	6	0	4.658895	1.695064	-1.150677
43	1	0	4.921217	2.402889	-0.343951
44	1	0	5.598864	1.191613	-1.453607
45	1	0	4.335579	2.311306	-2.006153
46	6	0	2.308782	3.731143	0.797125
47	1	0	2.978513	3.160074	1.456780

48	1	0	2.925663	4.077692	-0.047859
49	1	0	1.984428	4.633019	1.355035
50	6	0	-2.305420	3.731904	0.798340
51	1	0	-1.980469	4.633499	1.356353
52	1	0	-2.922478	4.078926	-0.046318
53	1	0	-2.975134	3.160950	1.458106
54	7	0	-0.001022	-2.171519	-2.008362
55	7	0	-0.001535	-2.651019	-3.067289
56	8	0	-0.001187	-2.626015	-0.753321

5.3.4   Experimental Details for X-ray Absorption Spectroscopy data

All data were measured at the Stanford Synchrotron Radiation Lightsource (SSRL) under ring conditions of 3.0 GeV and 500 mA. Samples were prepared in an inert-atmosphere glovebox and were measured as solids. For Cu K-edge measurements, samples were ground with BN to a final concentration of 5 weight % Cu, pressed into 1 mm aluminum spacers and sealed with 37μm Kapton tape. For S K-edge measurements, samples were prepared by grinding to a fine powder and spreading thinly onto 38 μm low-S Mylar tape.

Cu K-edge measurements were carried out at either SSRL Beamline 9-3. Beamline 9-3 is equipped with a 16-pole, 2-Tesla wiggler source. Incident X-ray radiation was monochromated using a double Si(220) crystal monochromator. Samples were maintained at 10 K in a liquid He cryostat during data collection. Spectra were collected in fluorescence mode, with X-rays detected by a passivated implanted planar silicon (PIPS) detector placed at a 90° angle to the sample. Inelastic scatter was attenuated using a Soller slits fitted with a Ni filter. A Cu foil and a third ionization chamber upstream of the sample were used for internal energy calibration, setting the first inflection point of the Cu foil scan to 8980.3 eV. Data were collected from 8660 eV to 9380 eV. Three scans were measured and averaged for each compound. Spectra were processed using Sixpack[3] and Igor Pro. The region below 8970 eV was used to fit a linear background, while the region above 9000 eV was flattened with a piecewise spline and set to an average intensity of 1.0.

S K-edge measurements were carried out at SSRL Beamline 4-3, which is equipped with a 20-pole, 2 Tesla wiggler source. All samples were measured in a He atmosphere at room temperature in fluorescence mode using a Lytle detector. Intensity was normalized with respect to the incident beam using a He-filled ion chamber upstream of the sample. The incident beam energy was calibrated by setting the first inflection point in the S K-edge spectrum of $Na_2S_2O_3$ to 2472.02 eV. Data were collected from 2420 to 2700 eV. Three scans were measured and averaged for each compound. The region below 2460 eV was used to fit a linear background, and the region above 2475 eV was flattened with a piecewise spline and set to an average intensity of 1. Raw data was processed using Sixpack and Igor Pro. An in-house developed, Monte-Carlo based, nonlinear least squares fitting algorithm was used to fit the S K-edge XAS spectra in Python as described previously for N K-edge XAS.[4]
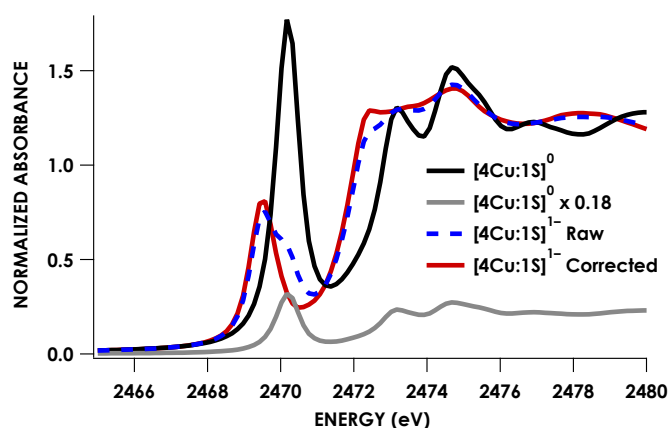
FIGURE S 127 The raw S K-edge XAS obtained for the $[4Cu:1S]^{1-}$ cluster contained a ca. 18% impurity of $[4Cu:1S]^{0}$. The proportion of impurity was determined by iteratively subtracting portions of the $[4Cu:1S]^{0}$ spectrum until the second derivative of the corrected $[4Cu:1S]^{1-}$ spectrum gave a single minimum in the pre-edge region.

Computational Details for X-ray Spectroscopy

Calculations carried out to facilitate XAS interpretation were carried out using version 4.0 of the ORCA quantum chemistry package.[5] For computational expediency, electronic structure calculations were carried out on crystallographic structures with NCN ligands whose mesityl substituents were truncated to methyl groups. H-atom positions of these structures were optimized using the BP86 generalized gradient approximation (GGA) density functional[6] with the scalar relativistically recontracted ZORA-def2-TZVP(-f)[7] basis set on all atoms. Solvation was

modeled with the conductor-like polarizable continuum model (CPCM) in the dielectric of CH_2Cl_2 (9.08). The zeroth-order regular approximation (ZORA)[9] as implemented by van Wüllen[10] was used to model relativistic effects.

TDDFT calculations[11] of the S K-edge XAS of the [4Cu:1S]$^{1-/0}$ redox series were carried out using the B3LYP hybrid density functional[12] with the CP(PPP) basis set[13] on Cu with a special grid accuracy of ORCA Grid7 and ZORA-def2-TZVP(-f)[7] basis set with a grid accuracy of ORCA Grid7 on S and ORCA Grid4 on all other atoms. The RIJCOSX approximation[14] was used to speed the calculation of Hartree-Fock exchange. A total of 100 roots were calculated with the S 1s orbital serving as the sole donor orbital and all vacancies allowed as acceptors. A 1 eV Gaussian line broadening was applied to all transitions to produce the final, plotted spectra. Calculated energies were shifted by +40.4 eV to align calculated data with experiment.

H-Atom Optimized Truncated Model of [4Cu:1S]^0

Cu -0.16712034498453	8.96786482433254	6.11520027228238
S 0.00094742532157	10.91177901281958	7.08515097396027
N 1.32125950507055	7.97309368900697	6.91516644755009
N 2.91450882321073	9.55216114905658	6.16060399143354
C 2.56366591700838	8.41714564585269	6.76364707087451
H 3.37628897367932	7.78917993059245	7.16946199906332
C 4.29975709876559	9.85662810328748	6.04820940596390
Cu -1.69883048725913	10.77703976118424	5.70336987733961
N -2.55368908864038	9.63250843515467	4.37313165049402
N -1.22688853217347	7.81164068122838	5.01638388328573
C -2.21172564118221	8.34840873538204	4.30182861125846
H -2.77287520048941	7.69328325946795	3.61223393418429
C -1.04863231047925	6.40100626037658	4.99940270304433
Cu 0.16853485025717	12.85606293978586	6.11523169624865
N -1.32056326591928	13.85003560101613	6.91493558823146
N -2.91452485491438	12.26906641356324	6.16542810430978
C -1.03018386207460	15.08700555130366	7.54139383892603
C -2.56292488315693	13.40480760172095	6.76657497050799
H -3.37497707885279	14.03212255654098	7.17445857610008
C -4.29975213975465	11.96233501569793	6.05860274441652

Cu 1.69920050388744   11.04540961135531   5.70182217262509

N 2.55265968153641   12.18910456591208   4.36979047557958

N 1.22781070078539   14.01088152105834   5.01520813678770

C 2.21114815067777   13.47324205589540   4.29922352587709

H 2.77199797811610   14.12819987563306   3.60918308852714

C 1.05298204043031   15.42196044722632   5.00072916849447

C 1.03010934056401   6.73730815623383   7.54343821189094

H 0.12557235948532   6.82026381710840   8.16615017745468

H 1.84893459935065   6.40497185355537   8.20923651212140

H 0.85270189074219   5.92174550892748   6.82269812686469

H -1.67334900045114   5.91923115009483   4.22418695480199

H -1.32083886386218   5.93909310901822   5.96345128650384

H -0.00184760590852   6.12908330392414   4.79041410782954

C 3.58375792872827   11.70608421179314   3.52448207469924

H 3.69866218673609   12.32648623685364   2.61647480018969

H 3.36706494294488   10.68172842601468   3.18686366416063

H 4.56862780896281   11.67956432654975   4.02166994086873

H 4.49618273708894   10.91166026707746   6.29380041928239

H 4.68372793275555   9.68549918614894   5.02832341857510

H 4.91941450210187   9.24601382966963   6.73130632662218

H 1.67988350012992   15.90371413715653   4.22726194216942

H 1.32533278726925   15.88127326312442   5.96595910064939

H 0.00716419100349   15.69704880623189   4.79100624331404

H -0.12583799472373   15.00559493675608   8.16463174914842

H -1.84956077208833   15.42024903750503   8.20601888852638

H -0.85280779567864   15.90131520660660   6.81925527329181

C -3.58763223689624   10.11514012570801   3.53137029146966

H -3.70302878722921   9.49683603361224   2.62199304506825

H -3.37400183831410   11.14087492860645   3.19605446609778

H -4.57164069057182   10.13828215204932   4.03053172119644

H -4.49346184310415   10.90699702778337   6.30503048167494

H -4.68802178923379   12.13288609701682   5.04024781751798

H -4.91773144866709   12.57201162042223   6.74410005064440

H-Atom Optimized Truncated Model of [4Cu:1S]$^{1-}$

Cu	7.03453113740897	7.55993973700832	11.05209362594193
Cu	9.47559039409535	7.22869884113902	10.88045109096620
Cu	8.96917609016007	7.61962029144022	8.24186262751464
Cu	6.51307031376902	7.37397611633347	8.39096489829336
S	7.97220485510672	6.18550118463537	9.59780835279663
N	7.38364684724101	8.91172040119965	12.41347861341600
N	9.64450372531640	8.30749224073309	12.49247419691284
N	11.24968319963926	6.52073406168340	10.29413006572949
N	10.84013556936995	6.92359771581322	8.00580364977950
N	8.67534108355277	9.06356870507787	6.96094989453601
N	6.39283392526912	8.54796572110296	6.84439374640637
N	4.71385084782665	6.70115572364220	8.94272739858532
N	5.13523949826517	6.93648829186997	11.25181244312673
C	8.59903121296441	8.99605315762092	12.94425529512397
H	8.75209986329926	9.67953115688900	13.80244171629646
C	6.35025288178661	9.76254832842535	12.86806525025677
C	10.86987522949424	8.38475797200440	13.20209296797282
C	11.57357070757024	6.44598293760471	9.00630418164364
H	12.52133850135693	5.92809748206697	8.74707038631889
C	11.29291487692464	6.71605329507202	6.68119145220354
C	7.46565763830179	9.21954307125744	6.43317270851326
H	7.34286731598966	9.95182532697273	5.61125458303900
C	9.73711861056280	9.89894476737125	6.54305172438304
C	5.18016472133609	8.70452901465385	6.12596136285546
C	4.38387941753758	6.55686843683470	10.22284891616851
H	3.41690188268257	6.05903640412195	10.44832021327123
C	3.83714991876594	6.24459034439722	7.93230333814167
C	4.67367304955783	6.67017601435347	12.56252696014419
H	9.42518559247431	10.62461482556143	5.76508469542065
H	10.58079443539921	9.32406126783157	6.12712332514499

H	10.14867526016778	10.48931114276728	7.38215446499560
H	10.52300135984795	6.22539468554427	6.05797893280268
H	12.19674773899361	6.07436417672314	6.63249857889314
H	11.54989101955935	7.65968808839939	6.16523476719763
C	12.11250170442186	5.97347878835987	11.26998944787322
H	12.90046571920146	5.32817203556993	10.82814549502925
H	11.55884865374053	5.34799076408306	11.99255666660225
H	12.63368554393406	6.74439960330587	11.86676363304763
H	11.70786309550291	8.64007102628213	12.53182552818208
H	11.13649948695993	7.42511029042553	13.68167824110703
H	10.84568040131011	9.14895182393129	14.00443668422985
H	5.48300579301647	9.19911756379213	13.24894227691069
H	5.96824370267652	10.41076560338081	12.05821511018203
H	6.68191644092665	10.43538319491228	13.68479983029382
H	3.75509124648444	6.04801382161376	12.57500666231676
H	4.43703148408244	7.59144573740967	13.12691651500946
H	5.43158110578411	6.13098177730917	13.15907842575013
H	4.37358049556054	5.64512059438439	7.17578316838019
H	3.34809995831152	7.06962208401423	7.38308957926065
H	3.02406207999242	5.60275150743267	8.33147194750251
H	5.23944598582331	9.51131547825375	5.36806431375095
H	4.34232569874404	8.95311470154421	6.79873779476944
H	4.88808268193335	7.78341267584340	5.58911225500993

5.4   Reference

[1]   (a) Johnson, B. J.; Antholine, W. E.; Lindeman, S. V; Mankad, N. P. *Chem. Commun.* **2015**, *51*, 11860. (b) Johnson, B. J.; Antholine, W. E.; Lindeman, S. V; Graham, M. J.; Mankad, N. P. *J. Am. Chem. Soc.* **2016**, *138*, 13107.

[2]   Gaussian 16, Revision B.01, Frisch, M. J.; Trucks, G. W.; Schlegel, H. B.; Scuseria, G. E.; Robb, M. A.; Cheeseman, J. R.; Scalmani, G.; Barone, V.; Petersson, G. A.; Nakatsuji, H.; Li, X.; Caricato, M.; Marenich, A. V.; Bloino, J.; Janesko, B. G.; Gomperts, R.; Mennucci, B.; Hratchian, H. P.; Ortiz, J. V.; Izmaylov, A. F.; Sonnenberg, J. L.; Williams-Young, D.; Ding, F.; Lipparini, F.; Egidi, F.; Goings, J.; Peng, B.; Petrone, A.; Henderson, T.; Ranasinghe, D.; Zakrzewski, V. G.; Gao, J.; Rega, N.; Zheng, G.; Liang, W.; Hada, M.; Ehara, M.; Toyota, K.; Fukuda, R.; Hasegawa, J.; Ishida, M.; Nakajima, T.; Honda, Y.; Kitao, O.; Nakai, H.; Vreven, T.; Throssell, K.; Montgomery, J. A., Jr.; Peralta, J. E.; Ogliaro, F.; Bearpark, M. J.; Heyd, J. J.; Brothers, E. N.; Kudin, K. N.; Staroverov, V. N.; Keith, T. A.; Kobayashi, R.; Normand, J.; Raghavachari, K.; Rendell, A. P.; Burant, J. C.; Iyengar, S. S.; Tomasi, J.; Cossi, M.; Millam, J. M.; Klene, M.; Adamo, C.; Cammi, R.; Ochterski, J. W.; Martin, R. L.; Morokuma, K.; Farkas, O.; Foresman, J. B.; Fox, D. J. Gaussian, Inc., Wallingford CT, 2016.

[3]   Webb, S. M. *Phys. Scr.* **2005**, 1011.

[4]   (a) Walroth, R. C.; Miles, K. C.; Lukens, J. T.; MacMillan, S. N.; Stahl, S. S.; Lancaster, K. M. *J. Am. Chem. Soc.* **2017**, *139*, 13507–13517. (b) Lukens, J. T.; DiMucci, I. M.; Kurogi, T.; Mindiola, D. J.; Lancaster, K. M. *Chem. Sci.* **2019**, *10*, 5044-5055. (c) Delgado-Jaime, M. U.; Mewis, C. P.; Kennepohl, P. *J. Synch. Rad.* **2010**, *17*, 132-137. (d) Hunter, J. D., *Comput. Sci. Eng.* **2007**, *9*, 90-95. € McKinney, W., *Proc. of the 9th Python in Science Conf.* **2010**, 51 - 56. (f) Walt, S. v. d.; Colbert, S. C.; Varoquaux, G., *Comput. Sci. Eng.* **2011**, *13*, 22-30. (g) Jones, E.; Oliphant, T.; Peterson, P. SciPy: Open Source Scientific Tools for Python. (f) Oliphant, T. E., *Comput. Sci. Eng.* **2007**, *9*, 10-20. (g) Millman, K. J.; Aivazis, M., *Comput. Sci. Eng.* **2011**, 13, 9-12.

[5]   Neese, F. *WIREs Comput. Mol. Sci.* **2012,** *2*, 73-78.

[6]   (a) Becke, A. D. *Phys. Rev. A: At., Mol., Opt. Phys.* **1988**, *38*, 3098−3100. (b) Perdew, J. P. *Phys. Rev. B: Condens. Matter Mater. Phys.* **1986**, *33*, 8822−8824.

[7]   Weigend, F.; Ahlrichs, R. *Phys. Chem. Chem. Phys.* **2005,** *7*, 3297-3305.

[8]   Takano, Y.; Houk, K. N. *J. Chem. Theor. Comput.* **2005**, *1*, 70-77.

[9]   van Lenthe, E.; van der Avoird, A.; Wormer, P. E. S. *J. Chem. Phys.* **1998,** *108*, 4783-4796.

[10]   van Wüllen, C. *J. Chem. Phys.* **1998**, *109*, 392-399.

[11]   (a) Gross, E. K. U.; Kohn, W. *Adv. Quantum Chem.* **1990**, 255-291. (b) Debeer George, S.; Neese, F. Calibration of scalar relativistic density functional theory for the calculation of sulfur K-edge X-ray absorption spectra. *Inorg. Chem.* **2010,** *49*, 1849-1853.

[12]   Stephens, P.; Devlin, F.; Chabalowski, C.; Frisch, M. J. *J. Phys. Chem.* **1994**, *98*, 11623−11627.

[13]   Neese, F. *Inorg. Chim. Acta.* **2002**, *337*, 181-192.
[14]   Neese, F.; Wennmohs, F.; Hansen, A.; Becker, U. *Chem. Phys.* **2009,** *356*, 98-109.

APPENDICES
<u>APPENDIX A</u>: Copyright permissions for Chapter 1

SPRINGER NATURE LICENSE
TERMS AND CONDITIONS

Apr 02, 2020

This Agreement between Suresh C Rathnayaka ("You") and Springer Nature ("Springer Nature") consists of your license details and the terms and conditions provided by Springer Nature and Copyright Clearance Center.

License Number	4800971052532
License date	Apr 02, 2020
Licensed Content Publisher	Springer Nature
Licensed Content Publication	Nature
Licensed Content Title	N2O binding at a [4Cu:2S] copper–sulphur cluster in nitrous oxide reductase
Licensed Content Author	Anja Pomowski et al
Licensed Content Date	Aug 14, 2011
Type of Use	Thesis/Dissertation
Requestor type	academic/university or research institute
Format	print and electronic
Portion	figures/tables/illustrations
Number of figures/tables/illustrations	1

High-res required	no
Will you be translating?	no
Circulation/distribution	1 - 29
Author of this Springer Nature content	no
Title	Synthesis and Analysis of Model Complexes of the Active Site of Nitrous Oxide Reductase
Institution name	University of Illinois at Chicago
Expected presentation date	May 2020
Portions	Figure 3(a,b and c) with figure captions
Requestor Location	Suresh C Rathnayaka 2851 S. King Drive Apt 1013 Chicago, IL 60616 United States Attn:
Total	0.00 USD

Terms and Conditions

Springer Nature Customer Service Centre GmbH
Terms and Conditions

This agreement sets out the terms and conditions of the licence (the **Licence**) between you and **Springer Nature Customer Service Centre GmbH** (the **Licensor**). By clicking 'accept' and completing the transaction for the material (**Licensed Material**), you also confirm your acceptance of these terms and conditions.

1. Grant of License

    1. 1. The Licensor grants you a personal, non-exclusive, non-transferable, world-wide licence to reproduce the Licensed Material for the purpose specified in your order

only. Licences are granted for the specific use requested in the order and for no other use, subject to the conditions below.

1. 2. The Licensor warrants that it has, to the best of its knowledge, the rights to license reuse of the Licensed Material. However, you should ensure that the material you are requesting is original to the Licensor and does not carry the copyright of another entity (as credited in the published version).

1. 3. If the credit line on any part of the material you have requested indicates that it was reprinted or adapted with permission from another source, then you should also seek permission from that source to reuse the material.

2. Scope of Licence

2. 1. You may only use the Licensed Content in the manner and to the extent permitted by these Ts&Cs and any applicable laws.

2. 2. A separate licence may be required for any additional use of the Licensed Material, e.g. where a licence has been purchased for print only use, separate permission must be obtained for electronic re-use. Similarly, a licence is only valid in the language selected and does not apply for editions in other languages unless additional translation rights have been granted separately in the licence. Any content owned by third parties are expressly excluded from the licence.

2. 3. Similarly, rights for additional components such as custom editions and derivatives require additional permission and may be subject to an additional fee. Please apply to Journalpermissions@springernature.com/bookpermissions@springernature.com for these rights.

2. 4. Where permission has been granted **free of charge** for material in print, permission may also be granted for any electronic version of that work, provided that the material is incidental to your work as a whole and that the electronic version is essentially equivalent to, or substitutes for, the print version.

2. 5. An alternative scope of licence may apply to signatories of the STM Permissions Guidelines, as amended from time to time.

3. Duration of Licence

3. 1. A licence for is valid from the date of purchase ('Licence Date') at the end of the relevant period in the below table:

Scope of Licence	Duration of Licence
Post on a website	12 months
Presentations	12 months
Books and journals	Lifetime of the edition in the language purchased

4. Acknowledgement

4. 1. The Licensor's permission must be acknowledged next to the Licenced Material in print. In electronic form, this acknowledgement must be visible at the same time as the figures/tables/illustrations or abstract, and must be hyperlinked to the journal/book's homepage. Our required acknowledgement format is in the Appendix below.

5. Restrictions on use

5. 1. Use of the Licensed Material may be permitted for incidental promotional use and minor editing privileges e.g. minor adaptations of single figures, changes of format, colour and/or style where the adaptation is credited as set out in Appendix 1 below. Any other changes including but not limited to, cropping, adapting, omitting material that affect the meaning, intention or moral rights of the author are strictly prohibited.

5. 2. You must not use any Licensed Material as part of any design or trademark.

5. 3. Licensed Material may be used in Open Access Publications (OAP) before publication by Springer Nature, but any Licensed Material must be removed from OAP sites prior to final publication.

6. Ownership of Rights

6. 1. Licensed Material remains the property of either Licensor or the relevant third party and any rights not explicitly granted herein are expressly reserved.

7. Warranty

IN NO EVENT SHALL LICENSOR BE LIABLE TO YOU OR ANY OTHER PARTY OR ANY OTHER PERSON OR FOR ANY SPECIAL, CONSEQUENTIAL, INCIDENTAL OR INDIRECT DAMAGES, HOWEVER CAUSED, ARISING OUT OF OR IN CONNECTION WITH THE DOWNLOADING, VIEWING OR USE OF THE MATERIALS REGARDLESS OF THE FORM OF ACTION, WHETHER FOR BREACH OF CONTRACT, BREACH OF WARRANTY, TORT, NEGLIGENCE, INFRINGEMENT OR OTHERWISE (INCLUDING, WITHOUT LIMITATION, DAMAGES BASED ON LOSS OF PROFITS, DATA, FILES, USE, BUSINESS OPPORTUNITY OR CLAIMS OF THIRD PARTIES), AND
WHETHER OR NOT THE PARTY HAS BEEN ADVISED OF THE POSSIBILITY OF SUCH DAMAGES. THIS LIMITATION SHALL APPLY NOTWITHSTANDING ANY FAILURE OF ESSENTIAL PURPOSE OF ANY LIMITED REMEDY PROVIDED HEREIN.

8. Limitations

8. 1. _**BOOKS ONLY:**_Where **'reuse in a dissertation/thesis'** has been selected the following terms apply: Print rights of the final author's accepted manuscript (for clarity, NOT the published version) for up to 100 copies, electronic rights for use only on a personal website or institutional repository as defined by the Sherpa guideline

(www.sherpa.ac.uk/romeo/).

9. Termination and Cancellation

9. 1. Licences will expire after the period shown in Clause 3 (above).

9. 2. Licensee reserves the right to terminate the Licence in the event that payment is not received in full or if there has been a breach of this agreement by you.

Copyright Clearance Center

RightsLink®

Home | Help | Email Support | Suresh Rathnayaka ⌄

Assembly, Structure, and Reactivity of Cu4S and Cu3S Models for the Nitrous Oxide Reductase Active Site, CuZ*

ACS Publications
Most Trusted. Most Cited. Most Read.

Author: Brittany J. Johnson, Sergey V. Lindeman, Neal P. Mankad

Publication: Inorganic Chemistry

Publisher: American Chemical Society

Date: Oct 1, 2014

Copyright © 2014, American Chemical Society

PERMISSION/LICENSE IS GRANTED FOR YOUR ORDER AT NO CHARGE

APPENDIX B: Copyright permissions for Chapter 2

Copyright Clearance Center

RightsLink®

Home   Help   Email Support   Suresh Rathnayaka ⌄

ACS Publications
Most Trusted. Most Cited. Most Read.

Multinuclear Cu(I) Clusters Featuring a New Triply Bridging Coordination Mode of Phosphaamidinate Ligands

Author: Suresh C. Rathnayaka, Sergey V. Lindeman, Neal P. Mankad

Publication: Inorganic Chemistry

Publisher: American Chemical Society

Date: Aug 1, 2018

Copyright © 2018, American Chemical Society

RightsLink®

Home   Help   Email Support   Suresh Rathnayaka ⌄

Impact of Electronic and Steric Changes of Ligands on the Assembly, Stability, and Redox Activity of Cu4(μ4-S) Model Compounds of the CuZ Active Site of Nitrous Oxide Reductase (N2OR)

ACS Publications
Most Trusted. Most Cited. Most Read.

Author: Suresh C. Rathnayaka, Chia-Wei Hsu, Brittany J. Johnson, et al

Publication: Inorganic Chemistry

Publisher: American Chemical Society

Date: Apr 1, 2020

Copyright © 2020, American Chemical Society

APPENDIX C: Copyright permissions for Chapter 3

JOHN WILEY AND SONS LICENSE
TERMS AND CONDITIONS

Apr 14, 2020

This Agreement between Suresh C Rathnayaka ("You") and John Wiley and Sons ("John Wiley and Sons") consists of your license details and the terms and conditions provided by John Wiley and Sons and Copyright Clearance Center.

License Number	4807451347232
License date	Apr 14, 2020
Licensed Content Publisher	John Wiley and Sons
Licensed Content Publication	Angewandte Chemie International Edition
Licensed Content Title	N2O Reductase Activity of a [Cu4S] Cluster in the 4CuI Redox State Modulated by Hydrogen Bond Donors and Proton Relays in the Secondary Coordination Sphere
Licensed Content Author	Chia-Wei Hsu, Suresh C. Rathnayaka, Shahidul M. Islam, et al
Licensed Content Date	Nov 14, 2019
Licensed Content Volume	59
Licensed Content Issue	2

234

Licensed Content Pages	5
Type of use	Dissertation/Thesis
Requestor type	Author of this Wiley article
Format	Print and electronic
Portion	Full article
Will you be translating?	No
Title	Synthesis and Analysis of Model Complexes of the Active Site of Nitrous Oxide Reductase
Institution name	University of Illinois at Chicago
Expected presentation date	May 2020
Requestor Location	Suresh C Rathnayaka 2851 S. King Drive Apt 1013 Chicago, IL 60616 United States Attn:
Publisher Tax ID	EU826007151
Total	0.00 USD

Terms and Conditions

TERMS AND CONDITIONS

This copyrighted material is owned by or exclusively licensed to John Wiley & Sons, Inc. or one of its group companies (each a"Wiley Company") or handled on behalf of a society with which a Wiley Company has exclusive publishing rights in relation to a particular work (collectively "WILEY"). By clicking "accept" in connection with completing this licensing transaction, you agree that the following terms and conditions apply to this transaction (along with the billing and payment terms and conditions established by the Copyright Clearance Center Inc., ("CCC's Billing and Payment terms and conditions"), at the time that you opened your RightsLink account (these are available at any time at http://myaccount.copyright.com).

Terms and Conditions

- The materials you have requested permission to reproduce or reuse (the "Wiley Materials") are protected by copyright.

- You are hereby granted a personal, non-exclusive, non-sub licensable (on a stand-alone basis), non-transferable, worldwide, limited license to reproduce the Wiley Materials for the purpose specified in the licensing process. This license, **and any CONTENT (PDF or image file) purchased as part of your order,** is for a one-time use only and limited to any maximum distribution number specified in the license. The first instance of republication or reuse granted by this license must be completed within two years of the date of the grant of this license (although copies prepared before the end date may be distributed thereafter). The Wiley Materials shall not be used in any other manner or for any other purpose, beyond what is granted in the license. Permission is granted subject to an appropriate acknowledgement given to the author, title of the material/book/journal and the publisher. You shall also duplicate the copyright notice that appears in the Wiley publication in your use of the Wiley Material. Permission is also granted on the understanding that nowhere in the text is a previously published source acknowledged for all or part of this Wiley Material. Any third party content is expressly excluded from this permission.

- With respect to the Wiley Materials, all rights are reserved. Except as expressly granted by the terms of the license, no part of the Wiley Materials may be copied, modified, adapted (except for minor reformatting required by the new Publication), translated, reproduced, transferred or distributed, in any form or by any means, and no derivative works may be made based on the Wiley Materials without the prior permission of the respective copyright owner.**For STM Signatory Publishers clearing permission under the terms of the STM Permissions Guidelines only, the terms of the license are extended to include subsequent editions and for editions in other languages, provided such editions are for the work as a whole in situ and does not involve the separate exploitation of the permitted figures or extracts,** You may not alter, remove or suppress in any manner any copyright, trademark or other notices displayed by the Wiley Materials. You may not license, rent, sell, loan, lease, pledge, offer as security, transfer or assign the Wiley Materials on a stand-alone basis, or any of the rights granted to you hereunder to any other person.

- The Wiley Materials and all of the intellectual property rights therein shall at all times remain the exclusive property of John Wiley & Sons Inc, the Wiley Companies, or their respective licensors, and your interest therein is only that of having possession of and the right to reproduce the Wiley Materials pursuant to Section 2 herein during the continuance of this Agreement. You agree that you own no right, title or interest in or

to the Wiley Materials or any of the intellectual property rights therein. You shall have no rights hereunder other than the license as provided for above in Section 2. No right, license or interest to any trademark, trade name, service mark or other branding ("Marks") of WILEY or its licensors is granted hereunder, and you agree that you shall not assert any such right, license or interest with respect thereto

- NEITHER WILEY NOR ITS LICENSORS MAKES ANY WARRANTY OR REPRESENTATION OF ANY KIND TO YOU OR ANY THIRD PARTY, EXPRESS, IMPLIED OR STATUTORY, WITH RESPECT TO THE MATERIALS OR THE ACCURACY OF ANY INFORMATION CONTAINED IN THE MATERIALS, INCLUDING, WITHOUT LIMITATION, ANY IMPLIED WARRANTY OF MERCHANTABILITY, ACCURACY, SATISFACTORY QUALITY, FITNESS FOR A PARTICULAR PURPOSE, USABILITY, INTEGRATION OR NON-INFRINGEMENT AND ALL SUCH WARRANTIES ARE HEREBY EXCLUDED BY WILEY AND ITS LICENSORS AND WAIVED BY YOU.

- WILEY shall have the right to terminate this Agreement immediately upon breach of this Agreement by you.

- You shall indemnify, defend and hold harmless WILEY, its Licensors and their respective directors, officers, agents and employees, from and against any actual or threatened claims, demands, causes of action or proceedings arising from any breach of this Agreement by you.

- IN NO EVENT SHALL WILEY OR ITS LICENSORS BE LIABLE TO YOU OR ANY OTHER PARTY OR ANY OTHER PERSON OR ENTITY FOR ANY SPECIAL, CONSEQUENTIAL, INCIDENTAL, INDIRECT, EXEMPLARY OR PUNITIVE DAMAGES, HOWEVER CAUSED, ARISING OUT OF OR IN CONNECTION WITH THE DOWNLOADING, PROVISIONING, VIEWING OR USE OF THE MATERIALS REGARDLESS OF THE FORM OF ACTION, WHETHER FOR BREACH OF CONTRACT, BREACH OF WARRANTY, TORT, NEGLIGENCE, INFRINGEMENT OR OTHERWISE (INCLUDING, WITHOUT LIMITATION, DAMAGES BASED ON LOSS OF PROFITS, DATA, FILES, USE, BUSINESS OPPORTUNITY OR CLAIMS OF THIRD PARTIES), AND WHETHER OR NOT THE PARTY HAS BEEN ADVISED OF THE POSSIBILITY OF SUCH DAMAGES. THIS LIMITATION SHALL APPLY NOTWITHSTANDING ANY FAILURE OF ESSENTIAL PURPOSE OF ANY LIMITED REMEDY PROVIDED HEREIN.

- Should any provision of this Agreement be held by a court of competent jurisdiction to be illegal, invalid, or unenforceable, that provision shall be deemed amended to achieve as nearly as possible the same economic effect as the original provision, and the legality, validity and enforceability of the remaining provisions of this Agreement shall not be affected or impaired thereby.

- The failure of either party to enforce any term or condition of this Agreement shall not constitute a waiver of either party's right to enforce each and every term and condition of this Agreement. No breach under this agreement shall be deemed waived or excused by either party unless such waiver or consent is in writing signed by the party granting such waiver or consent. The waiver by or consent of a party to a breach of any provision of this Agreement shall not operate or be construed as a waiver of or consent to any other or subsequent breach by such other party.

- This Agreement may not be assigned (including by operation of law or otherwise) by you without WILEY's prior written consent.

- Any fee required for this permission shall be non-refundable after thirty (30) days from receipt by the CCC.

- These terms and conditions together with CCC's Billing and Payment terms and conditions (which are incorporated herein) form the entire agreement between you and WILEY concerning this licensing transaction and (in the absence of fraud) supersedes all prior agreements and representations of the parties, oral or written. This Agreement may not be amended except in writing signed by both parties. This Agreement shall be binding upon and inure to the benefit of the parties' successors, legal representatives, and authorized assigns.

- In the event of any conflict between your obligations established by these terms and conditions and those established by CCC's Billing and Payment terms and conditions, these terms and conditions shall prevail.

- WILEY expressly reserves all rights not specifically granted in the combination of (i) the license details provided by you and accepted in the course of this licensing transaction, (ii) these terms and conditions and (iii) CCC's Billing and Payment terms and conditions.

- This Agreement will be void if the Type of Use, Format, Circulation, or Requestor Type was misrepresented during the licensing process.

- This Agreement shall be governed by and construed in accordance with the laws of the State of New York, USA, without regards to such state's conflict of law rules. Any legal action, suit or proceeding arising out of or relating to these Terms and Conditions or the breach thereof shall be instituted in a court of competent jurisdiction in New York County in the State of New York in the United States of America and each party hereby consents and submits to the personal jurisdiction of such court, waives any objection to venue in such court and consents to service of process by registered or certified mail, return receipt requested, at the last known address of such party.

WILEY OPEN ACCESS TERMS AND CONDITIONS

Wiley Publishes Open Access Articles in fully Open Access Journals and in Subscription journals offering Online Open. Although most of the fully Open Access journals publish open access articles under the terms of the Creative Commons Attribution (CC BY) License only, the subscription journals and a few of the Open Access Journals offer a choice of Creative Commons Licenses. The license type is clearly identified on the article.

The Creative Commons Attribution License

The Creative Commons Attribution License (CC-BY) allows users to copy, distribute and transmit an article, adapt the article and make commercial use of the article. The CC-BY license permits commercial and non-

Creative Commons Attribution Non-Commercial License

The Creative Commons Attribution Non-Commercial (CC-BY-NC)License permits use, distribution and reproduction in any medium, provided the original work is properly cited

and is not used for commercial purposes.(see below)

Creative Commons Attribution-Non-Commercial-NoDerivs License

The Creative Commons Attribution Non-Commercial-NoDerivs License (CC-BY-NC-ND)
permits use, distribution and reproduction in any medium, provided the original work is
properly cited, is not used for commercial purposes and no modifications or adaptations are
made. (see below)

Use by commercial "for-profit" organizations

Use of Wiley Open Access articles for commercial, promotional, or marketing purposes
requires further explicit permission from Wiley and will be subject to a fee.

Further details can be found on Wiley Online Library
http://olabout.wiley.com/WileyCDA/Section/id-410895.html

APPENDIX D: Copyright permissions for Chapter 4

Re-use permission requests

Material published by the Royal Society of Chemistry and other publishers is subject to all applicable copyright, database protection, and other rights. Therefore, for any publication, whether printed or electronic, permission must be obtained to use material for which the author(s) does not already own the copyright. This material may be, for example, a figure, diagram, table, photo or some other image.

Author reusing their own work published by the Royal Society of Chemistry

You do not need to request permission to reuse your own figures, diagrams, etc, that were originally published in a Royal Society of Chemistry publication. However, permission should be requested for use of the whole article or chapter except if reusing it in a thesis. If you are including an article or book chapter published by us in your thesis please ensure that your co-authors are aware of this.

Reuse of material that was published originally by the Royal Society of Chemistry must be accompanied by the appropriate acknowledgement of the publication. The form of the acknowledgement is dependent on the journal in which it was published originally, as detailed in 'Acknowledgements'.

VITA

NAME	Suresh Chandranath Rathnayaka
EDUCATION	Ph.D. Inorganic Chemistry, GPA 4.00/4.00 University of Illinois at Chicago USA, 2020
	B.Sc. Chemistry, Second Class (Upper Division) Honors GPA 3.55/4.00, University of Kelaniya Sri Lanka, 2013
TEACHING	Department of Chemistry, University of Illinois at Chicago 2015-2017
	General Chemistry II (CHEM 114) and Inorganic Chemistry (CHEM 314) undergraduate laboratory courses
	Department of Chemistry, University of Kelaniya Sri Lanka 2014-2015
	Organic Chemistry, Inorganic Synthesis and Analysis, Introductory Biochemistry and Basic Chemical Analysis undergraduate laboratory courses
AWARDS	Chemistry Teaching Assistant Appreciation Award for Fall 2015 at UIC

PUBLICATIONS

Rathnayaka, S. C.; Islam, S. M.; DiMucci, I.; MacMillan, S. N.; Lancaster, K.; Mankad, N. P. Probing the Electronic and Mechanistic Roles of the μ_4-Sulfur Atom in a Synthetic Cu_Z Model System. *Chem. Sci*. **2020,** *11*, 3441–3447. **Chem. Sci. Pick of the Week (HOT Article)**

Hsu, C. W.; **Rathnayaka, S. C.**; Islam, S. M.; MacMillan, S. N.; Mankad, N. P. N_2O Reductase Activity of a $[Cu_4S]$ Cluster in the $4Cu^I$ Redox State Modulated by Hydrogen Bond Donors and Proton Relays in the Secondary Coordination Sphere. *Angew. Chem. Int. Ed*. **2020**, *59*, 627-631. (**Co-first author**)

Rathnayaka, S. C.; Lindeman, S. V.; Mankad, N. P. Multinuclear Cu(I) Clusters Featuring a New Triply Bridging Coordination Mode of Phosphaamidinate Ligands. *Inorg. Chem.* **2018**, *57*, 9439–9445.

Rathnayaka, S. C.; Hsu, C. W.; Johnson. B. J.; Iniguez. S. J., Mankad. N. P. Impact of Electronic and Steric Changes of Ligands on the Assembly, Stability, and Redox Activity

of Cu$_4$(μ_4-S) Model Compounds of the Cu$_Z$ Active Site of Nitrous Oxide Reductase (N$_2$OR). Accepted to *Inorg. Chem.* **2020**, *59*, 6496–6507.

Rathnayaka, S.C.; Rathnayake, P. V. G. M.; Pandithavidana, D. R. Computational investigation of thermodynamic and kinetic feasibilities of cyclopropenone decarbonylating mechanism. *In proceedings of the 70th annual sessions of Sri Lanka Association of the Advancement of Science (SLAAS)*. **2014**, 135 (Abstract publication)

PRESENTATIONS   **Rathnayaka, S. C.**; Mankad, N. P. Synthesis and Analysis of Structural and Functional Models of the Active Site of Nitrous Oxide Reductase. *Great Lakes Regional Meeting Lisle, IL, May 1, 2019* (**oral** presentation)

Rathnayaka, S. C.; Mankad, N. P. Impact of Ligands and Secondary Structure Effects on the Stability, Redox Activity, and N$_2$O Reduction Activity of Cu$_4$(μ_4-S) Clusters: Model Compounds of the Active Site of Nitrous Oxide Reductase (N$_2$OR). Accepted for the *ACS Spring 2020 National Meeting & Expo, Philadelphia, PA, March 22-26, 2020* (**oral** presentation, cancelled due to COVID-19)

Rathnayaka, S. C.; Mankad, N. P. Design of Cu$_4$(μ_4-S) Clusters that Mimic the Structure and Function of the Active Site of Nitrous Oxide Reductase (N$_2$OR). Accepted for the *ACS Spring 2020 National Meeting & Expo, Philadelphia, PA, March 22-26, 2020* (**poster** presentation, cancelled due to COVID-19)